Detecting AIS position spoofing using LEO satellites, Doppler shifts, and MCMC methods.

- Master thesis -

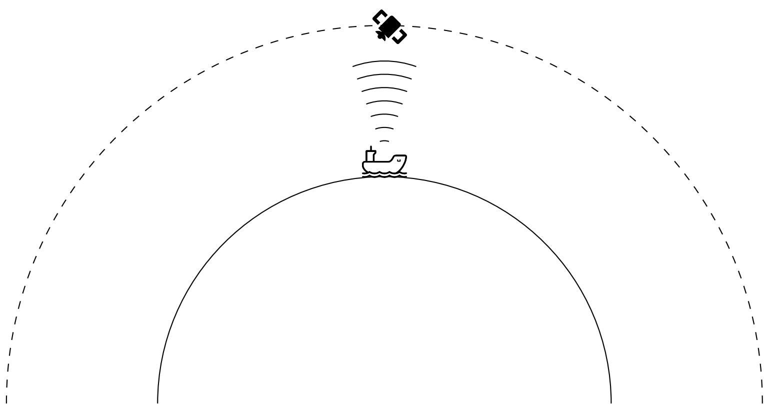

Gregersen, Emil Skovfoged
Nissen, Martin Mølbach

Aalborg University
Mathematical Engineering
2018

AALBORG UNIVERSITY
STUDENT REPORT

Department of Electronics and IT
& Department of Mathematical Sciences
Aalborg University
http://www.aau.dk

Title:
Detecting AIS position spoofing using LEO satellites, Doppler shifts and MCMC methods.

Project Period:
Autumn semester 2017 and spring semester 2018.

Project Group:
C4-212a

Participants:
Gregersen, Emil Skovfoged
Nissen, Martin Mølbach

Supervisors:
Møller, Jesper
Pedersen, Troels

Page Numbers: 187

Date of Completion:
2018/06/01

Abstract:

This master thesis is written in conjunction with nano-satellite manufacturer GomSpace. It concerns the use of Doppler shift data extracted from AIS signals received by low-earth-orbit satellites to detect AIS position spoofing. Vessels exceeding a certain size are required by law to send out AIS signals with their position encoded. The problem is that a vessel can falsify this information in said AIS signals. The act of doing so is referred to as AIS position spoofing. Spoofing of a vessel's position can be of interest if said vessel is e.g. fishing in protected waters. The system encompassing the vessel, the radio channel and the satellites is referred to as the space-based AIS system. The observable and unobserved variables that can aid in AIS position spoofing detection in this system are explored in this thesis. In order to determine whether AIS position spoofing is occuring in a given scenario, probability models describing the relationships between the variables in the system are created. The spoofing detection then consists of performing inference in the probability models using Markov chain Monte Carlo methods. The scenarios in which the developed methods are tested are constructed in order to determine how far away from its true position a vessel has to spoof its position in order for the developed methods to detect the spoofing. Results show that in some cases the developed methods can detect spoofing when a vessel is spoofing its position $5 - 10$ km away.

Preface

This thesis is written in the period from the 4th of September 2017 to the 1st of June 2018 by us, students at the 10. semester of the Mathematical Engineering education at Aalborg University. During this period, we were attached to both the Department of Electronics and IT and the Department of Mathematical Sciences, hence why our two supervisors are from each of the two departments, respectively.

The topic of this thesis is to use the Doppler shifts experienced by low-earth-orbit satellites to detect position spoofing by vessels at sea transmitting AIS signals.

We would like to thank Troels Pedersen and Jesper Møller for supervising this thesis, suggesting literature, and enlightening discussions on the direction of this thesis.

Aalborg University, 2018/06/01

Gregersen, Emil Skovfoged
<egrege12@student.aau.dk>

Nissen, Martin Mølbach
<mnis13@student.aau.dk>

Danish summary

Dette kandidat speciale er skrevet i samarbejde med nanosatellit producent virksomheden GomSpace. Specialet undersøger hvorvidt Doppler skift estimater udvundet fra AIS signaler sendt ud fra et skib og modtaget af GomSpaces satellitter kan benyttes til at beslutte om skibet forsøger at forfalske sin position. Det er lovpligtigt for skibe over en hvis størrelse at udsende AIS signaler, der blandt andet indeholder information om skibets position, fart, samt identifikationsnummer. Indkodningen af denne information foregår ombord på skibet. I og med at indkodningen af information forløber ombord på skibet, kan et skib vælge at kode falsk information om eksempelvis dets position ind i AIS signalet. Et eksempel på et tilfælde hvor besætningen ombord på et skib kunne finde på at udsende falsk information om deres position, er hvis skibet udøver piratfiskeri. I dette tilfælde vil det være oplagt for besætningen af få det til at se ud som om de befinder sig et andet sted, end hvor de i virkeligheden er. Systemet bestående af skibet, satellitten og radio kanalen imellem dem kaldes i dette speciale for space-based AIS systemet.

Måden hvorpå problemet om hvorvidt det ud fra Doppler skift estimater kan bestemmes om et skib forsøger at forfalske sin position er forsøgt løst, er ved først at undersøge hvorvidt det er muligt at modtage AIS signaler på GomSpace's satellitter. Denne undersøgelse har taget udgangspunkt i et af GomSpaces eksisterende satellit projekter, der går under navnet Starling projektet. Herefter er det undersøgt og analyseret hvilke observerbare og uobserverbare variable, der, udover Doppler skiftene, eksisterer i systemet. Herefter er der opstillet sandsynlighedsmodeller, der modellerer både de observerede og uobserverede variable i systemet. For at udføre statistisk inferens i de opstillede modeller, er der opbygget algoritmer baseret på Markovkæde Monte Carlo metoder. Mere specifikt er disse algoritmer bygget på Metropolis within Gibbs samplere.

I specialeperioden har der ikke været data fra satellitter tilgængeligt til at teste de udviklede algoritmer, og det har derfor været nødvendigt at simulere data til brug i de tests af algoritmerne, der er blevet udført. Dette data er simuleret under realistiske antagelser omkring hvordan space-based AIS systemet opfører sig, og inkluderer fejlmodellering. De test, der er blevet udført i dette speciale, omfatter detektion af forfalskning af positions information i tilfælde hvor både én og to satellitter benyttes til detekteringen. I begge disse tilfælde er det blevet testet hvor langt fra sin sande position et skib skal forfalske sin position for at de udviklede algoritmer kan detektere forfalskningen.

Resultater fra de udførte tests viser, at de udviklede algoritmer i nogle af de tilfælde

hvor en enkelt satellit benyttes, kan detektere når et skib forfalsker sin position 20 kilometer væk fra sin sande position. Derudover viser de tests, der er udført med to satellitter, at forfalskning af skibspositionen i nogle tilfælde kan detekteres når skibet blot forfalsker sin position $5 - 10$ kilometer væk fra sin sande position.

Contents

Lists of notation and fixed parameters

$\boldsymbol{x} \in \mathbb{C}^N$	N-dimensional vector.
$x^{(n)}$	n'th element of vector $\boldsymbol{x}$.
$\boldsymbol{X} \in \mathbb{C}^{m \times n}$	$(m \times n)$-dimensional matrix.
$\boldsymbol{x}^{(n)}$	n'th column of the matrix $\boldsymbol{X}$.
$x^{(i,j)}$	(i,j)'th entry of matrix $\boldsymbol{X}$.

Moreover, when a given symbol appears both with and without a tilde, e.g. ν and $\tilde{\nu}$, then ν is equal to $\tilde{\nu}$ and a noise contribution. This notation is used when simulating observed data.

Fixed parameters			
Description	**Symbol**	**Value**	**Unit**
Earth radius	R_E	6378.137	km
Speed of light	c	299792.458	km s^{-1}
Earth standard gravitational parameter	η	$3.986004418{\cdot}10^5$	km^3s^{-2}
AIS channel 1 frequency	f_1	161.975	MHz
AIS channel 2 frequency	f_2	162.025	MHz
AIS data rate	r_b	9600	bps
AIS message duration	T_{AIS}	0.02667	s
Earth angular rotation speed	ω_E	$7.272205 \cdot 10^{-5}$	rad s^{-1}
Boltzmann constant	k_0	-228.6	dBW/K/Hz
AIS message bit length	N_{bit}	256	
Day duration	T_E	86400	s

Table 1: Fixed parameters used in this thesis.

1 Introduction

The Automatic Identification System (AIS) is a radio communication system developed in the 1990s. AIS operates in the very high frequency (VHF) band. The VHF band is the radio wave band from 30 to 300 MHz [40]. Vessels use AIS to transmit AIS signals in which their identity, position, heading, velocity, and other parameters, the collection of which is referred to as an *AIS message*, are encoded. Originally, AIS was developed to ensure that a given vessel was aware of the identity, position etc. of surrounding vessels within a range limited by the horizon. This range is approximately 10-20 nautical miles, or 18.5 – 37.0 km.

More recently, space-based AIS reception, i.e. reception of AIS signals in space using low-earth-orbit (LEO) satellites has been considered, as illustrated in Figure 1.1. However, the AIS was not originally developed with space-based reception in mind. Being able to receive AIS signals from space has the potential to provide global vessel surveillance coverage.

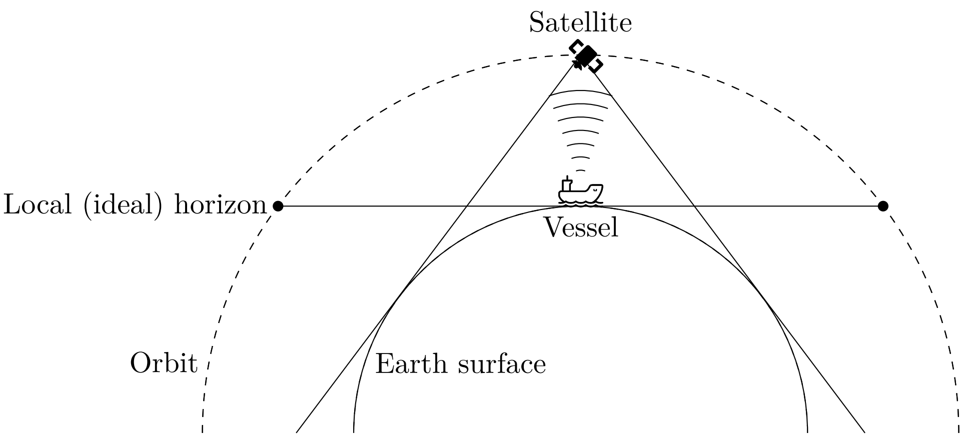

Figure 1.1: LEO satellite receiving an AIS signal transmitted by a vessel.

AIS signals are transmitted over two channels, corresponding to carrier frequencies of 161.975 MHz and 162.025 MHz [13, p. 912108-2], and vessels alternate between these frequencies when transmitting their AIS messages. These channels are referred to as AIS channel 1 and 2, respectively.

International maritime law requires internationally voyaging ships to be equipped with AIS transponders if they exceed 300 gross tons. Gross tonnage is a measure of the internal volume of a vessel. The definition can be found in [37]. Likewise, passenger vessels, independent of their size and weight, are required to be equipped with AIS.

Sea vessels can be categorized into two classes called class A and B. Class A is used by larger vessels and transmits signals carrying more information than class B, which are carried by smaller vessels. Smaller vessels include e.g. leisure vessels. Class A transmitters use more power when transmitting their AIS signals than class B transmitters, resulting in the AIS signals transmitted by class A vessels being able to travel further than those transmitted by class B vessels. Since class A is mandatory for both passenger vessels and vessels exceeding 300 gross tons, and since their AIS signals are transmitted using more power, this will be the class of vessels focused on in this thesis.

AIS is a self-reporting system. When a vessel transmits, amongst other parameters, its positional information, this information stems from a sensor on board the vessel. The naturally underlying assumption in AIS is that the information encoded in the transmitted signals is trustworthy. With the rise of space-based AIS reception and potentially global surveillance capacity, it may be wise to not blindly trust the positional information reported by a given vessel [4]. An example of why a given vessel would want to mask its true position is that of a vessel fishing in protected waters. Figure 1.2 shows an example, in which a vessel is fishing in what could be a protected fjord in Greenland. The vessel falsifies the positional information encoded in the AIS signal, an act referred to as *spoofing*. The positional information is falsified to indicate a position in which the vessel is allowed to fish. Space-based AIS reception can potentially also provide the

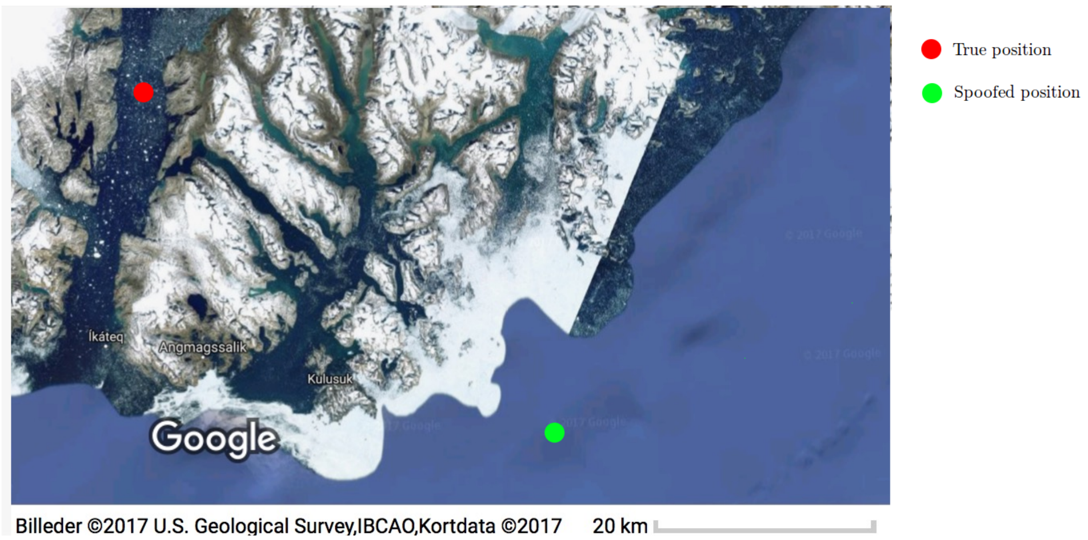

Figure 1.2: Illustration of vessel positional spoofing in a fjord in Greenland.

solution to the problem of spoofed positional information [13, p. 912108-1]. Using LEO satellites, as illustrated in Figure 1.1, spoofed AIS signals can be received, and, possibly, categorized as spoofed signals. In the case of position spoofing, being able to detect this spoofing is desireable. Ideally, this detection is to be based on the physical information about the received AIS signal in conjunction with the information encoded in the AIS signal. The general system is illustrated in Figure 1.3. This system will be referred to as the *space-based AIS system*. This leads to the core problem of this thesis, namely to

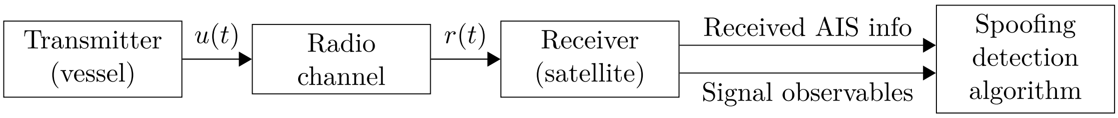

Figure 1.3: Block diagram illustration of the space-based AIS system. It includes transmission of an AIS signal, $u(t)$, the channel that $u(t)$ has to travel through to arrive at the satellite, and the satellite receiving the signal $r(t)$, consisting of the AIS signal along with interfering signals and noise. Finally, it includes the received AIS info (from the AIS message) and AIS signal observables, which are to be used in spoofing detection algorithms.

be able to detect AIS position spoofing using one or more LEO satellites. In order to choose the approach that will be used to solve the problem in this thesis, the following system analysis questions need to be answered.

- What is AIS and how does it work?
- How is the LEO satellite orbit geometry?
- Based on a GomSpace satellite project, what are the conditions under which space-based AIS reception is feasible?
- Which observable variables exist in the space-based AIS system that can potentially help solve the problem of AIS position spoofing detection?

GomSpace is a nano-satellite manufacturer, and this thesis is written in conjunction with this company.

The GomSpace satellite project under consideration in this thesis is known as the Starling project. Starling is a constellation of LEO satellites equipped with AIS signal receivers. Parallels to the Starling project will be drawn in this thesis, especially when presenting a link budget showing the feasibility of space-based reception of AIS signals. This link budget is heavily influenced by the link budget of the Starling project. Moreover, a selection of satellite and orbit parameter values in this thesis are chosen based on the Starling values for these parameters. When this is the case, it will be stated.

After analyzing the above questions in the succeeding chapters, the final problem statement of this thesis is given in Chapter 5. Chapter 2 serves as a preliminary for later analysis of the space-based AIS system. In Chapter 3, a link budget heavily influenced by the Starling project is presented, in order to examine the feasibility of space-based AIS signal reception. In chapter 4, an analysis of the space-based AIS system analysis is found, wherein the observable variables within the system that can potentially help solve the problem of this thesis are examined. Notice that all data used in the developed algorithms for spoofing detection in this thesis is simulated data, since no real-world data has been available.

2 | Space-based AIS system preliminaries

This chapter serves as preliminary information for the later space-based AIS system analysis. Initially, the chapter describes AIS. As mentioned in the introduction to this thesis, it is the position information encoded in AIS signals that can be subject to spoofing. Moreover, terms and concepts from LEO satellite orbit geometry needed in this thesis are introduced. Eventually, an effect known as the Doppler shift, which is experienced when receiveing signals at LEO satellites, is described.

2.1 Automatic identification system (AIS)

In the early 1990s, a proposal that vessels should be required by law to carry AIS equipment was set forth by the International Association of Marine Aids to Navigation and Lighthouse Authorities. This proposal was accepted by the International Maritime Organization (IMO), and AIS was made mandatory [16, p. 8]. Vessels send out AIS signals with AIS messages containing data such as their position, velocity, heading etc. The signals are sent out using carrier frequencies in the VHF band, which is the range of frequencies from 30-300 MHz. The IMO requested for two channels in the VHF band to be assigned to the use of AIS. The carrier frequencies, f_c, of these channels are $f_1 = 161.975$ and $f_2 = 162.025$ MHz, referred to as AIS channel 1 and 2, respectively. Vessels alternate between these two channels when sending out their AIS messages [16, p. 40].

When using either of the AIS channels, vessels are allowed to use carrier frequencies varying by up to ± 3 parts per million (ppm), creating frequency offsets from the designated AIS carrier frequencies of [31, p. 85]

$$f_{off} \in [-\Delta, \Delta], \qquad \text{(Hz)} \qquad (2.1)$$

where

$$\Delta = \begin{cases} 486.075 & \text{if } f_c = f_2 \\ 485.925 & \text{if } f_c = f_1. \end{cases}$$

The frequency offset in (2.1) is referred to as the AIS frequency offset.

Two categories of AIS shipborne equipment exist; class A and class B. Class A is shipborne mobile equipment using self-organized time division multiple access (SOTDMA) technology in compliance with requirements set forth by the IMO. For more details on SOTDMA, see Appendix K. Class B is shipborne mobile equipment not necessarily in compliance with the requirements set forth by the IMO [31, p. 6].

AIS was developed with collision avoidance and maritime security in mind. The system allows vessels to exchange the navigational information in their AIS messages between eachother or the shore. One of the important pieces of navigational information in the AIS messages is the position information, which is usually obtained using GPS [16, p. 44]. The AIS messages are sent out using the SOTDMA scheme at a data-rate r_b of 9600 bps using Gaussian minimum shift keying (GMSK) modulation. For a description of GMSK, see Appendix J. The AIS data in the AIS message is encoded using a non-return-to-zero inverted (NRZI) waveform. For a description of NRZI encoding, see Appendix J, Section J.4. The NRZI waveform is encoded using GMSK, and is then modulated onto the carrier wave with frequency correponding to one of the two AIS channels. For class A vessels, the resulting AIS signal, containing the AIS message, is sent out with transmission power 12.5 W. When operating on a single AIS channel, AIS fits 2250 AIS messages into one minute, and this capacity is doubled when both AIS channels are used.

A receiving vessel can receive AIS messages from other vessels, when said vessels are in the line-of-sight of the receiving vessel. If the number of vessels within the line-of-sight of a receiving vessel exceed the AIS message capacity in regards to how many AIS messages can be fit into one minute, the SOTDMA scheme reduces the range within which the receiving vessel can receive AIS messages. This is done by suppressing AIS message transmissions from far away, prioritizing those close to the receiving vessel [1].

A vessel encodes the information in an AIS message as part of a length-256 bit-string [31, pp. 24-26]. This is illustrated in Figure 2.1. The number of bits in an AIS message is denoted $N_{bit} = 256$.

8 bits	24 bits	8 bits	168 bits	16 bits	8 bits	24 bits
Ramp up	Training sequence	Start flag	Data	CRC	End flag	Buffer

Figure 2.1: AIS message bit string [31, p. 24].

The parts of these 256 bits that are significant for this thesis are the 168 bits containing the vessel data, the start and end flags, and the cyclic redundancy check (CRC). This thesis assumes that for successful decoding of the vessel data in an AIS message, none of the bits in these parts of the overall bit-string can be received in error.

The data part of the bit-string is divided into subsequences of varying length, each representing certain information about the vessel. An overview of the information encoded in the data bit-string is seen in Table 2.2. Notice that the table only shows the parts of the length-168 data bit-string relevant to this thesis.

Field (bit #)	Description
$0 - 5$	Message type
$8 - 37$	MMSI
$50 - 59$	Speed over ground
$60 - 60$	Position accuracy
$61 - 88$	Longitude
$89 - 115$	Latitude

Figure 2.2: Table of data field bit subsequences and which information they contain [29].

In Table 2.2, message type covers several different types of AIS messages. The ones relevant for this thesis are the ones indicating whether the AIS message is sent out by a class A vessel. MMSI is a unique vessel identification number, speed over ground is the speed of the vessel, and the position accuracy indicates whether the reported position has an accuracy of above or below 10 m.

Given that an AIS message is encoded as a length-265 bit-string, the AIS data-rate of 9600 bps yields the AIS message duration

$$T_{AIS} = \frac{256}{9600} \approx 0.02667. \qquad \text{(s)} \qquad (2.2)$$

Vessels using AIS are required to report, i.e. transmit their AIS information, at different time intervals. These time intervals depend on the state of the vessel, including whether the vessel is anchored, moored or changing course, along with the vessel's speed over ground (SOG). An overview of the different states a given class A vessel can be in, and the corresponding reporting intervals, t_r, is seen in Table 2.1 [31, p. 8].

Class A vessel reporting intervals	
Vessel status	Reporting intervals, t_r
If at anchor or moored, and not moving faster than 3 knots.	180 s
If at anchor or moored, and moving faster than 3 knots.	10 s
SOG $0 - 14$ knots and steady course.	10 s
SOG $0 - 14$ knots and changing course.	3.3 s
SOG $14 - 23$ knots and steady course.	6 s
SOG $14 - 23$ knots and changing course.	2 s
SOG > 23 knots and steady course.	2 s
SOG > 23 knots and changing course.	2 s

Table 2.1: States and reporting intervals for a class A vessel.

A knot is equal to a speed of one nautical mile per hour, where one nautical mile is equal to 1852 m. Hence, the conversion between knots and km/h is such that a speed of one knot is equal to 1.852 km/h.

2.2 Low-earth-orbit satellites and orbit geometry

In order to investigate the feasibility of space-based AIS signal reception using LEO satellites, the geometry of the orbits of these satellites is explored. A satellite orbit is the path followed by the satellite in space. This path lies in a plane, referred to as the orbit plane. LEO satellites travel in circular orbits with constant altitude [24, p. 10]. The altitudes for LEO satellites are approximately between 160 and 1500 km [17, p. 28].

The LEO satellites manufactured by GomSpace are known as cubesats. Cubesats are small satellites made up of $10 \times 10 \times 10$ cm cube units. The LEO satellites used in the Starling project are $3U$ cubesats, which means that they are made out of 3 of the above mentioned cube units. All satellites manufactured by GomSpace fall within a category called nano-satellites, which is a class of satellites with mass between 1 and 100 kg.

Figure 2.3 illustrates the field-of-view (FoV) of an LEO satellite. In this thesis, the FoV for a given moment in time is defined as the part of Earth from which an LEO satellite can receive AIS signals.

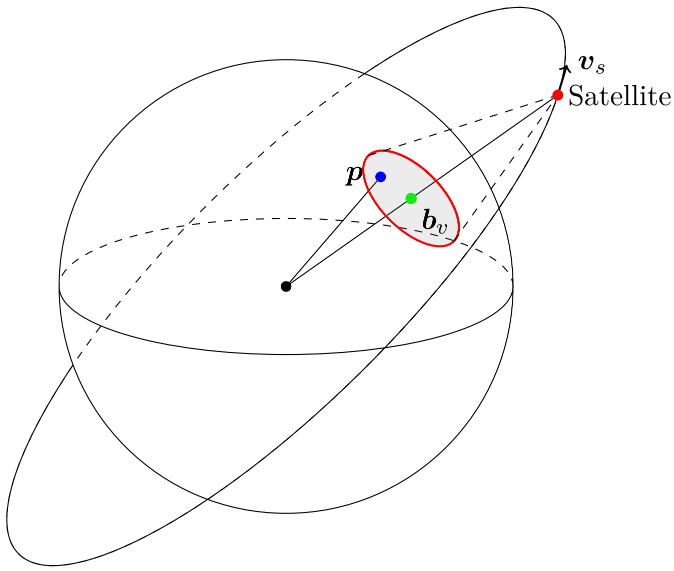

Figure 2.3: Illustration of FoV on earth for an LEO satellite. The satellite FoV is the red circle, $\boldsymbol{b}_v$ is the sub-satellite point, $\boldsymbol{v}_s$ is the velocity vector of the satellite, and $\boldsymbol{p}$ is the vessel.

In Figure 2.3, the sub-satellite point, $\boldsymbol{b}_v$, is the satellite position projected onto the surface of the Earth. The colatitude and longitude of this point are the spherical coordinates of the satellite. For colatitude and longitude, see Section F.1. The speed, v_s, of a satellite in a circular orbit is calculated as

$$v_s = \|\boldsymbol{v}_s\| = \sqrt{\frac{\eta}{R_E + h}}, \qquad (\text{km s}^{-1}) \qquad (2.3)$$

in which $\|\cdot\|$ is the ℓ^2-norm, R_E is the radius of Earth, h is the orbit height, and η is the standard gravitational parameter, which for Earth is $3.986 \cdot 10^5$ km^{3}s^{-2} [28, p. 19]. The Earth radius and the orbit height is illustrated in Figure 2.4. Notice that in this thesis, Earth is assumed to be a perfect sphere, and the orbits of LEO satellites are assumed to be perfectly circular. Moreover, the satellite orbit and the satellite speed are assumed unaffected by Earth's rotation. With these assumptions, the Earth's angular rotation speed can be calculated as

$$\omega_E = \frac{2\pi}{24 \cdot 60 \cdot 60} = 7.27 \cdot 10^{-5}, \qquad (\text{rad s}^{-1}) \quad (2.4)$$

in which the assumption is that a day is exactly 24 hours.

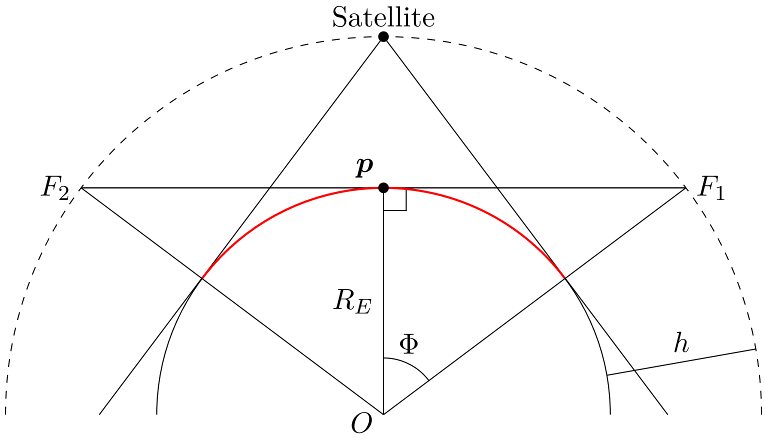

Figure 2.4: Cross section of Earth and a satellite orbiting Earth, flying directly above a vessel, $\boldsymbol{p}$ in a direction from right to left in the figure. The dashed line is the satellite orbit, the red circle arc is the field-of-view of the satellite, and the horizontal solid line is the ideal vessel horizon. Moreover, F_1 is the first point in which the satellite can receive AIS signals from the vessel, and F_2 is the last point.

The time period in which an LEO satellite is above the local horizon (as illustrated in Figure 2.4) and able to receive AIS signals from a given vessel is referred to as a *pass*. In practice, a satellite may not be able to receive AIS signals from a vessel until it is a certain height above the ideal vessel horizon. Due to this, an elevation angle, $e \in [0, \frac{\pi}{2})$, is introduced. This is an angle that determines how far above the ideal vessel horizon the satellite has to be in its orbit in order to be able to receive AIS signals from the vessel. The elevation angle is illustrated in Figure 2.5a. This figure illustrates that the point, F_1, has been moved in the satellite orbit, corresponding to the elevation angle. Effectively, this reduces the size of the satellite FoV.

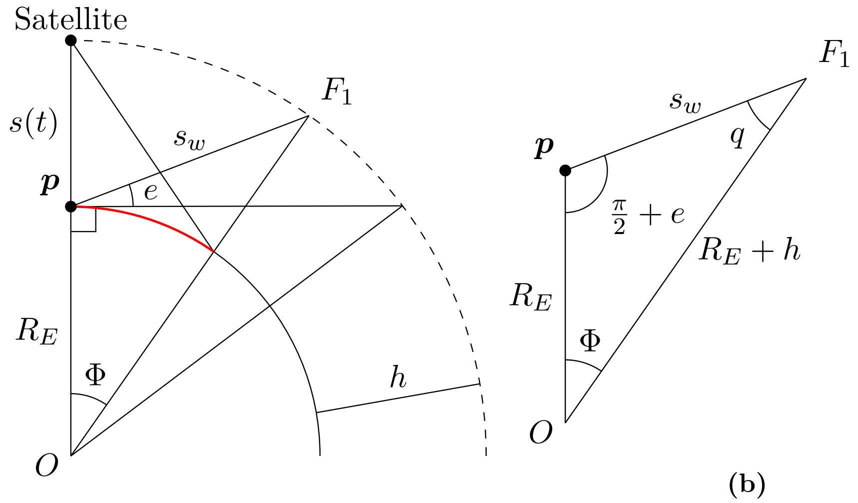

Figure 2.5: (a): The elevation angle, e, that determines how far above the ideal vessel horizon the satellite has to be in order to receive AIS signals from the vessel. The quantity $s(t)$ is the distance between the satellite and the vessel, and s_w is the distance from the vessel to the point F_1. **(b)**: Triangle extracted from Figure 6.8a.

In the triangle in Figure 2.5b, the distance s_w is the distance between the vessel and the satellite when the satellite is at the point in its orbit where it is first able to receive AIS signals. Making the natural restriction that this distance has to be positive, applying the law of cosines to the triangle, and solving a resulting quadratic equation, s_w can be expressed in terms of the elevation angle as

$$s_w = \sqrt{(R_E \sin(e))^2 + 2R_E h + h^2} - R_E \cdot \sin(e). \tag{2.5}$$

Another satellite orbit parameter used in this thesis is the inclination, $i \in [0, \pi]$. The satellite orbit lies in a plane, referred to as the orbit plane, containing the center of the Earth. The inclination is the angle between the orbit plane and the equator plane [28, p. 26]. The inclination is illustrated in Figure 2.6, in which the satellite orbit has been projected down onto Earth.

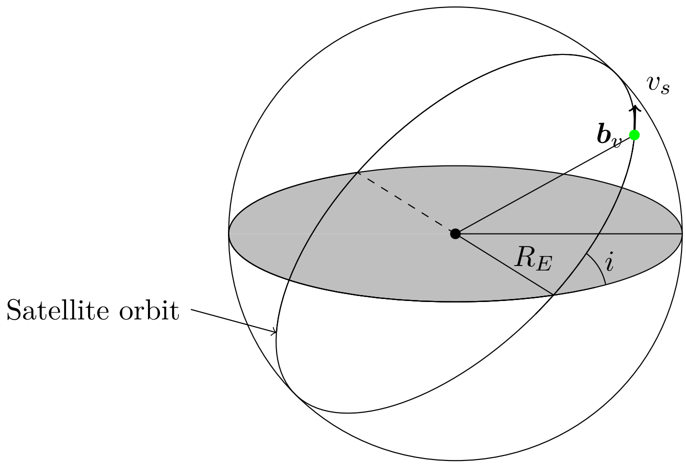

Figure 2.6: Inclination, i, of a satellite orbit. Figure inspired by [2, p. 311].

2.3 Doppler shift

The LEO satellites travel at very high velocities compared to the vessels at sea. This relative velocity causes what is known as a Doppler shift in the AIS signal frequency. In this thesis, the Doppler shift is a key parameter of the AIS signal received by a satellite, and it is used in determining whether the position information encoded in a received AIS signal has been spoofed. The velocities of the LEO satellites are several kilometers per second. The relative velocity between the vessel and the satellite is determined by the rate of change in the distance between them, i.e.

$$v_r(t) = -\frac{ds(t)}{dt}, \tag{2.6}$$

in which $s(t)$ is the distance between the vessel and the satellite, as illustrated in Figure 2.5a [43, p. 33]. When the satellite travels closer to the vessel, the relative velocity is positive, and vice versa. The consequence of the relative velocity is that the frequency of the AIS signal observed on the satellite is

$$f_{obs}(t) = \left(1 + \frac{v_r(t)}{c}\right) f_c,$$

where c is the speed of light and f_c is the carrier frequency of the AIS signal. The change in frequency, known as the Doppler shift, is

$$\nu(t) = \frac{v_r(t)}{c} f_c = f_{obs}(t) - f_c.$$

Due to the nature of the relative velocity in (2.6), the Doppler shift experienced on the satellite is positive when the satellite is moving towards the vessel and vice versa.

In Figure 2.7, a Doppler shift curve is seen. It is generated based on the scenario in Figure 1.1, in which the satellite passes directly above the (non-moving) vessel in its orbit.

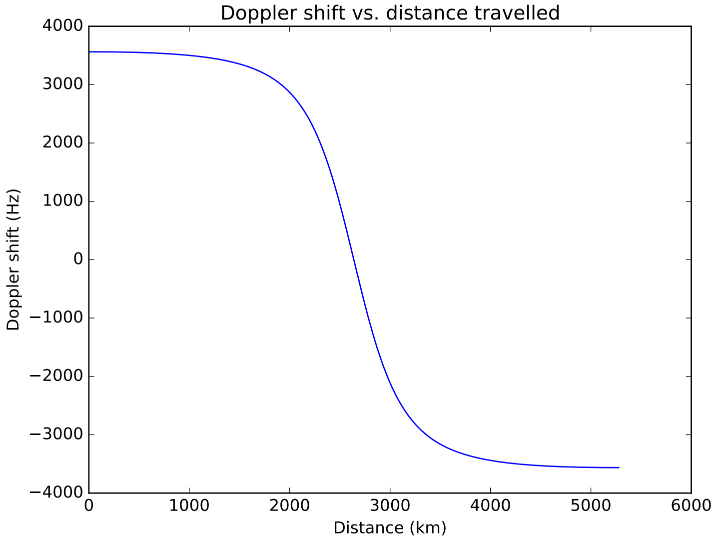

Figure 2.7: Doppler curve for an LEO satellite passing directly above a vessel. The illustration is made with a satellite with $h = 500$ km, as is the case in the Starling project. The vessel sends out a signal with carrier frequency corresponding to AIS channel 1. The elevation angle, e, is 0 degrees.

With the set-up in Figure 2.7, the satellite path from one end of the local horizon to the other, i.e. the length of the circle arc of the orbit from point F_2 to point F_1 in Figure 2.4, is 5829 km. The figure illustrates how the Doppler shift changes throughout this path. Notice that when the Doppler shift is 0 Hz, the satellite is directly above the vessel. Moreover, the absolute maximum Doppler shifts experienced by the satellite in this set-up is when the satellite ascend into the local horizon in the point F_1 and when the satellite descend out of it in the point F_2. These maximum Doppler shifts are ± 3563 Hz.

An additional illustration of a satellite's FoV is given in Figure 2.8a, along with an illustration of the Doppler shifts experienced by the satellite for different vessel positions within the satellite's FoV in Figure 2.8b. Notice that in the later figure, it is evident that a given Doppler shift value does not yield a unique vessel position when a single satellite is utilized. Notice that whenever an illustration like the one in Figure 2.8a is shown in this thesis, the geographical coordinates latitude and longitude are shown. This is in contrast to the spherical coordinates which are also utilized in this thesis. The definition of, and difference between, geographical and spherical coordinates can be found in Appendix F.

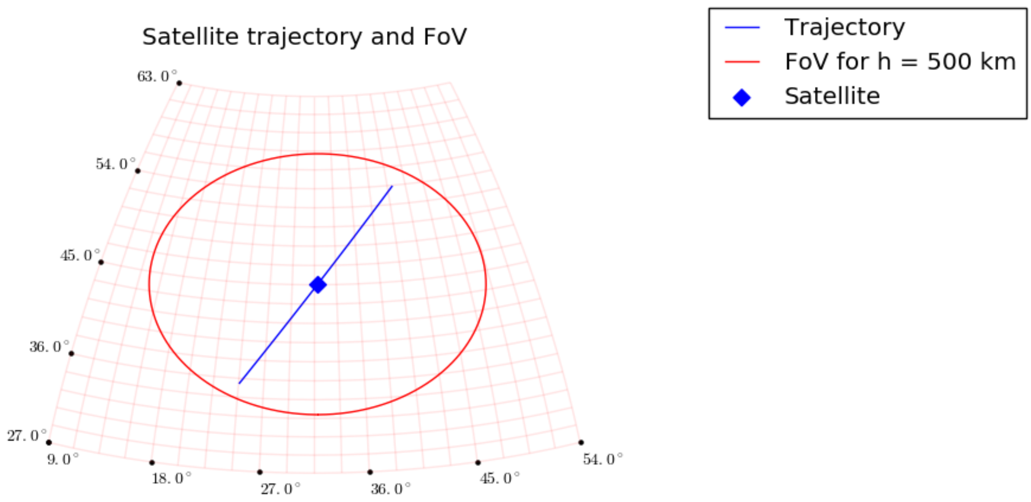

(a)

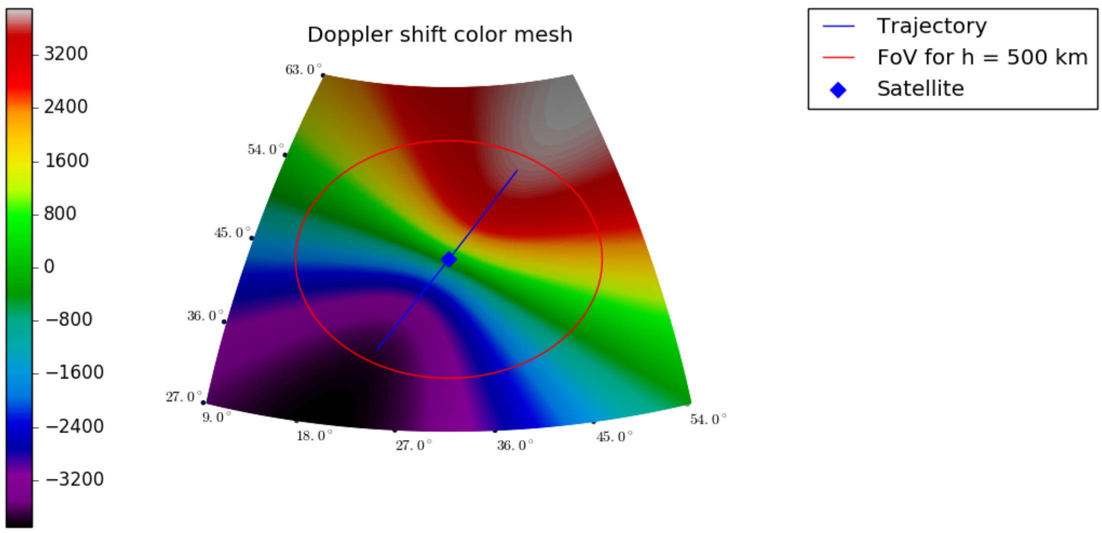

(b)

Figure 2.8: (a): Part of Earth with a part of a satellite trajectory projected onto it. The blue diamond is the satellite at a point in time, and the red circle is the satellite's FoV at that time. The satellite is travelling from the bottom of the figure to the top. Moreover, the geographical coordinates latitude and longitude are plotted for illustrative purposes. **(b)**: Illustration of the Doppler shifts experienced on the satellite at the given moment in time, had the AIS signal with carrier frequency f_1 been sent from a given point on the mesh grid. Notice that by assumption, the satellite can only receive AIS signals sent from within its FoV, but the part of the grid outside the FoV is shown for illustrative purposes.

3 | Link budget for space-based AIS signal reception

This chapter illustrates that reception of AIS signals on LEO satellites is feasible, even though AIS was not originally developed with space reception in mind. This is done by making a link budget, which is a calculation accounting for gains and losses in signal strength when the signal travels from transmitter to receiver. In satellite communication, the path between a transmitter on Earth and a satellite is called a satellite link. This link consists of a downlink, which is signal transmission from satellite to Earth, and an uplink, which is signal transmission from Earth to the satellite. This chapter focuses on the uplink, since in this thesis, LEO satellites receive AIS signals from vessels.

When designing a satellite communication system, knowledge about the required performance of both the down- and uplink is needed. This performance metric is usually a bit error rate (BER), which is the probability of bit errors in the transmission of data in a communications sytem. The BER is closely related to a quantity known as the carrier-to-noise ratio, measured at the receiver demodulator input. The carrier-to-noise ratio is the ratio between the signal carrier power and the noise power.

When transmitting radio frequency signals, a signal is sent out with a given power. When travelling to the receiver, the signal loses strength. Since the link budget accounts for the gains and losses in signal strength, it shows the strength of the signal at the receiver. It also shows the minimum requirements for obtaining a given performance level. The performance level can be expressed using a number of different quantities, but the most commonly used parameter is the carrier-to-noise ratio.

Unless otherwise stated, this chapter uses lower case letters to denote the numerical values of a parameter, and the corresponding upper case letters to denote the decibel (dB) value of the same parameter.

3.1 Transmitter parameters

The parameter describing transmitter performance is the effective isotropic radiated power (EIRP), defined as [28, p. 101]

$$eirp = p_{tx} g_{tx}, \qquad \text{(W)} \tag{3.1}$$

or in dBW

$$EIRP = 10 \cdot \log_{10}\left(\frac{eirp}{1\,[W]}\right) = P_{tx} + G_{tx}. \qquad \text{(dBW)} \quad (3.2)$$

In (3.2), P_{tx} is the transmission power in dBW, G_{tx} is the gain of the transmitter antenna expressed in dBi, i.e. the gain over an isotropic antenna, and $\log_{10}(\cdot)$ is the base-10 logarithm. In practice, the power sent out by the transmitter is reduced by cable and connector losses, and subtracting this quantity in decibel, referred to as L_{tx_cc}, yields the transmitter EIRP

$$EIRP_t = P_{tx} + G_{tx} - L_{tx\_cc}. \qquad \text{(dBW)} \quad (3.3)$$

3.2 Propagation parameters

When propagating from transmitter to receiver, a signal experiences attenuation. If propagating in empty space, the only loss experienced in the signal is equal to what is known as the free space path loss, namely [28, p. 103]

$$L_{fs} = 20 \log_{10}\left(\frac{4\pi r f_c}{c}\right). \qquad \text{(dB)} \quad (3.4)$$

In (3.4), r is the distance between transmitter and receiver, f_c is the carrier frequency, and c is the speed of light. The free space path loss is a large contributor to signal attenuation in satellite communication.

The distance, r, is often chosen to be the largest distance between transmitter and receiver such that the receiver is able to receive signals form the transmitter. In the case of a vessel transmitting signals to be received by an LEO satellite, this distance corresponds to the distance s_w in Figure 2.5a.

In practice, other signal attenuation effects occur, resulting in the total signal loss

$$L_{tot} = L_{fs} - L_{tx\_ap} + L_{pol} + L_{atm} + L_{ion}, \qquad \text{(dB)} \quad (3.5)$$

in which L_{tx_ap}, L_{pol}, L_{atm}, and L_{ion} are transmitter antenna pointing loss, polarization loss, atmospheric loss, and ionospheric loss, respectively, expressed in dB.

3.3 Receiver parameters

In satellite communication, a parameter describing the efficiency of the receiver is figure of merit. This is defined as [17, p. 72]

$$M = G_{rx} - T_{rx}, \qquad \text{(dB/K)} \quad (3.6)$$

in which G_{rx} is the receiver antenna gain expressed in dBi, and T_{rx} is the receiver system noise temperature expressed in dBK. The parameter T_{rx} includes temperature noise sources such as antenna temperature, equivalent noise temperature, and inference noise temperature. For a description of these noise sources, see [28, pp. 106-112]. Further accounting for cable and connector losses, L_{rx_cc}, as was done in the transmitter, and receiver antenna pointing loss, L_{rx_ap}, results in the figure of merit for the receiver

$$M_r = G_{rx} - T_{rx} - L_{rx\_ap} - L_{rx\_cc}. \qquad \text{(dB/K)} \quad (3.7)$$

3.4 Performance parameters and requirements

The primary parameter of interest when designing satellite communication systems is the carrier-to-noise ratio, $\frac{C_c}{N}$, where C_c is the signal carrier power and N is the noise power. Expressed in dB, this ratio is defined as [17, p. 74]

$$\frac{C_c}{N} = \mathrm{EIRP}_t + M_r - L_{tot} - k_0 - B, \qquad \text{(dB)} \quad (3.8)$$

where k_0 is the Boltzmann constant and B is the bandwidth in dBHz. A quantity closely related to the carrier-to-noise ratio is the carrier-to-noise density ratio (CNDR), which in dB is defined as [17, p. 74]

$$\frac{C_c}{N_0} = \frac{C_c}{N} + B. \qquad \text{(dBHz)} \quad (3.9)$$

Often in digital communications systems, a certain BER is desired. Depending on the modulation type used in the transmitted signal, a given BER equals an energy per bit to noise spectrum (Eb/N0), given as

$$\frac{E_b}{N_0} = \frac{C_c}{N_0} - 10 \cdot \log(r_b), \qquad \text{(dB)} \quad (3.10)$$

where r_b is the bit rate in bits per second. For GMSK, a plot of BER vs. Eb/N0 is seen in Figure 3.1. This figure is generated using (J.12) and the GMSK information found in Section J.3.

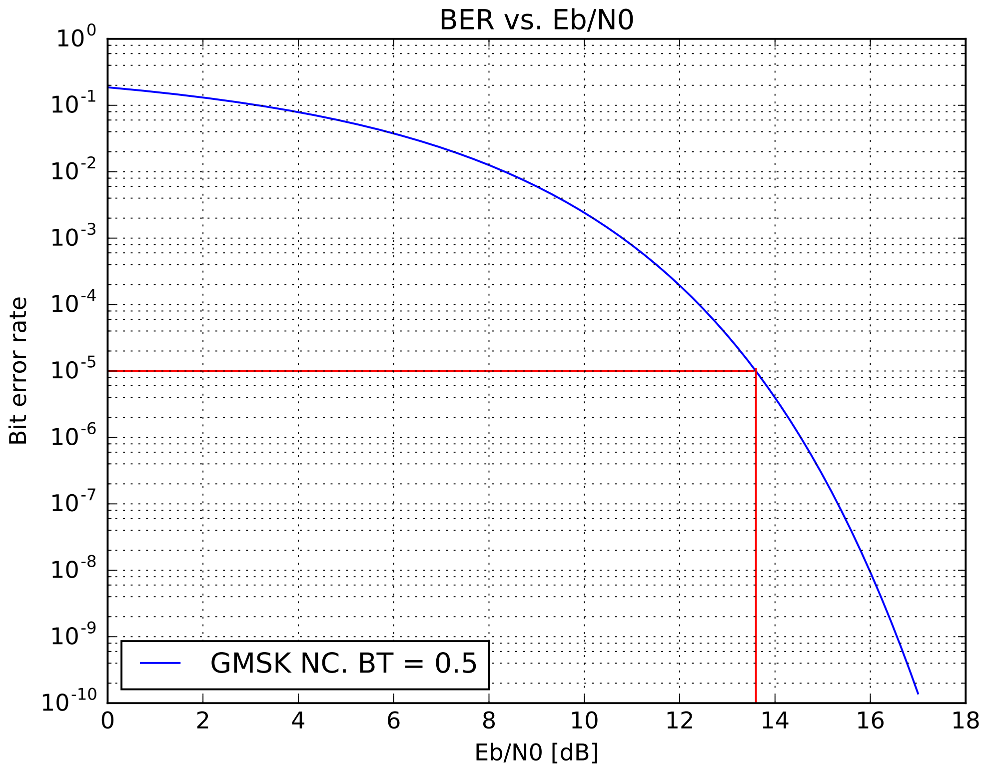

Figure 3.1: Plot of BER vs. Eb/N0 for non-coherent GMSK modulation with bandwidth-time product $B_bT = 0.5$. For B_bT product, see Appendix J.

As evident from Figure 3.1, a desired BER yields a required Eb/N0 value. Rearranging (3.10), a required Eb/N0 value yields a required carrier-to-noise density ratio on the receiver in order to obtain the desired BER, i.e.

$$\left(\frac{C_c}{N_0}\right)_{req} = \left(\frac{E_b}{N_0}\right)_{req} + 10 \cdot \log_{10}(r_b). \qquad \text{(dB)} \quad (3.11)$$

The difference between the required CNDR and the CNDR available at the receiver is called the system link margin. It is defined as

$$M_L = \frac{C_c}{N_0} - \left(\frac{C_c}{N_0}\right)_{req}. \qquad \text{(dB)} \quad (3.12)$$

A link budget for the GomSpace Starling project is seen in Table 3.1. Notice that the elevation angle in this table has been set to 16 degrees, and that the desired BER is 10^{-5}. For this BER, the required Eb/N0 value is 13.6 dB. This is illustrated by the red lines in Figure 3.1. A plot of link margin versus elevation angle can be seen in Figure 3.2.

Paramter	Variable	Note	Value	Unit
Link parameters				
Carrier frequency	f_c	AIS channel 1	161.975	MHz
Speed of light	c		299792.458	km·s^{-1}
Boltzmann constant	k_0		-228.6	dBW/K/Hz
Satellite parameters				
Orbit height	h		500	km
Earth radius	R_E		6378.137	km
Elevation angle	e		16	degrees
Tx-rx distance	r	Equation (2.5)	1359.46	km
Transmitter parameters (AIS transmitter)				
Tx antenna gain	G_{tx}	Considered isotropic	0	dBi
Tx power	p_{tx}	Class A vessel	12.5	W
Tx power	P_{tx}	$10 \cdot \log_{10}(p_{tx}) + 30$	40.97	dBm
Tx cable and connector loss	L_{tx_cc}		2	dB
EIRP tx	$EIRP_t$	Equation (3.3)	8.97	dBW
Propagation parameters				
Tx antenna pointing loss	L_{tx_ap}	Isotropic antenna	0	dB
Polarization loss	L_{pol}	Worst case	3	dB
Free space path loss	L_{fs}	Equation (3.4)	139.3	dB
Atmospheric loss	L_{atm}		2.1	dB
Ionospheric loss	L_{ion}		0.4	dB
Total signal loss	L_{tot}	Equation (3.5)	144.80	dB
Receiver parameters				
Rx antenna pointing loss	L_{rx_ap}		0 (N/A)	dB
Rx antenna gain	G_{rx}		0 (N/A)	dB
Rx cable and connector loss	L_{rx_cc}		2	dB
Rx system noise temperature	T_{rx}		34.24	dBK
Rx figure of merit	M_r	Equation (3.7)	-36.24	dB/K
Required carrier-to-noise density ratio				
Data rate	r_b	AIS data rate	9600	bps
Bit error rate	P_G	Desired BER at 10^{-5}	10^{-5}	
Desired E_b/N_0	$\left(\frac{E_b}{N_0}\right)_{req}$	Non-coherent GMSK, computer simulated	13.6	dB
Required CNDR	$\left(\frac{C_c}{N_0}\right)_{req}$	Equation (3.11)	53.4	dBHz
Available carrier-to-noise density ratio				
Available CNDR	$\frac{C_c}{N_0}$	Equation (3.9)	56.23	dBHz
System link margin				
System link margin	M_L	Equation (3.12)	3.11	dB

Table 3.1: Link budget for the GomSpace Starling project.

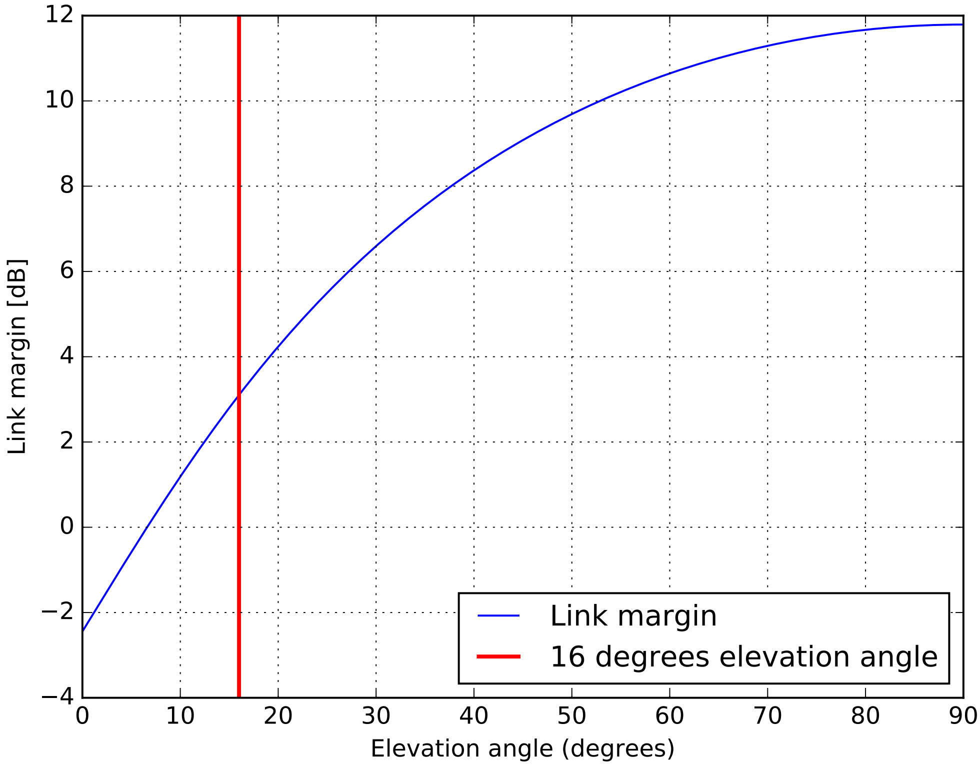

Figure 3.2: Link margin vs. elevation angle. Figure is generated with a desired BER of 10^{-5} percent.

The packet error probability (PEP) is

$$P_p(N_b) = 1 - (1 - P_G))^{N_b},$$

where N_b is the number of bits in the packet. With a desired BER of $P_G = 10^{-5}$ in the receival of AIS signals on-board LEO satellites,

$$P_p(200) = 1 - (1 - P_G))^{200} = 0.00199, \tag{3.13}$$

i.e. there is a 0.2 percent risk that an AIS message is received erroneously by the satellite. The factor 200 in (3.13) is the summation of the number of bits contained in the start and end flag, data, and CRC parts of the AIS message, as shown in Figure 2.1. This is the number of bits in the AIS message in which, if an error occurs, the message is received erroneously.

4 Space-based AIS system analysis

This chapter describes the generation and transmission of AIS signals on-board the vessel, and the reception and processing of these AIS signals on-board the satellite. The overall space-based AIS system is illustrated in Figure 1.3.

Initially, the transmission side is described. This corresponds to the first block in Figure 1.3. After this, the receiver side is described, corresponding to the third block in Figure 1.3. In both of these descriptions, the observable quantities such as the satellite position, Doppler shifts, and the alleged vessel position, i.e. the position that needs to be checked for position spoofing, are described. These observable quantities are what the position spoofing detection will be based on.

Eventually, GomSpace's Doppler shift estimator is described and its performance assessed. This includes simulating its mean square error, root mean square error, and bias.

4.1 Vessel AIS signal generation and transmission

Figure 4.1 shows a block diagram of the transmission of N AIS messages from a single vessel. Starting from left to right in the figure, the dashed-line block, named AIS info, is the encompassing of AIS data from data sources such as GPS. The collected AIS info is passed to an AIS encoder, which combines the AIS data to an AIS message. Each message is then NRZI encoded and GMSK modulated. The output of the GMSK modulator is a complex baseband signal denoted by $x(t)$. Translating $x(t)$ to a carrier frequency and highpass filtering this signal results in the AIS signal, $u(t)$ for transmission.

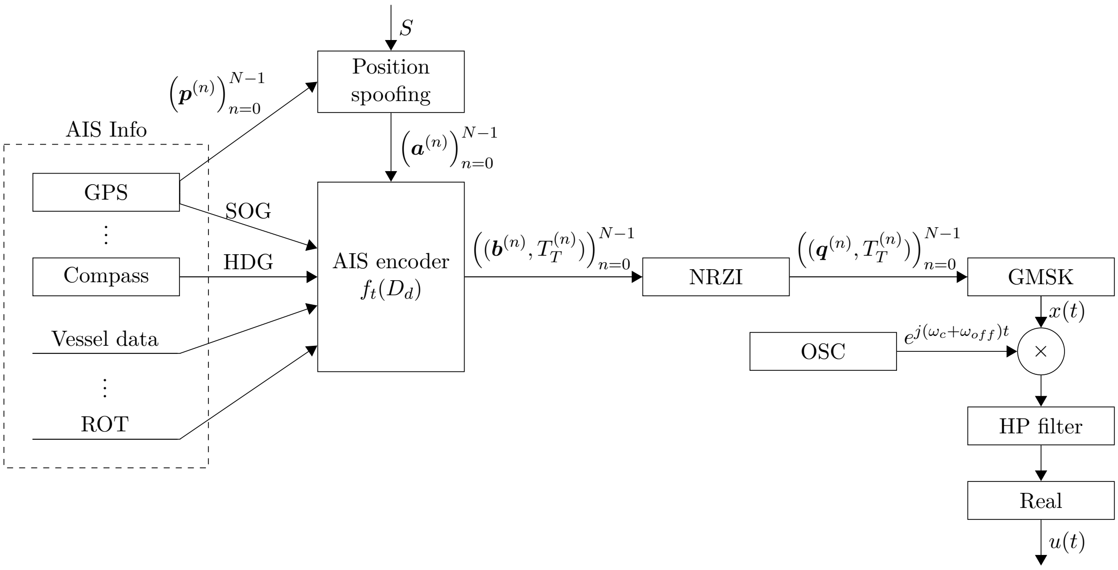

Figure 4.1: Block diagram of the AIS transmitter on-board a vessel. AIS information for N AIS messages is passed into the AIS encoder. The output of this encoder is a length-256 bit-string $\boldsymbol{b}^{(n)}$, as described in Section 2.1, and an AIS message starting time $T_T^{(n)}$ for each of the N AIS messages. These are NRZI encoded and GMSK modulated. From the GMSK block, the resulting signal $x(t)$ is mixed with a carrier wave produced by the oscillator of the vessel. Eventually, the mixed signal is high-pass filtered, resulting in the signal, $u(t)$, for transmission.

The AIS signal, $u(t)$, is modelled as

$$u(t) = \mathrm{Re}\left(x(t)e^{j(\omega_c+\omega_{off})t}\right),$$

where ω_c and ω_{off} are an angular carrier frequency and an angular carrier frequency offset, respectively, and

$$x(t) = \sum_{n=0}^{N-1} A_{tx}(t - T_T^{(n)}) e^{j\phi\left(t - T_T^{(n)}, \boldsymbol{q}^{(n)}\right)}, \tag{4.1}$$

is the complex baseband representation of $u(t)$. For theory concerning complex baseband signal representation, see Appendix I. Here, $T_T^{(n)}$ is the starting time of the n'th AIS message, $\phi\left(t, \boldsymbol{q}^{(n)}\right) \in \mathbb{R}$ is a time-varying phase conveying the AIS information encoded in the NRZI sequence, $\boldsymbol{q}^{(n)}$, and $A_{tx}(t)$ is a time-varying amplitude given by

$$A_{tx}(t) = \begin{cases} 1 & 0 \le t \le T_{AIS}, \\ 0 & \text{otherwise.} \end{cases}$$

Consider again the dashed line box in Figure 4.1, labelled AIS Info. This box illustrates different data generators, one of which is a GPS data generator that provides vessel colatitude and longitude, which in this thesis is denoted by the corresponding Cartesian coordinate vectors $\left(\boldsymbol{p}^{(n)}\right)_{n=0}^{N-1}$, which are referred to as the true vessel positions. These are the positions which may be subject to position spoofing. Furthermore, vessel data is provided, e.g. MMSI number. Lastly, info such as the speed over ground (SOG), heading (HDG) and rate-of-turn (ROT) is provided.

The true vessel positions are passed into a position spoofing block, in which a parameter S determines whether the vessel is spoofing its position or not. The output of this block is the alleged vessel positions, denoted as the cartesian coordinate vectors $\left(\boldsymbol{a}^{(n)}\right)_{n=0}^{N-1}$, which are equal to the true vessel positions if spoofing is not occuring, and not equal to the true vessel positions if spoofing is occuring.

Data is passed into the AIS encoder. Here, the AIS data is ordered and encoded. Moreover, a function $f_t(D_d)$ is shown in this box. This is a function which, based on the collection of data, D_d, passed into the AIS encoder box, determines the time instant $T_T^{(n)}$, in which a given AIS message is to be transmitted.

The output of the AIS encoder box is pairs of bit strings, $\boldsymbol{b}^{(n)}$, and time instants, $T_T^{(n)}$. These pairs are denoted $\left((\boldsymbol{b}^{(n)}, T_T^{(n)})\right)_{n=0}^{N-1}$, where

$$\boldsymbol{b}^{(n)} = \begin{bmatrix} b^{(n,0)} & b^{(n,1)} & \dots & b^{(n,N_{bit}-1)} \end{bmatrix}^\top$$

with

$$b^{(n,m)} \in \{0,1\} \qquad m = 0, 1, \dots, N_{bit} - 1.$$

is the bit string corresponding to the AIS message to be sent out at time $T_T^{(n)}$, and $T_T^{(i)} > T_T^{(j)} > 0$ for $i > j$, $i, j = 0, 1, \dots, N-1$.

Next, $\left((\boldsymbol{b}^{(n)}, T_T^{(n)})\right)_{n=0}^{N-1}$ is passed into the NRZI block. In this block, the bit strings, $\boldsymbol{b}^{(n)}$, are NRZI encoded, and a length-256 NRZI vector for each of the N AIS messages is the output of the block. These vectors are denoted as $\left(\boldsymbol{q}^{(n)}\right)_{n=0}^{N-1}$. The content of one of these vectors is

$$\boldsymbol{q}^{(n)} = \begin{bmatrix} q^{(n,0)} & q^{(n,1)} & \dots & q^{(n,N_{bit}-1)} \end{bmatrix}^\top \tag{4.2}$$

with

$$q^{(n,m)} \in \{\pm 1\} \qquad m = 0, 1, \dots, N_{bit} - 1.$$

The vector in (4.2) is referred to as the data symbols of the n'th AIS message. Also evident from (4.2) is the fact that NRZI encodes a bit string consisting of 1s and 0s into a string consisting of ±1s. This happens with a one-to-one correspondence between $\boldsymbol{b}^{(n)}$ and $\boldsymbol{q}^{(n)}$.

Next, $\left((\boldsymbol{q}^{(n)}, T_T^{(n)})\right)_{n=0}^{N-1}$ is passed as input to the GMSK box, where the GMSK signal $x(t)$ is generated. The signal $x(t)$ is passed through a complex mixer, where it is mixed with a complex exponential with frequency $\omega_c + \omega_{off}$, where $\omega_c = 2\pi f_c$. The mixer is described in Appendix H. Moreover, $\omega_{off} = 2\pi f_{off}$ corresponds to the frequency offset from ω_c happening in the oscillator (the OSC block) of the vessel. This frequency offset is due to the ±3 ppm frequency offset referred to in Section 2.1.

The signal resulting from the mixer is high-pass filtered to eliminate the difference frequencies created in the mixer. The output of the filter is $u(t)$.

4.2 Satellite AIS signal reception

On the receiver side of the system, i.e. the receiver block in Figure 1.3, reception, demodulation, and decoding take place. In Figure 4.2 the receiver side is illustrated. It illustrates the reception of N AIS messages.

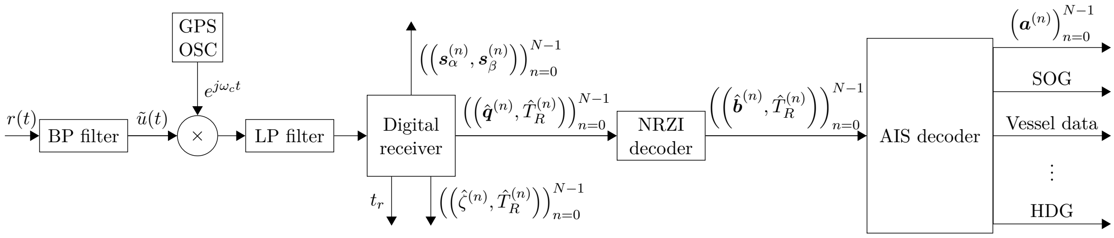

Figure 4.2: Block diagram over the AIS receiver embedded in the satellite. The signal, $r(t)$, received by the satellite is passed through a bandpass filter to filter out interfering signals and out of band noise. The filter output is then mixed with a complex exponential generated by the GPS disciplined oscillator of the satellite. The resulting signal is low-pass filtered and the resulting signal is passed into the digital receiver, which estimates the data symbols, $\boldsymbol{q}^{(n)}$, and the carrier-frequency offset, $\zeta^{(n)}$, for each of the N AIS messages. The data symbols are NRZI decoded, and eventually the bit-strings resulting from the NRZI decoder are decoded in the AIS decoder, and vessel data is returned.

The signal, $r(t)$, received by the satellite represents the AIS signal transmitted by the vessel, the channel effects, along with interfering signals and noise. It is given as

$$r(t) = h(t) + i(t) + n(t),$$

where $i(t)$ is interfering signals, $n(t)$ is assumed circularly symmetric gaussian noise with variance $\sigma_n^2 > 0$, and

$$h(t) = \mathrm{Re}\left(\tilde{y}(t)e^{j\omega_c t}\right),$$

where

$$\tilde{y}(t) = E(t)x(t - \tau(t))e^{j2\pi\zeta(t)t}, \tag{4.3}$$

$\zeta(t) = \nu(t) + f_{off}$ is the carrier frequency offset, and $\nu(t)$ is the Doppler shift. Moreover, $E(t)$ is real-valued attenuation of the AIS signal and $\tau(t)$ is a propagation delay.

Passing $r(t)$ through a bandpass filter designed to reduce image response and attenuate interfering signals and noise, the output of the filter, $\tilde{u}(t)$, is given as

$$\tilde{u}(t) = \mathrm{Re}\left(y(t)e^{j\omega_c t}\right),$$

where

$$y(t) = E(t)x(t - \tau(t))e^{j2\pi\zeta(t)t} + w(t). \tag{4.4}$$

In (4.4), $y(t)$ is the output of the low-pass filter illustrated in Figure 4.2 and $w(t)$ is assumed band-limited circularly symmetric gaussian noise with variance $\sigma_w^2 > 0$.

Next, $\tilde{u}(t)$ is mixed with a complex exponential with frequency ω_c. By assumption, this complex exponential stems from a GPS disciplined oscillator, which means that it oscillates at the given frequency with very little or no variation. Sum and difference frequencies are created, and the signal is passed to a low-pass filter in order to reject the sum frequencies. The filter output is passed to the digital receiver.

An important part of the digital receiver is the estimation of the carrier frequency offset. The digital receiver outputs an estimate, $\hat{\zeta}^{(n)}$ of the carrier frequency offset,

$$\zeta^{(n)} = \nu^{(n)} + f_{off}. \tag{4.5}$$

The assumption that the Doppler shift experienced by the satellite in the duration of the n'th AIS message is constant is made, hence the notation $\nu^{(n)}$ is used for the Doppler shift for the n'th AIS message in (4.5). Furthermore, data symbol estimates, $\hat{\boldsymbol{q}}^{(n)}$, and estimates, $\hat{T}_R^{(n)}$, of the time-of-arrival

$$T_R^{(n)} = T_T^{(n)} + \tau^{(n)}, \tag{4.6}$$

of the n'th AIS message are outputs from the digital receiver. In (4.6), the assumption that $\tau(t)$ is approximately constant during the duration of the n'th AIS message is made, hence the notation $\tau^{(n)}$. Based on the time-of-arrivals, it is assumed that GomSpace is able to determine the report interval, t_r, used by the vessel in question, hence why it is an output of the digital receiver.

When generating the data that is used in this thesis, the propagation delay is neglected, i.e. $T_T^{(n)} = T_R^{(n)}$ when generating data. The reasoning behind this is that the propagation delay is approximately equal to the time it takes light to travel the distance s_w in Figure 2.5a. In this worst-case scenario, the propagation delay can be calculated based on (2.5) and is approximately equal to 9.44 ms with an elevation angle $e = 0$ (raising the elevation angle only makes the propagation delay smaller). The change in vessel position during this timeframe is negligible. Since the vessel position does not change, whether the satellite receives the AIS signal at time $T_T^{(n)}$ or at time $T_R^{(n)}$ does not change the end result for the simulations carried out later in this thesis.

The last outputs of the digital receiver are pairs of satellite positions. The Starling project LEO satellites are equipped with GPS able to sample the satellite position with a frequency, f_p of up to 100 Hz. It is assumed that this maximum frequency is utilized. Another assumption is that for the n'th AIS message received at time $T_R^{(n)}$, two satellite positions are available. The first satellite position $\boldsymbol{s}_\alpha^{(n)}$ is the one sampled by the on-board satellite GPS at time

$$T_\alpha^{(n)} = \left\lfloor T_R^{(n)} \cdot f_p \right\rfloor \cdot f_p^{-1}. \tag{4.7}$$

The second satellite position $\boldsymbol{s}_\beta^{(n)}$ is the one sampled at time

$$T_\beta^{(n)} = \left\lceil T_R^{(n)} \cdot f_p \right\rceil \cdot f_p^{-1}. \tag{4.8}$$

In (4.7) and (4.8), $\lfloor\cdot\rfloor$ and $\lceil\cdot\rceil$ are the floor and ceiling operators, respectively. The expression in (4.7) corresponds to a mapping of $T_R^{(n)}$ to the greatest integer multiple of f_p^{-1} less than or equal to $T_R^{(n)}$, and the expression in (4.8) corresponds to a mapping of $T_R^{(n)}$ to the least integer multiple of f_p^{-1} greater than or equal to $T_R^{(n)}$.

After the digital receiver, $\left((\hat{\boldsymbol{q}}^{(n)}, \hat{T}_R^{(n)})\right)_{n=0}^{N-1}$ is passed to the NRZI decoder, which decodes the estimate of the data symbols, $\left(\hat{\boldsymbol{q}}^{(n)}\right)_{n=0}^{N-1}$. The output of this block is the estimate of the N bit strings. This output, $\left((\hat{\boldsymbol{b}}^{(n)}, \hat{T}_R^{(n)})\right)_{n=0}^{N-1}$, is now passed to the AIS decoder, which decodes the N bit strings, $\left(\hat{\boldsymbol{b}}^{(n)}\right)_{n=0}^{N-1}$. The output of this block is the AIS information. Specifically, the alleged vessel position, $\boldsymbol{a}^{(n)}$, of the n'th AIS message is among these outputs.

In conclusion, the observable quantities, on which position spoofing detection will be based, are the satellite positions, the carrier frequency offsets, the report interval, the time-of-arrivals, and the alleged vessel positions.

4.3 Carrier frequency offset estimator

This section introduces the carrier frequency offset estimator used by GomSpace.

Recalling the complex baseband representation in (4.4) of the received passband signal, the part of the signal corresponding to the n'th AIS message is

$$y^{(n)}(t) = E^{(n)} x^{(n)}(t - \tau^{(n)}) e^{j2\pi\zeta^{(n)} t} + w^{(n)}(t) \qquad T_R^{(n)} \leq t \leq T_R^{(n)} + T_{AIS}, \tag{4.9}$$

where the signal amplitude is assumed constant during the n'th AIS message, hence the notation $E^{(n)}$. Furthermore,

$$x^{(n)}(t) = A_{tx}(t - T_T^{(n)}) e^{j\phi\left(t - T_T^{(n)}, \boldsymbol{q}^{(n)}\right)}, \qquad T_T^{(n)} \leq t \leq T_T^{(n)} + T_{AIS}.$$

Now, (4.9) can be reduced to

$$y^{(n)}(t) = E^{(n)} e^{j\phi\left(t - T_T^{(n)}, \boldsymbol{q}^{(n)}\right)} e^{j2\pi\zeta^{(n)} t} + w^{(n)}(t), \qquad T_R^{(n)} \leq t \leq T_R^{(n)} + T_{AIS}, \tag{4.10}$$

since $A_{tx}(t)$ is equal to one during the n'th AIS message. Now, consider P_s samples of the n'th AIS message in (4.10) over its time duration, given as

$$y^{(n)}(pT_s) = y^{(n,p)} = E^{(n)} e^{j\left(2\pi\zeta^{(n)} p + \phi^{(n,p)} + \psi^{(n)}\right)} + w^{(n,p)}, \qquad p = 0, 1, \ldots, P_s - 1, \tag{4.11}$$

where T_s is the sampling period, and $w^{(n,p)}$ is a colored band-limited complex normal circular symmetric process. The correlation in the noise samples are created during the sampling process, in which GomSpace uses a sampling frequency $f_s > 2B$, where B is the bandwidth of $w(t)$. This is elaborated on in Section 4.4 and Appendix L. Furthermore, in (4.11), the samples of the phase $\phi^{(n,p)} \in \mathcal{P} = \left\{\frac{\pi}{4}, \frac{3\pi}{4}, \frac{5\pi}{4}, \frac{7\pi}{4}\right\}$, and $\psi^{(n)} \in \mathbb{R}$ is a phase offset caused by the sampling process that is assumed constant during the n'th AIS message.

The carrier frequency offset can be estimated utilizing the discrete Fourier transformation [7, p. 1725-1726]. In order to realize this, a non-linear transformation of the signal in (4.11) is carried out. This transformation raises the sampled signal in (4.11) to the K'th power, where $K = \text{card}(\mathcal{P})$. This results in

$$k^{(n,p)} = \left(y^{(n,p)}\right)^K = \left(E^{(n)}\right)^K e^{j\left(\zeta_K^{(n)} \cdot p + \phi_K^{(n,p)} + K\psi^{(n)}\right)} + v^{(n,p)}, \qquad p = 0, 1, \ldots, P_s - 1, \tag{4.12}$$

where $\zeta_K^{(n)} = 2K\pi\zeta^{(n)}$, $\phi_K^{(n,p)} = K\phi^{(n,p)}$, and by the binomial theorem

$$v^{(n,p)} = \sum_{i=0}^{K-1} \binom{K}{i} \left(E^{(n)}\right)^i \left(w^{(n,p)}\right)^{K-i} e^{ji\left(2\pi\zeta^{(n)} p + \psi^{(n)}\right)}.$$

In GMSK, $K = 4$, and thus $\phi_K^{(n,p)} \in \{\pi, 3\pi, 5\pi, 7\pi\}$. This makes $e^{j\phi_K^{(n,p)}} = -1$ in (4.12). Therefore, when raising the signal in (4.11) to the 4'th power, the resulting signal

$$k^{(n,p)} = -\left(E^{(n)}\right)^K e^{j\left(\zeta_K^{(n)} p + K\psi^{(n)}\right)} + v^{(n,p)}, \qquad p = 0, 1, \ldots, P_s - 1, \tag{4.13}$$

can be seen as a constant amplitude complex exponential with frequency $\zeta_K^{(n)}$ in complex non-Gaussian, zero-mean additive noise. Other modulation schemes have different K-values, e.g. $K = 2$ for pulse amplitude modulation, and $K = 4$ for quadrature amplitude modulation [7, p. 1725]. Due to this fact, and to preserve generality, K is kept as a variable in the succeeding derivations. In order to make these derivations easier, (4.13) is rewritten as

$$k^{(n,p)} = \left(E^{(n)}\right)^K e^{j\left(\zeta_K^{(n)} \cdot p + \psi_K^{(n)}\right)} + v^{(n,p)}, \qquad p = 0, 1, \ldots, P_s - 1,$$

where $\psi_K^{(n)} = K\psi^{(n)} + \pi$. Now, non-linear least squares (NLLS) can be utilized to estimate the scaled carrier frequency offset, $\zeta_K^{(n)}$. In this setup, the NLLS problem is that of determining values that minimize the expression

$$f_\Delta^{(n)} = \sum_{p=0}^{P-1} \left| k^{(n,p)} - \left(E^{(n)}\right)^K e^{j\left(\zeta_K^{(n)} \cdot p + \psi_K^{(n)}\right)} \right|^2. \tag{4.14}$$

In Appendix G, the derivations leading to the estimates of $\zeta_K^{(n)}$ and $\psi_K^{(n)}$ are found. These estimates are [41, p. 58]

$$\hat{\psi}_K^{(n)} = \arg\left(\sum_{p=0}^{P-1} k^{(n,p)} e^{-j\hat{\zeta}_K^{(n)} \cdot p}\right),$$

where arg(·) is the argument of a complex number, and

$$\hat{\zeta}_K^{(n)} = \underset{\zeta_K^{(n)}}{\operatorname{argmax}} \left| \sum_{p=0}^{P-1} \left(k^{(n,p)} e^{-j\zeta_K^{(n)} \cdot p} \right) \right|. \tag{4.15}$$

In (4.15), it is seen that the estimate of $\zeta_K^{(n)}$ corresponds to estimating the frequency yielding the highest value in the magnitude spectrum of $k^{(n,p)}$. Based on the estimate of $\zeta_K^{(n)}$, the digital receiver outputs estimates $\hat{\zeta}^{(n)}$.

4.4 Carrier frequency offset estimator simulation

GomSpace samples the complex baseband signal from (4.9) at the receiver on-board the Starling satellites with a sampling frequency $f_{gs} = 38.4$ kHz, yielding

$$P_{gs} = f_{gs} \cdot T_{AIS} = 1024$$

samples per AIS message. The company has provided software for simulating the transmission and receival of AIS messages, in which the carrier frequency offset, ζ, can be varied before its estimation. This process can be seen in Figure 4.3. In this figure, the software provided by GomSpace is represented by the second block. Notice that this block is treated as a black box. Based on (4.11), samples of the n'th transmitted AIS message can be defined as

$$x^{(n,p)} = e^{j(\phi^{(n,p)} + \psi^{(n)})}, \qquad p = 0, 1, \ldots, P_{gs} - 1$$

Omitting the superscript n, denoting a particular AIS message, for the remainder of this section, the output of the second box in Figure 4.3 is the Doppler shifted transmitted AIS signal samples without noise, where

$$\boldsymbol{x} = \begin{bmatrix} x^{(0)} & x^{(1)} & \ldots & x^{(P_{gs}-1)} \end{bmatrix}^\top,$$

and $x^{(p)} = e^{j(\phi^{(p)} + \psi)}$, $p = 0, 1, \ldots, P_{GS} - 1$, and

$$\boldsymbol{e_x} = \begin{bmatrix} 1 & e^{j2\pi\zeta} & e^{j4\pi\zeta} & \ldots & e^{j2\pi\zeta(P_{gs}-1)} \end{bmatrix}^\top.$$

Raising the P_{gs} samples to the 4'th power quadruples the carrier frequency offset, as evident from (4.12). Fast Fourier transforming the 1024 transformed samples yields an FFT bin width

$$\Delta_{\zeta_K} = \frac{f_{gs}}{P_{gs}} = 37.5, \qquad \text{(Hz)} \tag{4.16}$$

but when ζ_K has been estimated, it is divided by 4 to yield the estimate of ζ, which also reduces the FFT bin width to

$$\Delta_\zeta = \frac{\Delta_{\zeta_K}}{4} = 9.375. \qquad \text{(Hz)} \tag{4.17}$$

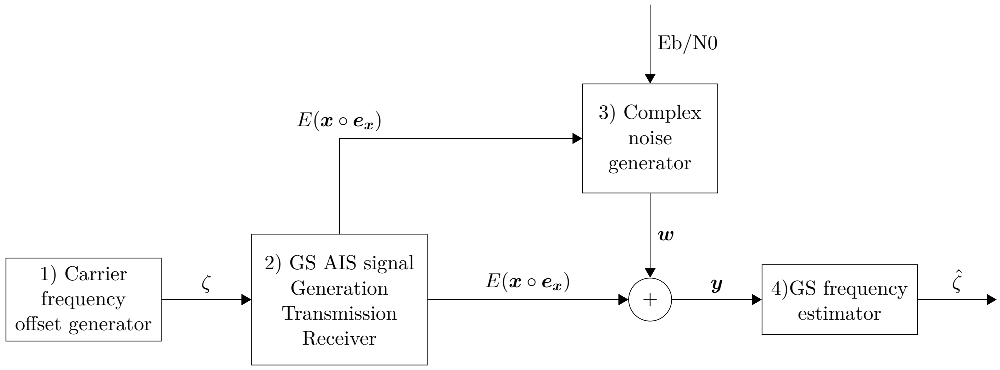

Figure 4.3: Block diagram illustrating the process of generating a single AIS message, adding complex noise to the signal, and estimating the carrier frequency offset. The symbol "$\circ$" denotes the Hadamard product, also called entry-wise multiplication. The GomSpace (GS) AIS signal block and the GS frequency estimator block are considered black boxes in this thesis.

In this thesis, the estimator in (4.15) is simulated for $N_{eb} = 200$ Eb/N0 values (in dB). These values are

$$\boldsymbol{e_b} = \begin{bmatrix} -6.07 & -6.07 + 0.126 & \dots & -6.07 + (N_{eb} - 1) \cdot 0.126 \end{bmatrix}^\top .$$

For a particular Eb/N0 value $e_b^{(i)}$, $i = 0, 1, \dots, N_{eb} - 1$, the number of simulations carried out are

$$N_{sim}^{(i)} = \begin{cases} 50000 & \text{if } e_b^{(i)} \in [7.4, 12] \\ 2000 & \text{otherwise.} \end{cases} \tag{4.18}$$

The reason for simulating certain Eb/N0 values more than others is that simulations have shown that the interval in (4.18) is the one in which the error on the estimator begins to increase. For the i'th Eb/N0 value, $N_{sim}^{(i)}$ AIS messages are independently generated using GomSpace software, illustrated by the second block in Figure 4.3, and corresponding carrier frequency offset values are drawn as

$$\zeta^{(i,l)} \sim \text{unif}\left[-(3564.42 + 485.925), (3564.42 + 485.925)\right], \tag{4.19}$$

for $l = 0, 1, \dots, N_{sim}^{(i)} - 1$. In (4.19), the start and end point of the interval corresponds to the sum of the maximum Doppler shift as seen in Figure 2.7 and the ± 3 ppm frequency offset for AIS channel 1 as seen in (2.1).

In order to obtain the given Eb/N0 value, correlated complex noise is added to each of the generated AIS signals according to the procedures described in Appendix L. Moreover, for the i'th Eb/N0 value, the mean square error (MSE) is calculated as

$$MSE^{(i)} = \frac{1}{N_{sim}^{(i)}} \sum_{l=0}^{N_{sim}^{(i)}-1} |\zeta^{(i,l)} - \hat{\zeta}^{(i,l)}|^2, \qquad i = 0, 1, \dots, N_{eb} - 1,$$

and the root mean square error (RMSE) is calculated as

$$RMSE^{(i)} = \sqrt{MSE^{(i)}},$$

where $\hat{\zeta}^{(i,l)} = \frac{\hat{\zeta}_K^{(i,l)}}{2\pi K}$, and $\hat{\zeta}_K^{(i,l)}$ is estimated by GomSpace's carrier frequency offset estimator, with $K = 4$, as shown in the fourth block in Figure 4.3. Notice that the implementation of the estimator is out of the scope of this thesis. A software implementation of the estimator has been provided by GomSpace.

Moreover, the bias of the estimator is estimated as

$$Bias^{(i)} = \frac{1}{N_{sim}^{(i)}} \sum_{l=0}^{N_{sim}^{(i)}-1} \zeta^{(i,l)} - \hat{\zeta}^{(i,l)}, \qquad i = 0, 1, \ldots, N_{eb} - 1.$$

The resulting simulations of the MSE and RMSE of GomSpace's carrier frequency offset estimator can be seen in the Figures 4.4 and 4.5. In these plots, two horizontal dashed lines are drawn, corresponding to the variance and standard deviation of a uniform random variable. These are calculated as

$$\sigma_u^2 = \frac{\Delta_\zeta^2}{12} = 7.32 \tag{4.20}$$

and

$$\sigma_u = \sqrt{\sigma_u^2} = 2.71.$$

The plots show that at high Eb/N0 values, i.e. higher than approximately 10.75 dB, the variance of the estimator is approximately equal to that of a continuous uniform random variable with support size equal to Δ_ζ from (4.17). Notice that this is variance conditioned on knowing the carrier frequency offsets, but in this thesis the errors are assumed independent of the carrier frequency offsets.

The simulations of the bias of the estimator can be seen in the Figures 4.6 and 4.7. These simulations show that the estimator is approximately unbiased at high Eb/N0 values, i.e. higher than approximately 10.75 dB. The variance on the bias estimator is seen to increase when going below this threshold value.

In combination, the MSE and bias simulations show that at high Eb/N0 values, the estimator is approximately unbiased, and hence the MSE is an estimate of the variance of the estimator.

In conclusion, it is evident from the simulation plots that the desired Eb/N0 of 13.6 dB from the link budget in Chapter 3 results in an estimator that is approximately unbiased and whose MSE is approximately equal to the variance of a continuous uniform random variable with support size equal to Δ_ζ.

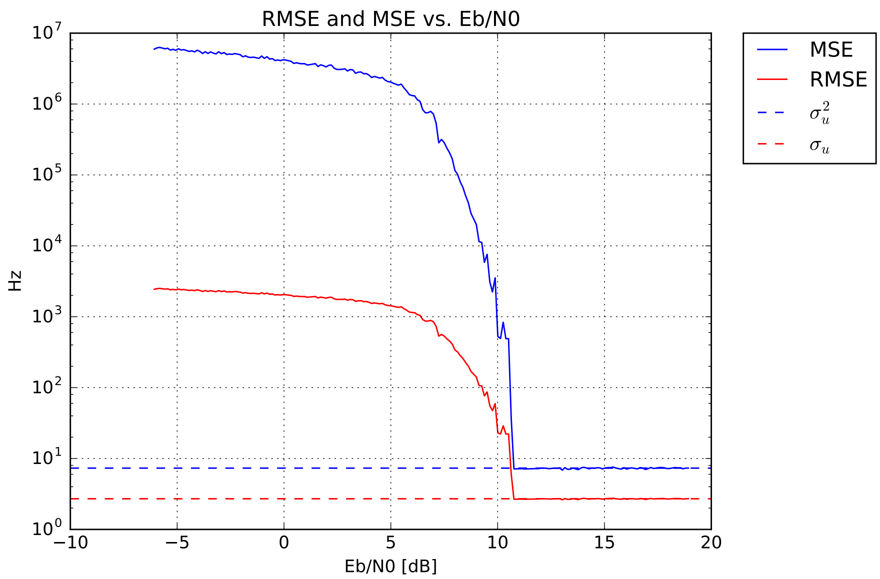

Figure 4.4: MSE and RMSE for the estimator in (4.15) for 200 different Eb/N0 values.

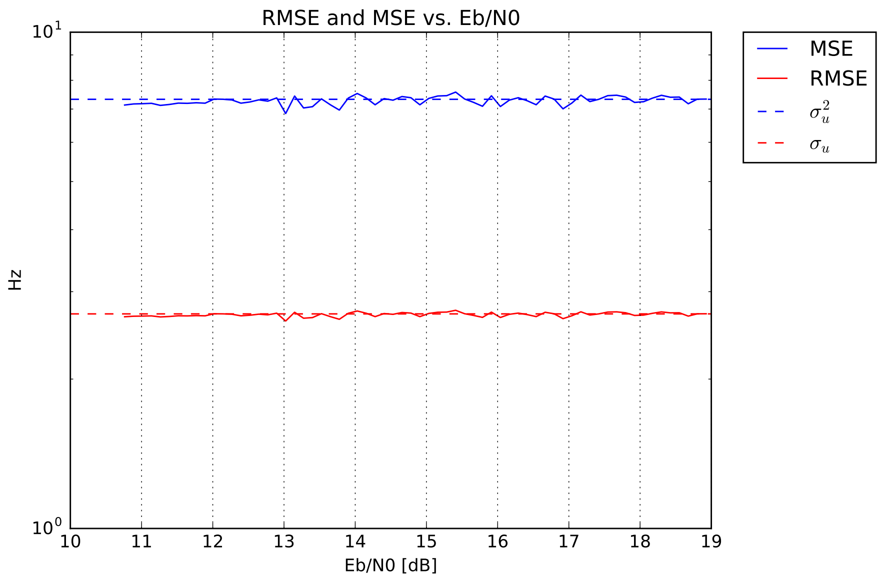

Figure 4.5: Zoom of the tail of the graph in Figure 4.4.

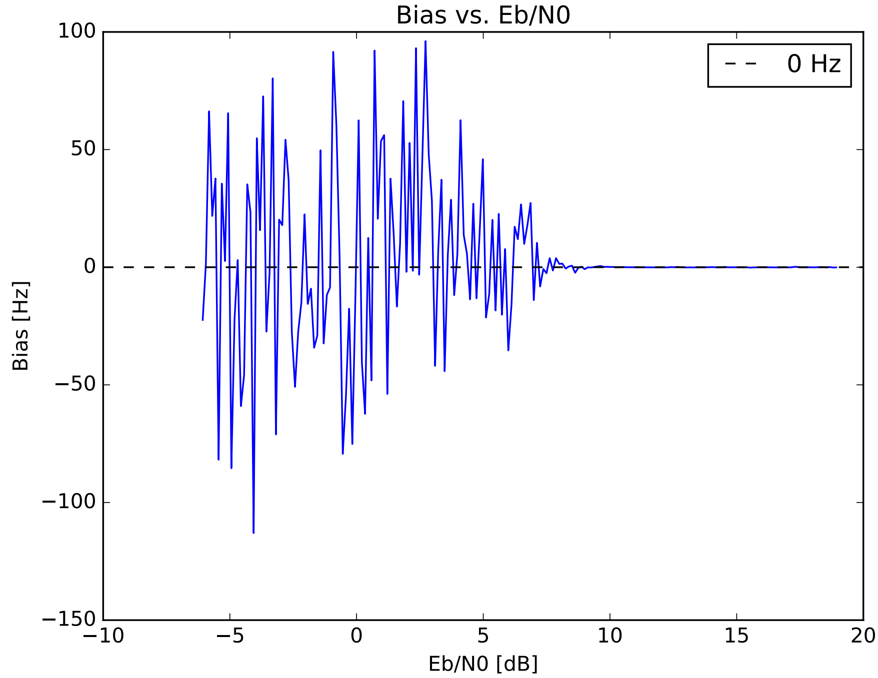

Figure 4.6: Estimate of bias for the estimator in (4.15) for 200 different Eb/N0 values.

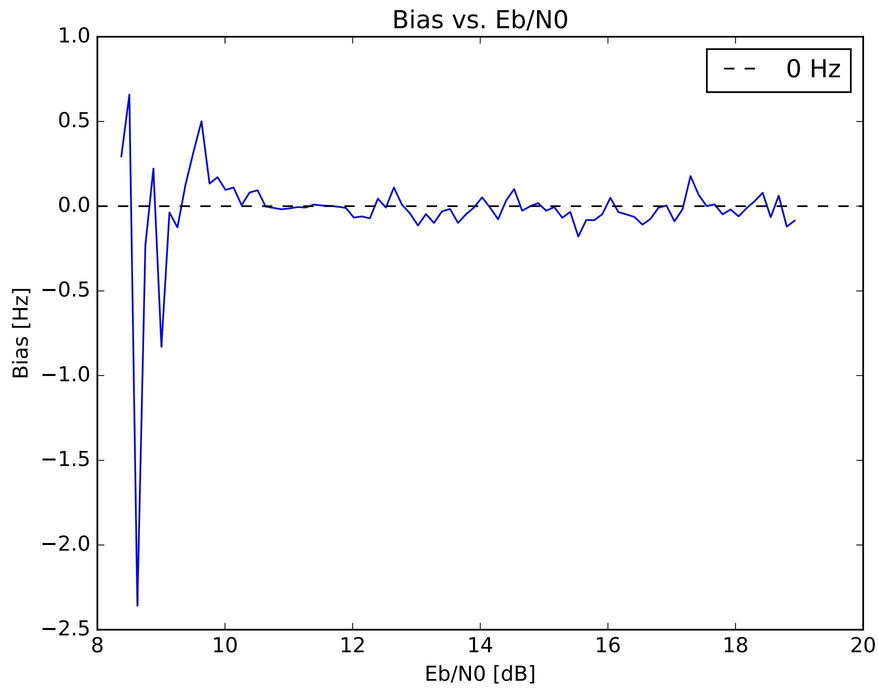

Figure 4.7: Zoom of the tail of the graph in Figure 4.6.

5 | Problem statement

Based on the space-based AIS system analysis up until this point of the thesis, the observable data available for AIS position spoofing detection is, amongst other, the carrier frequency offsets, the satellite positions and the alleged vessel positions. Detection of position spoofing will be examined based on estimates of the carrier frequency offsets experienced by LEO satellites receiving AIS signals. Cases in which a single LEO satellite is utilized are examined, as well as cases where two LEO satelites flying in constellation are examined.

Intuitively, basing the spoofing detection on said observables, and in particular the Doppler shift, seems reasonable. Individuals wanting to mask their position spoofing from Doppler shift based spoofing techniques would need to send out AIS signals from their true position with a carrier frequency that, when received by the satellite, match their spoofed position. This would require knowledge about the velocity, position and orbit of the satellite at the time of an AIS message transmission. Furthermore, it would require an oscillator on-board the vessel that can generate carrier waves across a relatively wide range of frequencies.

A disadvantage in the space-based AIS system is that of overlapping AIS messages from different vessels [44, pp. 2529-2530]. The partial, or complete, overlap of AIS messages is a consequence of receiving AIS messages from space. Depending on the degree of overlap, algorithms for the separation of overlapping AIS messages exist [44, p. 2529]. However, separation of colliding AIS messages is out of the scope of this thesis, hence the assumption is that no overlapping of AIS messages occurs and that the vessel information in the received messages is not contaminated by overlapping.

In conclusion, the aim of this thesis is to be able to detect AIS positon spoofing based on the carrier frequency offsets, and thus indirectly on the Doppler shifts, experienced on the LEO satellites.

5.1 Problem statement

Based on the system analysis and description in the Chapters 2 and 4, the problem statement in this thesis is

- Can AIS position spoofing be detected based on the observable variables in the space-based AIS sytem?

- How can a spoofing detection algorithm be constructed?
- When can AIS position spoofing be detected?

6 | Space-based AIS system data generation

This chapter describes how data is simulated in this thesis. Data is simulated in this thesis since no real world data has been available. Data simulated according to the descriptions in this chapter has no error modelling to compensate for real-world measurement errors and noise. The modelling of errors is described in Chapter 7. The procedures described in this chapter generate the data associated with $M \geq 1$ satellites simultaneously receiving N AIS messages sent out by a single vessel, i.e. each of the N AIS message are received by all of the M utilized satellites. This data includes the times at which the vessel sent out each of the N AIS messages, the position encoded in each of these messages, the carrier frequency used to send out each of these messages, and M pairs of satellite points upon receival of the n'th AIS message for $n = 0, 1, \dots, N-1$. A block diagram of the data generation can be seen in Figure 6.1. The output data that is denoted using a tilde is the data for which, in Chapter 7, errors will be modelled. A common notation in this chapter is $\mathbb{S}^2 = \{\boldsymbol{x} \in \mathbb{R}^3 \mid \|\boldsymbol{x}\| = 1\}$, which is the unit sphere.

The set of inputs when generating data is

$$\mathcal{D}_{input} = \left\{t_r, \boldsymbol{p}_v^{(0)}, v_v, S, d_s, \phi_{dir}, \mu_{dir}, i^{(0)}, \Omega_{off}^{(0)}, i^{(1)}, \Omega_{off}^{(1)}, \dots, i^{(M-1)}, \Omega_{off}^{(M-1)}\right\},$$

where

- t_r is the reporting interval of the vessel.
- $\boldsymbol{p}_v^{(0)} \in \mathbb{S}^2$ is the first true vessel position.
- $v_v \geq 0$ is the speed by which the vessel travels.
- $S \in \{0, 1\}$ determines whether the vessel is spoofing its position. If S is set to 0, the vessel is not spoofing its position. If S is set to 1, the vessel is spoofing its position.
- $d_s \geq 0$ is how far away the vessel is spoofing its position.
- $\phi_{dir} \in [0, 2\pi)$ determines the direction in which the vessel is spoofing its position if spoofing is occuring.

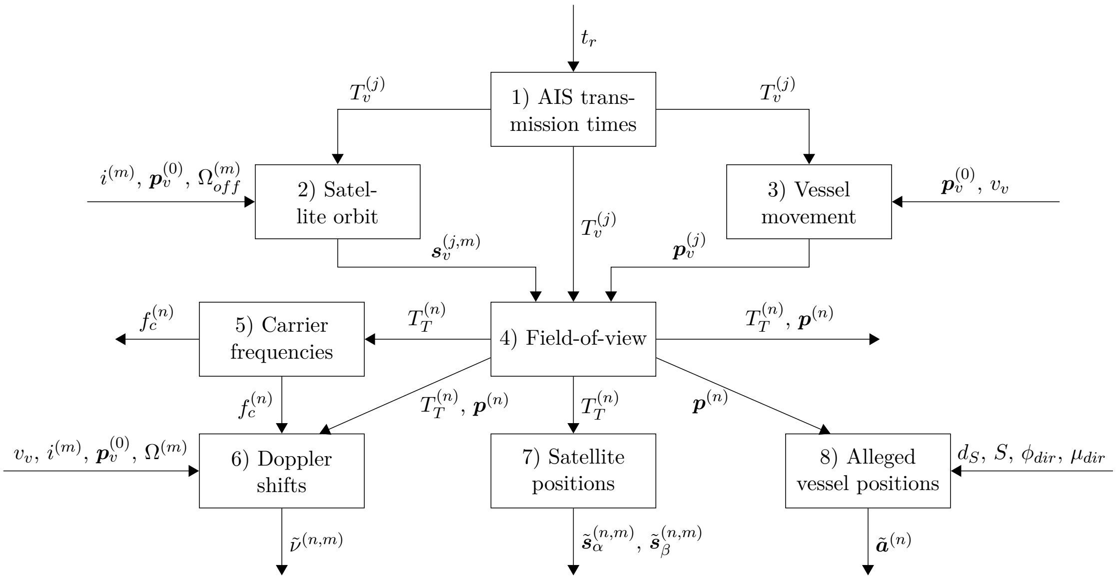

Figure 6.1: Data generation block diagram. The arrows not pointing to a block symbolize the data output. Notice that whenever index superscripts are used in this figure, this is to be understood as inputs and outputs being passed between the blocks for $n = 0, 1, \ldots, N-1$ and/or $m = 0, 1, \ldots, M-1$, e.g. when writing $\boldsymbol{p}^{(n)}$ this is to be understood as $\boldsymbol{p}^{(n)}$ for $n = 0, 1, \ldots, N-1$.

- $\mu_{dir} \in [0, 2\pi)$ determines the direction in which the vessel is heading.
- $i^{(m)} \in [0, \pi]$ is the orbit inclination of the m'th satellite for $m = 0, 1, \ldots, M-1$.
- $\Omega_{off}^{(m)} \in [0, 2\pi)$ is an angle used to make the m'th satellite orbit pass the vessel $\boldsymbol{p}_v^{(0)}$ at an angle.

The output of the data generation is, for $n = 0, 1, \ldots, N-1$,

- $T_T^{(n)} \geq 0$, the time at which the vessel sends out its n'th AIS message.
- $\tilde{\nu}^{(n,m)} \in \mathbb{R}$, the Doppler shift experienced on the m'th satellite upon receiving the n'th AIS message at time $T_T^{(n)}$.
- $\boldsymbol{p}^{(n)} \in \mathbb{S}^2$, the true vessel positions.
- $\tilde{\boldsymbol{a}}^{(n)} \in \mathbb{S}^2$, the alleged vessel positions, i.e. the positions encoded in the AIS messages, which may be subject to spoofing.
- $f_c^{(n)} \in \{f_1, f_2\}$, the carrier frequency used to send out the n'th AIS message.
- $\tilde{\boldsymbol{s}}_\alpha^{(n,m)}, \tilde{\boldsymbol{s}}_\beta^{(n,m)} \in \mathbb{S}^2$, pairs of satellite positions for the m'th satellite upon receiving the n'th AIS message.

Notice that the elevation angle, e, and the satellite orbit height, h, are also used in the data generation. These are assumed fixed at $e = 16$ degrees, due to the link budget from Chapter 3, and $h = 500$, which is chosen based on the GomSpace Starling project. Moreover, a parameter f_p is used in the data generation, which is the assumed sampling frequency of the GPS embedded on the satellite. This is set to 100 Hz, based on the GomSpace Starling project. Notice that in the succeeding chapters, whenever a single satellite receiving N AIS messages is used, i.e. when $M = 1$, the notation $\nu^{(n)}$ is used for the Doppler shift experienced on the satellite upon receiving the n'th AIS message and the pairs of satellite points are denoted $(\tilde{\boldsymbol{s}}_{\alpha}^{(n)}, \tilde{\boldsymbol{s}}_{\beta}^{(n)})$. In other words, the satellite superscript is suppressed in the notation. Whenever this is the case, it is clear from the context.

Notice that the data generation in this chapter does not compensate for the fact that some packages may be lost due to the packet error probability shown in (3.13). Instead, this is compensated for in the end of Chapter 7, in which error modelling is described.

6.1 Simulation of AIS transmission times

This section outlines the procedure in block 1 in Figure 6.1. The simulation of AIS message transmission times starts at time $t = 0$. The simulation of these transmission times is based on the SOTDMA scheme, which is described in Appendix K. The initial AIS message is sent out at time

$$T_v^{(0)} \sim \text{unif}[0, T_{AIS}, 2 \cdot T_{AIS}, \dots, t_r],$$

where t_r is the reporting interval in seconds of the vessel, as described in Section 2.1. The succeeding AIS message transmission times are generated as

$$T_v^{(j)} = T_v^{(0)} + j \cdot \frac{t_r}{T_{AIS}} + w^{(j)}, \qquad j = 1, 2, \dots, J-1,$$

where

$$w^{(j)} \sim \text{unif}\left([-I, I] \cap \mathbb{Z}\right),$$

and

$$I = \left\lfloor \frac{225}{t_r} \right\rfloor,$$

which corresponds to the selection interval described in Appendix K. This procedure is illustrated in Figure 6.2a and 6.2b. All the transmission times are collected in the set

$$\mathcal{T}_v = \left\{T_v^{(j)}\right\}_{j=0}^{J-1}. \tag{6.1}$$

Lastly, making the assumption that the speed, v_v of a given vessel is constant during a pass, the report interval, t_r, used by said vessel can be determined by GomSpace by utilizing the relatively large gap between different report intervals, as evident from Table 2.1.

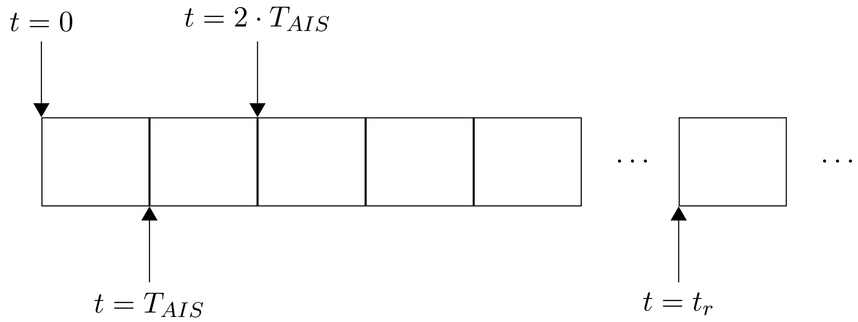

(a)

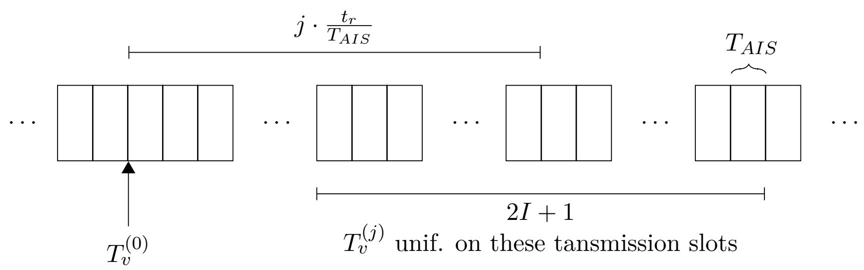

(b)

Figure 6.2: **(a)**: SOTDMA transmission slots on which $T_v^{(0)}$ is chosen. **(b)**: SOTDMA transmission slots on which $T_v^{(j)}$ is chosen for $j = 1, 2, \dots, J-1$.

6.2 Simulation of satellite orbit

This section outlines the procedure in block 2 in Figure 6.1. It proceeds by constructing a mathematical expression that describes a circular satellite orbit, which can be sampled in time to obtain satellite positions. Having created this expression, a new expression describing a satellite orbit in which Earth's rotation has been accounted for is created. The expression in which Earth's rotation has been taken into account can also be sampled in time in order to obtain satellite positions. The expression accounting for Earth's rotation is named g_1, and is the one utilized when creating satellite positions.

The mathematical expressions developed in this section to describe satellite orbits are based on the expression for a circle in three dimensions with unit radius and center in origo. This is a function $g : \mathbb{R}_+ \times \mathbb{S}^2 \times \mathbb{S}^2 \mapsto \mathbb{S}^2$ expressed as

$$g(t, \boldsymbol{u}, \boldsymbol{n}) = \cos\left(\frac{2\pi t}{T_o}\right)\boldsymbol{u} + \sin\left(\frac{2\pi t}{T_o}\right)\boldsymbol{n} \times \boldsymbol{u}, \tag{6.2}$$

where

$$T_o = \frac{2\pi(R_E + h)}{v_s} \qquad \text{(s)} \tag{6.3}$$

is the time it takes for the satellite to travel one orbit, $\boldsymbol{n}$ is a normal vector, $\boldsymbol{u}$ is a vector perpendicular to $\boldsymbol{n}$, and "$\times$" is the vector cross product. Moreover, v_s is the speed of the satellite as calculated in (2.3). Notice that the function in (6.2) is such that $g(0, \boldsymbol{u}, \boldsymbol{n}) = \boldsymbol{u}$.

Generating a circular satellite orbit that crosses directly above a vessel position

$$\boldsymbol{p}_v^{(0)} = \begin{bmatrix}\sin(\theta_p)\cos(\phi_p) & \sin(\theta_p)\sin(\phi_p) & \cos(\theta_p)\end{bmatrix}^\top$$

is done with the function

$$g_0\left(t, \boldsymbol{p}_v^{(0)}, i\right) = g\left(t, \boldsymbol{u}_0, \boldsymbol{n}_0\left(\boldsymbol{u}_0\right)\right). \tag{6.4}$$

In (6.4), $\boldsymbol{u}_0$ is given as

$$\boldsymbol{u}_0 = \begin{bmatrix}\cos\left(\phi_0\right) & \sin\left(\phi_0\right) & 0\end{bmatrix}^\top, \tag{6.5}$$

in which

$$\phi_0 = \begin{cases} \phi_p - a_2 & \text{if } \phi_p \geq a_2 \\ 2\pi + \phi_p - a_2 & \text{if } \phi_p < a_2 \end{cases}$$

and

$$a_2 = \cos^{-1}\left(\frac{\cos(a_3)}{\cos(a_1)}\right), \tag{6.6}$$

in which

$$a_3 = \sin^{-1}\left(\frac{\sin(a_1)}{\sin(i)}\right) \tag{6.7}$$

and

$$a_1 = \frac{\pi}{2} - \theta_p. \tag{6.8}$$

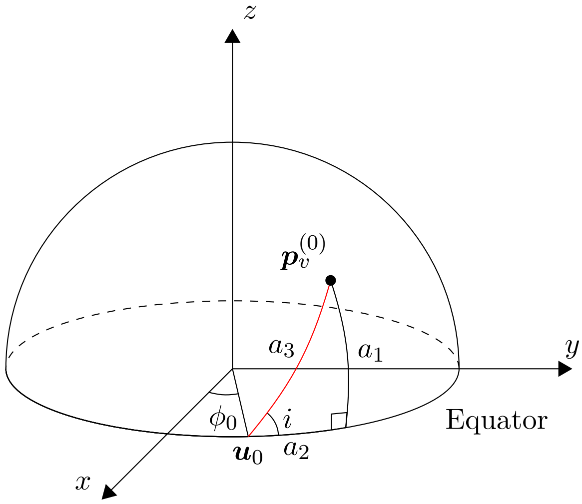

Figure 6.3: Earth depicted as a unit sphere. Vessel position, $\boldsymbol{p}_v^{(0)}$, on the northern hemisphere and part of a satellite orbit (red solid line).

The calculation of $\boldsymbol{u}_0$ relies on the geometry seen in Figure 6.3, and the calculation of the triangle sides in (6.6)-(6.8) follows from right spherical triangle identities. Notice that choosing $\boldsymbol{u}_0$ as described above ensures that it lies in the $x - y$ plane. Thus, the generated orbit starts at Equator at time $t = 0$. All LEO satellite orbits cross Equator, hence this choice. Moreover,

$$\boldsymbol{n}_0(\boldsymbol{u}_0) = \boldsymbol{R}\left(\boldsymbol{u}_0, -\left(i - \frac{\pi}{2}\right)\right)\boldsymbol{R}_z\left(-\frac{\pi}{2}\right)\boldsymbol{u}_0. \tag{6.9}$$

Choosing $\boldsymbol{n}$ as in (6.9) ensures that the normal vector is perpendicular to $\boldsymbol{u}_0$ and that the satellite orbit generated from the function g_0 has the right orbit inclination. In (6.9), $\boldsymbol{n}_0$ is the result of a clockwise rotation of $\boldsymbol{u}_0$ around the z-axis followed by a clockwise rotation around $\boldsymbol{u}_0$. The matrices $\boldsymbol{R}_z$ and $\boldsymbol{R}$, which are rotations around the z-axis and an arbitrary axis, respectively, are described in Appendix F, Section F.2. Notice that the condition

$$i \geq \frac{\pi}{2} - \theta_p, \qquad \text{for } 0 \leq i \leq \frac{\pi}{2}.$$

must be fulfilled for the satellite to be able to fly directly above the point $\boldsymbol{p}_v^{(0)}$. An example of an orbit generated using (6.4) can be seen in Figure 6.4. In order to generate a satellite orbit in which Earth's rotation has been accounted for, the expression

$$g_1(t, i, \boldsymbol{p}_v^{(0)}, \Omega_{off}) = \boldsymbol{R}_z(\omega_E \cdot t)g(t, \boldsymbol{u}_1, \boldsymbol{n}_1(\boldsymbol{u}_1)) \tag{6.10}$$

is used. The quantity

$$\omega_E = \frac{2\pi}{T_E}, \qquad (\text{rad s}^{-1}) \tag{6.11}$$

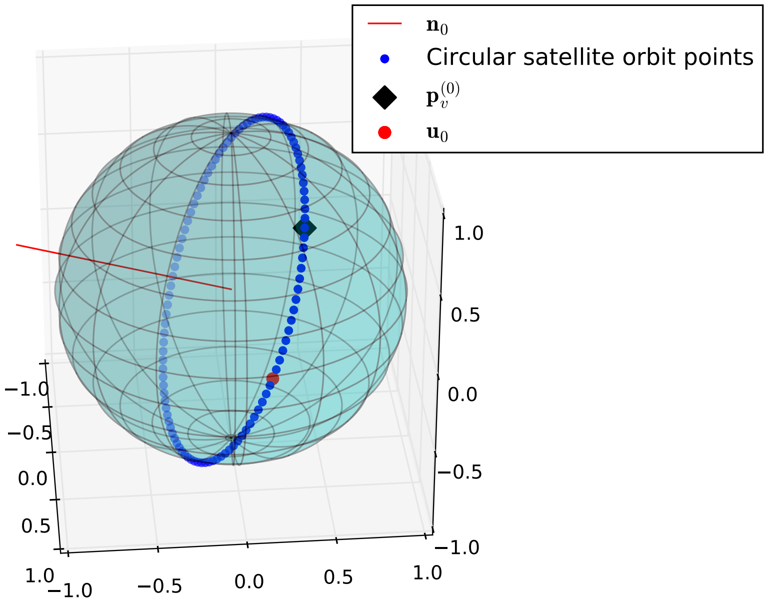

Figure 6.4: A vessel, $\boldsymbol{p}_v^{(0)}$, at colatitude 0.80 and longitude 0.52 and with $i = 70 \cdot \frac{\pi}{180}$ as inclination angle. Moreover, 109 evenly spaced satellite orbit points are illustrated. The length of the normal vector, $\boldsymbol{n}_0$, has been extended for illustrative purposes.

is the angular rotation speed of Earth and T_E is the duration of a day. In (6.10), $\boldsymbol{u}_1$ is based on $\boldsymbol{u}_0$ from (6.5) and a_3 as given in (6.7). It is given as

$$\boldsymbol{u}_1 = \boldsymbol{R}_z(\Omega_{off})\boldsymbol{R}_z(-\Omega)\boldsymbol{u}_0, \tag{6.12}$$

where

$$\Omega = \omega_E \cdot t_s, \qquad \text{(rad)} \tag{6.13}$$

and t_s is the time it takes the satellite to travel the distance corresponding to the angle a_3 in Figure 6.3. It is given as

$$t_s = \frac{a_3}{\omega_s}, \qquad \text{(s)} \tag{6.14}$$

where

$$\omega_s = \frac{v_s}{2\pi(R_E + h)} \qquad (\text{rad s}^{-1}) \tag{6.15}$$

is the radian speed of the satellite. Moreover,

$$\boldsymbol{n}_1(\boldsymbol{u}_1) = \boldsymbol{R}\left(\boldsymbol{u}_1, -\left(i - \frac{\pi}{2}\right)\right)\boldsymbol{R}_z\left(-\frac{\pi}{2}\right)\boldsymbol{u}_1,$$

and $\Omega_{off} \in [-\pi, \pi)$ is an offset angle with which the satellite is supposed to pass the point $\boldsymbol{p}_v^{(0)}$. For $\Omega_{off} = 0$, the satellite passes directly above the point $\boldsymbol{p}_v^{(0)}$. In Figure 6.5, this is illustrated. This figure illustrates the satellite orbit passing directly above $\boldsymbol{p}_v^{(0)}$, i.e. the figure illustrates the case in which $\Omega_{off} = 0$. This would not have been the case

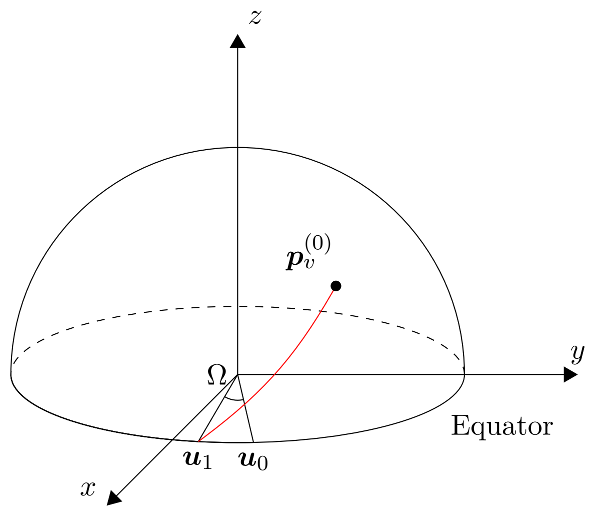

Figure 6.5: Part of a satellite orbit in which $\boldsymbol{u}_0$ has been shifted to $\boldsymbol{u}_1$ to ensure that the satellite flies directly over the vessel, $\boldsymbol{p}_v^{(0)}$, after compensating for Earth's rotation.

if the time-dependent rotation in (6.10), which is used to include Earth's rotation, had been applied directly to the expression in (6.4). Notice that the way the time-dependent rotation is applied is under the assumption that Earth revolves in a counterclockwise direction around the z-axis. An example of an orbit generated using (6.10) with $\Omega_{off} = 0$ can be seen in Figure 6.6.

In order to later find out which of the time values in the set $\mathcal{T}_v$ from (6.1) that correspond to times at which the vessel is within the FoV of all of the M satellites at once, satellite orbit points for the m'th satellite are generated as

$$\boldsymbol{s}_v^{(j,m)} = g_1\left(T_v^{(j)}, i^{(m)}, \boldsymbol{p}_v^{(0)}, \Omega_{off}^{(m)}\right), \qquad j = 0, 1, \ldots, J-1.$$

6.3 Simulation of vessel movement

This section outlines the procedure in block 3 in Figure 6.1. To simulate vessel movement, the von Mises distribution and the principles behind the sampling of a Fisher distribution are used. The von Mises distribution is described in Appendix E and the sampling of a Fisher distribution is described in Section 7.1. Vessel movement is generated stochastically in this thesis. The directions in which a vessel is moving between

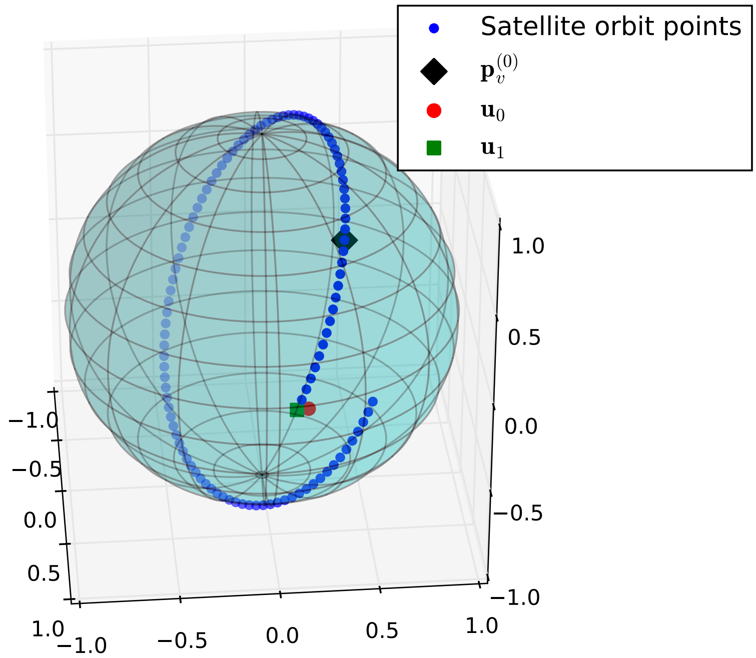

Figure 6.6: A vessel, $\boldsymbol{p}_v^{(0)}$, at colatitude 0.80 and longitude 0.52 and with $i = 70 \cdot \frac{\pi}{180}$ as inclination angle. Moreover, 109 evenly spaced satellite orbit points are illustrated.

successive AIS message transmissions are generated as

$$\begin{aligned} \mu_v^{(1)} &= \mu_{dir} \\ \mu_v^{(2)} &\sim \mathrm{VM}(\bar{\mu}^{(2)}, \kappa_r) \\ &\vdots \\ \mu_v^{(J-1)} &\sim \mathrm{VM}(\bar{\mu}^{(J-1)}, \kappa_r), \end{aligned} \tag{6.16}$$

where

$$\bar{\mu}^{(j)} = \operatorname{atan2}\left(\sum_{i=\max(1,j-N_{avg})}^{j-1} \sin\left(\mu_v^{(i)}\right), \sum_{i=\max(1,j-N_{avg})}^{j-1} \cos\left(\mu_v^{(i)}\right) \right), \qquad j = 2, 3, \ldots, J-1. \tag{6.17}$$

The expression in (6.17) is an estimate of the mean of a collection of angles as given in [39, p. 5]. The variable N_{avg} is the amount of angles the mean angle estimate is to be estimated from. In this thesis, the value $N_{avg} = 10$ is used.

Next, the distances travelled by the vessel between successive transmission times are calculated as

$$d^{(j)} = \left(T_v^{(j-1)} - T_v^{(j)}\right) v_v, \qquad j = 1, 2, \ldots, J-1, \tag{6.18}$$

where v_v is the speed of the vessel, which is assumed constant when generating data.

Now, in order to generate the vessel path points, the distances in (6.18) are used to generate points around the North Pole with colatitudes

$$\theta_0^{(j)} = \frac{d^{(j)}}{R_E}, \qquad j = 1, 2, \ldots, J-1, \tag{6.19}$$

and longitudes

$$\phi_0^{(j)} = \mu_v^{(j)}, \qquad j = 1, 2, \ldots, J-1.$$

These points are converted to Cartesian coordinates and denoted $\boldsymbol{p}_0^{(j)} \in \mathbb{S}^2$ for $j = 1, 2, \ldots, J-1$. The points are rotated, creating the vessel path points. This is done using the same principles as the rotations happening in Algorithm 1 used to draw samples from a Fisher distribution. The vessel path points then becomes

$$\boldsymbol{p}_v^{(j)} = \boldsymbol{R}\left(\boldsymbol{k}^{(j)}, \psi^{(j)}\right) \boldsymbol{p}_0^{(j)}, \qquad j = 1, 2, \ldots, J-1, \tag{6.20}$$

where

$$\boldsymbol{k}^{(j)} = \frac{\boldsymbol{z} \times \boldsymbol{p}_v^{(j-1)}}{\|\boldsymbol{z} \times \boldsymbol{p}_v^{(j-1)}\|}, \qquad j = 1, 2, \ldots, J-1,$$

in which $\boldsymbol{z} = \begin{bmatrix} 0 & 0 & 1 \end{bmatrix}^\top$ and

$$\psi^{(j)} = \cos^{-1}\left(\boldsymbol{z}^\top \boldsymbol{p}_v^{(j-1)}\right).$$

Naturally, if no vessel movement is desired, v_v is set to zero, yielding

$$\boldsymbol{p}_v^{(0)} = \boldsymbol{p}_v^{(1)} = \ldots = \boldsymbol{p}_v^{(J-1)}.$$

Examples of generated vessel movement are seen in Figure 6.7. This is an azimuthal equidistant projection (AEP) plot in which the center point is $\boldsymbol{p}_v^{(0)}$ and 10 realizations of vessel movement with a report interval $t_r = 10$ s and a vessel speed $v_v = 25.9$ km/h are shown. AEP is described in Appendix M. Circles of different radii are drawn for illustrative purposes.

6.4 Computation of satellite field-of-view

This section outlines the procedure in block 4 in Figure 6.1. The times in the set $\mathcal{T}_v$ that correspond to vessel positions from which a satellite can receive AIS messages can be found based on the FoV geometry, as shown in Figures 6.8a and 6.8b, and the vessel positions generated in Equation (6.20). They are collected in the set

$$\begin{aligned}\mathcal{T}_T = \Bigg\{ T_v^{(j)} \,\Bigg|\, &\cos^{-1}\left(\left(\boldsymbol{s}_v^{(j,0)}\right)^\top \boldsymbol{p}_v^{(j)}\right) \leq \Phi,\ \cos^{-1}\left(\left(\boldsymbol{s}_v^{(j,1)}\right)^\top \boldsymbol{p}_v^{(j)}\right) \leq \Phi,\\ &\ldots, \cos^{-1}\left(\left(\boldsymbol{s}_v^{(j,M-1)}\right)^\top \boldsymbol{p}_v^{(j)}\right) \leq \Phi,\ j = 0, 1, \ldots, J-1 \Bigg\},\end{aligned}$$

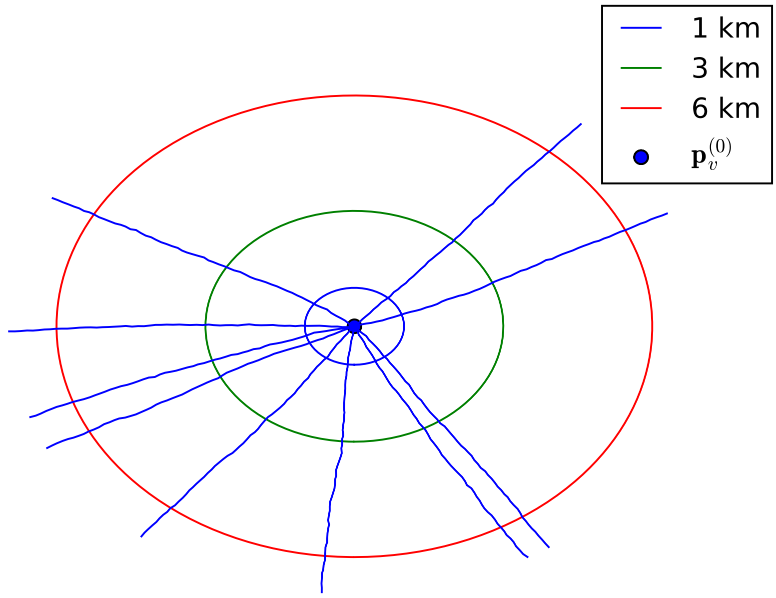

Figure 6.7: Illustration of generated vessel movements.

where

$$\Phi = \frac{\pi}{2} - e - q, \tag{6.21}$$

in which e is the elevation angle and

$$q = \sin^{-1}\left(\frac{R_E \sin\left(\frac{\pi}{2} + e\right)}{R_E + h}\right), \tag{6.22}$$

which follows from applying the law of sines to the triangle in Figure 6.8b. Notice that $|\mathcal{T}_T| = N$, where $N \leq J$ is the number of AIS messages simultaneously received by all M satellites in a pass. The elements in the set $\mathcal{T}_T$ are denoted as $T_T^{(n)}$ for $n = 0, 1, \ldots, N-1$. Moreover, the vessel positions $\boldsymbol{p}_v^{(j)}$ corresponding to the AIS transmission times $T_T^{(n)}$, $n = 0, 1, \ldots, N-1$ are denoted as $\boldsymbol{p}^{(n)}$.

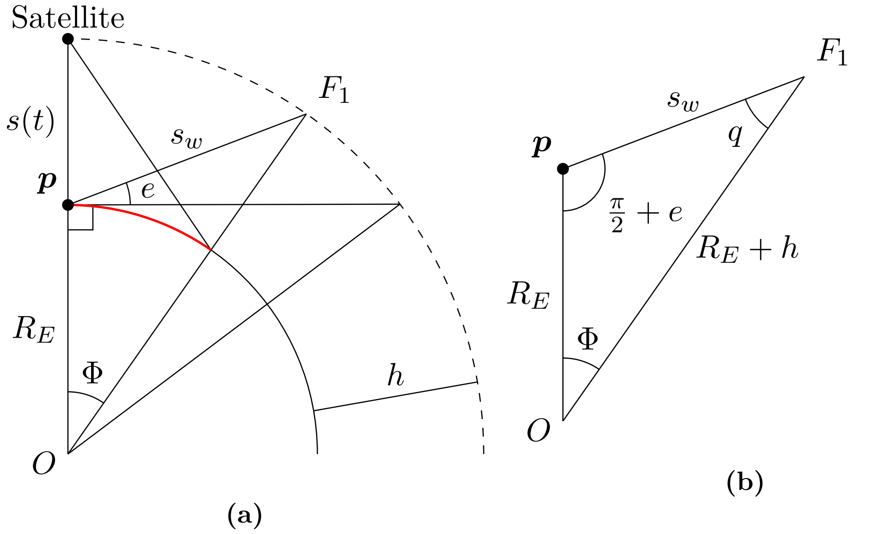

Figure 6.8: **(a)**: The elevation angle, e, determining how far above the ideal vessel horizon the satellite has to be in order to receive AIS signals from the vessel. **(b)**: Triangle extracted from Figure 6.8a.

6.5 Simulation of carrier frequencies

This section outlines the procedure in block 5 in Figure 6.1. It is taken into account that vessels alternate between the two AIS frequencies f_1 and f_2 when sending out their AIS messages. The initial AIS message is sent out using a carrier frequency of

$$f_c^{(0)} \sim \text{unif}\left(\{f_1, f_2\}\right),$$

and $f_c^{(n)}$, for $n = 0, 1, \ldots, N-1$, is equal to $f_1, f_2, f_1, \ldots$ if $f_c^{(0)} = f_1$, and equal to $f_2, f_1, f_2, \ldots$ if $f_c^{(0)} = f_2$.

6.6 Simulation of Doppler shifts

This section outlines the procedure in block 6 in Figure 6.1. The Doppler shift, $\nu^{(n,m)}$, experienced by the m'th satellite when receiving the n'th AIS message in a pass is calculated using an approximation of the derivative in (2.6). For the m'th satellite, the relative velocities are approximated as

$$v_r^{(n,m)} = \frac{\left\|(R_E+h)\cdot \boldsymbol{b}_2^{(n,m)} - R_E \cdot \boldsymbol{p}_-^{(n)}\right\| - \left\|(R_E+h)\cdot \boldsymbol{b}_1^{(n,m)} - R_E \cdot \boldsymbol{p}^{(n)}\right\|}{\delta}, \qquad (6.23)$$

for $n = 0, 1, \ldots, N-1$, where $\|\cdot\|$ is the ℓ^2-norm,

$$\boldsymbol{b}_1^{(n,m)} = g_1\left(T_T^{(n)}, i^{(m)}, \boldsymbol{p}_v^{(0)}, \Omega_{off}^{(m)}\right),$$

and

$$\boldsymbol{b}_2^{(n,m)} = g_1\left(T_T^{(n)} - \delta, i^{(m)}, \boldsymbol{p}_v^{(0)}, \Omega_{off}^{(m)}\right),$$

in which $\delta > 0$ is a quantity determining the accuracy of the approximation of the derivative in (2.6). Moreover,

$$\boldsymbol{p}_-^{(n)} = \begin{cases} \boldsymbol{p}^{(n)} & \text{if } v_v = 0 \\ \boldsymbol{R}\left(\boldsymbol{k}^{(n)}, \psi^{(n)}\right)\boldsymbol{p}^{(n)} & \text{if } v_v > 0, \end{cases} \qquad n = 0, 1, \ldots, N-2,$$

in which

$$\boldsymbol{k}^{(n)} = \frac{\boldsymbol{p}^{(n)} \times \boldsymbol{p}^{(n+1)}}{\|\boldsymbol{p}^{(n)} \times \boldsymbol{p}^{(n+1)}\|} \qquad n = 0, 1, \ldots, N-2$$

and

$$\psi^{(n)} = \frac{\delta \cdot v_v}{R_E} \qquad n = 0, 1, \ldots, N-2.$$

In the case of the last received AIS message,

$$\boldsymbol{p}_-^{(N-1)} = \begin{cases} \boldsymbol{p}^{(N-1)} & \text{if } v_v = 0 \\ \boldsymbol{R}\left(\boldsymbol{k}^{(N-2)}, \psi^{(N-2)}\right)\boldsymbol{p}^{(N-1)} & \text{if } v_v > 0. \end{cases}$$

For the m'th satellite, the Doppler shifts are then calculated from (6.23) as

$$\tilde{\nu}^{(n,m)} = \frac{v_r^{(n,m)}}{c} f_c^{(n)}, \qquad n = 0, 1, \ldots, N-1.$$

6.7 Simulation of satellite positions

This section outlines the procedure in block 7 in Figure 6.1. The satellite positions at the times at which these are available, i.e. the times at which the GPS on-board the satellite samples the satellite position, are generated. The Starling satellites are assumed to be able to sample their position with a frequency of $f_p = 100$ Hz. Two satellite positions will be generated for each of the N AIS message transmission times. The reason for generating $2N$ satellite points for each of the M satellites, instead of N satellite points, is due to the nature of the spoofing detection algorithms presented later in this thesis. These utilize two satellite positions for each AIS message transmission, in order to calculate Doppler shifts. This is carried out using the same approximation principle of the relative velocity as in (6.23). The above mentioned sampling frequency is the maximum sampling frequency available with the GPS that is to be embedded in the Starling project. Naturally, a lower sampling frequency could be used, but the maximum frequency is chosen in order to get the minimum temporal spacing between pairs of satellite points, since this yields better approximations of relative velocity.

The pairs of satellite positions $(\tilde{\boldsymbol{s}}_\alpha^{(n,m)}, \tilde{\boldsymbol{s}}_\beta^{(n,m)})$ are generated, where

$$\tilde{\boldsymbol{s}}_\alpha^{(n,m)} = g_1\left(T_{SAT1}^{(n)}, i^{(m)}, \boldsymbol{p}_v^{(0)}, \Omega_{off}^{(m)}\right)$$

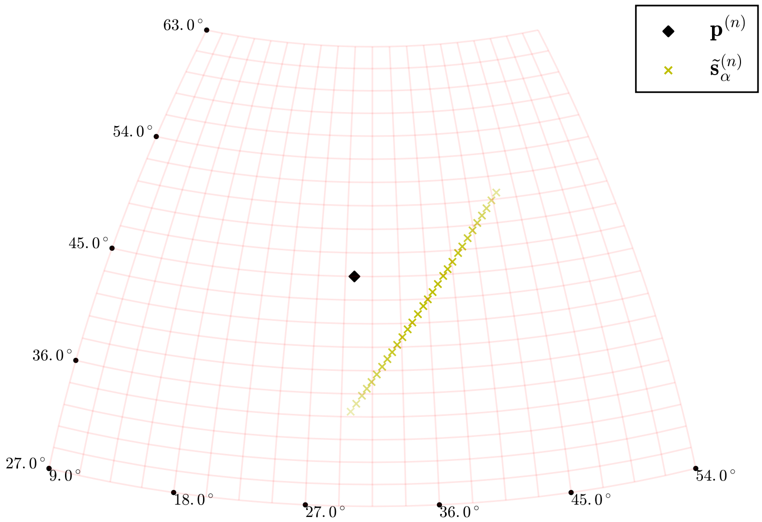

Figure 6.9: Example illustration. Geographical coodinates are included for illustrative purposes.

and

$$\tilde{\boldsymbol{s}}_{\beta}^{(n,m)} = g_1\left(T_{SAT2}^{(n)}, i^{(m)}, \boldsymbol{p}_v^{(0)}, \Omega_{off}^{(m)}\right),$$

in which

$$T_{SAT1}^{(n)} = \left\lfloor T_T^{(n)} \cdot f_p \right\rfloor \cdot f_p^{-1} \tag{6.24}$$

and

$$T_{SAT2}^{(n)} = \left\lceil T_T^{(n)} \cdot f_p \right\rceil \cdot f_p^{-1}. \tag{6.25}$$

In (6.24) and (6.25), $\lfloor \cdot \rfloor$ and $\lceil \cdot \rceil$ are the floor and ceiling operators, respectively. The expression in (6.24) corresponds to a mapping of $T_T^{(n)}$ to the greatest integer multiple of f_p^{-1} less than or equal to $T_T^{(n)}$, and the expression in (6.25) corresponds to a mapping of $T_T^{(n)}$ to the least integer multiple of f_p^{-1} greater than or equal to $T_T^{(n)}$.

Figure 6.9 shows an example of a vessel and a satellite orbit generated according to the descriptions thus far in this chapter. The vessel is non-moving, and hence $\boldsymbol{p}^{(0)} = \boldsymbol{p}^{(1)} = \ldots = \boldsymbol{p}^{(N-1)}$. The plot of the satellite orbit consists of the points $\tilde{\boldsymbol{s}}_{\alpha}^{(n)}$ for $n = 0, 1, \ldots, N-1$. Notice that in this figure, and in all other similar figures shown in this thesis, the satellite is flying in a direction from the bottom of the figure towards the top. Thus $\tilde{\boldsymbol{s}}_{\alpha}^{(0)}$ is the bottom-most satellite point in the figure and $\tilde{\boldsymbol{s}}_{\alpha}^{(N-1)}$ is the top-most satellite point. In this simulation, $N = 31$ AIS messages were received. The figure is made with $\boldsymbol{p}_v^{(0)}$ at a colatitude $\frac{\pi}{4}$, a longitude of $\frac{\pi}{6}$, an inclination of 70°, an orbit offset of $\frac{\pi}{24}$, a report interval of 10 s, and a vessel speed of 0 knots.

6.8 Simulation of alleged vessel positions

This section outlines the procedure in block 8 in Figure 6.1. For $n = 0, 1, \ldots, N-1$, the generation of the positions encoded in the transmitted AIS messages that can be subject to position spoofing is done as

$$\tilde{\boldsymbol{a}}^{(n)} = \begin{cases} \boldsymbol{p}^{(n)} & \text{if } S = 0 \\ \boldsymbol{R}(\boldsymbol{k}^{(n)}, \psi^{(n)})\boldsymbol{R}(\boldsymbol{z}, \phi_{dir})\boldsymbol{R}(\boldsymbol{y}, \theta_s)\boldsymbol{z} & \text{if } S = 1. \end{cases} \tag{6.26}$$

In (6.26),

$$\boldsymbol{k}^{(n)} = \frac{\boldsymbol{z} \times \boldsymbol{p}^{(n)}}{\|\boldsymbol{z} \times \boldsymbol{p}^{(n)}\|},$$

$$\psi^{(n)} = \cos^{-1}\left(\boldsymbol{z}^\top \boldsymbol{p}^{(n)}\right),$$

$$\boldsymbol{y} = \begin{bmatrix} 0 & 1 & 0 \end{bmatrix}^\top,$$

and

$$\theta_s = \frac{d_s}{R_E},$$

in which d_s is the spoofing distance, i.e. how far away from the true position of the vessel the alleged position lies. Moreover, S is an indication of whether the alleged vessel positions should be generated as spoofed positions or not and $\phi_{dir} \in [0, 2\pi)$ is an angle determining the direction in which the vessel positions are spoofed. Notice that the underlying assumption in how the AIS vessel positions are generated is that if a vessel is spoofing its position, all AIS messages sent out by said vessel contain spoofed position information.

Notice that when a vessel is moving and $S = 1$, using (6.26) to generate the spoofed vessel path ensures that $\cos^{-1}\left(\left(\tilde{\boldsymbol{a}}^{(n)}\right)^\top \boldsymbol{p}^{(n)}\right) \cdot R_E = d_s$ for $n = 0, 1, \ldots, N-1$, i.e. the distance between a true vessel position and the corresponding spoofed position is equal to the desired spoofing distance. The trade-off is that the geometry of the true vessel path is slightly distorted in the spoofed vessel position path.

7 | Data error modelling and the Fisher distribution

Data simulated according to the descriptions in Chapter 6 is generated without taking real-world measurement errors and noise into account. The modelling of such errors in the generated data is described in this chapter.

One of the distributions used to model errors in this thesis is the Fisher distribution. Hence, this chapter introduces the Fisher distribution and an algorithm for drawing samples from the distribution. One of the parameters in this distribution is the concentration parameter κ. Several times in this thesis, this parameter is to be chosen based on certain criteria. These criteria are described after the distribution is introduced.

After this, the chapter describes the error modelling, starting with how errors are modelled in the single satellite case, and finishing with a description of error modelling in the case in which M satellites are utilized.

7.1 Fisher distribution and sampling

A well known probability distribution on the $(p-1)$-dimensional sphere is the von Mises-Fisher distribution. For the case of $p = 3$, it is one of the most frequently used distributions in this thesis. The case $p = 3$ is explored in this section. For the general case, see [25]. When $p = 3$, the distribution is often referred to as the Fisher distribution [25, p. 168] on the unit sphere. The Fisher distribution has a probability density function (pdf) given by

$$f_F(\boldsymbol{x} \mid \boldsymbol{\mu}, \kappa) = \frac{\kappa}{4\pi \sinh(\kappa)} \exp(\kappa \boldsymbol{\mu}^\top \boldsymbol{x}), \qquad \boldsymbol{x} \in \mathbb{S}^2, \tag{7.1}$$

where $\kappa \geq 0$ and $\boldsymbol{\mu} \in \mathbb{S}^2$ are the concentration parameter and mean direction, respectively. In this thesis, a Fisher distributed random vector is denoted $\boldsymbol{u} \sim F(\boldsymbol{\mu}, \kappa)$. The Fisher distribution has close ties to the three-dimensional normal distribution, as shown in Appendix D.

The problem of sampling from the Fisher distribution reduces to that of knowing how to sample a Fisher distribution with mean direction equal to a vector $\boldsymbol{z} = [0\,0\,1]^\top$. A rotation can then be applied to obtain samples from a Fisher distribution with an arbitrary mean direction $\boldsymbol{\mu} \in \mathbb{S}^2$. Assume for now that it is know how to obatin samples from a variable distributed according to the pdf $f_F(\boldsymbol{x} \mid \boldsymbol{z}, \kappa)$. Then the problem of sampling from a random variable distributed according to $f_F(\boldsymbol{x} \mid \boldsymbol{\mu}, \kappa)$ with $\boldsymbol{\mu} \neq \boldsymbol{z}$ is to find a rotation matrix $\boldsymbol{R}$ such that

$$\boldsymbol{\mu} = \boldsymbol{R}\boldsymbol{z}.$$

Disregarding the normalization constant for a moment, the rotation matrix is then inserted in the density in (7.1), yielding

$$\exp(\kappa \boldsymbol{\mu}^\top \boldsymbol{x}) = \exp(\kappa \boldsymbol{z}^\top \boldsymbol{R}^\top \boldsymbol{x}) = \exp(\kappa \boldsymbol{z}^\top \boldsymbol{y}), \tag{7.2}$$

where $\boldsymbol{y} = \boldsymbol{R}^\top \boldsymbol{x}$. If the normalization constant is included, the expression in (7.2) is a Fisher density with a change of variables corresponding to a rotation. It is seen that this density has mean direction equal to $\boldsymbol{z}$. Thus, when sampling the Fisher distribution with mean direction $\boldsymbol{\mu}$, the first step is to generate a sample $\boldsymbol{y} \sim F(\boldsymbol{z}, \kappa)$, and then simulate $\boldsymbol{x} = \boldsymbol{R}\boldsymbol{y}$.

It is often more convenient to work with the Fisher distribution when it is parameterized using spherical coordinates. An example of the convenience of such a parameterization will be evident in the algorithm for sampling the Fisher distribution. Changing the variables of the distribution from Cartesian to spherical coordinates using the variable transformation method described in Appendix C and the Jacobian determinant in (F.4) with $r = 1$ yields

$$f_F\left((\theta, \phi) \mid (\alpha, \beta), \kappa\right) = \frac{\kappa}{4\pi \sinh(\kappa)} \exp\left(\kappa \left(\cos(\theta)\cos(\alpha) + \sin(\theta)\sin(\alpha)\cos(\phi - \beta)\right)\right)\sin(\theta), \tag{7.3}$$

where $\alpha \in [0, \pi]$ and $\beta \in [0, 2\pi)$ are the spherical coordinates of the mean direction. When (θ, ϕ) is distributed according to (7.3), this is written as $(\theta, \phi) \sim F\left((\alpha, \beta), \kappa\right)$ in this thesis.

In the algorithm for drawing samples from the Fisher distribution, which is presented at the end of this section, a sample (θ_0, ϕ_0) is generated from the $F\left((0, 0), \kappa\right)$ distribution [10, p. 232], i.e. with the spherical coordinate point $(0, 0)$ as mean direction. This mean direction is referred to as the North Pole. The samples are then rotated such that the new mean direction is the same as the mean direction given as input to the algorithm.

To be able to sample from the Fisher distribution, the inverse transformation method is used. This method states that if the distribution function F is continuous and strictly increasing, and $v \sim \mathrm{unif}[0, 1]$, then the random variable $y = F^{-1}(v)$ has distribution function F.

When the mean direction is equal to the North Pole, θ_0 and ϕ_0 are independent. This is evident when evaluating (7.3) in the mean direction $(\alpha, \beta) = (0, \beta)$, resulting in the pdf

$$f\left((\theta_0, \phi_0) \mid (0, \beta), \kappa\right) = \frac{\kappa}{4\pi \sinh(\kappa)} e^{\kappa \cos(\theta_0)} \sin(\theta_0) \tag{7.4}$$

which does not depend on ϕ_0. Marginalizing over ϕ_0 in (7.4) yields the pdf

$$f\left(\theta_0 \mid \kappa\right) = \frac{\kappa}{2\sinh(\kappa)} e^{\kappa \cos(\theta_0)} \sin(\theta_0) \tag{7.5}$$

of θ_0. Moreover, marginalizing out θ_0 in (7.4) yields the pdf

$$f(\phi_0) = \frac{1}{2\pi}, \tag{7.6}$$

of ϕ_0, i.e. ϕ_0 has a uniform distribution on the unit circle. Using the above result, θ_0 and ϕ_0 can be drawn independently of each other, a fact which will be utilized in the algorithm for sampling the Fisher distribution. The density $f(\theta_0 \mid \kappa)$ can be seen for a selection of κ values in Figure 7.1. In this Figure, one of the curves represents the density for $\kappa \to 0$. Using L'Hospital's rule in (7.5) for $\kappa \to 0$, the density tends towards $\frac{1}{2}\sin(\theta)$. This corresponds to the uniform distribution on the sphere.

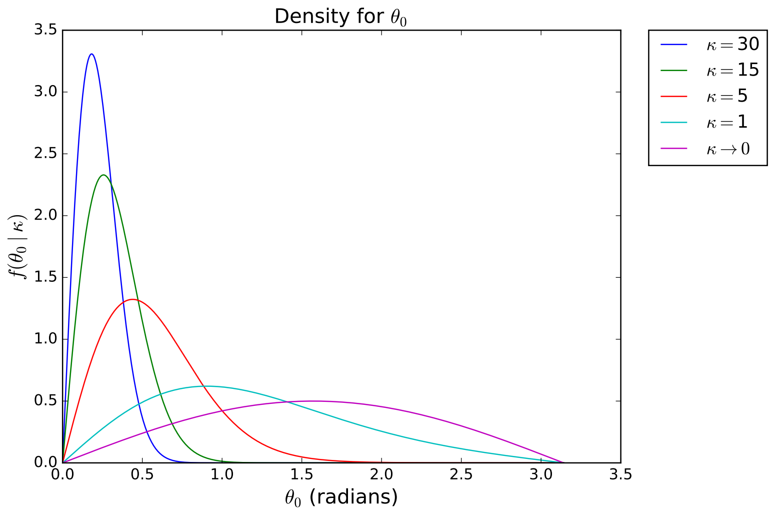

Figure 7.1: The Fisher density from (7.5) for different κ values

In order to use the inverse transformation method to sample both θ_0 and ϕ_0, the distribution functions $F(\theta_0)$ and $F(\phi_0)$ are required. For θ_0, $1 - F(\theta_0)$ is derived instead of $F(\theta_0)$. This is done in order to simplify the calculations and does not change the end result, since

$$\theta_0 \sim F \Rightarrow F(\theta_0) \sim \text{unif}[0,1] \Leftrightarrow (1 - F(\theta_0)) \sim \text{unif}[0,1].$$

Now, the expression becomes

$$1 - F(\theta_0) = \frac{\kappa}{2\sinh(\kappa)} \int_{\theta_0}^{\pi} e^{\kappa\cos(\theta)} \sin(\theta) d\theta.$$

Using integration by substitution, and setting $t = -\cos(\theta)$ and $dt = \sin(\theta)d\theta$,

$$\begin{aligned}1 - F(\theta_0) &= \frac{\kappa}{2\sinh(\kappa)} \int_{-\cos(\theta_0)}^{1} e^{-\kappa t} dt \\ &= -\frac{1}{2\sinh(\kappa)} \left(e^{-\kappa} - e^{\kappa\cos(\theta_0)}\right) \\ &= \frac{e^{\kappa\cos(\theta_0)} - e^{-\kappa}}{e^{\kappa} - e^{-\kappa}} \qquad (7.7) \\ &= \frac{e^{\kappa(\cos(\theta_0)-1)} - e^{-2\kappa}}{1 - e^{-2\kappa}}, \qquad (7.8)\end{aligned}$$

where the equality in (7.7) comes from a rewriting of the hyperbolic sine function, and the equality in (7.8) comes from multiplying (7.7) by $\frac{e^{-\kappa}}{e^{-\kappa}}$. Now, introducing $v = 1-F(\theta_0)$ and $\lambda = e^{-2\kappa}$, it evident from (7.8) that

$$\kappa(\cos(\theta_0) - 1) = \log(v(1 - \lambda) + \lambda), \qquad (7.9)$$

where $\log(\cdot)$ is the natural logarithm. For $\theta_0 \in [0, \pi]$ the trigonometric identity,

$$\sin\left(\frac{\theta_0}{2}\right) = \sqrt{\frac{1 - \cos(\theta_0)}{2}},$$

can be used to rewrite (7.9) as

$$-2\kappa \sin^2\left(\frac{\theta_0}{2}\right) = \log(v(1 - \lambda) + \lambda),$$

which further can be rewritten as

$$\theta_0 = 2\sin^{-1}\left(\sqrt{-\frac{\log\left(v(1 - \lambda) + \lambda\right)}{2\kappa}}\right). \qquad (7.10)$$

The expression in (7.10) is utilized in the algorithm for drawing samples from a Fisher distribution. Moreover, from (7.6) it is seen that

$$F(\phi_0) = \frac{\phi_0}{2\pi}.$$

With the above results, the only stochastic requirement in the algorithm for drawing a sample from the Fisher distribution is the ability to draw realizations v and w from the i.i.d. random variables $V, W \sim \text{unif}[0, 1]$.

Defining the Cartesian coordinate vector for the sample $(\theta_0, \phi_0) \sim F\left((0, 0), \kappa\right)$ as

$$\boldsymbol{f_0} = \begin{bmatrix}\sin(\theta_0)\cos(\phi_0) & \sin(\theta_0)\sin(\theta_0) & \cos(\theta_0)\end{bmatrix}^\top,$$

the mean direction vector for the sample $(\theta, \phi) \sim F\left((\alpha, \beta), \kappa\right)$ as

$$\boldsymbol{\mu}(\alpha, \beta) = \begin{bmatrix}\sin(\alpha)\cos(\beta) & \sin(\alpha)\sin(\beta) & \cos(\alpha)\end{bmatrix}^\top,$$

and the Cartesian vector for the sample $(\theta, \phi) \sim F\left((\alpha, \beta), \kappa\right)$ as

$$\boldsymbol{f} = \begin{bmatrix}\sin(\theta)\cos(\phi) & \sin(\theta)\sin(\theta) & \cos(\theta)\end{bmatrix}^\top,$$

the algorithm for drawing a sample from the $F\left((\alpha, \beta), \kappa\right)$ distribution is [11, p. 58-59]

Algorithm 1 Drawing a sample $(\theta, \phi) \sim F((\alpha, \beta), \kappa)$

Input parameters: (α, β), κ.
Output: $(\theta, \phi) \sim F((\alpha, \beta), \kappa)$.

1. Set $\lambda = \exp(-2\kappa)$.
2. Draw $v, w \overset{\text{i.i.d.}}{\sim} \text{unif}[0, 1]$.
3. Set colatitude $\theta_0 = 2\sin^{-1}\left(\sqrt{-\log(v\,(1-\lambda)+\lambda)\,\frac{1}{2\kappa}}\right)$.
4. Set longitude $\phi_0 = 2\pi w$.
5. Set $\boldsymbol{z} = [0\ 0\ 1]^\top$ and $\boldsymbol{k} = \frac{\boldsymbol{z}\times\boldsymbol{\mu}(\alpha,\beta)}{\|\boldsymbol{z}\times\boldsymbol{\mu}(\alpha,\beta)\|}$.
6. Set $\psi = \cos^{-1}\left(\boldsymbol{z}^\top\boldsymbol{\mu}(\alpha, \beta)\right)$.
7. Set $\boldsymbol{f} = \boldsymbol{R}(\boldsymbol{k}, \psi)\boldsymbol{f_0}$.
8. Calculate θ and ϕ from $\boldsymbol{f}$ according to (F.2).

In algorithm 1, $\boldsymbol{R}$ is Rodrigues' rotation matrix, which rotates a point in $\mathbb{R}^3$ around an arbitrary axis. This matrix is defined in Appendix F, Section F.2.

7.2 Selection of κ-values

In several of the Fisher distributions used in this thesis, κ-values are chosen such that 95% of the drawn values are expected to fall within a certain angle from the mean direction of the distribution. This angle is often chosen to correspond to a certain distance on Earth. Given a distance, d, on Earth, this corresponds to an angle

$$\theta_k(d) = \frac{d}{R_E},$$

in which the restriction that $d \leq \pi R_E$, i.e. the distance is less than or equal to half the circumference of Earth, is made. This restriction is made such that $\theta_k(d) \in [0, \pi]$. In order to find the κ-value that makes 95% of values drawn from the distribution in which it is used fall within an angle $\theta_k(d)$ from the mean direction of the distribution, the expression in (7.8) is used. This yields

$$0 = 1 - 0.95 - \frac{\exp(\kappa(\cos(\theta_k(d)) - 1) - \exp(-2\kappa)}{1 - \exp(-2\kappa)}, \tag{7.11}$$

Parameters for the secant method	
Parameter	Value
Max iterations	1000
Start guess	100
Allowable error	$1.48 \cdot 10^{-8}$

Figure 7.2: Table of parameters used in the secant method for estimating κ-values.

which is to be solved for κ. This is done using an optimization method. The secant method is used in this thesis, and in practice, the Python module from Scipy named "optimize.newton" is used to do this. When using this Python module, the parameters in table 7.2 are used.

The value of the start guess has been chosen such that the method converges both for small and large values of d. An example graph of κ-value vs. distance (d) can be seen in Figure 7.3.

When the techniques described in this section are used to choose κ-values in Fisher distributions, the terminology "*the κ-value is chosen such that* 95% *of the values from the Fisher distribution in which it is used fall within a distance d of the mean of the distribution*" is used.

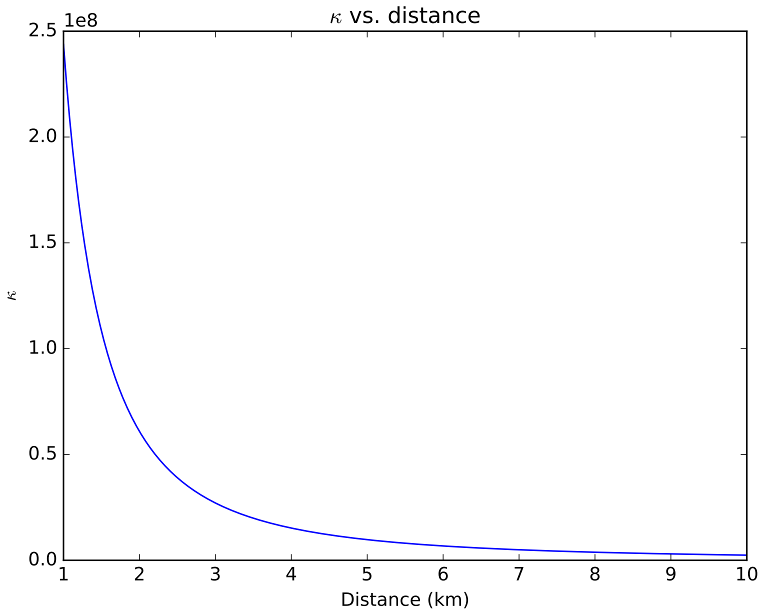

Figure 7.3: κ-values vs. distances.

7.3 Error modelling

If data was to be obtained in the real world, errors such as e.g. measurement errors will be present. These errors are modelled in this section.

When a single satellite is used, the Doppler shift data error is modelled as additive Gaussian noise, i.e. the Doppler shift with error is

$$\nu^{(n)} = \tilde{\nu}^{(n)} + \epsilon_\nu^{(n)}, \qquad n = 0, 1, \ldots, N-1,$$

where

$$\epsilon_\nu^{(n)} \overset{\text{i.i.d.}}{\sim} \mathcal{N}(0, \sigma_d^2),$$

in which $\sigma_d^2 = 7.32$ as found in Section 4.4 where GomSpace's Doppler shift estimator was simulated and its variance was found. Errors for the carrier frequency $f_c^{(n)}$ used for the n'th AIS message are not modelled, since it is assumed that due to the 50 kHz spacing between the AIS channels, GomSpace should be able to, without error, determine whether a given AIS message was sent out using the frequency f_1 or f_2.

The errors on the observed vessel positions are modelled according to an assumption on the accuracy of the AIS position accuracy. This assumption is that the position measured by the GPS embedded in a vessel falls within a 20 m radius of the vessel's true position. The errors are modelled using the Fisher distribution such that

$$\boldsymbol{a}^{(n)} \sim F(\tilde{\boldsymbol{a}}^{(n)}, \kappa_a), \qquad n = 0, 1, \ldots, N-1,$$

where $\kappa_a \approx 6.1 \cdot 10^{13}$, which is determined such that 95% of the values from the distribution fall within a distance of 20 m from the mean of the distribution. This is done according to the methods described in Section 7.2.

The errors on the satellite positions are modelled as a single sample of additive noise drawn from a three-dimensional normal distribution yielding

$$\boldsymbol{s}_\alpha^{(n)} = \tilde{\boldsymbol{s}}_\alpha^{(n)} + \boldsymbol{\epsilon}_s, \qquad n = 0, 1, \ldots, N-1 \tag{7.12}$$

and

$$\boldsymbol{s}_\beta^{(n)} = \tilde{\boldsymbol{s}}_\beta^{(n)} + \boldsymbol{\epsilon}_s, \qquad n = 0, 1, \ldots, N-1, \tag{7.13}$$

where

$$\boldsymbol{\epsilon}_s \sim \mathcal{N}_3(\boldsymbol{0}, \sigma_s^2 \boldsymbol{I}). \tag{7.14}$$

In the process of working on this thesis, access to information about how errors on the satellite positions, obtained from the GPS on-board GomSpace's Starling satellites, can be modelled have been sparse. The modelling in (7.12)-(7.14) are made under the assumption that since a satellite follows a given orbit which can be estimated based on GPS satellite position samples, the obtained satellite positions correspond to an offset of the estimated orbit from the true orbit. This estimation of the satellite orbit is not investigated in this thesis.

When utilizing M satellites, the error modelling for the satellite positions for $n = 0, 1, \ldots, N-1$ is, for the m'th satellite,

$$\boldsymbol{s}_{\alpha}^{(n,m)} = \tilde{\boldsymbol{s}}_{\alpha}^{(n,m)} + \boldsymbol{\epsilon}_{s}^{(m)},$$

and

$$\boldsymbol{s}_{\beta}^{(n,m)} = \tilde{\boldsymbol{s}}_{\beta}^{(n,m)} + \boldsymbol{\epsilon}_{s}^{(m)},$$

where

$$\boldsymbol{\epsilon}_{s}^{(m)} \overset{\text{i.i.d.}}{\sim} \mathcal{N}_3(\boldsymbol{0}, \sigma_s^2 \boldsymbol{I}),$$

in which σ_s^2 is set to 5 due to the lack of information about how to model satellite position error. Moreover, the Doppler shift data with error is modelled as

$$\nu^{(n,m)} = \tilde{\nu}^{(n,m)} + \epsilon_{\nu}^{(n,m)},$$

where

$$\epsilon_{\nu}^{(n,m)} \overset{\text{i.i.d.}}{\sim} \mathcal{N}(0, \sigma_d^2).$$

No error is modelled for the AIS transmission times $T_T^{(n)}$, $n = 0, 1, \ldots, N-1$.

Lastly, the packet error probability from (3.13) is modelled such that from the the N received AIS messages, a selection of these are randomly selected and the corresponding data removed. For the single satellite case, the data is collected in the set

$$\mathcal{E}_1 = \left\{ \left(\nu^{(n)}, \boldsymbol{a}^{(n)}, \boldsymbol{s}_{\alpha}^{(n)}, \boldsymbol{s}_{\beta}^{(n)}, T_T^{(n)}, f_c^{(n)} \right) \right\}_{n=0}^{N-1}.$$

The packet error probability is modelled by randomly discarding tuples from the set $\mathcal{E}_1$ according to the packet error probability. The selection of the N received AIS messages that are not removed are collected as the set

$$\mathcal{D}_1 = \left\{ \left(\nu^{(n)}, \boldsymbol{a}^{(n)}, \boldsymbol{s}_{\alpha}^{(n)}, \boldsymbol{s}_{\beta}^{(n)}, T_T^{(n)}, f_c^{(n)} \right) \mid p_{t1}^{(n)} = 1, n = 0, 1, \ldots, N-1 \right\},$$

where $p_{t1}^{(n)} \overset{\text{i.i.d.}}{\sim} \text{Bern}\left(1 - P_p(200)\right)$, $n = 0, 1, \ldots, N-1$, is a sequence of realizations of a Bernoulli random variable. In the single satellite case, N, which was the number of elements in the set $\mathcal{E}_1$ is redefined to be the number of elements in the set $\mathcal{D}_1$.

For the case of M satellites, the assumption is that if the package is lost, none of the satellites receive the package. The probability with which an AIS message is received in this case is $p_{t2}^{(n)} \overset{\text{i.i.d.}}{\sim} \text{Bern}\left(1 - M \cdot P_p(200)\right)$, and AIS messages are randomly discarded accordingly. Moreover, an assumption is that if a given AIS message is lost, the succeeding AIS message can not be lost. As was the case in the single satellite case, the number N is here redefined to be the number of AIS messages that were not discarded according to the packet error probability.

8 Probability model for space-based AIS system

This chapter introduces the probability models for the space-based AIS system and the inference problem in this thesis. The probability models are constructed with the aid of Bayesian networks. Four Bayesian networks are contructed. The first one is a general one, in the sense that the succeeding networks are special cases of the first one. The special cases are introduced since later in this thesis, these are the ones in which inference is performed.

8.1 Inference problem

The problem in this thesis is that of determining whether a vessel is spoofing its position. This is done based on the observable variables in the space-based AIS system. Stated in terms of an inference problem, the problem is that of determining $P(S \mid D)$, where S is an unobserved Bernoulli variable determining whether spoofing occurs of not, and D is the collection of observable variables from the system. To solve the problem, a probability model for the system is developed. The dependence relationships between the unobserved and observed variables in the system are illustrated with a Bayesian network. Bayesian networks are defined in Section A.1 in Appendix A.

8.2 Bayesian network

The Bayesian network modelling the dependencies between the variables in the space-based AIS system in which M satellites are used is seen in Figure 8.1. In this figure, squared boxes are observed variables and circles are unobserved variables. The arrows show dependence relations, e.g. the relation $\boldsymbol{p}^{(n)} \rightarrow \boldsymbol{a}^{(n)}$ means that $\boldsymbol{a}^{(n)}$ is dependent on $\boldsymbol{p}^{(n)}$. Notice that the observed variables in the set

$$\begin{aligned}\mathcal{V}gen = \Bigg\{ & t_r, \left(T_T^{(n)}\right)_{n=0}^{N-1}, \left(f_c^{(n)}\right)_{n=0}^{N-1}, \left(\boldsymbol{s}_\alpha^{(n,0)}\right)_{n=0}^{N-1}, \left(\boldsymbol{s}_\beta^{(n,0)}\right)_{n=0}^{N-1}, \left(\boldsymbol{s}_\alpha^{(n,1)}\right)_{n=0}^{N-1}, \left(\boldsymbol{s}_\beta^{(n,1)}\right)_{n=0}^{N-1}, \\ & \ldots, \left(\boldsymbol{s}_\alpha^{(n,M-1)}\right)_{n=0}^{N-1}, \left(\boldsymbol{s}_\beta^{(n,M-1)}\right)_{n=0}^{N-1} \Bigg\}\end{aligned}$$

are assumed known. The reason for modelling the dependence relations between the true vessel positions, $\boldsymbol{p}^{(n)}$, for $n = 0, 1, \ldots, N-1$, is that the position of a moving vessel is dependent of its previous position. The carrier frequency offsets, $\zeta^{(n,m)}$ are modelled as being dependent on where the vessel truly is, and what the AIS frequency offset f_{off} is. The observed positions, $\boldsymbol{a}^{(n)}$, are modelled as being dependent on where the vessel truly is and whether the vessel is spoofing its position.

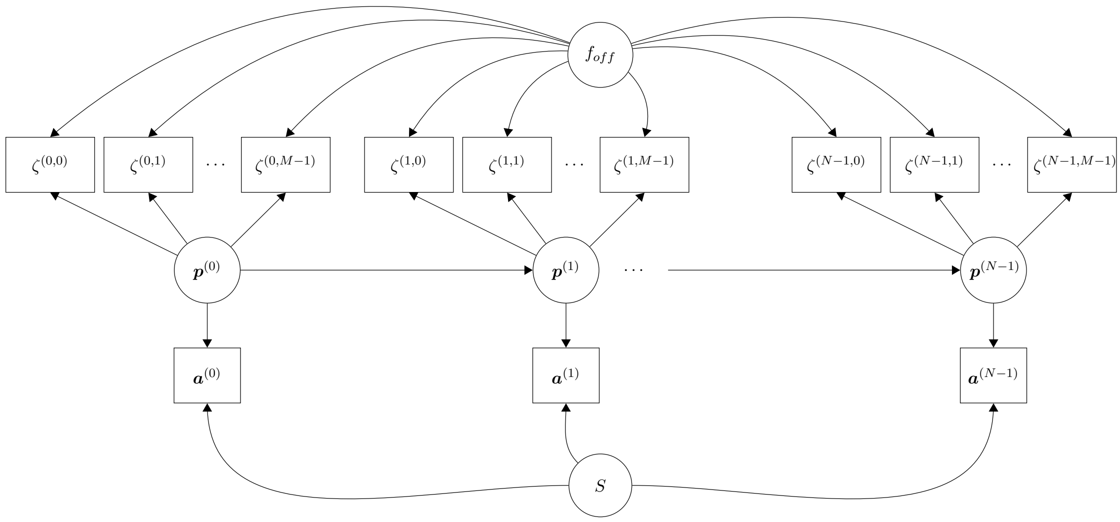

Figure 8.1: Bayesian network for the system consisting of a single vessel and M satellites.

Introducing the set

$$C_{gen} = \left\{S, f_{off}, \left(\boldsymbol{a}^{(n)}\right)_{n=0}^{N-1}, \left(\boldsymbol{p}^{(n)}\right)_{n=0}^{N-1}, \left(\zeta^{(n,0)}\right)_{n=0}^{N-1}, \left(\zeta^{(n,1)}\right)_{n=0}^{N-1}, \ldots, \left(\zeta^{(n,M-1)}\right)_{n=0}^{N-1}\right\}$$

as the collection of variables in the Bayesian network, the joint density, $f(C_{gen})$, represented by the network factorizes as

$$\begin{aligned} f(C_{gen}) =& f(S)f(f_{off})f(\boldsymbol{p}^{(0)})f(\boldsymbol{a}^{(0)} \mid \boldsymbol{p}^{(0)}, S)\left(\prod_{m=0}^{M-1} f(\zeta^{(0,m)} \mid \boldsymbol{p}^{(0)}, f_{off})\right) \\ & \prod_{n=1}^{N-1}\left(f(\boldsymbol{p}^{(n)} \mid \boldsymbol{p}^{(n-1)})f(\boldsymbol{a}^{(n)} \mid \boldsymbol{p}^{(n)}, S)\prod_{m=0}^{M-1} f(\zeta^{(n,m)} \mid \boldsymbol{p}^{(n)}, f_{off})\right). \end{aligned} \tag{8.1}$$

Assumptions about the terms in (8.1) are now made. The unobserved variable S is assumed to take on values of either 1 or 0, indicating whether the alleged position is spoofed or not, i.e. it is assumed to follow the Bernoulli probability mass function

$$f_B(S \mid q_S) = \begin{cases} 1 - q_S & \text{for } S = 0 \\ q_S & \text{for } S = 1 \end{cases} \tag{8.2}$$

where $q_S \in (0,1)$ is the probability that spoofing is occuring, which is assumed known. Notice that when a value for S is drawn from a Bernoulli distribution with probability parameter q_S, this is denoted as

$$S \sim \mathrm{Bern}(q_S). \tag{8.3}$$

The AIS frequency offset, f_{off}, is assumed to follow the normal density

$$f_N(f_{off} \mid 0, \sigma^2_{off}) = \frac{1}{\sqrt{2\pi\sigma^2_{off}}} \exp\left(-\frac{f^2_{off}}{2\sigma^2_d}\right),$$

where σ^2_{off} is assumed known.

The true vessel position $\boldsymbol{p}^{(0)}$ is assumed to follow the Fisher density $f_F\left(\boldsymbol{p}^{(0)} \mid \boldsymbol{s}_{avg}, \kappa_{sat}\right)$, where

$$\boldsymbol{s}_{avg} = \frac{\sum_{m=0}^{M-1} \boldsymbol{s}_\alpha^{(0,m)}}{\|\sum_{m=0}^{M-1} \boldsymbol{s}_\alpha^{(0,m)}\|}$$

is an average satellite position, based on the first satellite point for each of the M satellites. Moreover, $\kappa_{sat} > 0$ is assumed known. The remaining vessel positions, i.e. $\boldsymbol{p}^{(n)} \mid \boldsymbol{p}^{(n-1)}$ for $n = 1, 2, \ldots, N-1$, are assumed to follow Fisher densities $f_F\left(\boldsymbol{p}^{(n)} \mid \boldsymbol{p}^{(n-1)}, \kappa_v^{(n)}\right)$ where

$$\kappa_v^{(n)} = \begin{cases} \kappa_{v1} & \text{if } T_T^{(n)} - T_T^{(n-1)} < 1.5 \cdot t_r \\ \kappa_{v2} & \text{otherwise.} \end{cases}$$

is assumed known. From here, $\boldsymbol{p}^{(n)}$, for $n = 0, 1, \ldots, N-1$ may be referred to as either the true vessel position, or node n.

The alleged positions, $\boldsymbol{a}^{(n)} \mid \boldsymbol{p}^{(n)}, S$, for $n = 0, 1, \ldots, N-1$, are assumed to follow the Fisher densities $f_F\left(\boldsymbol{a}^{(n)} \mid \boldsymbol{p}^{(n)}, \kappa\right)$, where

$$\kappa = \begin{cases} \kappa_S & \text{if } S = 1 \\ \kappa_{NS} & \text{otherwise,} \end{cases}$$

in which $\kappa_S > 0$ and $\kappa_{NS} > 0$ are assumed known.

Finally, the carrier frequency offset $\zeta^{(n,m)} \mid \boldsymbol{p}^{(n)}, f_{off}$ for the n'th AIS message received by the m'th satellite is assumed to follow a normal density $f_N(\zeta^{(n,m)} \mid \nu_T^{(n,m)} + f_{off}, \sigma^2_d)$, where

$$\nu_T^{(n,m)} = \frac{v_r^{(n,m)}}{c} f_c^{(n)}, \tag{8.4}$$

where

$$v_r^{(n,m)} = \frac{\left\|(R_E + h) \cdot \boldsymbol{s}_\beta^{(n,m)} - R_E \cdot \boldsymbol{p}^{(n)}\right\| - \left\|(R_E + h) \cdot \boldsymbol{s}_\alpha^{(n,m)} - R_E \cdot \boldsymbol{p}^{(n)}\right\|}{f_p^{-1}},$$

and $f_p = 100$ Hz is the highest frequency with which the GPS embeded in the Starling satellites can sample satellite positions.

The posterior densities for the unobserved variables in the network are

$$f\left(S \mid C_{gen} \setminus \{S\}\right) \propto f_B\left(S \mid q_S\right) \prod_{n=0}^{N-1} f_F\left(\boldsymbol{a}^{(n)} \mid \boldsymbol{p}^{(n)}, \kappa\right) \tag{8.5}$$

for the variable S, in which $C_{gen} \setminus \{S\}$ denotes the set C_{gen} without S,

$$f\left(\boldsymbol{p}^{(0)} \mid C_{gen} \setminus \left\{\boldsymbol{p}^{(0)}\right\}\right) \propto$$

$$f_F\left(\boldsymbol{p}^{(0)} \mid \boldsymbol{s}_{avg}, \kappa_{sat}\right) f_F\left(\boldsymbol{a}^{(0)} \mid \boldsymbol{p}^{(0)}, \kappa\right) \prod_{m=0}^{M-1} f_N\left(\zeta^{(0,m)} \mid \nu_T^{(0,m)} + f_{off}, \sigma_d^2\right)$$

for the first true vessel position,

$$f\left(\boldsymbol{p}^{(n)} \mid C_{gen} \setminus \left\{\boldsymbol{p}^{(n)}\right\}\right) \propto \tag{8.6}$$

$$f_F\left(\boldsymbol{p}^{(n)} \mid \boldsymbol{p}^{(n-1)}, \kappa_v\right) f_F\left(\boldsymbol{a}^{(n)} \mid \boldsymbol{p}^{(n)}, \kappa\right) \prod_{m=0}^{M-1} f_N\left(\zeta^{(n,m)} \mid \nu_T^{(n,m)} + f_{off}, \sigma_d^2\right)$$

for the remaining true vessel positions for $n = 1, 2, \ldots, N-1$, and

$$f\left(f_{off} \mid C_{gen} \setminus \{f_{off}\}\right) \propto$$

$$f_N\left(f_{off} \mid 0, \sigma_{off}^2\right) \prod_{n=0}^{N-1} \left(\prod_{m=0}^{M-1} f_N\left(\zeta^{(n,m)} \mid \nu_T^{(n,m)} + f_{off}, \sigma_d^2\right)\right) \tag{8.7}$$

for the AIS frequency offset.

8.3 Bayesian network special case with one satellite and no AIS frequency offset

A special case of the network in Figure 8.1 can be seen in Figure 8.2 in which $M = 1$ satellite is used. In this special case, f_{off} is assumed known for simplicity, and hence the carrier frequency offsets only consist of the Doppler shifts. Moreover, since only a single satellite is used, the satellite indexing notation is suppressed in this section.

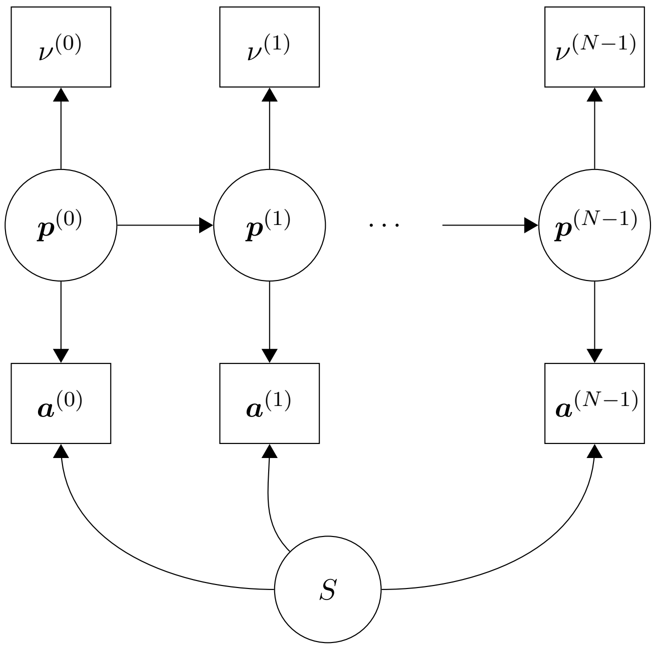

Figure 8.2: Bayesian network for the system consisting of a single vessel, a single satellite, and no AIS frequency offset.

Introducing the set

$$C_1 = \left\{ S, \boldsymbol{p}^{(0)}, \boldsymbol{a}^{(0)}, \nu^{(0)}, \boldsymbol{p}^{(1)}, \boldsymbol{a}^{(1)}, \nu^{(1)}, \dots, \boldsymbol{p}^{(N-1)}, \boldsymbol{a}^{(N-1)}, \nu^{(N-1)} \right\}$$

as the collection of elements in the Bayesian network, the joint density $f(C_1)$ represented by the network factorizes as

$$\begin{aligned} f\left(C_1\right) = & f\left(S\right) f\left(\boldsymbol{p}^{(0)}\right) f\left(\boldsymbol{a}^{(0)} \mid \boldsymbol{p}^{(0)}, S\right) f\left(\nu^{(0)} \mid \boldsymbol{p}^{(0)}\right) \\ & \prod_{n=1}^{N-1} f\left(\boldsymbol{p}^{(n)} \mid \boldsymbol{p}^{(n-1)}\right) f\left(\boldsymbol{a}^{(n)} \mid \boldsymbol{p}^{(n)}, S\right) f\left(\nu^{(n)} \mid \boldsymbol{p}^{(n)}\right). \end{aligned} \tag{8.8}$$

In (8.8), the assumptions made about the densities are the same as those made in Section 8.2, with the exception that the Doppler shifts $\nu^{(n)} \mid \boldsymbol{p}^{(n)}$, for $n = 0, 1, \dots, N-1$, are assumed to follow normal densities $f_N(\nu^{(n)} \mid \nu_T^{(n)}, \sigma_d^2)$, in which

$$\nu_T^{(n)} = \frac{v_r^{(n)}}{c} f_c^{(n)}, \tag{8.9}$$

where

$$v_r^{(n)} = \frac{\left\| (R_E + h) \cdot \boldsymbol{s}_\beta^{(n)} - R_E \cdot \boldsymbol{p}^{(n)} \right\| - \left\| (R_E + h) \cdot \boldsymbol{s}_\alpha^{(n)} - R_E \cdot \boldsymbol{p}^{(n)} \right\|}{f_p^{-1}}.$$

With the assumptions made on the densities in (8.8), the posterior densities for the unobserved variables in the network are

$$f\left(S \mid C_1 \setminus \{S\}\right) \propto f_B\left(S \mid q_S\right) \prod_{n=0}^{N-1} f_F\left(\boldsymbol{a}^{(n)} \mid \boldsymbol{p}^{(n)}, \kappa\right), \tag{8.10}$$

for the variable S,

$$f\left(\boldsymbol{p}^{(0)} \mid C_1 \setminus \left\{\boldsymbol{p}^{(0)}\right\}\right) \propto f_F\left(\boldsymbol{p}^{(0)} \mid \boldsymbol{s}_{\alpha}^{(0)}, \kappa_{sat}\right) f_F\left(\boldsymbol{a}^{(0)} \mid \boldsymbol{p}^{(0)}, \kappa\right) f_N\left(\nu^{(0)} \mid \nu_T^{(0)}, \sigma_d^2\right) \tag{8.11}$$

for the first true vessel position, and

$$f\left(\boldsymbol{p}^{(n)} \mid C_1 \setminus \left\{\boldsymbol{p}^{(n)}\right\}\right) \propto f_F\left(\boldsymbol{p}^{(n)} \mid \boldsymbol{p}^{(n-1)}, \kappa_v^{(n)}\right) f_F\left(\boldsymbol{a}^{(n)} \mid \boldsymbol{p}^{(n)}, \kappa\right) f_N\left(\nu^{(n)} \mid \nu_T^{(n)}, \sigma_d^2\right), \tag{8.12}$$

for the remaining true vessel positions, for $n = 1, 2, \ldots, N-1$.

8.4 Bayesian network special case with two satellites and no AIS frequency offset

A special case of the network in Figure 8.1 can be seen in Figure 8.3 in which $M = 2$ satellite are used. In this special case, f_{off} is assumed known for simplicity, and hence the carrier frequency offsets only consist of the Doppler shifts. Moreover, $M = 2$ satellites are used.

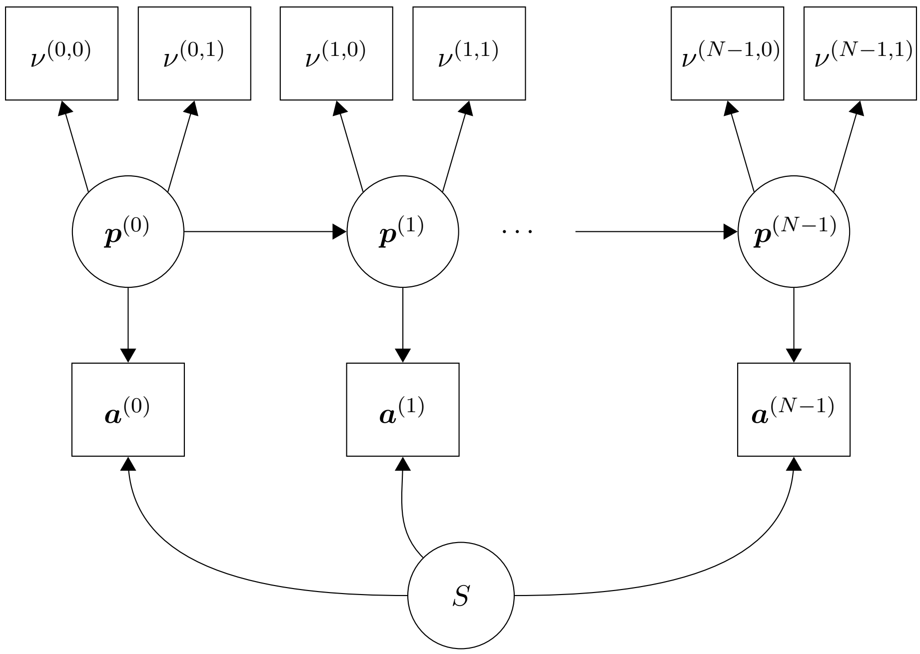

Figure 8.3: Bayesian network for the system consisting of a single vessel, $M = 2$ satellites, and no AIS frequency offset.

Introducing the set

$$C_2 = \left\{S, \boldsymbol{p}^{(0)}, \boldsymbol{a}^{(0)}, \nu^{(0,0)}, \nu^{(0,1)}, \ldots, \boldsymbol{p}^{(N-1)}, \boldsymbol{a}^{(N-1)}, \nu^{(N-1,0)}, \nu^{(N-1,1)}\right\}$$

as the collection of elements in the Bayesian network, the joint density $f(C_2)$ represented by the network factorizes as

$$\begin{aligned} f\left(C_2\right) =& f\left(S\right) f\left(\boldsymbol{p}^{(0)}\right) f\left(\boldsymbol{a}^{(0)} \mid \boldsymbol{p}^{(0)}, S\right) f\left(\nu^{(0,0)} \mid \boldsymbol{p}^{(0)}\right) f\left(\nu^{(0,1)} \mid \boldsymbol{p}^{(0)}\right) \\ & \prod_{n=1}^{N-1} f\left(\boldsymbol{p}^{(n)} \mid \boldsymbol{p}^{(n-1)}\right) f\left(\boldsymbol{a}^{(n)} \mid \boldsymbol{p}^{(n)}, S\right) f\left(\nu^{(n,0)} \mid \boldsymbol{p}^{(n)}\right) f\left(\nu^{(n,1)} \mid \boldsymbol{p}^{(n)}\right). \end{aligned} \tag{8.13}$$

In (8.13), the assumptions made about the densities are the same as those made in Section 8.2, except for the Doppler shifts $\nu^{(n,0)} \mid \boldsymbol{p}^{(n)}$, which, for $n = 0, 1, \ldots, N-1$, are assumed to follow normal densities $f_N(\nu^{(n,0)} \mid \nu_T^{(n,0)}, \sigma_d^2)$, where

$$\nu_T^{(n,0)} = \frac{v_r^{(n,0)}}{c} f_c^{(n)}, \tag{8.14}$$

where

$$v_r^{(n,0)} = \frac{\left\|(R_E + h) \cdot \boldsymbol{s}_\beta^{(n,0)} - R_E \cdot \boldsymbol{p}^{(n)}\right\| - \left\|(R_E + h) \cdot \boldsymbol{s}_\alpha^{(n,0)} - R_E \cdot \boldsymbol{p}^{(n)}\right\|}{f_p^{-1}}.$$

Similar arguments can be made for $\nu^{(n,1)} \mid \boldsymbol{p}^{(n)}$.

The posterior densities for the unobserved variables in the network are

$$f\left(S \mid C_2 \setminus \{S\}\right) \propto f_B\left(S \mid q_S\right) \prod_{n=0}^{N-1} f_F\left(\boldsymbol{a}^{(n)} \mid \boldsymbol{p}^{(n)}, \kappa\right) \tag{8.15}$$

for S,

$$\begin{aligned} & f\left(\boldsymbol{p}^{(n)} \mid C_2 \setminus \left\{\boldsymbol{p}^{(n)}\right\}\right) \propto \\ & f_F\left(\boldsymbol{p}^{(n)} \mid \boldsymbol{p}^{(n-1)}, \kappa_v\right) f_F\left(\boldsymbol{a}^{(n)} \mid \boldsymbol{p}^{(n)}, \kappa\right) f_N\left(\nu^{(n,0)} \mid \nu_T^{(n,0)}, \sigma_d^2\right) f_N\left(\nu^{(n,1)} \mid \nu_T^{(n,1)}, \sigma_d^2\right) \end{aligned} \tag{8.16}$$

for $\boldsymbol{p}^{(n)}$, $n = 1, 2, \ldots, N-1$, and

$$\begin{aligned} & f\left(\boldsymbol{p}^{(0)} \mid C_2 \setminus \left\{\boldsymbol{p}^{(0)}\right\}\right) \propto \\ & f_F\left(\boldsymbol{p}^{(0)} \mid \boldsymbol{s}_{avg}, \kappa_{sat}\right) f_F\left(\boldsymbol{a}^{(0)} \mid \boldsymbol{p}^{(0)}, \kappa\right) f_N\left(\nu^{(0,0)} \mid \nu_T^{(0,0)}, \sigma_d^2\right) f_N\left(\nu^{(0,1)} \mid \nu_T^{(0,1)}, \sigma_d^2\right) \end{aligned}$$

for $\boldsymbol{p}^{(0)}$.

8.5 Bayesian network special case with two satellites and AIS frequency offset

A special case of the network in Figure 8.1 can be seen in Figure 8.4. Here, $M = 2$ satellites are used. The joint density, the specification of the kind of densities in the joint density, and the posterior densities for the unobserved variables in the network follow the same lines as those in Section 8.2 for $M = 2$.

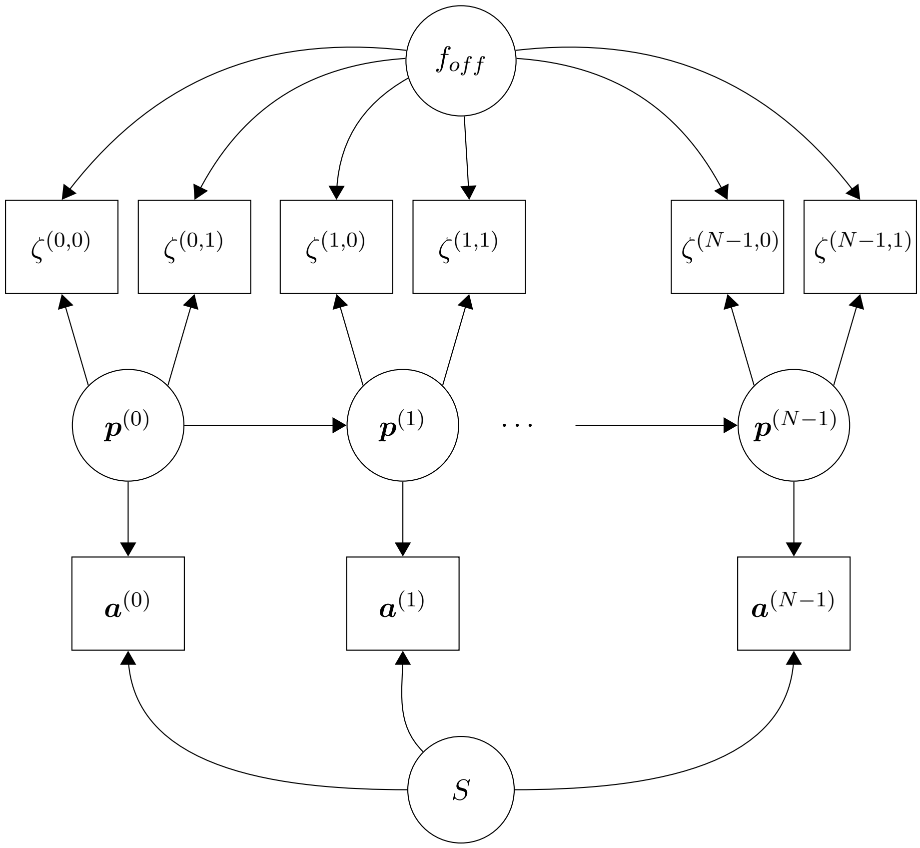

Figure 8.4: Bayesian network for the system consisting of a single vessel and $M = 2$ satellites. In this network, f_{off} is included as an unobserved variable.

8.6 Inference method choice: Metropolis within Gibbs sampling

The inference problem in this thesis is that of determining $P(S \mid D)$, which is hard to calculate directly. The posterior density for the spoofing variable, S, for the general case in which M satellites are utilized in the space-based AIS system is seen in (8.5).

One method to determine whether spoofing is occuring given the observable variables is maximum a posteriori (MAP). In making inference about the spoofing variable, S, this method requires the calculation of the posterior probabilities

$$P\left(S=1 \mid D\right) \tag{8.17}$$

and

$$P\left(S=0 \mid D\right). \tag{8.18}$$

The MAP decision rule would then be

$$\hat{S}_{MAP} = \begin{cases} 1 & \text{if } \frac{P(S=1|D)}{P(S=0|D)} > 1 \\ 0 & \text{otherwise.} \end{cases} \tag{8.19}$$

To calculate the quantities in (8.17) and (8.18), the posterior density in (8.5) should be considered. The problem is that this posterior density is the posterior density for S given both observed and unobserved variables. To calculate the posterior density for S given only the observed variables, the unobserved variables would have to be marginalized out of the expression. This would require integrating out $\boldsymbol{p}^{(n)}$, for $n = 0, 1, \ldots, N-1$, and f_{off}. This would result in having to solve several integrals, which are not easily solved.

An alternative approach to performing inference in the model is belief propagation, which is a message-passing algorithm [5]. Such approach often requires the conversion of the Bayesian network into a factor graph and the computation of the messages passed along the edges in the factor graph. The computation of these messages can sometimes be time consuming, and in some cases Monte Carlo methods are needed to compute the messages.

Another approach would be to sample directly from the posterior density of S. The posterior densities for S for the general case and the three special cases have the thing in common that they are hard to sample from. If samples from these densities are available, such samples can be used to estimate the probability of spoofing given the observable variables in the space-based AIS system, namely the probability $P(S \mid D)$. Drawing samples from the posterior densities can be done using a statistical sampling approach. This approach only requires choosing a suitable sampler once the model is specified. For this reason, statistical sampling is chosen to perform inference in the probability models. Markov chain Monte Carlo methods are used in this thesis, and the type of sampler chosen is the Metropolis within Gibbs (MWG) sampler. The MWG sampler and the theory behind it is described in Appendix A and B.

In short, the way the MWG sampler algorithms developed in the succeeding chapters help determining $P(S \mid D)$ is that they output samples $S^{(g)}$, for $g = 0, 1, \ldots, G-1$ of the posterior distributions for S, where G is the number of iterations carried out in the algorithm. These samples are used to estimate the probability that a vessel is spoofing its position, i.e. $P(S = 1 \mid D)$. This estimate is denoted $\hat{S}$, and is given as

$$\hat{S} = \frac{1}{G - N_{BI}} \sum_{k=N_{BI}}^{G-1} S^{(k)}, \tag{8.20}$$

in which N_{BI} is a number of samples that are discarded, referred to as the burn-in of the sampler. Notice that N_{BI} refers to the discarding of the first N_{BI} samples of S

from the sampler algorithms. This number is chosen such that after this number of iterations in the sampler algorithms, the sampler is believed to have converged to the invariant distribution of the Markov chain that it creates. The MWG sampler algorithms developed in this thesis all have properties that ensure that the estimator in (8.20) is consistent. These properties are introduced in Section 9.2, in which a proof that the samplers have these properties is also given.

In the simulations and tests carried out in the succeeding chapters in this thesis, the decision of whether spoofing occurs is such that if $\hat{S} \leq 0.1$ in a given test, it is determined that no spoofing is happening. If $\hat{S} \geq 0.95$, it is determined that spoofing is happening. If $0.95 > \hat{S} > 0.1$, it is not certain whether spoofing is occuring and in a real-world application, caution should be raised in this case. The choice of the decision is such that a relatively high value of $\hat{S}$ is needed in order to determine that spoofing is occuring in a given case. This is done to prevent creating a false alarm, i.e. to prevent detection of spoofing when no spoofing is occuring.

9 Sampler algorithm: One satellite and no AIS frequency offset

In this chapter, the MWG sampler algorithm for the special case in which a single satellite is used is introduced. The probability model for this case is described in Section 8.3, in which the posterior densities for the unobserved variables in the Bayesian network are also described. These posterior densities are used in the MWG sampler in this chapter.

How the sampler is initialized, and how the variable updating steps in the algorithm are carried out are described along with the sampler algorithm. After this is a proof that the sampler is aperiodic and irreducible. This proof is based on the theory and results concerning Markov chains on continuous state spaces, which are found in Appendix A and B.

Finally, a description of the choice of input parameter values for the algorithm is given. These input parameter values are to be used in the simulations and tests of the algorithm carried out in the succeeding chapter.

9.1 Metropolis within Gibbs sampler

The MWG sampler algorithm used in this chapter is seen in Algorithm 2. This MWG sampler utilizes a cyclic updating scheme of the variables. Cyclic updating schemes are described in Section B.2 in Appendix B. The unobserved variables in the network in Figure 8.2 needs to be initialized in the first iteration of the algorithm. The algorithm is run for G iterations. These iterations are referred to as Gibbs iterations. The algorithm outputs G samples $\left(S^{(g)}\right)_{g=0}^{G-1}$ of the variable S. The initialization of the variables in the 0'th (first, i.e. $g = 0$) Gibbs iteration is done by drawing

$$S^{(0)} \sim \mathrm{Bern}(q_S),$$

$$\boldsymbol{p}^{(0,0)} \sim F\left(\boldsymbol{a}^{(0)}, \kappa_{init}\right),$$

where the first superscript corresponds to $n = 0$ and the second superscript refers to the 0'th Gibbs iteration, and

$$\boldsymbol{p}^{(n,0)} \sim F\left(\boldsymbol{p}^{(n-1,0)}, \kappa_v^{(n)}\right), \qquad n = 1, 2, \dots, N-1.$$

where the second superscript refers to the 0'th Gibbs iteration.

Now, the updating steps of the unobserved variables in the network are described. Only two instances need to be considered when updating S in the sampler. Based on the posterior density for S in (8.10), these instances are

$$f\left(S = 1 \mid C_1 \setminus \{S\}\right) \propto c_1$$

and

$$f\left(S = 0 \mid C_1 \setminus \{S\}\right) \propto c_0,$$

where c_0 and c_1 are constants. Choosing the value of S is then done by drawing $u \sim$ unif$[0, 1]$ and

$$S = \begin{cases} 1 & \text{if } u \leq \frac{c_1}{c_1 + c_0} \\ 0 & \text{otherwise.} \end{cases}$$

When updating $\boldsymbol{p}^{(n)}$ for $n = 0, 1, \dots, N-1$, the posterior densities in (8.11) and (8.12) are considered. Here, it is seen that they are products of Fisher distributions and a normal distribution, resulting in a distribution that is not easy to obtain samples from. Therefore, Metropolis-Hastings steps are employed in these cases, with Fisher distributions as proposal distributions. Notice that the Fisher distribution is symmetric, which is why the proposal distribution does not appear in the Hastings ratio in the updating steps for $\boldsymbol{p}^{(n)}$ for $n = 0, 1, \dots, N-1$.

Algorithm 2 MWG sampler for one satellite model

Input data: $\boldsymbol{a}^{(n)}$, $\nu^{(n)}$, $\boldsymbol{s}_\alpha^{(n)}, \boldsymbol{s}_\beta^{(n)}, f_c^{(n)}, T_T^{(n)}, t_r$ for $n = 0, 1, \ldots, N-1$.
Input parameters: G, q_S, κ_{init}, κ_{v1}, κ_{v2}, κ_S, κ_{NS}, κ_{MH}, κ_{sat}, σ_d^2.
Output data: $S^{(g)}$ for $g = 0, 1, \ldots, G-1$.

1. Initialize unobservables:
   (a) Draw $S^{(0)} \sim \text{Bern}(q_S)$.
   (b) Draw $\boldsymbol{p}^{(0,0)} \sim F\left(\boldsymbol{a}^{(0)}, \kappa_{init}\right)$.
   (c) Calculate $\nu_T^{(0,0)}$ according to (8.9), using $\boldsymbol{p}^{(0,0)}, \boldsymbol{s}_\alpha^{(0)}$, $\boldsymbol{s}_\beta^{(0)}$, and $f_c^{(0)}$.
   (d) For $n = 1, 2, \ldots, N-1$.
      i) Set $\kappa_v^{(n)} = \begin{cases} \kappa_{v1} & \text{if } T_T^{(n)} - T_T^{(n-1)} < 1.5 \cdot t_r \\ \kappa_{v2} & \text{otherwise.} \end{cases}$
      ii) Draw $\boldsymbol{p}^{(n,0)} \sim F\left(\boldsymbol{p}^{(n-1,0)}, \kappa_v^{(n)}\right)$.
      iii) Calculate $\nu_T^{(n,0)}$ according to (8.9), using $\boldsymbol{p}^{(n,0)}, \boldsymbol{s}_\alpha^{(n)}$, $\boldsymbol{s}_\beta^{(n)}$, and $f_c^{(n)}$.
2. For $g = 1, 2, \ldots, G-1$.
   (a) Update $S^{(g)}$.
      i) Set $c_1 = q_S \prod_{n=0}^{N-1} f_F\left(\boldsymbol{a}^{(n)} \mid \boldsymbol{p}^{(n,g-1)}, \kappa_S\right)$.
      ii) Set $c_0 = (1-q_S) \prod_{n=0}^{N-1} f_F\left(\boldsymbol{a}^{(n)} \mid \boldsymbol{p}^{(n,g-1)}, \kappa_{NS}\right)$.
      iii) Draw $u \sim \text{unif}[0,1]$.
      iv) Set $S^{(g)} = \begin{cases} 1 & \text{if } u \leq \frac{c_1}{c_1+c_0} \\ 0 & \text{otherwise.} \end{cases}$
   (b) Update $\boldsymbol{p}^{(n,g)}$ by applying a Metropolis-Hastings step for $n = 0, 1, \ldots, N-1$.
      i) Draw $\boldsymbol{p}_{pro}^{(n,g)} \sim F\left(\boldsymbol{p}^{(n,g-1)}, \kappa_{MH}\right)$ as proposal for true vessel position.
      ii) Calculate Doppler shift proposal $\nu_{pro}^{(n,g)}$ according to (8.9), using $\boldsymbol{p}_{pro}^{(n,g)}, \boldsymbol{s}_\alpha^{(n)}$, $\boldsymbol{s}_\beta^{(n)}$, and $f_c^{(n)}$.
      iii) Set $\kappa = \begin{cases} \kappa_S, & \text{if } S^{(g)} = 1 \\ \kappa_{NS}, & \text{otherwise.} \end{cases}$
      iv) If $n = 0$:
      $$\text{Set } H = \frac{f_F\left(\boldsymbol{p}_{pro}^{(0,g)} \mid \boldsymbol{s}_\alpha^{(0)}, \kappa_{sat}\right) \cdot f_F\left(\boldsymbol{p}_{pro}^{(0,g)} \mid \boldsymbol{a}^{(0)}, \kappa\right) \cdot f_N\left(\nu^{(0)} \mid \nu_{pro}^{(0,g)}, \sigma_d^2\right)}{f_F\left(\boldsymbol{p}^{(0,g-1)} \mid \boldsymbol{s}_\alpha^{(0)}, \kappa_{sat}\right) \cdot f_F\left(\boldsymbol{p}^{(0,g-1)} \mid \boldsymbol{a}^{(0)}, \kappa\right) \cdot f_N\left(\nu^{(0)} \mid \nu_T^{(0,g-1)}, \sigma_d^2\right)}$$
      v) Else:
      $$\text{Set } \kappa_v^{(n)} = \begin{cases} \kappa_{v1} & \text{if } T_T^{(n)} - T_T^{(n-1)} < 1.5 \cdot t_r \\ \kappa_{v2} & \text{otherwise.} \end{cases}$$
      $$\text{Set } H = \frac{f_F\left(\boldsymbol{p}_{pro}^{(n,g)} \mid \boldsymbol{p}^{(n-1,g)}, \kappa_v^{(n)}\right) \cdot f_F\left(\boldsymbol{p}_{pro}^{(n,g)} \mid \boldsymbol{a}^{(n)}, \kappa\right) \cdot f_N\left(\nu^{(n)} \mid \nu_{pro}^{(n,g)}, \sigma_d^2\right)}{f_F\left(\boldsymbol{p}^{(n,g-1)} \mid \boldsymbol{p}^{(n-1,g)}, \kappa_v^{(n)}\right) \cdot f_F\left(\boldsymbol{p}^{(n,g-1)} \mid \boldsymbol{a}^{(n)}, \kappa\right) \cdot f_N\left(\nu^{(n)} \mid \nu_T^{(n,g-1)}, \sigma_d^2\right)}$$

MWG sampler for one satellite model continued

vi) Draw $v \sim \text{unif}[0,1]$.

vii) Set $a_{accept}^{(n,g)} = \min[1, H]$

viii) Set $\boldsymbol{p}^{(n,g)} = \begin{cases} \boldsymbol{p}_{pro}^{(n,g)} & \text{if } v \leq a_{accept}^{(n,g)} \\ \boldsymbol{p}^{(n,g-1)} & \text{otherwise.} \end{cases}$

ix) Set $\nu_T^{(n,g)} = \begin{cases} \nu_{pro}^{(n,g)} & \text{if } v \leq a_{accept}^{(n,g)} \\ \nu_T^{(n,g-1)} & \text{otherwise.} \end{cases}$

9.2 Metropolis within Gibbs sampler properties

In this section, it is shown that the Metropolis within Gibbs sampler in Algorithm 2 has the properties that it is both irreducible and aperiodic. These properties are described Section A.3 of Appendix A. The way these properties are shown is based on the theory concerning Markov chains on continuous state spaces.

Let

$$\boldsymbol{g}^{(g)} = \left[S^{(g)} \quad \left(\boldsymbol{p}^{(0,g)}\right)^{\top} \quad \left(\boldsymbol{p}^{(1,g)}\right)^{\top} \quad \dots \quad \left(\boldsymbol{p}^{(N-1,g)}\right)^{\top}\right]^{\top}, \qquad g = 1, 2, \dots, G-1$$

be the vector consisting of the updated values of the unobserved values in the network in Figure 8.2 after the g'th cycle in Algorithm 2.

Initially, irreducibility of the sampler is established. This is done by showing that in a single Gibbs iteration, the vector $\boldsymbol{g}^{(g)}$ can be drawn from anywhere in the sample space. The updating of the variable S is constructed such that there is always a positive probability for S being 1 and a positive probability for S being 0. Moreover, since Fisher distributions are used to draw proposals for the updates of the true vessel positions, $\boldsymbol{p}^{(n)}$, proposals can be drawn from all areas of the unit sphere with positive probability. The Hastings ratios in Algorithm 2 can not be zero, due to the nature of the products in both numerator and denominator. Hence, there is always a non-zero probability of accepting a given proposal, which means that in one Gibbs iteration, a vessel position can be updated to a position anywhere on the unit sphere. This fact, along with the fact that S has positive probability for both of its values, establishes irreducibility of a Markov chain resulting from running the sampler in Algorithm 2.

Next, aperioidicity of the Markov chain resulting from the sampler is established. To show aperiodicity, it suffices to show that the possibility that

$$\boldsymbol{g}^{(g-1)} = \boldsymbol{g}^{(g)}, \qquad g = 0, 1, \dots G-1$$

exists. That the value of g form one Gibbs iteration to the next has the possibility of remaining unchanged shows that the sampler is aperiodic. To show this, the updating

Parameter	**Value**
q_S	0.01
κ_{init}	2437366
κ_{v1}	Case specific
κ_{v2}	Case specific
κ_S	975
κ_{NS}	Case specific
κ_{MH}	2437366
κ_{sat}	164
σ_d^2	7.32

Table 9.1: Input parameters for the MWG sampler in Algorithm 2.

steps of the unobserved variable S and the unobserved true vessel positions $\boldsymbol{p}^{(n)}$ are considered. Evident from the way that S is updated in the algorithm is the fact that there is a positive probability that $S^{(g-1)} = S^{(g)}$. The values of the true vessel positions are updated using Metropolis-Hastings steps. From this, it is evident that there is a positive probability that $\boldsymbol{p}^{(n,g-1)} = \boldsymbol{p}^{(n,g)}$ for $n = 0, 1, \dots, N-1$. With these results, it is evident that the possibility that

$$\boldsymbol{g}^{(g-1)} = \boldsymbol{g}^{(g)}, \qquad g = 0, 1, \dots G-1$$

exists.

The fact that the MWG sampler is irreducible ensures that the estimator in (8.20) is consistent by the strong law of large numbers for Markov chains, which is presented in Theorem A.2.

9.3 Metropolis within Gibbs sampler input parameters

The chosen input paramter values are seen in Table 9.1. For each parameter, an argument for choosing a particular value is given in this section.

9.3.1 Probability parameter q_S

The value of q_S symbolizes the prior belief that a given vessel is spoofing its position. This value is chosen to reflect the belief that only a small number of vessels are trying to spoof their position.

9.3.2 Concentration parameter κ_{init}

In the MWG sampler, the parameter κ_{init} is used in the initialization of the first true vessel position, $\boldsymbol{p}^{(0,0)}$. It is used as the concentration parameter in a Fisher distribution with mean direction equal to the first observed vessel position, $\boldsymbol{a}^{(0)}$, from which $\boldsymbol{p}^{(0,0)}$ is drawn. The value of the parameter is chosen such that 95% of the values from the Fisher distribution fall within 10 km of its mean direction, as described in Section 7.2.

9.3.3 Concentration parameters κ_{v1} and κ_{v2}

These values are used in the Fisher distributions that describe how the true vessel positions are subsequently drawn after each other. The value of κ_{v1} is chosen such that 95% of the values from the Fisher distribution fall within a certain distance of its mean direction. This distance is chosen as the maximum distance a vessel can travel between successive AIS message transmissions. When a vessel uses a report interval t_r to transmit its AIS messages, the vessel is travelling at a speed determined by the report interval as per Table 2.1. For a given report interval in Table 2.1 the maximum speed is used, and it is denoted $v_{max}(t_r)$. For the last two entries in the table, corresponding to report intervals of 2 s, it is assumed that the vessels under consideration in this thesis do not move at speeds exceeding 80 km/h. This corresponds to approximately 43.2 knots. Hence, $v_{max}(2) = 80$ km/h.

Thus, the maximum distance travelled by a vessel between successive AIS message transmissions is

$$d_{max}(t_r) = t_r \cdot \frac{v_{max}(t_r)}{3600.} \qquad \text{(km/s)} \tag{9.1}$$

Moreover, κ_{v2} is used when an AIS message is lost. When this is the case, the vessel has moved approximately twice the distance between successive AIS messages compared to if the given AIS message had not been lost. Thus κ_{v2} is chosen such that the 95% of the values from the Fisher distribution fall within a distance $2 \cdot d_{max}(t_r)$ from the mean direction.

Evident from the above description, these values are dependent on the report interval, and they are given on a case-by-case basis. The possible parameter values are seen in Table 9.2. Whenever an MWG sampler algorithm is run, κ_{v1} and κ_{v2} are chosen according to the report interval being tested.

t_r	κ_{v1}	κ_{v2}
10 s (14 knots)	47017094414	11754268483
6 s (23 knots)	48361766596	12090430814
2 s (80 km/h)	123393883625	30848541441

Table 9.2: Possible values of κ_{v1} and κ_{v2}.

9.3.4 Concentration parameters κ_S and κ_{NS}

These two concentration parameters are used to express the size of the area around the true vessel positions in which the alleged vessel positions are believed to lie.

The parameter κ_S expresses this area when spoofing is occuring, and is chosen such that 95% of the values from the Fisher distribution in which it is used fall within 500 km of its mean direction.

On the other hand, κ_{NS} expresses the size of the area around the true vessel positions in which the observed vessel positions are believed to lie if spoofing is not occuring. This value is case specific, and it will often be chosen such that for a given scenario, no false alarm is reported when no spoofing is occuring.

9.3.5 Concentration parameter κ_{MH}

This parameter is used in the proposal distribution, which is a Fisher distribution, for the true vessel positions. This parameter is chosen based on simulations such that all of the average acceptance probabilities

$$\bar{a}^{(n)}_{accept} = \frac{1}{G}\sum_{g=0}^{G-1} a^{(n,g)}_{accept}, \qquad n = 0, 1, \ldots, N-1 \tag{9.2}$$

are approximately between 0.2 and 0.4. This interval is chosen based on a rule of thumb found in [27].

9.3.6 Concentration parameter κ_{sat}

This parameter is used in the distribution of the first vessel position. Its value is chosen such that 95% of the values of the Fisher distribution in which it is used fall within a distance corresponding to the FoV radius of the satellite of its mean direction. This is done since, in practice, it is known that when receiving the first AIS message, the first true vessel position must be within the FoV of the satellite. The FoV size is calculated based on the Equations (6.21) and (6.22). For an orbit height $h = 500$ km as is the case for the Starling satellites, and an elevation angle $e = 16$ degrees, as shown in the link budget in Chapter 3, the FoV radius is approximately 1219 km, corresponding to the length of the red circle segment in Figure 6.8a.

9.3.7 Variance parameter σ_d^2

As mentioned earlier, this parameter describes the variance on the carrier frequency offset estimates as described in Section 4.4.

10 | Sampler algorithm test: One satellite and no AIS frequency offset

This chapter describes the tests of the sampler in Algorithm 2, which is a sampling algorithm designed and developed to help perform inference in the model described in Section 8.3. This model was the one created for the variables in the space-based AIS system in which a single satellite is used and no AIS frequency offset is included.

Initially, it is tested whether the algorithm is able to detect cases in which no spoofing is occuring, such that no false alarms are given. A false alarm is defined as the case in which an estimate $\hat{S}$ is greater than 0.1 in a scenario in which a vessel is not spoofing its position. This false alarm test consists of choosing a value of κ_{NS} that ensures that no false alarm is reported when no spoofing is occuring in a given scenario. Having found a κ_{NS}-value and verified that using it in the sampler does not result in a false alarm for a given data set, it is tested how far away from its true position a vessel has to spoof its position in order for the algorithm to detect it. This last test is based on the same scenario as that used in the false alarm test. All of the data that is used to test the sampler algorithm in this chapter is generated according to the descriptions in Chapter 6. Simulated data is used, since no data collected by actual LEO satellites has been available.

In order to understand the figures shown in this chapter and some of the succeeding chapters in this thesis, the concepts of a node trace plot and an AEP plot are introduced. Azimuthal equidistant projection is described in Appendix M. Figure 10.1a shows a scenario in which a non-moving vessel, using a report interval of 10 s, has spoofed its position 400 km away form its true position. The large spoofing distance is chosen for illustrative purposes. The data from this scenario is used in the sampler in Algorithm 2, with the input parameters from Table 9.1 and a κ_{NS} value arbitrarily chosen such that 95% of the values from the Fisher distribution in which it is used fall within a distance of 13 km from its mean direction. A trace plot of the samples $\boldsymbol{p}^{(n,g)}$ from the sampler are seen in Figure 10.1b for node 0, i.e. the samples of $\boldsymbol{p}^{(0)}$. The sampler was run with $G = 25000$ iterations. It is seen that the trace starts around the alleged vessel position and converges to an area around the true vessel position. Figure 10.1c shows an AEP plot of the scenario from Figure 10.1b. In this figure, the true vessel position is the center point, and circles of different radii are drawn for illustrative purposes. Moreover, an indication of which direction is north is given in the figure.

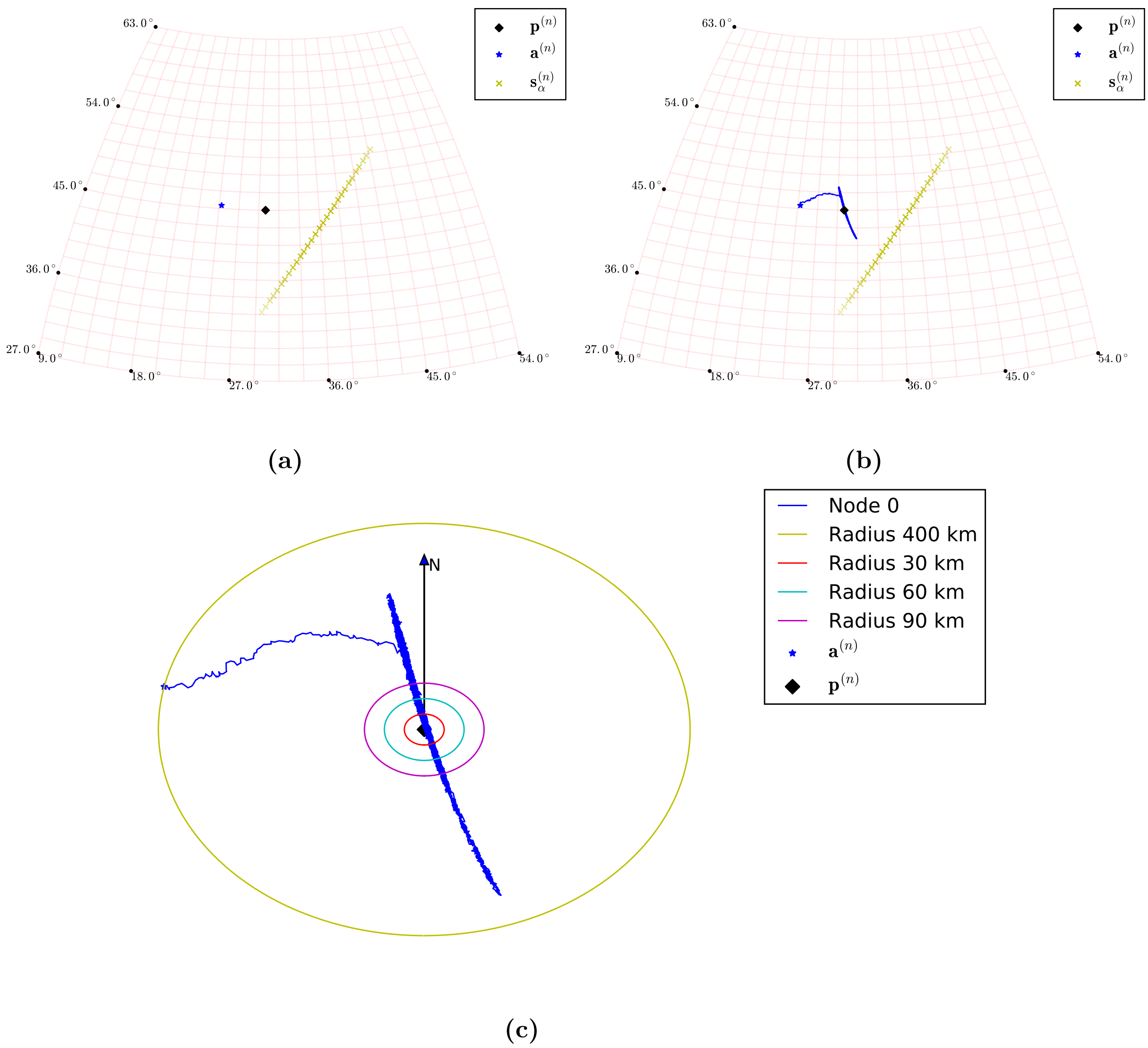

Figure 10.1: **(a)**: Scenario example. **(b)**: Scenario with trace plot. **(c)**: AEP plot of the scenario from **(b)**.

10.1 False alarm test

It is crucial that if a vessel is not spoofing its position, no false alarm is created. To test whether the spoofing detection works as intended in the case of no position spoofing, data is generated where no position spoofing is occuring. The inputs for the data generation of this data is seen in Table 10.1. The scenario of the generated data can be seen in

t_r	10 s
θ_p	$\frac{\pi}{4}$
ϕ_p	$\frac{\pi}{6}$
v_v	0 km/s
S	0
d_s	0
ϕ_{dir}	0
μ_{dir}	0
i	70°
Ω_{off}	$\frac{\pi}{24}$

Table 10.1: Input data generation parameters for the false alarm test. Notice that the data generation input parameter $\boldsymbol{p}_v^{(0)}$ is given as a colatitude θ_p and longitude ϕ_p.

Figure 10.2. In the simulations carried out with this scenario, $N = 31$ AIS messages were received.

In order to find the κ_{NS}-value such that no false alarm is created, an initial κ_{NS}-value is chosen such that 95% of the values fall within a distance of 0.5 km of the mean direction of the Fisher distribution. With this initial κ_{NS}-value, the sampler algorithm is run for 10 times, each time with a new data set generated with the input parameters in Table 10.1. Each run of the algorithm was carried out for $G = 100000$ iterations and it is checked whether the resulting value of $\hat{S}$, with a burn-in of $N_{BI} = 1000$ samples, is below the spoofing limit of 0.1 as mentioned in Section 8.6. The value of κ_{NS} was incremented by 0.5 km until all 10 estimates of $\hat{S}$ fell below 0.1. The resulting κ_{NS}-value was found at 13 km, corresponding to a κ_{NS}-value of 1442228.

In conclusion, using this κ_{NS}-value in in the sampler ensures that no false alarm is reported in the scenario shown in Figure 10.2. This κ_{NS}-value is used in the succeeding tests in this chapter.

10.2 Spoofing distance test

With the κ_{NS}-value found in the previous section, it is now tested how far away a vessel can spoof its position without being detected, or, in other words, how far away it has to spoof its position in order for it to be detected.

The same scenario as in Figure 10.2 is used in this test, and 10 different spoofing distances d_s, starting at 10 km and then incrementing by 10 km, are tested. Each of these spoofing distances is tested $N_{SA} = 10$ times with 10 equally spaced spoofing angles

$$\phi_{dir}^{(k)} = \frac{2\pi}{N_{SA}} \cdot k, \qquad k = 0, 1, \ldots, N_{SA}. \tag{10.1}$$

The reason for choosing several different spoofing angles for each spoofing distance is done in order to test whether the direction in which a vessel is spoofing its position has an influence on the results.

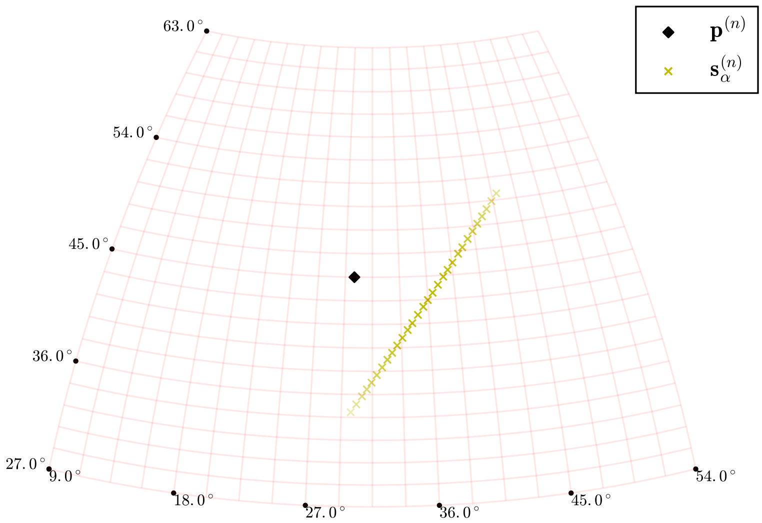

Figure 10.2: Scenario for both the false alarm test and the spoofing distance test. Geographical coordinates are plotted in degrees for illustrative purposes. Geographical coordinates are described in Appendix F.

To illustrate the principle of this test, Figure 10.3 shows an AEP plot of the spoofed positions with the vessel as center point for the spoofing distances 30, 60, and 90 km, which are shown as circles of corresponding radii. The labels on the spoofed positions in the figure are such that a 0 corresponds to $\phi_{dir}^{(0)}$, a 1 corresponds to $\phi_{dir}^{(1)}$ and so on.

Running the sampler for $G = 25000$ iterations for each of the spoofed positions yields the estimates $\hat{S}$ as seen in Table 10.4. Notice that all of these estimates were calculated with a burn-in of $N_{BI} = 1000$ samples. In the table, the spoofing distances d_s are given in kilometers, and the estimates $\hat{S}$ are given in percent. In the table, it is seen that the columns corresponding to the spoofing angles $\phi_{dir}^{(1)}$ and $\phi_{dir}^{(6)}$ show odd behaviour, while the remaining columns show 100% spoofing at a spoofing distance of 60 km and above.

The reason for this behaviour is now investigated. Consider the series of Figures 10.5a-10.6b. In Figure 10.5a, an AEP plot of the true vessel position and the spoofed position corresponding to $d_s = 50$ km and $\phi_{dir}^{(4)}$ is shown. From table 10.4 it is evident that this is a scenario where $\hat{S}$ is 1.0. Figure 10.5b, shows a trace plot of node 0 for the simulation in which the spoofed position in question has been used in the simulation. The trace of node 0 converges from its initialization around the spoofed position, marked with a 4 in the figure, towards an area around the true vessel position. The shape of this area is what is causing the behaviour for some of the spoofed positions. In the next figure, namely Figure 10.6a, the remaining spoofed positions for $d_s = 50$ km are plotted for illustrative purposes. In this figure, it is evident that the spoofed positions labelled with a 6 and a 1 fall approximately within the area that the trace plot is moving in. The shapes and orientations of these areas are similar for all $N - 1$ nodes. To further

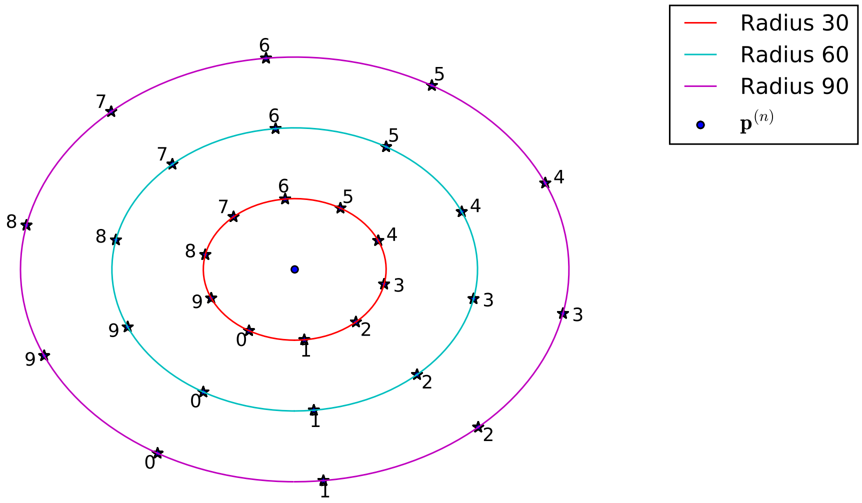

Figure 10.3: AEP plot of the spoofed positions with $\boldsymbol{p}^{(n)}$ as center point. A selection of the spoofing distances d_s are plotted.

$t_r = 10$ s										
d_s	Spoofing angles									
	0	1	2	3	4	5	6	7	8	9
0	0.0	0.0	0.0	0.0	0.0	0.0	0.0	0.0	0.0	0.0
10	0.0	0.0	0.0	0.0	5.1	0.0	0.0	0.0	0.0	0.0
20	2.4	0.0	0.0	94.0	76.1	0.1	0.0	0.0	72.0	99.4
30	100	0.0	0.9	100	100	10.1	0.0	0.1	100	100
40	100	0.0	100	100	100	100	0.0	97.9	100	100
50	100	0.3	88.3	100	100	100	0.0	100	100	100
60	100	0.0	100	100	100	100	0.0	100	100	100
70	100	2.3	100	100	100	100	0.0	100	100	100
80	100	52.4	100	100	100	100	0.0	100	100	100
90	100	0.1	100	100	100	100	28.2	100	100	100
100	100	75.8	100	100	100	100	12.6	100	100	100

Figure 10.4: Table showing $\hat{S}$ for 10 different spoofing angles and 10 different spoofing distances. Notice that d_s is given in km and the estimates $\hat{S}$ are given in percent. In all of the simulations the number of received AIS messages was between 29 and 31.

illustrate this point, an illustration of the same concept as in Figure 10.6a is given for node 10 in Figure 10.6b.

The Figures 10.7a and 10.7b show trace plots of node 0 and 10, respectively, from the run of the sampler in which the spoofed positions was the one corresponding to a spoofing distance $d_s = 50$ km and spoofing angle $\phi_{dir}^{(6)}$. These figures show that the trace converges to the spoofed positions. The reason for this is that this spoofed position lies within the area shown in Figure 10.6a. The Figures 10.8a and 10.8b show the same thing, but for the spoofed position corresponding to the spoofed angle $\phi_{dir}^{(1)}$.

In conclusion, the tests carried out in this section show that the spoofing detection capability is largely dependent on how far away a vessel has spoofed its position, and the direction in which it has spoofed its position. Evident from Table 10.4 is the fact that if the vessel in the scenario seen in Figure 10.2 is spoofing its position in the direction of the spoofing angles $\phi_{dir}^{(1)}$ and $\phi_{dir}^{(6)}$, spoofing can not be determined with the wanted certainty for the spoofing distances tested. Evident from Figure 10.6a is the fact that the trace plot area stretches beyond the tested spoofing distances. Hence, spoofing detection with the wanted certainty might be possible if the spoofing distances are large enough. These spoofing distances would need to go beyond 100 km for the developed algorithms to detect the spoofing. This is considered poor spoofing detection capability, which is why this is not further examined. For the remaining spoofing directions in the table, it is seen that they all have in common that at a spoofing distance of 60 km and above, spoofing is detected with the wanted certainty. On the other hand, it is also evident from the table that, for some spoofing angles, spoofing can already be detected at a spoofing distance $d_s = 20$ km, as evident from the last column in the table, corresponding to the spoofing angle $\phi_{dir}^{(9)}$.

In order to see if the spoofing capabilities can be improved by utilizing two LEO satellites, this is described and tested in the succeeding chapters.

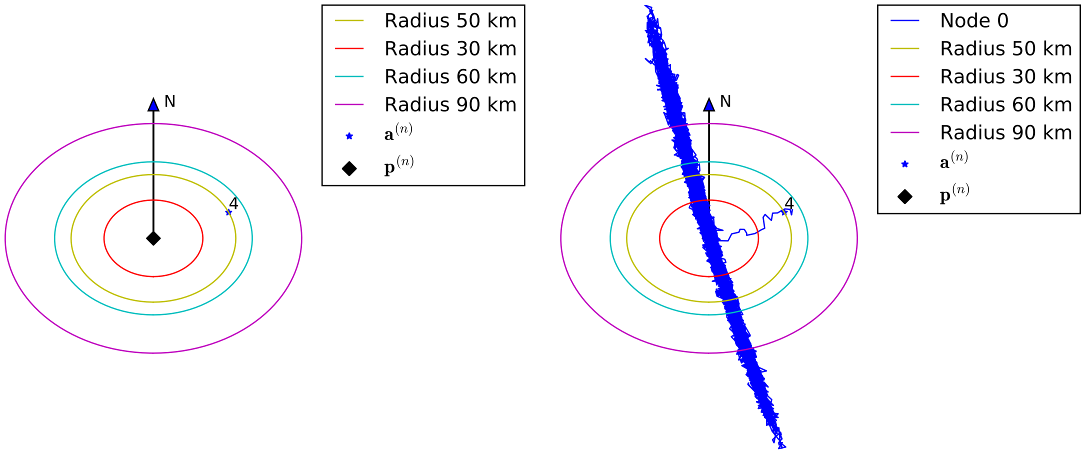

(a) **(b)**

Figure 10.5: **(a)**: AEP plot of the spoofed position corresponding to $d_s = 50$ km and the spoofing angle $\phi_{dir}^{(4)}$ and $\boldsymbol{p}^{(n)}$ as center point. **(b)**: Addition of trace plot of node 0.

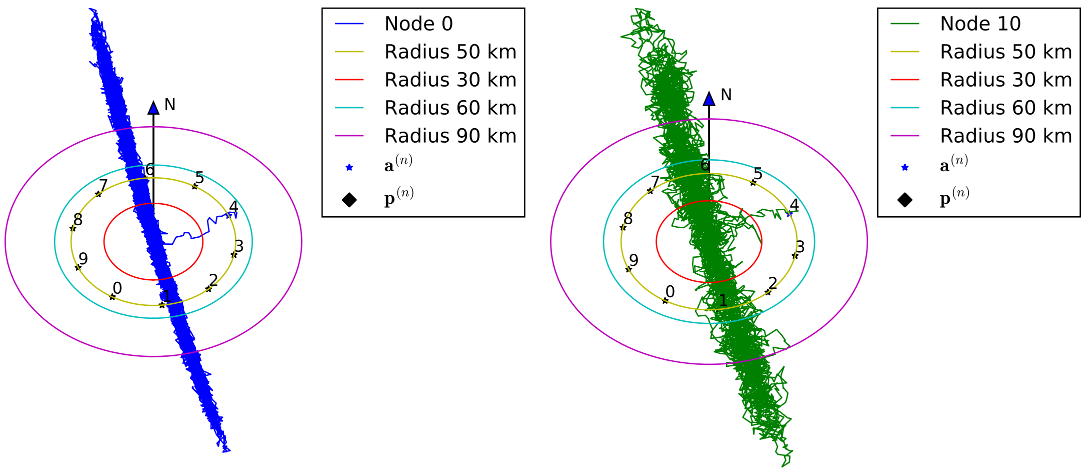

(a) **(b)**

Figure 10.6: **(a)**: Same as Figure 10.5b with the addition of the spoofed positions for $d_s = 50$ km for all $\phi_{dir}^{(k)}$. **(b)**: Same as Figure 10.6a but with trace plot of node 10 instead of node 0.

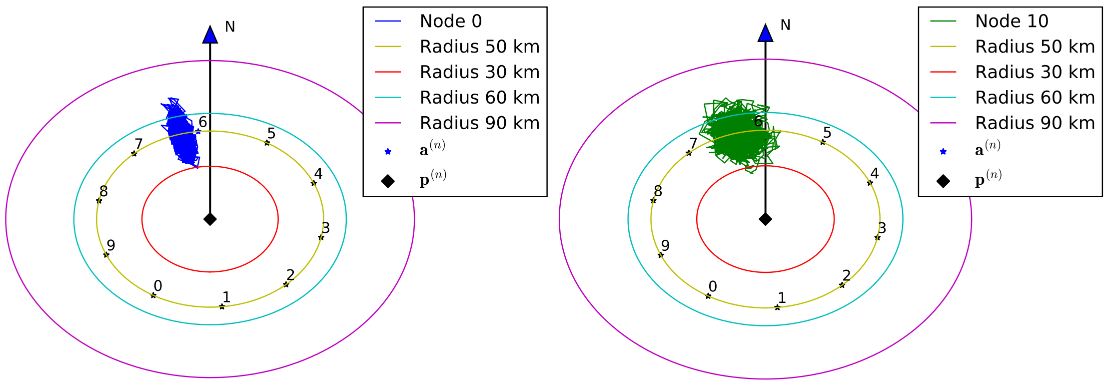

(a) **(b)**

Figure 10.7: **(a)**: Trace plot of node 0 for the simulation in which the spoofed position was the one corresponding to $d_s = 50$ km and $\phi_{dir}^{(6)}$. **(b)**: Same as Figure 10.7a, but for node 10.

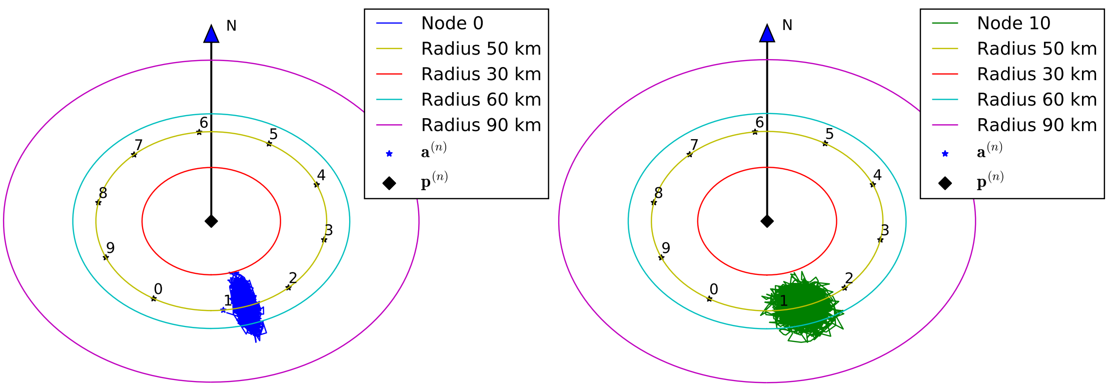

(a) **(b)**

Figure 10.8: **(a)**: Trace plot of node 0 for the simulation in which the spoofed position was the one corresponding to $d_s = 50$ km and $\phi_{dir}^{(1)}$. **(b)**: Same as Figure 10.7a, but for node 10.

11 Sampler algorithm: Two satellites and no AIS frequency offset

This chapter introduces the MWG sampler algorithm for the model in which two satellites are used and no AIS frequency offset is included. The probability model for this case is described in Section 8.4, in which the posterior densities for the unobserved variables in the Bayesian network are also described. These posterior densities are used in the MWG sampler in this chapter. In the last section of this chapter, a description of the choice of input parameters for the algorithm is given. These parameters are used in the algorithm when it is tested in the succeeding chapter.

11.1 Metropolis within Gibbs sampler

The MWG sampler algorithm used in this chapter is seen in Algorithm 3. This sampler uses a cyclic updating scheme of the variables. The initialization of the unobserved variables follows the same lines as in Section 9.1, as does the variable updating steps. Notice that in Algorithm 3, a triple superscript refers to AIS message number in the first entry, satellite number in the second entry, and Gibbs iteration in the third entry, e.g. $\nu_T^{(n,m,g)}$ is the value of ν_T for the n'th AIS message for the m'th satellite in the g'th Gibbs iteration.

Algorithm 3 MWG sampler for two satellite model

Input data: $\boldsymbol{a}^{(n)}$, $\nu^{(n,0)}$, $\nu^{(n,1)}$, $\boldsymbol{s}_\alpha^{(n,0)}$, $\boldsymbol{s}_\beta^{(n,0)}$, $\boldsymbol{s}_\alpha^{(n,1)}$, $\boldsymbol{s}_\beta^{(n,1)}$, $f_c^{(n)}$, $T_T^{(n)}$, t_r for $n = 0, 1, \ldots, N-1$.
Input parameters: G, q_S, κ_{init}, κ_{v1}, κ_{v2}, κ_S, κ_{NS}, κ_{MH}, κ_{sat} σ_d^2.
Output data: $S^{(g)}$ for $g = 0, 1, \ldots, G-1$.

1. Initialize unobservables:
   (a) Draw $S^{(0)} \sim \text{Bern}(q_S)$.
   (b) Draw $\boldsymbol{p}^{(0,0)} \sim F\left(\boldsymbol{a}^{(0)}, \kappa_{init}\right)$.
   (c) Calculate $\nu_T^{(0,0,0)}$ according to (8.14), using $\boldsymbol{p}^{(0,0)}$, $\boldsymbol{s}_\alpha^{(0,0)}$, $\boldsymbol{s}_\beta^{(0,0)}$, and $f_c^{(0)}$.
   (d) Calculate $\nu_T^{(0,1,0)}$ according to (8.14), using $\boldsymbol{p}^{(0,0)}$, $\boldsymbol{s}_\alpha^{(0,1)}$, $\boldsymbol{s}_\beta^{(0,1)}$, and $f_c^{(0)}$.
   (e) For $n = 1, 2, \ldots, N-1$.
      i) Set $\kappa_v^{(n)} = \begin{cases} \kappa_{v1} & \text{if } T_T^{(n)} - T_T^{(n-1)} < 1.5 \cdot t_r \\ \kappa_{v2} & \text{otherwise.} \end{cases}$
      ii) Draw $\boldsymbol{p}^{(n,0)} \sim F\left(\boldsymbol{p}^{(n-1,0)}, \kappa_v^{(n)}\right)$.
      iii) Calculate $\nu_T^{(n,0,0)}$ according to (8.14), using $\boldsymbol{p}^{(n,0)}$, $\boldsymbol{s}_\alpha^{(n,0)}$, $\boldsymbol{s}_\beta^{(n,0)}$, and $f_c^{(n)}$.
      iv) Calculate $\nu_T^{(n,1,0)}$ according to (8.14), using $\boldsymbol{p}^{(n,0)}$, $\boldsymbol{s}_\alpha^{(n,1)}$, $\boldsymbol{s}_\beta^{(n,1)}$, and $f_c^{(n)}$.
2. Use Metropolis-Hastings within Gibbs sampling for $g = 1, 2, \ldots, G-1$.
   (a) Update $S^{(g)}$ by:
      i) Set $c_1 = q_S \prod_{n=0}^{N-1} f_F\left(\boldsymbol{a}^{(n)} \mid \boldsymbol{p}^{(n,g-1)}, \kappa_S\right)$.
      ii) Set $c_0 = (1 - q_S) \prod_{n=0}^{N-1} f_F\left(\boldsymbol{a}^{(n)} \mid \boldsymbol{p}^{(n,g-1)}, \kappa_{NS}\right)$.
      iii) Draw $u \sim \text{unif}[0, 1]$.
      iv) Set $S^{(g)} = \begin{cases} 1 & \text{if } u \leq \frac{c_1}{c_1 + c_0} \\ 0 & \text{otherwise.} \end{cases}$
   (b) Update $\boldsymbol{p}^{(n,g)}$ by applying a Metropolis-Hastings step for $n = 0, 1, \ldots, N-1$.
      i) Draw $\boldsymbol{p}_{pro}^{(n,g)} \sim F\left(\boldsymbol{p}^{(n,g-1)}, \kappa_{MH}\right)$ as proposal for true vessel position.
      ii) Calculate Doppler shift proposal $\nu_{pro}^{(n,0,g)}$ according to (8.14), using $\boldsymbol{p}_{pro}^{(n,g)}$, $\boldsymbol{s}_\alpha^{(n,0)}$, $\boldsymbol{s}_\beta^{(n,0)}$, and $f_c^{(n)}$.
      iii) Calculate Doppler shift proposal $\nu_{pro}^{(n,1,g)}$ according to (8.14), using $\boldsymbol{p}_{pro}^{(n,g)}$, $\boldsymbol{s}_\alpha^{(n,1)}$, $\boldsymbol{s}_\beta^{(n,1)}$, and $f_c^{(n)}$.
      iv) Set $\kappa = \begin{cases} \kappa_S, & \text{if } S^{(g)} = 1 \\ \kappa_{NS}, & \text{otherwise.} \end{cases}$
      v) If $n = 0$:

$$H = \frac{f_F\left(\boldsymbol{p}_{pro}^{(0,g)} \mid \boldsymbol{s}_{avg}, \kappa_{sat}\right) \cdot f_F\left(\boldsymbol{p}_{pro}^{(0,g)} \mid \boldsymbol{a}^{(0)}, \kappa\right) \cdot f_N\left(\nu^{(0,0)} \mid \nu_{pro}^{(0,0,g)}, \sigma_d^2\right) \cdot f_N\left(\nu^{(0,1)} \mid \nu_{pro}^{(0,1,g)}, \sigma_d^2\right)}{f_F\left(\boldsymbol{p}^{(0,g-1)} \mid \boldsymbol{s}_{avg}, \kappa_{sat}\right) \cdot f_F\left(\boldsymbol{p}^{(0,g-1)} \mid \boldsymbol{a}^{(0)}, \kappa\right) \cdot f_N\left(\nu^{(0,0)} \mid \nu_T^{(0,0,g-1)}, \sigma_d^2\right) \cdot f_N\left(\nu^{(0,1)} \mid \nu_T^{(0,1,g-1)}, \sigma_d^2\right)}$$

MWG sampler for two satellite model continued

vi) Else:

Set $\kappa_v^{(n)} = \begin{cases} \kappa_{v1} & \text{if } T_T^{(n)} - T_T^{(n-1)} < 1.5 \cdot t_r \\ \kappa_{v2} & \text{otherwise.} \end{cases}$

and

$$H = \frac{f_F\left(\boldsymbol{p}_{pro}^{(n,g)} \mid \boldsymbol{p}^{(n-1,g)}, \kappa_v^{(n)}\right) \cdot f_F\left(\boldsymbol{p}_{pro}^{(n,g)} \mid \boldsymbol{a}^{(n)}, \kappa\right) \cdot f_N\left(\nu^{(n,0)} \mid \nu_{pro}^{(n,0,g)}, \sigma_d^2\right) \cdot f_N\left(\nu^{(n,1)} \mid \nu_{pro}^{(n,1,g)}, \sigma_d^2\right)}{f_F\left(\boldsymbol{p}^{(n,g-1)} \mid \boldsymbol{p}^{(n-1,g)}, \kappa_v^{(n)}\right) \cdot f_F\left(\boldsymbol{p}^{(n,g-1)} \mid \boldsymbol{a}^{(n)}, \kappa\right) \cdot f_N\left(\nu^{(n,0)} \mid \nu_T^{(n,0,g-1)}, \sigma_d^2\right) \cdot f_N\left(\nu^{(n,1)} \mid \nu_T^{(n,1,g-1)}, \sigma_d^2\right)}$$

vii) Draw $v \sim \text{unif}[0,1]$.

viii) Set $a_{accept}^{(n,g)} = \min[1, H]$

ix) Set $\boldsymbol{p}^{(n,g)} = \begin{cases} \boldsymbol{p}_{pro}^{(n,g)} & \text{if } v \leq a_{accept}^{(n,g)} \\ \boldsymbol{p}^{(n,g-1)} & \text{otherwise.} \end{cases}$

x) Set $\nu_T^{(n,0,g)} = \begin{cases} \nu_{pro}^{(n,0,g)} & \text{if } v \leq a_{accept}^{(n,g)} \\ \nu_T^{(n,0,g-1)} & \text{otherwise.} \end{cases}$

xi) Set $\nu_T^{(n,1,g)} = \begin{cases} \nu_{pro}^{(n,1,g)} & \text{if } v \leq a_{accept}^{(n,g)} \\ \nu_T^{(n,1,g-1)} & \text{otherwise.} \end{cases}$

Irreducibility and aperiodicity of the sampler in Algorithm 3 can be established using arguments similar to those made in the one satellite case in Section 9.2 in Chapter 9.

11.2 Metropolis within Gibbs sampler input parameters

The input parameters for the MWG sampler used in this chapter are the same as those in the one satellite case, except for one of the parameters. The parameter that is different is κ_{MH}, which is chosen such that the average accept probabilities from (9.2) fall between 0.16 and 0.43. The input parameters used in this chapter can be seen in Table 11.1. The case-by-case choice of κ_{v1} and κ_{v2} relies on Table 9.2 in Chapter 9 as was also the case in said chapter.

Parameter	**Value**
q_S	0.01
κ_{init}	2437366
κ_{v1}	Case specific
κ_{v2}	Case specific
κ_S	975
κ_{NS}	Case specific
κ_{MH}	15233535
κ_{sat}	164
σ_d^2	7.32

Table 11.1: Input parameters for the two satellite MWG sampler.

12 | Sampler algorithm test: Two satellites and no AIS frequency offset

This chapter describes the tests of the sampler in Algorithm 3, which is a sampling algorithm designed and developed to help perform inference in the model described in Section 8.4. This model was the one created for the variables in the space-based AIS system in which two satellites are used and no AIS frequency offset is included. All tests carried out in this chapter are based on the scenario seen in Figure 12.1. Four true vessel positions are shown in this figure, which, when generating data, correspond to four different $\boldsymbol{p}_v^{(0)}$ positions used as input for the data generation described in Chapter 6. The colatitude and longitudes of these vessel positions are seen in Table 12.1. Whenever a data set is generated for use in the tests in this chapter the orbit offset, Ω_{off}, is chosen such that the two satellites fly in the same orbits regardless of which one of the four vessel positions is in question. These orbits always have an inclination of 70° degrees. These two orbit trajectories are also seen in the figure. This scenario is chosen to see how different vessel positions, relative to the satellite orbits, affect the position spoofing detection capabilities of the developed algorithm.

These four vessel positions will be used in tests where the vessel has different report intervals, i.e. tests in which the vessel is either idle or travelling with a speed dictated by the report interval that is being tested. In tests where the vessel is idle, $\boldsymbol{p}^{(0)} = \boldsymbol{p}^{(1)} = \ldots = \boldsymbol{p}^{(N-1)}$. When the vessel is moving, the four vessel positions shown in Figure 12.1

	θ_p	ϕ_p
Vessel position 1	$\frac{\pi}{4}$	$\frac{5\pi}{48}$
Vessel position 2	$\frac{\pi}{4}$	$\frac{\pi}{6}$
Vessel position 3	$\frac{3\pi}{20}$	$\frac{5\pi}{12}$
Vessel position 4	$\frac{7\pi}{40}$	$\frac{\pi}{5}$

Table 12.1: Colatitude and longitude of the four vessel positions from Figure 12.1.

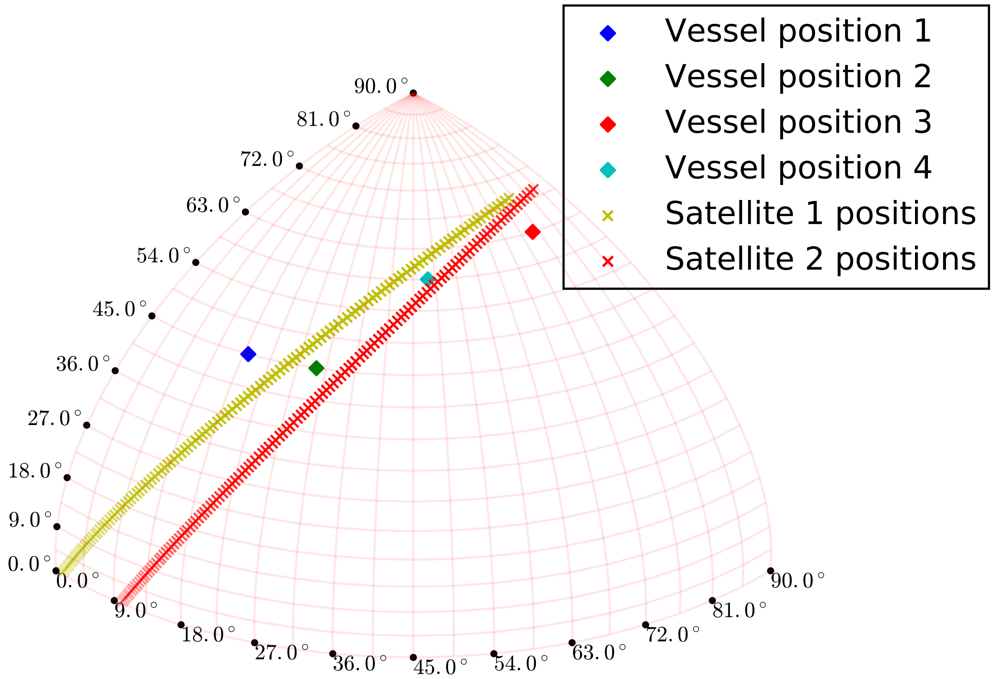

Figure 12.1: Four vessel positions and two satellite orbits.

serve as $\boldsymbol{p}_v^{(0)}$ positions, i.e. the position from which the vessel movement starts. The report intervals that will be tested are 10, 6, and 2 s, in which a vessel moves at speeds according to Table 2.1. The report interval of 10 s covers both the case in which the vessel is idle and the one in which it is moving, hence both scenarios are tested when using this report interval.

For each tested report interval, a κ_{NS}-value is chosen as to not create a false alarm. When such κ_{NS}-value has been chosen, it is used to test how far away from its true position a vessel has to spoof its position in order for the algorithm to be able to detect the spoofing.

12.1 False alarm test

In this section κ_{NS}-values are found such that no false alarm is created. Four different κ_{NS} values are needed. Two of these are for the report interval of 10 s, where the case in which the vessel is idle and the case in which the vessel is moving at speeds up to 14 knots are included. The next value the one needed for the 6 s report interval, and the last value is the one needed for the 2 s report interval.

In order to describe the procedure for choosing these κ_{NS}-values, a description of how the κ_{NS}-value for the report interval of 10 s in which the vessel is moving is given. The same procedure is used to find the κ_{NS}-values for the remaining report intervals.

To find the κ_{NS}-value, $N_{DS} = 10$ data sets are created for each of the 4 vessel positions in Figure 12.1. Each data set is created without spoofing, and with a vessel speed corresponding to the maximal vessel speed in the 10 s reporting interval, namely 14 knots. For each one of the vessel positions in Figure 12.1, the 10 data sets corresponding to this position are created such that the vessel is heading in different directions

$$\mu_{dir}^{(k)} = \frac{2\pi}{N_{DS}} \cdot k, \qquad k = 0, 1, \ldots, N_{DS} - 1. \tag{12.1}$$

This is done such that the vessel is moving in different directions in each data set for each of the vessel positions from Figure 12.1. As an example, the true vessel positions, $\boldsymbol{p}^{(n)}$, for $n = 0, 1, \ldots, N-1$, from the 10 data sets created for vessel position 2 in Figure 12.1 are seen in an AEP plot in Figure 12.2.

The sampler in Algorithm 3 was then run with each of the, in total, 40 data sets for $G = 25000$ iterations each, using the input parameter values from Table 11.1, and a κ_{NS}-value chosen such that 95% of the values in the Fisher distribution fall within a distance of 0.5 km from its mean direction, and $\hat{S}$ was estimated for each run. This was done several times, each time incrementing the value of κ_{NS} with 0.5 km, until all 40 estimates of $\hat{S}$ were below 0.1, i.e. until no false alarm was created in any of the 4 vessel positions. These estimates were calculated with a burn-in of $N_{BI} = 1000$ samples.

The above procedure was also carried out for the remaining report intervals. The resulting κ_{NS}-values for the tested report intervals can be seen in Table 12.2. These are the κ_{NS}-values that are used in the succeeding simulations when different report intervals are used.

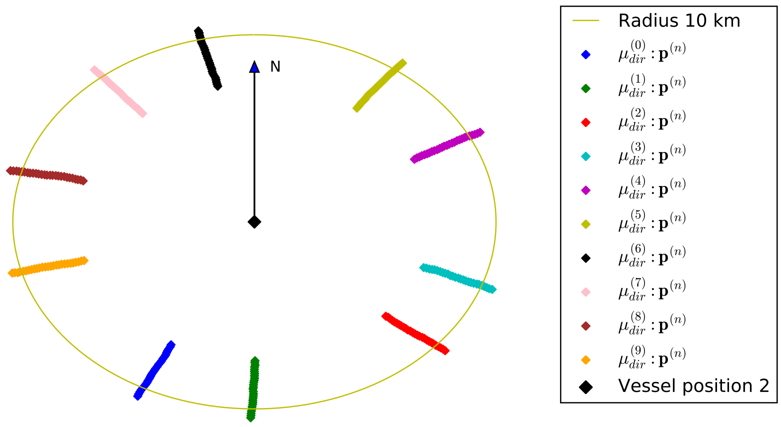

Figure 12.2: AEP plot illustrating 10 vessel paths.

t_r (s)	κ_{NS}
10 (not moving)	19896862
10 (moving)	12036373
6	9749462
2	4333094

Table 12.2: Values of κ_{NS} that ensure that no false alarm is created for different reporting intervals.

12.2 Spoofing distance test for 10 s report interval without vessel movement

For each of the 4 vessel positions in Figure 12.1, the spoofing detection capabilities are tested when the vessel is not moving. For each of the 4 vessel positions, data is generated in the same way as the data used in the one satellite case in Section 10.2, with the same spoofing angles. The principle is illustrated in Figure 10.3 from the one satellite case test section. The only difference is that this test utilizes two satellites. The scenarios for vessel positions $1-4$ are seen in the Figures 12.3a, 12.3b, 12.4a, and 12.4b, respectively.

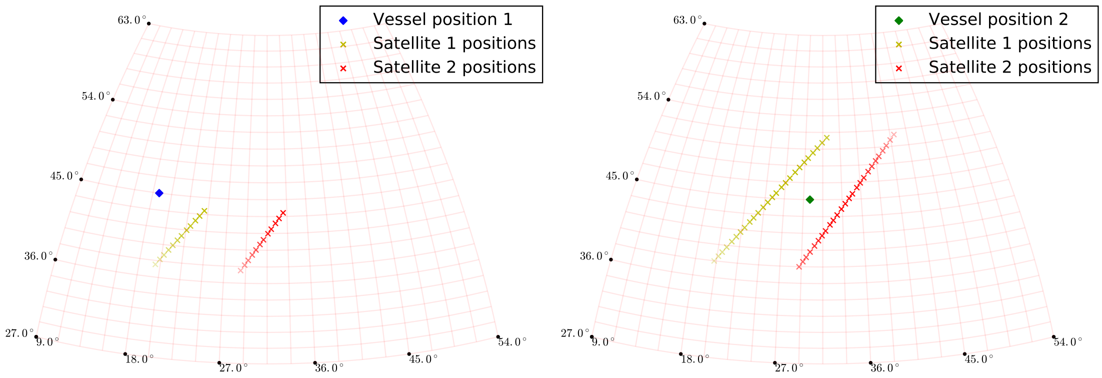

(a) (b)

Figure 12.3: **(a)**: Scenario for vessel position 1. **(b)**: Scenario for vessel position 2.

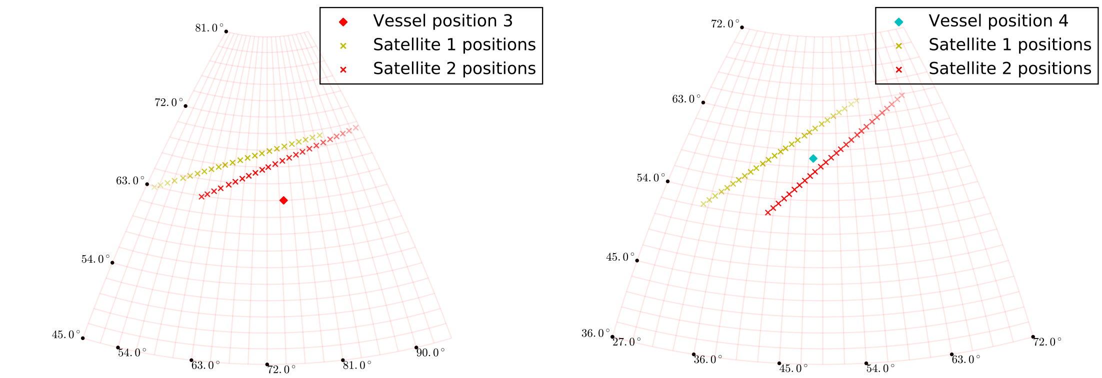

(a) (b)

Figure 12.4: **(a)**: Scenario for vessel position 3. **(b)**: Scenario for vessel position 4.

For each of the 4 vessel positions, the estimates of $\hat{S}$ are seen in the Tables 12.5-12.8. Notice that the tables show that for each of the 4 vessel positions, a different number of spoofing distances, d_s, have been tested. For a given vessel positions, the spoofing distances were incremented until spoofing was detected for all 10 spoofing angles.

Evident from all of the tables is the fact that compared to the case in which a single satellite was used, the spoofing capabilities have been improved by using two satellites. They have been improved in the sense that a vessel does not have to spoof its position as far away as in the single satellite case for the spoofing to be detected.

Moreover, as was the case in the single satellite case, when a vessel is spoofing its position in a certain direction, the spoofing capabilities suffer in the sense that a vessel has to spoof its position further away for the spoofing to be detected. The spoofing angles in which this is the case are dependent on the vessel position relative to the satellite orbits. As an example, consider Table 12.7, in which the results from vessel position 3 are shown. When the vessel is spoofing its position in the direction of $\phi_{dir}^{(4)}$ or $\phi_{dir}^{(9)}$, the spoofing capabilities suffer. As was the case in the single satellite case, this behavior is illustrated in the Figures 12.10a and 12.10b, in which trace plots of node 0 and 10, respectively, for vessel position 3 are seen for the simulations in which the spoofed position corresponding to $d_s = 25$ km and $\phi_{dir}^{(7)}$ was used. In these figures it is evident that the spoofing angles $\phi_{dir}^{(4)}$ and $\phi_{dir}^{(9)}$ correspond to spoofed positions that fall within the area. The areas of the trace plots in these figures have shapes similar to that in Figure 10.5a. The shape of node trace plot areas are not always shaped like in these two examples. An example of areas that are shaped differently is seen in the Figures 12.9a and 12.9b, in which trace plots of node 0 and 10, respectively, for vessel position 2 are seen for the simulations in which the spoofed position corresponding to $d_s = 25$ km and $\phi_{dir}^{(7)}$ was used.

Thus, in conclusion, utilizing two satellites when the vessel is not moving has improved the overall spoofing capabilities, but the problems with certain spoofing angles making the spoofing capabilities suffer still exist. The scenario in which the spoofing capabilities are best is the one with vessel position 2. With the way the satellites pass this vessel position, which is illustrated in Figure 12.3b, the spoofing capabilities are such that at a spoofing distance of 15 km, spoofing can be detected at all the tested spoofing angles. This is evident from Table 12.6.

Considering all the tables in this section, they have in common that spoofing is detected, for all of the spoofing angles used if the vessel is spoofing its position 30 km away from its true position. Overall, in vessel positions $2 - 4$, corresponding to Tables 12.6-12.8, it is evident that for some spoofing angles, spoofing starts being detected at spoofing distances as low as $d_s = 5$ km.

t_r = 10 s, no vessel movement (Vessel position 1)										
d_s	Spoofing angles									
	0	1	2	3	4	5	6	7	8	9
0	0.1	0.1	0.2	0.1	0.1	0.1	0.0	0.2	0.2	0.1
0.5	0.2	0.1	0.9	0.2	0.3	0.0	0.1	0.1	0.1	0.2
5	0.3	1.9	0.6	10.1	60.3	51.7	0.7	0.3	0.7	16.5
10	97.7	24.0	95.9	98.9	100	100	97.1	93.3	99.2	100
15	100	75.8	100	100	100	100	100	80.6	100	100
20	100	100	100	100	100	100	100	100	100	100

Figure 12.5: Table showing $\hat{S}$ for 10 different spoofing angles and different spoofing distances, d_s, for vessel position 1. Notice that d_s is given in km and the estimates $\hat{S}$ are given in percent. In all of the simulations, the number of received AIS messages was between 12 and 14.

t_r = 10 s, no vessel movement (Vessel position 2)										
d_s	Spoofing angles									
	0	1	2	3	4	5	6	7	8	9
0	4.4	0.9	1.1	2.1	3.0	2.1	1.4	2.4	1.1	1.1
0.5	0.4	3.9	0.7	1.1	1.3	1.3	2.3	1.1	1.6	0.6
5	100	13.0	0.9	72.3	3.6	22.3	4.4	7.7	2.5	6.4
10	100	100	8.7	99.9	98.3	53.8	92.5	100	100	78.5
15	100	100	100	100	100	100	100	100	100	100

Figure 12.6: Table showing $\hat{S}$ for 10 different spoofing angles and different spoofing distances, d_s, for vessel position 2. Notice that d_s is given in km and the estimates $\hat{S}$ are given in percent. In all of the simulations, the number of received AIS messages was between 24 and 27.

t_r = 10 s, no vessel movement (Vessel position 3)										
d_s	Spoofing angles									
	0	1	2	3	4	5	6	7	8	9
0	0.6	1.1	1.3	0.1	5.8	1.2	9.2	0.6	3.3	2.7
0.5	0.4	0.5	0.9	17.2	0.2	0.3	2.9	0.6	43.6	7.7
5	42.3	99.9	66.6	10.0	0.6	55.6	84.9	73.0	9.6	1.9
10	97.9	100	100	56.9	15.3	94.4	100	100	90.1	35.6
15	100	100	100	98.9	94.8	100	100	100	66	35.3
20	100	100	100	100	21.1	100	100	100	100	46.0
25	100	100	100	100	84.9	100	100	100	100	42.8
30	100	100	100	100	99.5	100	100	100	100	96.0

Figure 12.7: Table showing $\hat{S}$ for 10 different spoofing angles and different spoofing distances, d_s, for vessel position 3. Notice that d_s is given in km and the estimates $\hat{S}$ are given in percent. In all of the simulations, the number of received AIS messages was between 22 and 24.

t_r = 10 s, no vessel movement (Vessel position 4)										
d_s	Spoofing angles									
	0	1	2	3	4	5	6	7	8	9
0	0.6	1.6	2.4	0.8	3.4	2.2	2.2	3.0	2.1	2.2
0.5	1.3	2.3	1.0	0.6	1.2	1.2	1.0	71.2	0.8	1.3
5	46.8	1.7	4.1	2.1	23.3	100	19.5	1.3	0.4	8.2
10	92.0	31.4	100	11.4	100	100	100	1.6	100	100
15	100	100	13.4	100	100	100	100	100	100	100
20	100	100	99.5	100	100	100	100	100	100	100

Figure 12.8: Table showing $\hat{S}$ for 10 different spoofing angles and different spoofing distances, d_s, for vessel position 4. Notice that d_s is given in km and the estimates $\hat{S}$ are given in percent. In all of the simulations, the number of received AIS messages was between 26 and 28.

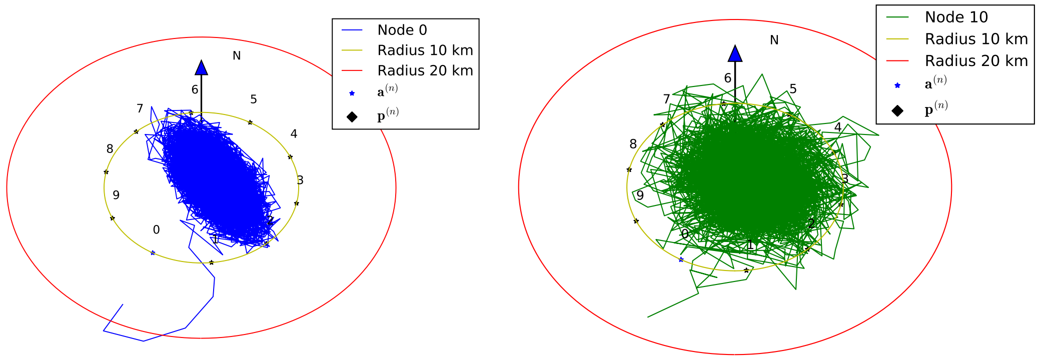

(a) **(b)**

Figure 12.9: **(a)**: Scenario for vessel position 3. **(b)**: Scenario for vessel position 4.

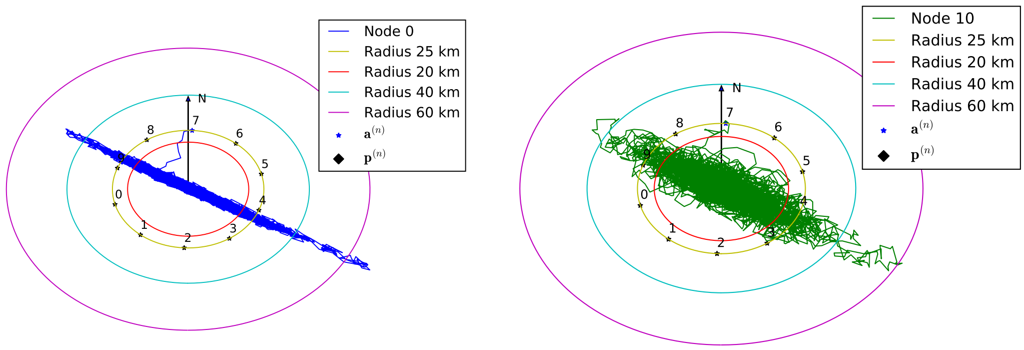

(a) **(b)**

Figure 12.10: **(a)**: Scenario for vessel position 3. **(b)**: Scenario for vessel position 4.

12.3 Spoofing distance test for 10 s report interval with vessel movement

This section explores the case in which a vessel is moving at speeds corresponding to the report interval of 10 s. For the test in this section, the spoofing angles from (10.1) are reused. For each of the 4 vessel positions, 10 data sets are generated per spoofing distance that is tested. To generate one of these data sets for a given vessel position and spoofing direction is done as described in Chapter 6 with $\phi_{dir}^{(k)}$ as the spoofing direction for the k'th data set. In contrast to how the vessel movement directions were fixed when generating data based on (12.1), they are not fixed in this section, and are chosen randomly such that for each data set generated in this section, the input vessel movement direction, μ_{dir}, is drawn uniformly on the interval from 0 to 2π. An example of the generated vessel paths and corresponding spoofed vessel paths for vessel position 2 and the spoofing distance $d_s = 15$ km can be seen in the Figures 12.11a and 12.11b showing AEP plots. In Figure 12.11a the true vessel paths are seen, and in Figure 12.11b both the true vessel paths and the spoofed vessel paths are seen. In all of the data sets generated for the test in this section, the vessel speeds have been drawn uniformly on the vessel speed interval corresponding to the report interval of 10 s. This speed interval is seen in Table 2.1.

The spoofing detection results can be seen in Tables 12.12-12.15. The results in these tables show that the vessel position with the poorest spoofing capabilities is vessel position 3, where vessel position spoofing is not reliably detectable until a spoofing distance of 35 km. As was the case in the single satellite case and the case with two satellites without vessel movement, there are still spoofing angles in which the position spoofing capabilities are worse than others. On the other hand, it is evident from Table 12.13 that spoofing starts being detected, for some spoofing angles, at spoofing distances as low as $d_s = 5$ km for vessel position 2.

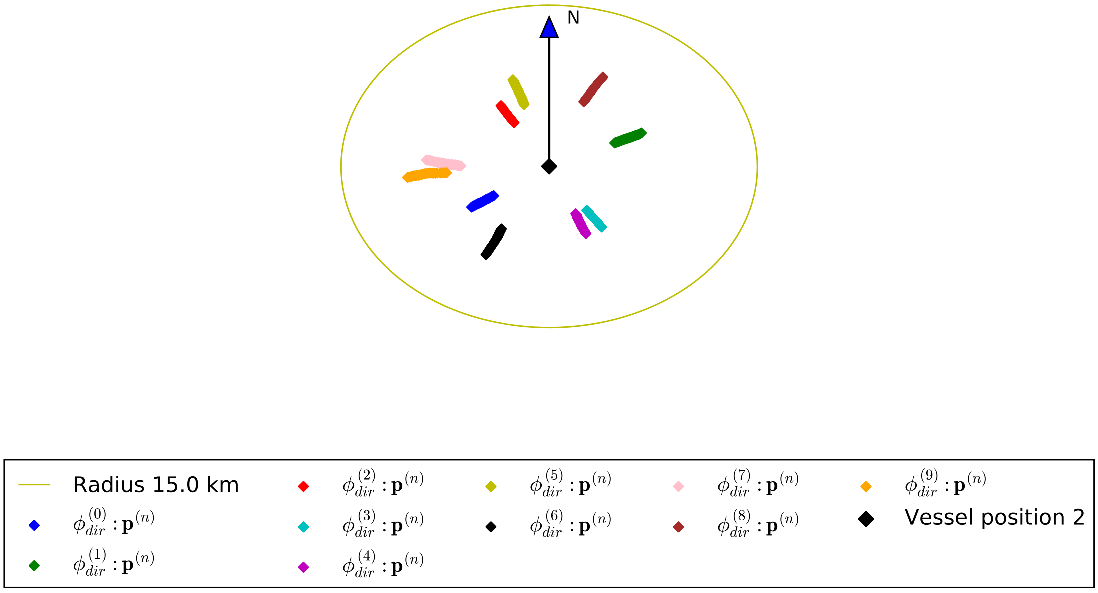

(a)

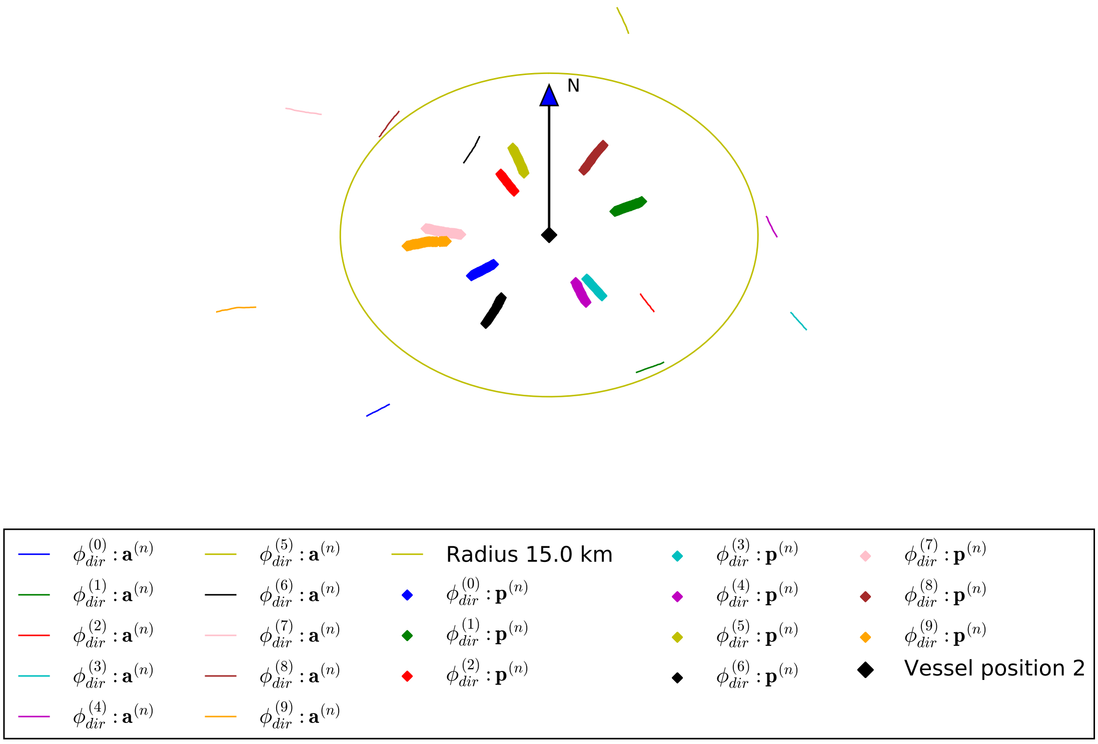

(b)

Figure 12.11: **(a)**: The 10 generated true vessel paths for vessel position 2 for the simulations in which a spoofing distance $d_s = 15$ km is used. **(b)**: The same, but with the spoofed vessel paths plotted as well.

t_r = 10 s, vessel movement (Vessel position 1)										
d_s	Spoofing angles									
	0	1	2	3	4	5	6	7	8	9
0	0.0	0.0	0.0	0.0	0.0	0.0	0.	0.0	0.0	0.1
0.5	0.0	0.0	0.0	0.1	0.0	0.1	0.0	0.0	0.0	0.0
5	2.2	0.0	0.0	21.5	1.0	0.2	0.3	0.2	0.0	0.0
10	33.79	87.9	0.1	1.2	95.2	67.4	4.7	0.0	91.3	99.8
15	100	86.3	0.9	100	100	100	12.9	60.3	99.9	100
20	100	99.9	100	100	100	100	100	100	100	100

Figure 12.12: Table showing $\hat{S}$ for 10 different spoofing angles and different spoofing distances, d_s, for vessel position 1. Notice that d_s is given in km and the estimates $\hat{S}$ are given in percent. In all of the simulations, the number of received AIS messages was between 12 and 14.

t_r = 10 s, vessel movement (Vessel position 2)										
d_s	Spoofing angles									
	0	1	2	3	4	5	6	7	8	9
0	0.1	0.0	0.1	3.6	0.4	0.0	1.6	0.1	0.0	0.0
0.5	0.0	0.8	0.1	0.3	0.3	0.1	0.4	0.1	0.7	0.0
5	0.0	100	49.9	3.5	0.1	100	0.0	0.1	0.6	91.0
10	1.6	0.4	0.0	99.2	99.8	99.4	90.5	98.3	69.3	74.9
15	100	86.6	100	100	100	100	1.1	100	100	100
20	100	5.7	100	100	100	100	8.9	100	100	100
25	100	100	100	100	100	100	100	100	100	100

Figure 12.13: Table showing $\hat{S}$ for 10 different spoofing angles and different spoofing distances, d_s, for vessel position 2. Notice that d_s is given in km and the estimates $\hat{S}$ are given in percent. In all of the simulations, the number of received AIS messages was between 24 and 27.

t_r = 10 s, vessel movement (Vessel position 3)										
d_s	Spoofing angles									
	0	1	2	3	4	5	6	7	8	9
0	0.0	1.5	0.0	0.1	0.0	0.0	0.0	0.2	0.0	0.0
0.5	0.0	0.0	0.1	0.0	0.0	0.0	0.0	1.2	0.1	0.0
5	0.1	6.5	34.5	0.9	0.0	0.0	14.8	13.1	0.2	0.1
10	89.0	87.6	98.9	1.2	0.0	26.5	99.8	10.4	0.1	0.2
15	100	100	100	0.5	19.3	100	100	100	48.3	0.0
20	100	100	100	100	6.5	100	100	100	99.7	5.1
25	100	100	100	100	20.6	100	100	100	100	0.1
30	100	100	100	100	71.1	100	100	100	100	0.1
35	100	100	100	100	100	100	100	100	100	100

Figure 12.14: Table showing $\hat{S}$ for 10 different spoofing angles and different spoofing distances, d_s, for vessel position 3. Notice that d_s is given in km and the estimates $\hat{S}$ are given in percent. In all of the simulations, the number of received AIS messages was between 22 and 24.

t_r = 10 s, vessel movement (Vessel position 4)										
d_s	Spoofing angles									
	0	1	2	3	4	5	6	7	8	9
0	0.0	0.0	1.2	0.2	0.0	0.3	0.0	0.2	0.1	3.9
0.5	0.0	0.1	0.0	0.0	0.0	0.1	0.0	0.0	0.0	2.7
5	0.3	21.3	0.0	0.0	0.1	0.1	16.4	0.1	0.2	0.0
10	100	0.2	95.4	92.1	0.1	100	100	0.0	3.3	100
15	99.5	100	80.9	0.6	100	0.3	100	0.0	5.3	100
20	100	100	94.1	99.8	100	100	100	4.9	100	100
25	100	100	100	100	100	100	100	100	100	100

Figure 12.15: Table showing $\hat{S}$ for 10 different spoofing angles and different spoofing distances, d_s, for vessel position 4. Notice that d_s is given in km and the estimates $\hat{S}$ are given in percent. In all of the simulations, the number of received AIS messages was between 26 and 28.

12.4 Spoofing distance test for 6 and 2 s report interval with vessel movement

This section covers both the case in which a vessel is moving at speeds corresponding to the report interval of 6 s and the case in which it moves according to the report interval of 2 s. Data for the test carried out in this section is generated in the same way as was the case in Section 12.3. The only difference is that when the 6 s report interval is tested, vessel speeds are drawn uniformly on the speed interval from Table 2.1 that corresponds to the given report interval. This is also the case when the 2 s report interval is tested. The tables containing the estimates $\hat{S}$ for each of the 4 vessel positions for both of the tested report intervals are found in Appendix N.

For the report interval of 6 s, the tests carried out show that if vessel position 3 is excluded, spoofing can be detected in all spoofing angles at a spoofing distance of $d_s = 25$ km. If vessel position 3 is included, this distance is raised such that spoofing can first be detected at a spoofing distance of $d_s = 60$ km. This is evident from the results for vessel position 3, which are seen in Table N.3. In this table, it is seen that the spoofing angle $\phi_{dir}^{(4)}$ results in poor spoofing detection capability. On the other hand, with some of the other spoofing angles in the same table, spoofing can start being detected at a spoofing distance as low as $d_s = 5$ km. This is seen in the table of the spoofing angle $\phi_{dir}^{(7)}$.

For the report interval 2 s, the tests carried out show that if vessel position 3 is excluded, spoofing can be detected in all spoofing angles at a spoofing distance of $d_s = 30$ km. If vessel position 3 is included, this distance is raised such that spoofing can first be detected at a spoofing distance of $d_s = 50$ km. This is evident from the results for vessel position 3, which are seen in Table N.7. In this table, it is seen that the spoofing angle $\phi_{dir}^{(4)}$ results in poor spoofing detection capability. On the other hand, all 4 vessel positions has spoofing angles at which spoofing can start being detected at a spoofing distance as low as $d_s = 10$ km. This is evident from the Tables N.5-N.8.

13 Sampler algorithm and test: Two satellites and AIS frequency offset

In this chapter, the MWG sampler algorithm for the special case in which two satellites are used and the AIS frequency offset is included is introduced. The probability model for this case is described in Section 8.5, in which the posterior densities for the unobserved variables in the Bayesian network are described. These posterior densities are used in the MWG sampler in this chapter.

Finally, testing of this algorithm with data simulated according to the descriptions in Chapter 6 is carried out, and a description of the choice of input parameters used for the algorithm is given.

13.1 Metropolis within Gibbs sampler

The MWG sampler algorithm used in this chapter is seen in Algorithm 4. The initialization of the unobserved variables follows the same lines as in Section 11.1, with the addition that the initialization of f_{off} is done by drawing

$$f_{off} \sim \mathcal{N}(0, \sigma_{off}^2). \tag{13.1}$$

As with the other MWG sampler algorithms presented in this thesis, the MWG sampler in this chapter utilizes a cyclic updating scheme. The updating of the variable S and the true vessel positions $\boldsymbol{p}^{(n)}$ for $n = 0, 1, \dots, N-1$ are done in the same fashion as in the MWG samplers in the chapters 9 and 11.

The updating of f_{off} is done based on the fact that its posterior density from (8.7) is a product of normal densities. Based on this posterior density in the case of $M = 2$, this yields that

$$f\left(f_{off} \mid C_{gen} \setminus \{f_{off}\}\right)$$

$$
\begin{aligned}
&\propto f_N\left(f_{off} \mid 0, \sigma_{off}^2\right) \prod_{n=0}^{N-1} f_N\left(\zeta^{(n,0)} \mid \nu_T^{(n,0)} + f_{off}, \sigma_d^2\right) f_N\left(\zeta^{(n,1)} \mid \nu_T^{(n,1)} + f_{off}, \sigma_d^2\right) \\
&= \exp\left(-\frac{1}{2\sigma_{off}^2} \cdot f_{off}^2 - \frac{1}{2\sigma_d^2} \cdot \sum_{n=0}^{N-1} \left(\left(\zeta^{(n,0)} - \nu_T^{(n,0)} - f_{off}\right)^2 + \left(\zeta^{(n,1)} - \nu_T^{(n,1)} - f_{off}\right)^2\right)\right) \\
&\propto \exp\left(-\left(\frac{1}{2\sigma_{off}^2} + \frac{2N}{2\sigma_d^2}\right) f_{off}^2 + \frac{2}{2\sigma_d^2} \sum_{n=0}^{N-1} \left(\zeta^{(n,0)} - \nu_T^{(n,0)} + \zeta^{(n,1)} - \nu_T^{(n,1)}\right) f_{off}\right) \\
&= \exp\left(-\frac{f_{off}^2}{2\sigma_{post}^2} + \frac{\mu_{post} \cdot f_{off}}{\sigma_{post}^2}\right) \qquad (13.2)
\end{aligned}
$$

where

$$\sigma_{post}^2 = \frac{2}{\frac{1}{2\sigma_{off}^2} + \frac{N}{\sigma_d^2}} \qquad (13.3)$$

and

$$\mu_{post} = \left(\frac{1}{\sigma_d^2} \sum_{n=0}^{N-1} \left(\zeta^{(n,0)} - \nu_T^{(n,0)} + \zeta^{(n,1)} - \nu_T^{(n,1)}\right)\right) \sigma_{post}^2. \qquad (13.4)$$

From (13.2), it is evident that the posterior distribution for f_{off} is proportional to an unnormalized normal distribution with mean value μ_{post} as given in (13.4) and variance σ_{post}^2 as given in (13.3). The updating of f_{off} is done using (13.2), employing a Metropolis-Hastings updating step. The proposal distribution from which proposal updates are drawn is chosen as a normal distribution with mean equal to the value of f_{off} in the previous Gibbs iteration and variance σ_{MH}^2. This distribution is symmetric and is hence not shown in the Hastings ratios in the updating steps for f_{off} in Algorithm 4.

Algorithm 4 MWG sampler for two satellite model and f_{off}

Input data: $\boldsymbol{a}^{(n)}$, $\zeta^{(n,0)}$, $\zeta^{(n,1)}$, $\boldsymbol{s}_\alpha^{(n,0)}$, $\boldsymbol{s}_\beta^{(n,0)}$, $\boldsymbol{s}_\alpha^{(n,1)}$, $\boldsymbol{s}_\beta^{(n,1)}$, $f_c^{(n)}$, $T_T^{(n)}$, t_r for $n = 0, 1, \ldots, N-1$.

Input parameters: G, q_S, κ_{init}, κ_{v1}, κ_{v2}, κ_S, κ_{NS}, κ_{MH}, κ_{sat} σ_d^2, σ_{post}^2, σ_{MH}^2, σ_{off}^2.

Output data: $S^{(g)}$ for $g = 0, 1, \ldots, G-1$.

1. Initialize unobservables by doing:
   (a) Draw $S^{(0)} \sim \text{Bern}(q_S)$.
   (b) Draw $f_{off}^{(0)} \sim \mathcal{N}(0, \sigma_{off}^2)$.
   (c) Draw $\boldsymbol{p}^{(0,0)} \sim F\left(\boldsymbol{a}^{(0)}, \kappa_{init}\right)$.
   (d) Calculate $\nu_T^{(0,0,0)}$ according to (8.14), using $\boldsymbol{p}^{(0,0)}$, $\boldsymbol{s}_\alpha^{(0,0)}$, $\boldsymbol{s}_\beta^{(0,0)}$, and $f_c^{(0)}$.
   (e) Calculate $\nu_T^{(0,1,0)}$ according to (8.14), using $\boldsymbol{p}^{(0,0)}$, $\boldsymbol{s}_\alpha^{(0,1)}$, $\boldsymbol{s}_\beta^{(0,1)}$, and $f_c^{(0)}$.
   (f) For $n = 1, 2, \ldots, N-1$.
      i) Set $\kappa_v^{(n)} = \begin{cases} \kappa_{v1} & \text{if } T_T^{(n)} - T_T^{(n-1)} < 1.5 \cdot t_r \\ \kappa_{v2} & \text{otherwise.} \end{cases}$
      ii) Draw $\boldsymbol{p}^{(n,0)} \sim F\left(\boldsymbol{p}^{(n-1,0)}, \kappa_v^{(n)}\right)$.
      iii) Calculate $\nu_T^{(n,0,0)}$ according to (8.14), using $\boldsymbol{p}^{(n,0)}$, $\boldsymbol{s}_\alpha^{(n,0)}$, $\boldsymbol{s}_\beta^{(n,0)}$, and $f_c^{(n)}$.
      iv) Calculate $\nu_T^{(n,1,0)}$ according to (8.14), using $\boldsymbol{p}^{(n,0)}$, $\boldsymbol{s}_\alpha^{(n,1)}$, $\boldsymbol{s}_\beta^{(n,1)}$, and $f_c^{(n)}$.
2. Use Metropolis-Hastings within Gibbs sampling for $g = 1, 2, \ldots, G-1$.
   (a) Update $S^{(g)}$ by:
      i) Set $c_1 = q_S \prod_{n=0}^{N-1} f_F\left(\boldsymbol{a}^{(n)} \mid \boldsymbol{p}^{(n,g-1)}, \kappa_S\right)$.
      ii) Set $c_0 = (1-q_S) \prod_{n=0}^{N-1} f_F\left(\boldsymbol{a}^{(n)} \mid \boldsymbol{p}^{(n,g-1)}, \kappa_{NS}\right)$.
      iii) Draw $u \sim \text{unif}[0,1]$.
      iv) Set $S^{(g)} = \begin{cases} 1 & \text{if } u \le \frac{c_1}{c_1+c_0} \\ 0 & \text{otherwise.} \end{cases}$
   (b) Update $f_{off}^{(g)}$ by:
      i) Set $\mu_{post} = \frac{\sigma_{post}^2}{\sigma_d^2} \sum_{n=0}^{N-1} \left(\zeta^{(n,0)} - \nu_T^{(n,0,g-1)} + \zeta^{(n,1)} - \nu_T^{(n,1,g-1)}\right)$
      ii) Draw $f_{pro}^{(g)} \sim \mathcal{N}\left(f_{off}^{(g-1)}, \sigma_{MH}^2\right)$.
      iii) Set $H = \exp\left(-\frac{\left(f_{pro}^{(g)} - \mu_{post}\right)^2}{2\sigma_{post}^2}\right) \cdot \left(\exp\left(-\frac{\left(f_{off}^{(g-1)} - \mu_{post}\right)^2}{2\sigma_{post}^2}\right)\right)^{-1}$
      iv) Draw $w \sim \text{unif}[0,1]$.
      v) Set $f_{accept}^{(g)} = \min[1, H]$
      vi) Set $f_{off}^{(g)} = \begin{cases} f_{pro}^{(g)} & \text{if } w \le f_{accept}^{(g)} \\ f_{off}^{(g-1)} & \text{otherwise.} \end{cases}$

MWG sampler for two satellite model and f_{off} continued

(c) Update $\boldsymbol{p}^{(n,g)}$ by applying a Metropolis-Hastings step for $n = 0, 1, \ldots, N-1$.

i) Draw $\boldsymbol{p}_{pro}^{(n,g)} \sim F\left(\boldsymbol{p}^{(n,g-1)}, \kappa_{MH}\right)$ as proposal for true vessel position.

ii) Calculate Doppler shift proposal $\nu_{pro}^{(n,0,g)}$ according to (8.14), using $\boldsymbol{p}_{pro}^{(n,g)}$, $\boldsymbol{s}_{\alpha}^{(n,0)}$, $\boldsymbol{s}_{\beta}^{(n,0)}$, and $f_c^{(n)}$.

iii) Calculate Doppler shift proposal $\nu_{pro}^{(n,1,g)}$ according to (8.14), using $\boldsymbol{p}_{pro}^{(n,g)}$, $\boldsymbol{s}_{\alpha}^{(n,1)}$, $\boldsymbol{s}_{\beta}^{(n,1)}$, and $f_c^{(n)}$.

iv) Set $\kappa = \begin{cases} \kappa_S, & \text{if } S^{(g)} = 1 \\ \kappa_{NS}, & \text{otherwise.} \end{cases}$

v) If $n = 0$:

$$H = \frac{f_F\left(\boldsymbol{p}_{pro}^{(0,g)} \,|\, \boldsymbol{s}_{avg}, \kappa_{sat}\right) \cdot f_F\left(\boldsymbol{p}_{pro}^{(0,g)} \,|\, \boldsymbol{a}^{(0)}, \kappa\right) \cdot f_N\left(\zeta^{(0,0)} - f_{off}^{(g)} \,|\, \nu_{pro}^{(0,0,g)}, \sigma_d^2\right) \cdot f_N\left(\zeta^{(0,1)} - f_{off}^{(g)} \,|\, \nu_{pro}^{(0,1,g)}, \sigma_d^2\right)}{f_F\left(\boldsymbol{p}^{(0,g-1)} \,|\, \boldsymbol{s}_{avg}, \kappa_{sat}\right) \cdot f_F\left(\boldsymbol{p}^{(0,g-1)} \,|\, \boldsymbol{a}^{(0)}, \kappa\right) \cdot f_N\left(\zeta^{(0,0)} - f_{off}^{(g)} \,|\, \nu_T^{(0,0,g-1)}, \sigma_d^2\right) \cdot f_N\left(\zeta^{(0,1)} - f_{off}^{(g)} \,|\, \nu_T^{(0,1,g-1)}, \sigma_d^2\right)}$$

vi) Else:

Set $\kappa_v^{(n)} = \begin{cases} \kappa_{v1} & \text{if } T_T^{(n)} - T_T^{(n-1)} < 1.5 \cdot t_r \\ \kappa_{v2} & \text{otherwise.} \end{cases}$

and

$$H = \frac{f_F\left(\boldsymbol{p}_{pro}^{(n,g)} \,|\, \boldsymbol{p}^{(n-1,g)}, \kappa_v^{(n)}\right) \cdot f_F\left(\boldsymbol{p}_{pro}^{(n,g)} \,|\, \boldsymbol{a}^{(n)}, \kappa\right) \cdot f_N\left(\zeta^{(n,0)} - f_{off}^{(g)} \,|\, \nu_{pro}^{(n,0,g)}, \sigma_d^2\right) \cdot f_N\left(\zeta^{(n,1)} - f_{off}^{(g)} \,|\, \nu_{pro}^{(n,1,g)}, \sigma_d^2\right)}{f_F\left(\boldsymbol{p}^{(n,g-1)} \,|\, \boldsymbol{p}^{(n-1,g)}, \kappa_v^{(n)}\right) \cdot f_F\left(\boldsymbol{p}^{(n,g-1)} \,|\, \boldsymbol{a}^{(n)}, \kappa\right) \cdot f_N\left(\zeta^{(n,0)} - f_{off}^{(g)} \,|\, \nu_T^{(n,0,g-1)}, \sigma_d^2\right) \cdot f_N\left(\zeta^{(n,1)} - f_{off}^{(g)} \,|\, \nu_T^{(n,1,g-1)}, \sigma_d^2\right)}$$

vii) Draw $v \sim \text{unif}[0, 1]$.

viii) Set $a_{accept}^{(n,g)} = \min[1, H]$

ix) Set $\boldsymbol{p}^{(n,g)} = \begin{cases} \boldsymbol{p}_{pro}^{(n,g)} & \text{if } v \leq a_{accept}^{(n,g)} \\ \boldsymbol{p}^{(n,g-1)} & \text{otherwise.} \end{cases}$

x) Set $\nu_T^{(n,0,g)} = \begin{cases} \nu_{pro}^{(n,0,g)} & \text{if } v \leq a_{accept}^{(n,g)} \\ \nu_T^{(n,0,g-1)} & \text{otherwise.} \end{cases}$

xi) Set $\nu_T^{(n,1,g)} = \begin{cases} \nu_{pro}^{(n,1,g)} & \text{if } v \leq a_{accept}^{(n,g)} \\ \nu_T^{(n,1,g-1)} & \text{otherwise.} \end{cases}$

Irreducibility and aperiodicity of the sampler in Algorithm 4 can be established using arguments similar to those made in the one satellite case in Section 9.2 in Chapter 9.

Parameter	Value
q_S	0.01
κ_{init}	2437366
κ_{v1}	47017094414
κ_{v2}	11754268483
κ_S	975
κ_{NS}	27081840
κ_{MH}	15233535
κ_{sat}	164
σ_d^2	7.32
σ_{MH}^2	0.01
σ_{off}^2	243^2

Table 13.1: Simulation parameters for the two satellite MWG sampler in which f_{off} is included. The variance parameter σ_{MH}^2 has been varied in the simulations, and the value of σ_{MH}^2 shown in this table is the one that was used in the divergence example presented in this section.

13.2 Metropolis within Gibbs sampler test

Several simulations with runs of the sampler in Algorithm 4 have been carried out in order to test the spoofing detection capabilities of the algorithm. In all simulations, the vessel has not been moving. Except for the introduction of the input parameters σ_{off}^2, σ_{MH}^2, and σ_{post}^2 (which is dependent on σ_d^2 and σ_{off}^2), the input parameters for the simulations have been the same as the ones in Table 11.1 in Chapter 11 with the caveat that κ_{NS} has been arbitrarily chosen such that 95% of the values in the Fisher distribution in which it is used fall within 3 km of its mean direction. Notice that the values of κ_{v1} and κ_{v2} are chosen from Table 9.2 based on a report interval, t_r, of 10 s.

The variance σ_{off}^2 has been chosen such that about 95% of the values drawn from the normal distribution in which it is used fall within two standard deviations from the mean. The standard deviation is chosen such that $\sigma_{off} = 243$, where 243 is approximately half of the maximum value of f_{off}, as evident from (2.1).

The only parameter that has been varied in these simulations is σ_{MH}^2. The simulations show that regardless of the choice of σ_{MH}^2 value, the values of f_{off} diverges when running the sampler in Algorithm 4. Data has been simulated according to the descriptions in Chapter 6, and a value of f_{off} of 100 Hz has been added to the generated Doppler shift data. An example of this divergence is seen in Figure 13.1, in which the algorithm input parameter values in Table 13.1 have been used. In this figure the AIS frequency offset is illustrated as the horizontal green line. The scenario for this example is shown in Figure 13.2, in which $\boldsymbol{p}^{(0)} = \boldsymbol{p}^{(1)} = \ldots = \boldsymbol{p}^{(N-1)}$, i.e. the vessel has not been moving. Moreover, in the example, $N = 26$ AIS messages have been received.

When the value of f_{off} diverges, the simulations show that the resulting samples of the spoofing variable, $S^{(g)}$ for $g = 0, 1, \ldots, G-1$, can not be used to detect position spoofing.

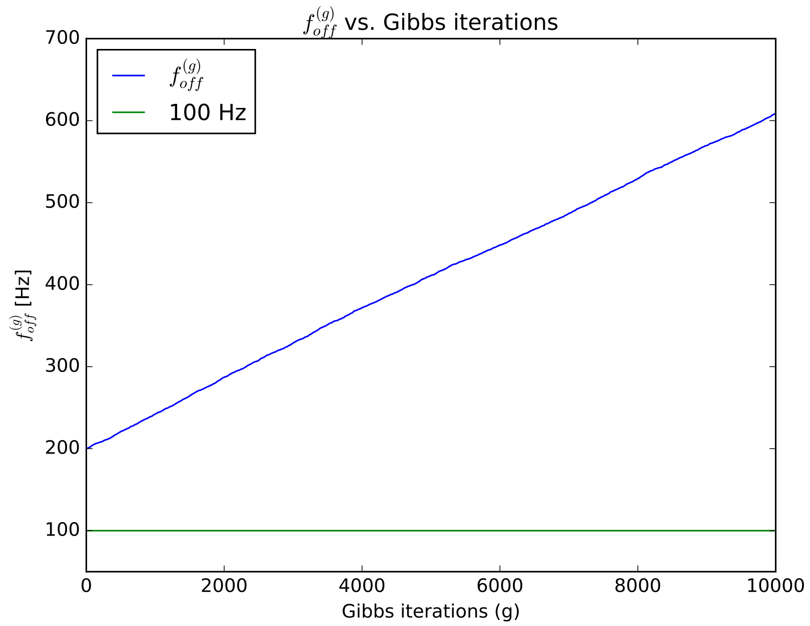

Figure 13.1: Illustration of divergence of f_{off} values when running the sampler in Algorithm 4.

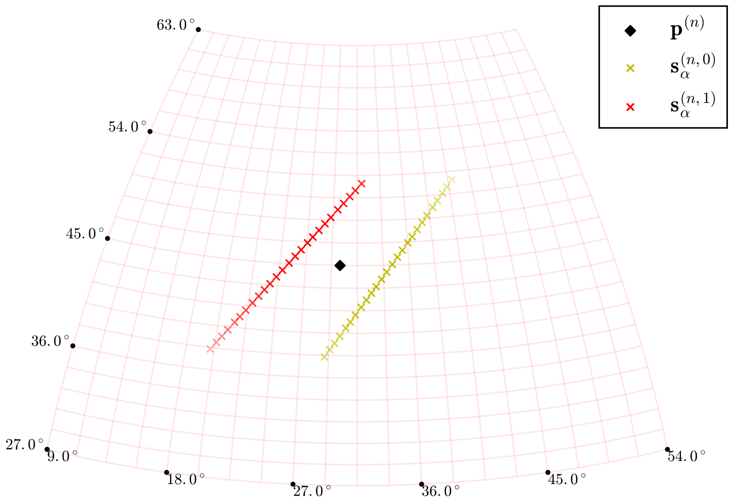

Figure 13.2: The scenario for the simulation example in this section. $N = 26$ AIS messages have been received.

13.3 Alternative AIS frequency offset compensation method

Since including f_{off} in the Bayesian network, and hence in the MWG sampler, made the Gibbs iteration values of f_{off} diverge, a curve fitting method is proposed to obtain an estimate of f_{off}. Having an estimate of f_{off} makes it possible to e.g. subtract this estimate from the carrier frequency offset data.

The method is based on the information about f_{off} that is contained in the Doppler shift curve, i.e. the Doppler shift over a pass. An example of such a curve is seen in Figure 2.7. In this figure, only Doppler shifts are plotted; the figure does not contain f_{off}. If f_{off} is included, it is assumed that f_{off} is a constant addition to the Doppler shifts. The curve generated by the carrier frequency offset corresponds to a Doppler shift curve to which a constant has been added.

Now, the curve to which carrier frequency offset data is proposed to be fitted is a modified version of the sigmoid function

$$y(x) = \frac{1}{1 + e^{-x}}. \tag{13.5}$$

This modified function is

$$\zeta(t) = \frac{c}{1 + \exp(-k(t - t_0))} + y_0, \tag{13.6}$$

in which the parameter c scales the curve vertically, t_0 translates the function in time, k determines the steepness of the curve, and y_0 translates the function values. The reason for choosing a modified version of a sigmoid function is the similarities between the sigmoid function and the Doppler shift curve over a satellite pass.

The sigmoid function in (13.5) has the greatest slope in $t = 0$, and hence when it is translated in time by an amount t_0, as is the case with the modified function in (13.6), it has greatest slope in $t = t_0$.

The Doppler shift curve has greatest (absolute) slope when the Doppler shift is zero. Hence, when a frequency offset f_{off} is added to the curve, the function value in which the curve has greatest slope is approximately equal to f_{off}. This principle is illustrated in Figure 13.3, in which the curve from Figure 2.7 is shown, along with a version of the same curve to which an f_{off} value of 1000 Hz has been added.

Now, this method is tested for carrier frequency offset data simulated from one satellite. This data is generated based on the descriptions in Chapter 6 with a report interval, t_r, of 10 s. Two different passes in which the vessel is not moving are tested. These passes are seen in the Figures 13.4a and 13.5a, and are referred to as pass one and pass two, respectively. Doppler shift data was generated for the two passes, and for both passes a frequency offset, f_{off}, of 200 Hz was added to the Doppler shift data, resulting in the carrier frequency offset data. The curve fitted to the carrier frequency offset data from pass one is seen in Figure 13.4b, and the corresponding curve for pass two is seen in Figure 13.5b. The curve fits have been made using a non-linear least squares method, implemented in the Scipy Python module named ”optimize.curve_fit”. The parameters for the fitted curves are seen in Table 13.2 along with the number, N,

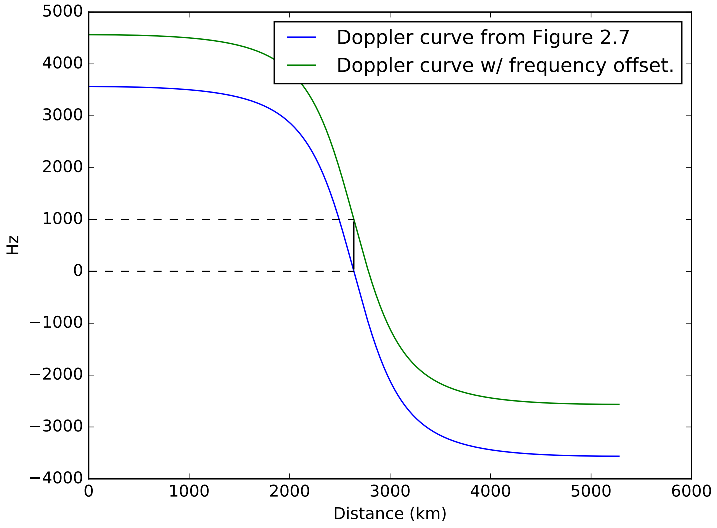

Figure 13.3: Blue curve is Doppler shift curve from Figure 2.7, and green curve is the same curve with an f_{off} value of 1000 Hz added.

Parameter	Pass 1	Pass 2
N	33	14
t_0	769.6	693.1
y_0	3923.7	−3101.2
c	−7444.7	6626.8
k	0.03108	−0.01415
$\hat{f}_{off}$	201.35	212.2

Table 13.2: Parameters for the curves fitted to the carrier frequency offset data for the two satellite passes.

of AIS messages received and the estimate, $\hat{f}_{off}$ of f_{off}. These estimates are obtained by inserting the parameters from the table into 13.6 and evaluating the function in the estimated t_0 value.

Evident from the estimated f_{off} values from this section is the fact that the accuracy of them depends on the pass, i.e. how many AIS messages are received in a pass, and the geometry of the satellite orbit relative to the vessel.

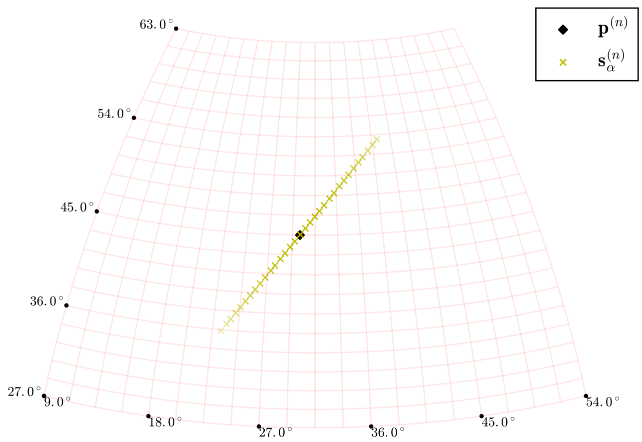

(a)

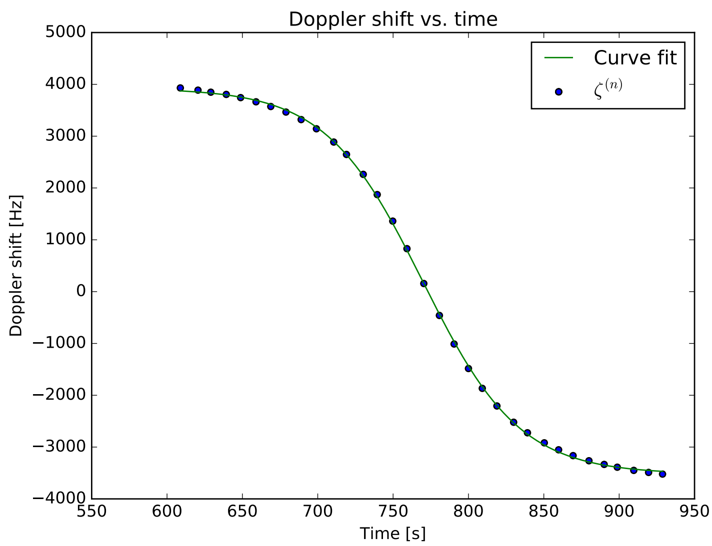

(b)

Figure 13.4: (a): Illustration of pass one. Notice that the satellite points $\boldsymbol{s}_\alpha^{(n)}$ are plotted for $n = 0, 1, \dots, N-1$. **(b)**: Curve fitted to carrier frequency offset data from pass one. Notice that the carrier frequency offset data is plotted for $n = 0, 1, \dots, N-1$.

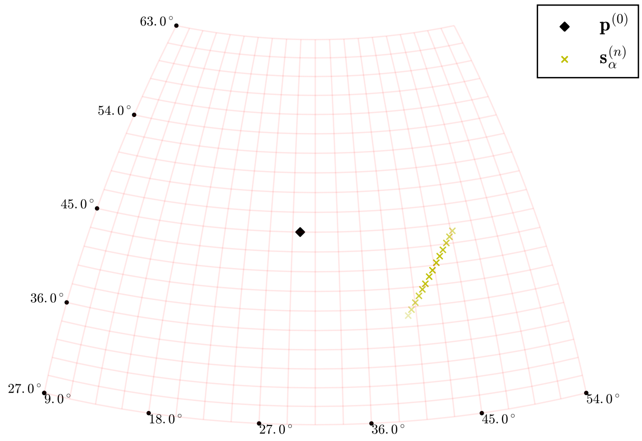

(a)

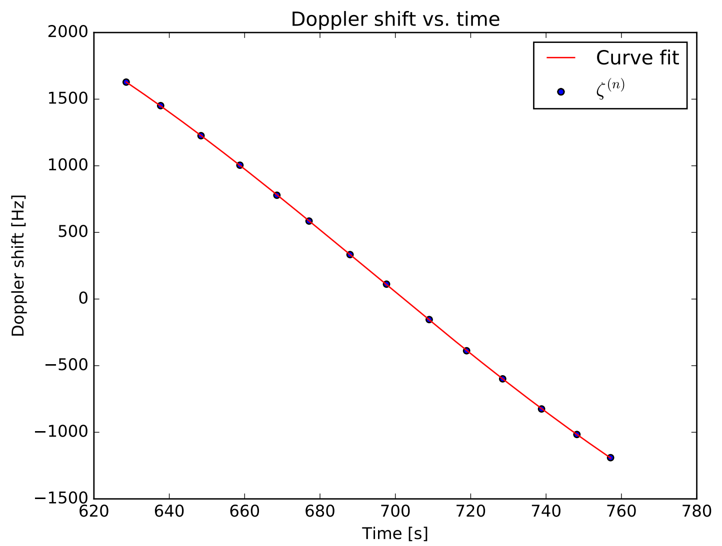

(b)

Figure 13.5: **(a)**: Illustration of pass two. Notice that the satellite points $\boldsymbol{s}_{\alpha}^{(n)}$ are plotted for $n = 0, 1, \ldots, N-1$. **(b)**: Curve fitted to carrier frequency offset data from pass two. Notice that the carrier frequency offset data is plotted for $n = 0, 1, \ldots, N-1$.

14 Complexity analysis and data downlink

14.1 Algorithm complexity analysis

All of the MWG sampler algorithms used in this thesis, i.e. Algorithm 2, 3 and 4, has the same overall structure for G iterations and N AIS messages received by M satellites. The outer loop of the algorithms is over G, and in each iteration of this loop, an inner loop of N iterations is to be run. In each of these iterations, the number of computations scales linearly with M. Hence, the complexity of the algorithm scales linearly in both N, G, and M.

Two runs of Algorithm 3 in which N is different have been carried out to illustrate the running time of the algorithm. The results can be seen in Table 14.1. Both of these were carried out with the algorithm implemented in Python 2.7 on a computer with specifications shown in Table 14.2.

For both all of the algorithm, the output data that needs to be stored from the algorithms is $S^{(g)}$ for $g = 0, 1, \dots, G-1$. In other words, G integers need to be stored.

14.2 Satellite data storage and downlink

The algorithms for spoofing detection are assumed to happen on the ground, i.e. data to be used in the algorithms will have to be downlinked (sent down) to a ground station. Had MWG sampler algorithms for the use of M satellites been developed, the overall amount of data needed to be stored before being downlinked scales with N and M. The m'th satellite would have to store the MMSI number of the vessel in question in order to keep track of which vessel the data has been obtained from. That is, for the n'th AIS

N	66	137
G	25000	25000
Running time	521 s	1098 s

Table 14.1: Running time complexity for two different runs of algorithm 3.

MacBook Pro	
OS	macOS Sierra, v. 10.12.6
Processor	2.4 GHz Intel Core i5
Memory	8 GB 1600 MHz DDR3

Table 14.2: Specifications of computer used to carry out running time simulations.

message it has to store the data in the set

$$\mathcal{D}_{storage} = \left\{ \boldsymbol{a}^{(n)}, \boldsymbol{s}_{\alpha}^{(n,m)}, \boldsymbol{s}_{\beta}^{(n,m)}, \nu^{(n,m)}, f_c^{(n)}, T_T^{(n)}, MMSI \right\}.$$

The quantity $f_c^{(n)}$ can take two values and can thus be represented by an integer in storage. The MMSI number is also an integer. Thus, each satellite has to store three three-dimensional vectors, two integers, and two floating point numbers. For a single satellite, this amount of data scales by the number N of AIS messages received. Each satellite will have to downlink this amount of data.

15 | Conclusion

The way the AIS position spoofing problem has been approached in this thesis has been to construct probability models describing the dependencies between the unobserved and observed variables in the space-based AIS system. In these probability models, statistical inference about whether or not spoofing was occuring in a given scenario was performed. The statistical inference was performed using statistical sampling methods. Specifically, Metropolis within Gibbs samplers have been used.

The spoofing detection results for the case in which a single satellite is used and the vessel is not moving show that the spoofing detection capabilities are largely dependent on the direction in which the vessel is spoofing its position and how far away the vessel is spoofing its position. It was found that when the vessel was spoofing its position in certain directions, spoofing started being detected at spoofing distances of 20 km. In other directions, spoofing was not detected until spoofing distances of 60 km. The case with a single satellite was only tested with a single vessel position, in which the vessel was not moving. Based on the poor spoofing capabilities in the tested scenario, the decision to move on to two satellites was made.

In the case where two satellites were utilized, it was also found that the spoofing detection capabilities depended on the spoofing direction and distance. Different report intervals, i.e. cases in which the vessel was moving, and different spoofing directions were tested in the case of two satellites. For certain spoofing directions, spoofing started being detected at spoofing distances of 5 km for report intervals of 10 and 6 s, and at spoofing distances of 10 km for the report interval of 2 s. In other directions, spoofing detection did not start until spoofing distances of 60 km for the report interval of 6 s, and 50 km for the report interval of 2 s.

The space-based AIS system contains the AIS frequency offset, f_{off}. This frequency offset was included in the last model in this thesis. During the testing of the spoofing detection capabilities when the offset was included, it was found that the way the MWG sampler was constructed made the sampled values of f_{off} diverge, and hence making the algorithm unable to detect spoofing. An alternative method for estimating the value of the frequency offset was proposed instead. This method involved fitting a modified sigmoid curve to the observed carrier frequency offsets. It was found that this method is highly dependent on the number of AIS messages received in the satellite pass. The method was tested in a good and a bad pass, where these refer to passes in which the number of received AIS messages was high and low, respectively. In the test of the good pass, it was found that a good estimate of the AIS frequency offset was obtained, and in the bad pass, a poor estimate of the frequency offset was obtained.

Thus, in summary, based on the observable variables in the space-based AIS system, AIS position spoofing can be detected when a vessel is spoofing its true position a certain distance away. This distance is largely dependent on the given scenario and on whether one or two satellites are utilized.

16 | Discussion

In this thesis, real-world data has not been available. Instead, data has been simulated as if it had been collected by LEO satellites in the space-based AIS system. Testing the developed spoofing detection algorithms with simulated data has both advantages and disadvantages. The advantages are that scenarios to be tested can be easily simulated and things such as noise sources can be easily controlled. Some of the disadvantages are that the simulated data is simulated under certain simplifying assumptions about how real-world data would look like. When real-world data becomes available and the developed algorithms are tested using real-world data, the spoofing detection capabilities of the algorithms may suffer. The reason for this is that most likely, the real-world data will contain noise from sources that have not been accounted for when generating the simulated data. Examples of assumptions that have been made when generating data is that Earth is a perfect sphere and that LEO satellites fly at constant altitudes. In the real-world, Earth is not a perfect sphere, and LEO satellites slowly lose altitude during their life-time. In regards to noise sources, access to information on how errors on the satellite position can be modelled has been limited. In order to test the developed algorithms with simulated data in which the satellite positon errors have been properly modelled, more information about the way the satellite positions are obtained in the real world is needed.

The spoofing detection results for the case in which a single satellite is used show that the spoofing detection capabilities are largely dependent on the direction in which the vessel is spoofing its position and how far away the vessel is spoofing its position. This case was only tested for a single scenario in which the vessel was not moving. If this spoofing detection method is to be implemented in a real-world application in which only a single satellite is available, the spoofing detection capabilities would also have to be tested in the scenario in which the vessel is moving.

In the case of two satellites, the spoofing detection capabilities are also largely dependent on spoofing direction and distance. Moreover, they were also shown to be dependent on the vessel position relative to the satellite orbits. Four different vessel positions were tested. If the method is to be implemented in a real-world application, more scenarios would need to be tested. The tests carried out in this thesis show a proof of concept, but in order to get a clearer picture of the spoofing capabilities of the developed methods, further testing would need to be done. This would include testing e.g. scenarios in which other orbit inclinations and orbit offsets are used. Moreover, the methods would need to be tested using real-world data.

In the cases in which the AIS frequency offset was included, it was found that the way the MWG sampler was constructed made the sampled values of f_{off} diverge. This can be due to a problem with how the probability model for this case is constructed. In the real world, the AIS frequency offset will be present, and for the developed methods to work in the real world, more research into how f_{off} can be compensated for will need to be done. This research could e.g. be to look into whether f_{off} can be estimated from carrier frequency offset data, and then compensated for by subtracting the estimate from the carrier frequency offset data. This approach is pre-processing of the data used for the sampler algorithms. The pre-processed data could then be the input for the sampler algorithms that are built upon the probability models in which f_{off} is not included. Another approach could be to modify and further develop the probability model for this case, construct an MWG sampler, and subsequently test its spoofing capabilities.

When generating carrier frequency offset data in this thesis, vessel movement is taken into account, and this causes a slightly different Doppler shift compared to if the vessel had not been moving. In the probability models developed in this thesis, Doppler shifts have been modelled as if the vessel has been idle, and hence they do not take into account the change in Doppler shift experienced when a vessel is moving. This slight discrepancy between the generation and modelling of this data might have impacted the spoofing detection capabilities. Thus the way carrier frequency offset data is generated and how it is modelled in the probability models is a subject for future work. A possible path of solving this problem could be to incorporate information about the heading and speed of the vessel in the probability model. In a real-world application, this information can be obtained from the received AIS messages, in which the vessel's speed and heading is encoded in addition to the position information.

Only cases in which either one or two satellites have been utilized have been tested. The general probability model developed in this thesis can handle M satellites, and an MWG sampler could be constructed to make inference in a model with M satellites. This means that cases with three or more satellites could be tested, in order to see if utilizing more satellites could improve the spoofing detection capabilities. Moreover, the spoofing detection has only been based on a single satellite pass, and in the cases where two satellites were utilized, only on the AIS messages that both satellites simultaneously received. This means that in cases where two satellites were used, the AIS messages received by the first satellite, but not by the second, have been discarded and vice versa. Methods for utilizing all of the AIS messages received by both satellites could be a subject for future work. In extension of this, spoofing detection methods in which multiple satellite passes are taken into account are also a potential subject for future work.

In terms of inference method choice, statistical sampling was chosen. Another option is utilizing message-passing algorithms in order to perform inference in the probability models. This is also a potential subject for future work.

The last subject for potential future work is that of developing a method to estimate the true position of a vessel in the case in which position spoofing is detected. Potentially, the samples of the true vessel positions from the MWG samplers in this thesis can be used for this purpose.

Bibliography

[1] *SOTDMA*. http://www.allaboutais.com/index.php/en/technical-info/transmission-types/105-ais-technicals/technical-lfundamentals/93-sotdma, 2012. Accessed 26-11-2017.

[2] I. Ali, N. Al-Dhahir, and J. E. Hershey. Doppler characterization for leo satellites. *IEEE Transactions on Communications*, 46(3), 1998.

[3] T. Bajd, M. Mihelj, and M. Munih. *Introduction to robotics*. Springer, 2013.

[4] M. Balduzzi. *AIS exposed. Understanding vulnerabilities and attacks 2.0*. https://www.blackhat.com/docs/asia-14/materials/Balduzzi/Asia-14-Balduzzi-AIS-Exposed-Understanding-Vulnerabilities-And-Attacks.pdf, 2014. Accessed 16-10-2017.

[5] C. M. Bishop. *Pattern Recognition and Machine Learning*. Springer, 2006.

[6] E. Çinlar. *Probability and Stochastics*. Springer, 2010.

[7] P. Ciblat and M. Ghogho. Blind nlls carrier frequency-offset estimation for qam, psk, and pam modulations: Performance at low snr. *IEEE TRANSACTIONS ON COMMUNICATIONS*, 54(10), 2006.

[8] I. R. Cole. *Modelling CPV*. PhD thesis, Loughborough University, 2015. Accessible from https://dspace.lboro.ac.uk/2134/18050. Accessed 29-05-2018.

[9] C. W. Curtis. *Linear algebra: an introductory approach, fourth ed*. Springer, 1984.

[10] N. I. Fisher, T. Lewis, and M. E. Willcox. Tests of discordancy for samples from fisher's distribution on the sphere. *Journal of the Royal Statistical Society. Series C (Applied Statistics)*, 30(3):230–237, 1981.

[11] N. I. Fisher, T. Lewis, and B. J. J. Embleton. *Statistical analysis of spherical data*. Cambridge University Press, 1987.

[12] C. J. Geyer. *Markov chain Monte Carlo lecture notes*. http://www.stat.umn.edu/geyer/f05/8931/n1998.pdf, 2005. Accessed 19-04-2018.

[13] S. Guo. Space-based detection of spoofing ais signals using doppler frequency. *Proc.SPIE*, 9121, 2014.

[14] S. Haykin. *Communication Systems, 4th ed.* John Wiley and Sons, 2001.

[15] R. V. Hogg, J. W. McKean, and A. T. Craig. *Introduction to mathematical statistics, seventh ed.* Pearson, 2012.

[16] IALA. *IALA Guideline No. 1028 On The Automatic Identification (AIS) Vol. 1, Part I (Operational Issues)*. https://www.navcen.uscg.gov/pdf/AIS/IALA_AIS_Guidelines_Vol1_Pt1%20OPS%20(1.3).pdf, 2004. Accessed 21-02-2018.

[17] L. J. Ippolito. *Satellite Communications System Engineering: Atmospheric Effects, Satellite Link Design and System Performance*. Wiley, 2008.

[18] T. Jensen, J. Ledet-Pedersen, and H. P. Mortensen. *Software Defined AIS Receiver for AAUSAT3*. Bachelor's thesis, Aalborg University, 2009.

[19] S. M. Kay. *Intuitive Probability and Random Processes using MATLAB*. Springer, 2006.

[20] D. Koks. *Explorations in Mathematical Physics: The Concepts Behind an Elegant Language*. Springer, 2006.

[21] D. Koller and N. Friedman. *Probabilistic Graphical Models: principles and techniques*. The MIT press, 2009.

[22] T. Koski. *On the Metropolis-Hastings Algorithm on Continuous State Spaces*. https://www.math.kth.se/matstat/gru/sf2955/metropolisB3.pdf, 2009. Accessed 19-01-2018.

[23] U. Madhow. *Fundamentals of Digital Communication*. Cambridge University Press, 2008.

[24] G. Maral and M. Bousquet. *Satellite communications systems: systems, techniques and technology, 5th ed.* Wiley, 2010.

[25] K. V. Mardia and P. E. Jupp. *Directional statistics*. Wiley, 1999.

[26] K. Murota and K. Hirade. Gmsk modulation for digital mobile radio telephony. *IEEE Transactions on Communications*, 29(7):1044–1050, 1981.

[27] J. Møller and K. K. Berthelsen. *A short diversion into the theory of Markov chains, with a view to Markov chain Monte Carlo methods*. http://people.math.aau.dk/~jm/courses/PhD06StocSim/GulrapportRevKKB.pdf, 2004. Accessed 24-04-2018.

[28] T. Pratt, C. W. Bostian, and J. E. Allnutt. *Satellite communications, second ed.* Wiley, 2003.

[29] E. S. Raymond. *AIVDM/AIVDO protocol decoding.* http://catb.org/gpsd/AIVDM.html#_types_1_2_and_3_position_report_class_a, 2017. Accessed 13-09-2017.

[30] C. P. Robert and G. Casella. *Monte carlo Statistical Methods.* Springer, 1999.

[31] M. Series. *Technical characteristics for an automatic identification system using time-division multiple access in the VHF maritime mobile band.* http://www.itu.int/rec/R-REC-M.1371-5-201402-I, 2014. Accessed 01-06-2018.

[32] M. K. Simon. *Bandwidth-Efficient Digital Modulation with Application to Deep-Space Communications.* John Wiley and Sons, Inc., 2001.

[33] J. P. Snyder. *Map Projections - A Working Manual.* Books Express Publishing, 2012.

[34] L. E. Spence, A. J. Insel, and S. H. Friedberg. *Elementary linear algebra: A matrix approach, second ed.* Pearson, 2008.

[35] N. L. Stokey, R. E. Lucas, and E. C. Prescott. *Recursive methods in economic dynamics.* Harvard University Press, 1989.

[36] G. L. Stüber. *Principles of Mobile Communication, 4th ed.* Springer International Publishing AG, 2017.

[37] The Editors of Encyclopaedia Britannica. *Tonnage.* https://www.britannica.com/technology/tonnage, 1998. Accessed 24-04-2018.

[38] W. Tomasi. *Advanced electronic communications systems.* Pearson education limited, 2014.

[39] G. S. Watson. *Statistics on spheres.* Wiley, 1983.

[40] Wikipedia. *Very high frequency.* https://en.wikipedia.org/wiki/Very_high_frequency, 2017. Accessed 16-10-2017.

[41] J. Wramberg and M. Tausen. Soc-based monitoring and analysis of digital radio signals in space. Master thesis, Aalborg University, June 2015.

[42] F. Xiong. *Digital modulation techniques.* Artech House, Inc., 2000.

[43] M. You, S. Lee, and Y. Han. Adaptive compensation method using the prediction algorithm for the doppler frequency shift in the leo mobile satellite communication system. *ETRI Journal*, 22(4), 2000.

[44] M. Zhou, A. J. van der Veen, and R. van Leuken. Multi-user leo-satellite receiver for robust space detection of ais messages. In *2012 IEEE International Conference on Acoustics, Speech and Signal Processing (ICASSP)*, pages 2529–2532, March 2012. doi: 10.1109/ICASSP.2012.6288431.

A | Graph theory, Bayesian networks, and Markov chains

In this chapter, a Bayesian network is formally defined. When doing this, basic graph theory is needed, and is therefore also presented. Succeeding this is an introduction to basic measure theory. This is needed to understand the theory concerning Markov chains with continuous state spaces. The Markov chain theory is introduced to understand the mechanisms underlying Markov chain Monte Carlo (MCMC) methods. These methods are used to make inference in Bayesian networks in this work.

A.1 Graph theory and Bayesian network

A graph $\mathcal{K} = (\mathcal{X}, \mathcal{E})$ is a collection of a set of nodes, $\mathcal{X} = \left\{X^{(0)}, \ldots, X^{(n-1)}\right\}$, and a set of edges, $\mathcal{E}$. The set of edges consists of pairs of either $X^{(i)} \to X^{(j)}$, $X^{(j)} \to X^{(i)}$ or $X^{(i)} - X^{(j)}$, where the notation "$\to$" and "$-$" means a directed and an undirected edge, respectively, for $X^{(i)}, X^{(j)} \in \mathcal{X}$, $i < j$. Moreover, the notation $X^{(i)} \to X^{(j)}$ and $X^{(j)} \leftarrow X^{(i)}$ are equivalent as are $X^{(i)} - X^{(j)}$ and $X^{(j)} - X^{(i)}$ [21, p. 34].

In a directed graph, all the edges are either $X^{(i)} \to X^{(j)}$ or $X^{(j)} \to X^{(i)}$. Given a graph $\mathcal{K}$ where $X^{(i)} \to X^{(j)} \in \mathcal{E}$, $X^{(j)}$ is the child of $X^{(i)}$ and $X^{(i)}$ is the parent of $X^{(j)}$. For an arbitrary node, $X^{(i)}$, $i = 0, 1, \ldots, n-1$, the set of parents of $X^{(i)}$ is denoted $\mathrm{pa}_{X^{(i)}}$. To further develop the graph theory needed to be able to define a Bayesian network, the concept of a graph path is defined.

Definition A.1 (Graph path)
$X^{(0)}, \ldots, X^{(k-1)}$ form a path in the graph, $\mathcal{K}$, if either $X^{(i)} \to X^{(i+1)}$ or $X^{(i)} - X^{(i+1)}$ for every $i = 0, \ldots, k-2$. Moreover, the path is directed if $X^{(i)} \to X^{(i+1)}$ for at least one i [21, p. 36].

Building upon the definition of a path, the descendants and ancestors of a node in the graph are defined.

Definition A.2 (Ancestors and descendants)
In a graph $\mathcal{K} = (\mathcal{X}, \mathcal{E})$, X is an ancestor of Y and Y is a descendant of X if a directed path $X^{(0)}, \ldots, X^{(k-1)}$ with $X^{(0)} = X$ and $X^{(k-1)} = Y$ exists. For a given $X^{(i)} \in \mathcal{X}$, $i = 0, \ldots, n-1$, the notation $D_{X^{(i)}}$ is used for the set of descendants of $X^{(i)}$, $A_{X^{(i)}}$ is used for the set of its ancestors, and $ND_{X^{(i)}}$ is used for the set of its non-descendants, i.e. the set of nodes in $\mathcal{X}$ not in $D_{X^{(i)}}$ [21, p. 36].

Part of the definition of a Bayesian network is that it is a graph in which no cycles exist. It is a so-called directed acyclic graph (DAG). In order to understand this, a graph cycle is defined.

Definition A.3 (Graph cycle)
Given a graph, $\mathcal{K}$, a cycle in the graph is a directed path $X^{(0)}, \ldots, X^{(k-1)}$ in which $X^{(0)} = X^{(k-1)}$. The graph is acyclic if it does not contain cycles [21, p. 37].

In Bayesian networks, a joint probability distribution, f, is graphically represented using a DAG in which the nodes represent the random variables, $\mathcal{X} = \left\{X^{(0)}, \ldots, X^{(n-1)}\right\}$, in the joint probability distribution, and the directed edges represent their mutual dependence relationships.

Definition A.4 (Bayesian network structure)
A DAG, $\mathcal{G}$, with nodes representing random variables $X^{(0)}, \ldots, X^{(n-1)}$ is called a Bayesian network structure. The Bayesian network structure encodes the set of local conditional independence assumptions

$$\mathcal{I}_l(\mathcal{G}) = \left\{\left(X^{(i)} \perp\!\!\!\perp \mathrm{ND}_{X^{(i)}} \,|\, \mathrm{pa}_{X^{(i)}}\right)\right\}_{i=0}^{n-1},$$

where $\perp\!\!\!\perp$ denotes independence between random variables [21, p. 57].

Furthermore, the set of independencies of a distribution, f, is defined.

Definition A.5 (Independecies in joint probability distribution)
For a probability distribution f over $\mathcal{X}$, $\mathcal{I}(f)$ is defined as the set of independencies of the form $(X \perp\!\!\!\perp Y \,|\, Z)$ that hold in f [21, p. 60].

Using Definition A.5, f is said to satisfy the local independencies of $\mathcal{G}$ if $\mathcal{I}_l(\mathcal{G}) \subseteq \mathcal{I}(f)$. If that is the case, $\mathcal{G}$ is said to be an I-map (independency map) for f.

Definition A.6 (Independency map)
Let $\mathcal{K}$ be any graph associated with a set of independencies $\mathcal{I}(\mathcal{K})$. Then $\mathcal{K}$ is said to be an I-map for a set of independencies $\mathcal{I}$ if $\mathcal{I}(\mathcal{K}) \subseteq \mathcal{I}$ [21, p. 60].

As mentioned, a set of conditional independence assumptions are encoded by a Bayesian network structure, $\mathcal{G}$, and thus every joint probability distribution that $\mathcal{G}$ is an I-map for have to satisfy these.

Definition A.7 (Bayesian network structure factorization)
Let $\mathcal{G}$ be a Bayesian network structure over the variables $X^{(0)}, \dots, X^{(n-1)}$. A distribution f over these variables factorizes according to $\mathcal{G}$ if f can be expressed as

$$f(X^{(0)}, \dots, X^{(n-1)}) = \prod_{i=0}^{n-1} f(X^{(i)} \mid \mathrm{pa}_{X^{(i)}}),$$

where the individual factors $f(X^{(i)} \mid \mathrm{pa}_{X^{(i)}})$ are referred to as conditional probability distributions [21, p. 62].

Now, a Bayesian network is defined.

Definition A.8
A pair $\mathcal{B} = (\mathcal{G}, f)$ where f factorizes over $\mathcal{G}$, and where f is specified as a set of conditional probability distributions associated with the nodes of $\mathcal{G}$ is called a Bayesian network [21, p. 62].

A.2 Measure theory

Let C be a set, and let $\mathcal{C}$ be a non-empty collection of subsets of C. If for all $A \in \mathcal{C}$,

$$A \in \mathcal{C} \Rightarrow C \setminus A \in \mathcal{C},$$

and

$$A^{(1)}, A^{(2)}, \dots \in \mathcal{C} \Rightarrow \cup_{n=1}^{\infty} A^{(n)} \in \mathcal{C},$$

that is, if $\mathcal{C}$ is closed under complements and countable unions it is called a σ-algebra on C [6, p. 2]. Every σ-algebra on C contains C and the empty set, $\emptyset$, making $\mathcal{C} = \{\emptyset, C\}$ the simplest σ-algebra on C.

The pair $(C, \mathcal{C})$ is called a measurable space. Given $(C, \mathcal{C})$, each $A \in \mathcal{C}$ is called a measurable set [6, p. 14]. A measure on $(C, \mathcal{C})$ is a mapping $\mu : \mathcal{C} \to [0, \infty]$ with

$$\mu(\emptyset) = 0,$$

and

$$\mu\left(\cup_{n=1}^{\infty} A^{(n)}\right) = \sum_{n=1}^{\infty} \mu\left(A^{(n)}\right), \tag{A.1}$$

where the condition in (A.1) is for every countable collection $\{A_n\}_{n=1}^{\infty}$ of pairwise disjoint sets in $\mathcal{C}$ and is called countable additivity. The number $\mu(A)$ is referred to as the measure of A.

A triple $(C, \mathcal{C}, \mu)$ is called a measure space, in which $(C, \mathcal{C})$ is a measurable space with measure μ. Such a triple is called a probability space if its measure has total measure $\mu(C) = 1$. Such a measure is called a probability measure. A probability space is often denoted as $(\Omega, \mathcal{H}, \mathbb{P})$, where Ω is a set, $\mathcal{H}$ is a σ-algebra on Ω and $\mathbb{P}$ is a probability measure on $(\Omega, \mathcal{H})$ such that $\mathbb{P}(\Omega) = 1$. The set Ω is the collection of possible outcomes of an experiment. A subset H of Ω is said to occur if the experiment outcome belongs to H. The σ-algebra $\mathcal{H}$ is the collection of these subsets, which are referred to as events. The probability that an event H occurs is the number assigned to H by the probability measure, i.e. $\mathbb{P}(H)$ [6, pp. 49-50].

Next, the concept of a measurable function is introduced

Definition A.9 (Measurable function)
Let $(C, \mathcal{C})$ and $(F, \mathcal{F})$ be measurable spaces. A function $f : C \to F$ is measurable if $f^{-1}(B) \in \mathcal{C}$ for every $B \in \mathcal{F}$, where [6, p. 6]

$$f^{-1}(B) = \{x \in C : f(x) \in B\}. \tag{A.2}$$

In other words, Definition A.9 states that $f : C \to F$ is measurable if the pre-image of each measurable set is measurable [35, p. 183].

A.3 Markov chains on continuous state spaces

This section uses the non-boldface, capital letters X and Y to denote random vectors. Realizations of these vectors are denoted by the corresponding lower-case letters, namely x and y. Moreover, superscripts denote elements in a sequence, i.e. $X^{(n)}$ is the n'th random vector in a sequence of random vectors with corresponding realization $x^{(n)}$.

In the theory concerning Markov chains on continuous state spaces, it is natural to start with the definition of a transition kernel. A transition kernel, $K(A \mid x)$, gives the conditional probability of transitioning from $x \in \Omega$ to a set $A \in \sigma(\Omega)$, where $\sigma(\Omega)$ is the σ-algebra of the general state space Ω, which, in this section, is defined as $\Omega \subseteq \mathbb{R}^d$. The transition kernel is denoted $K(x, A)$ from here.

Notice that since $\Omega \subseteq \mathbb{R}^d$ in this thesis, all $A \in \sigma(\Omega)$ are measurable sets. Since this is the case, the short-hand notation $A \subseteq \Omega$ is used to denote a measurable subset of Ω.

MCMC algorithms construct Markov chains with a given target distribution Π as invariant distribution. The conditions under which a Markov chain with a given distribution Π as invariant distribution can be created, and hence how MCMC algorithms can be built, are explored in this section. In the succeeding appendix, namely Appendix B, the MCMC algorithms built based on this theory are introduced.

Unless other citations are mentioned, this appendix is based on [27, pp. 1-12].

Definition A.10 (Transition kernel)
For a state space Ω, a function

$$K(x^{(n)}, A) = P(X^{(n+1)} \in A \mid X^{(n)} = x^{(n)})$$

is a transition kernel if for each $x \in \Omega$, $K(x, \cdot)$ is a probability measure and for each $A \subseteq \Omega$, $K(\cdot, A)$ is a measurable function [22, p. 2]. Furthermore, the n-step transition kernel is defined as

$$K^n(x, A) = P\left(X^{(n)} \in A \mid X^{(0)} = x\right), \qquad A \subseteq \Omega. \tag{A.3}$$

With the definition of the transition kernel, the definition of a Markov chain is given.

Definition A.11 (Markov chain)
A stochastic process $\left(X^{(0)}, X^{(1)}, \dots\right)$ with state space Ω is said to be a Markov chain with transition kernel K if for all integers $n \geq 0$, all subsets $A \subseteq \Omega$, and all $x^{(0)}, \dots, x^{(n)} \in \Omega$,

$$\begin{aligned} P\left(X^{(n+1)} \in A \mid X^{(0)} = x^{(0)}, \dots, X^{(n)} = x^{(n)}\right) &= P\left(X^{(n+1)} \in A \mid X^{(n)} = x^{(n)}\right) \\ &= K\left(x^{(n)}, A\right) \\ &= \int_A K(x^{(n)}, y) dy. \end{aligned}$$

Moreover, the initial distribution of a Markov chain is the distribution of $X^{(0)}$. Knowledge of the initial distribution and the transition kernel completely specifiy a Markov chain.

In Definition A.11, it is evident that given the present, $X^{(n)}$, the future, $X^{(n+1)}$, is independent of the past, $X^{(0)}, \dots, X^{(n-1)}$. This is a property known as the local Markov property.

For $x \in \Omega$ and $A^{(1)}, A^{(2)}, \ldots, A^{(n)} \subseteq \Omega$, iterates of the transition kernel are made as [22, p. 4]

$$P(X^{(1)} \in A^{(1)} \mid X^{(0)} = x) = \int_{A^{(1)}} K(x, y^{(1)}) dy^{(1)} = K(x, A^{(1)})$$

and

$$\begin{aligned} &P((X^{(1)}, X^{(2)}) \in A^{(1)} \times A^{(2)} \mid X^{(0)} = x) \\ &= P(X^{(2)} \in A^{(2)} \mid X^{(1)} \in A^{(1)}) P(X^{(1)} \in A^{(1)} \mid X^{(0)} = x) && \text{(A.4)} \\ &= \int_{A^{(1)}} P(X^{(2)} \in A^{(2)} \mid X^{(1)} = y^{(1)}) K(x, y^{(1)}) dy^{(1)} && \text{(A.5)} \\ &= \int_{A^{(1)}} K(y^{(1)}, A^{(2)}) K(x, y^{(1)}) dy^{(1)}, && \text{(A.6)} \end{aligned}$$

where (A.4) follows from the local Markov property, (A.5) follows from the definition of a (probability) measure from (A.1), and (A.6) follows from the definition of the transition kernel. Moreover, this yields

$$\begin{aligned} &P((X^{(1)}, X^{(2)}, \ldots X^{(n)}) \in A^{(1)} \times \ldots \times A^{(n)} \mid X^{(0)} = x) \\ &= \int_{A^{(1)}} \cdots \int_{A^{(n-1)}} K(x, y^{(1)}) \ldots K(y^{(n-2)}, y^{(n-1)}) K(y^{(n-1)}, A^{(n)}) dy^{(1)} \ldots dy^{(n-1)}. \end{aligned}$$

With $K^1(x, A) = K(x, A)$, the n-step transition kernel in (A.3) can be written as

$$K^n(x, A) = P\left(X^{(n)} \in A \mid X^{(0)} = x\right) = \int_\Omega K^{n-1}(y, A) K(x, y) dy.$$

Now, let π be a density, referred to as the target density, defined on Ω. Wanting to simulate from the target density, the aim is to construct a Markov chain with π as an invariant density. Let

$$\Pi(A) = \int_A \pi(x) dx, \qquad A \subseteq \Omega$$

denote the target distribution.

Definition A.12 (Invariant density)
Let π be a density on Ω. A Markov chain with transition kernel K, is said to have π as its invariant density if for all $A \subseteq \Omega$,

$$\Pi(A) = \int_\Omega \pi(x) K(x, A) dx.$$

In other words, Definition A.12 states that if $X^{(n)} \sim \pi$, then $X^{(n+m)} \sim \pi$ for integers $m \geq 1$, where π is the invariant density of the Markov chain. Moreover, if the initial distribution of a given Markov chain is π, i.e. $X^{(0)} \sim \pi$, the chain is said to be reversible if $\left(X^{(0)}, X^{(1)}\right)$ and $\left(X^{(1)}, X^{(0)}\right)$ are identically distributed. More formally, reversibility is defined as follows.

Definition A.13 (Reversibility)
A transition kernel K is reversible with respect to π if

$$\int_B \pi(x)K(x,A)dx = \int_A \pi(x)K(x,B)dx, \qquad A, B \subseteq \Omega,$$

which is equivalent with stating that if $X^{(0)} \sim \pi$, and

$$P\left(X^{(n)} \in A, X^{(n+1)} \in B\right) = P\left(X^{(n)} \in B, X^{(n+1)} \in A\right)$$

for all $n \geq 0$, the Markov chain is reversible with respect to π [12, p. 46].

If a Markov chain has the reversibility property with respect to π, then π is the invariant density of the chain. MCMC methods, which are used in this thesis, are methods that construct a Markov chain with π, the distribution of interest, as the invariant distribution.

A condition that ensures reversibility of a Markov chain is the detailed balance condition (DBC).

Definition A.14 (Detailed balance condition)
A Markov chain with transition kernel K fulfills the detailed balance condition with respect to π if

$$K(y,x)\pi(y) = K(x,y)\pi(x)$$

for all states $x, y \in \Omega$ [12, p. 8].

The following theorem relates the DBC to reversibility and the invariant density, π.

Theorem A.1 (DBC, reversibility and invariant density)
If a Markov chain with transition kernel K fulfills the DBC with respect to π, then the chain is reversible with π as invariant density [12, pp. 8-9].

Proof. To prove reversibility, Definitions A.13 and A.14 are used, resulting in

$$\begin{aligned}
\int_B \pi(x)K(x,A)dx &= \int_B \pi(x)\int_A K(x,y)dydx \\
&= \int_B\int_A \pi(x)K(x,y)dydx \\
&= \int_B\int_A \pi(y)K(y,x)dydx \\
&= \int_A\int_B \pi(y)K(y,x)dxdy \\
&= \int_A \pi(y)\int_B K(y,x)dxdy \\
&= \int_A \pi(y)K(y,B)dy,
\end{aligned}$$

where the third equality follows from the DBC assumption, and the fourth equality follows from Tonelli's theorem, which can be utilized since the functions to be integrated are non-negative. Hence, the order of integration can be switched. To prove that π is the invariant density, Definition A.12 is used, resulting in

$$\begin{aligned}
\Pi(A) &= \int_\Omega \pi(x)K(x,A)dx \\
&= \int_\Omega \pi(x)\int_A K(x,y)dydx \\
&= \int_\Omega\int_A \pi(x)K(x,y)dydx \\
&= \int_\Omega\int_A \pi(y)K(y,x)dydx \\
&= \int_A\int_\Omega \pi(y)K(y,x)dxdy \\
&= \int_A \pi(y)\int_\Omega K(y,x)dxdy \\
&= \int_A \pi(y)dy,
\end{aligned}$$

where, again, the fourth equality follows from the DBC assumption, the fifth equality follows from Fubini's theorem, and the last equality follows from the fact that

$$\int_\Omega K(y,x)dx = 1. \qquad \square$$

Now, the aim is to construct an algorithm that constructs a Markov chain that has a given, desired density π as invariant density. One such algorithm is the Metropolis-Hastings algorithm, which constructs a Markov chain that fulfills the DBC with respect to π.

In order to introduce this algorithm, what will be referred to as a proposal density is defined. Let $q(x,y)$ be a probability density function on Ω and let

$$Q(x,A) = \int_A q(x,y)dy, \qquad A\subseteq\Omega$$

be a probability measure for any $x \in \Omega$. The probability measure $Q(x, A)$ assigns probabilities to measurable subsets A of Ω. The function $q(x, y)$ is referred to as the proposal density, and $Q(x, A)$ as the proposal distribution. Given $x \in \Omega$, $q(x, y)$ is a conditional density. Moreover, define $a(x, y)$ as an acceptance probability, which, given x is the probability of accepting a proposal y drawn from the proposal distribution $Q(x, y)$.

Using the proposal density and the acceptance probability, a DBC can be set up as

$$\pi(x)a(x, y)q(x, y) = \pi(y)a(y, x)q(y, x), \tag{A.7}$$

for all states $x, y \in \Omega$. If a Markov chain fulfills the DBC, the chain is reversible and has π as its invariant density [30, p. 235]. If $\pi(x)q(x, y) > 0$, then

$$a(x, y) = H(x, y)a(y, x),$$

where

$$H(x, y) = \frac{\pi(y)q(y, x)}{\pi(x)q(x, y)}$$

is known as the Hastings ratio with $H(x, y) = \infty$ for $\pi(x)q(x, y) = 0$. If the acceptance probability is defined as

$$a(x, y) = \min\left\{1, H(x, y)\right\}, \tag{A.8}$$

the DBC in (A.7) is fulfilled with respect to π. This is evident from using (A.7) as

$$\begin{aligned}\pi(x)a(x, y)q(x, y) &= \pi(x)q(x, y)\min\left\{1, \frac{\pi(y)q(y, x)}{\pi(x)q(x, y)}\right\}\\ &= \min\left\{\pi(x)q(x, y), \pi(y)q(y, x)\right\}\end{aligned} \tag{A.9}$$

for the left-hand side, and

$$\begin{aligned}\pi(y)a(y, x)q(y, x) &= \pi(y)q(y, x)\min\left\{1, \frac{\pi(x)q(x, y)}{\pi(y)q(y, x)}\right\}\\ &= \min\left\{\pi(y)q(y, x), \pi(x)q(x, y)\right\}\end{aligned} \tag{A.10}$$

for the right-hand side. It is evident that (A.9) and (A.10) are equal, and hence the DBC is fulfilled with respect to π. The above derivations are the basis for the Metropolis-Hastings algorithm described in Appendix B.

The next question is whether the invariant density, π is unique. If the Markov chain is irreducible, it has a unique invariant density.

Definition A.15 (Irreducibility)
Let Π be the invariant distribution of a Markov chain. This chain is π-irreducible if for all $x \in \Omega$ and $A \subseteq \Omega$ for which $\Pi(A) > 0$, there exists an $n \geq 1$ such that for the n-step transition kernel, $K^n(x, A) > 0$. Moreover, if

$$P(X^{(n)} \in A \text{ for infinitely many } n \mid X^{(0)} = x) = 1,$$

the chain is said to be Harris recurrent.

Definition A.15 indicates that if a chain is π-irreducible, it can reach any region A with $\Pi(A) > 0$ irrespective of the region in which it started, or, in other words, the chain can reach any interesting region in a finite number of steps. Moreover, if the chain is Harris recurrent, the chain visits all subsets $A \subseteq \Omega$, for which $\Pi(A) > 0$, an infinite number of times.

In MCMC methods, inference about expectations are often of interest. Consider the empirical average

$$\hat{\theta}_n = \frac{1}{n+1} \sum_{i=m}^{m+n} h\left(X^{(i)}\right), \tag{A.11}$$

where $m \geq 0$ and $h : \Omega \to \mathbb{R}$ is a function such that the mean $\theta = \int_\Omega h(x)\pi(x)dx$ exists. When a Markov chain statisfies certain conditions, the estimator, $\hat{\theta}_n$, in (A.11) is consistent by the strong law of large numbers for Markov chains.

Theorem A.2 (Strong law of large numbers for Markov chains)
Let $\left(X^{(0)}, X^{(1)}, \ldots\right)$ be a π-irreducible Markov chain with invariant density π. Then there exists a set $C \subseteq \Omega$ such that $\Pi(C) = 1$ and for all $x \in C$,

$$P\left(\hat{\theta}_n \to \theta \,\text{as}\, n \to \infty \mid X^{(0)} = x\right) = 1.$$

If the chain is Harris recurrent, then a choice of C is $C = \Omega$.

Theorem A.2 implies consistency of the estimator in (A.11) if $x \in C$ and the chain is π-irreducible, and $x \in \Omega$ if the chain is Harris recurrent. Intuitively, Harris recurrence is when the chain visits every state in Ω an infinite number of times in the limit as $n \to \infty$. The integer, m, in (A.11) is referred to as the burn-in. This is a time in which the Markov chain is considered to have approximately reached its invariant distribution. That the Markov chain even converges towards a limiting distribution is the next question. In order to answer this, the definition of periodicity of a Markov chain is needed.

Definition A.16 (Periodicity)
A π-irreducible Markov chain is said to be periodic if there exists a disjoint union $\Omega = \cup_{i=0}^{n} A^{(i)}$ for $n > 1$ such that $\Pi(A^{(n)}) = 0$ and

$$\begin{aligned} x \in A^{(0)} &\Rightarrow K(x, A^{(1)}) = 1 \\ x \in A^{(1)} &\Rightarrow K(x, A^{(2)}) = 1 \\ &\vdots \\ x \in A^{(n-1)} &\Rightarrow K(x, A^{(0)}) = 1. \end{aligned}$$

Otherwise, the chain is said to be aperiodic.

Any π-irreducible Markov chain that allows the event $X^{(n)} = X^{(n+1)}$ when $X^{(n)} \sim \pi$ is aperiodic.

Now, the limiting distribution of a Markov chain statisfying certain conditions can be shown to be the invariant distribution of the chain.

Theorem A.3 (The Markov chain convergence theorem)
For a π-irreducible and aperiodic Markov chain with invariant distribution Π, there exists a set $C \subseteq \Omega$ such that $\Pi(C) = 1$ and for all $x \in C$ and $A \subseteq \Omega$, the n-step transition kernel converges towards Π, i.e.

$$K^n(x, A) \to \Pi(A) \qquad \text{as } n \to \infty.$$

Furthermore, if the chain is Harris recurrent, a choice of C is $C = \Omega$.

In the succeeding appendix, algorithms that construct Markov chains that fulfill Theorem A.3 are described.

B Markov chain Monte Carlo algorithms

In the theory concerning Markov chain Monte Carlo (MCMC) methods, the aim is to construct a Markov chain with a desired distribution, Π, as its invariant distribution. If the chain converges towards this desired distribution, samples from the chain can be considered samples from the invariant distribution. If the invariant distribution is known (up to proportionality), but intractable, sampling from it is hard. When this is the case, Markov chain Monte Carlo methods can be used to draw samples from the distribution. In these methods, a requirement is the ability to evaluate the intractable distribution. Initially, this appendix introduces the Metopolis-Hastings (MH) algorithm, followed by the Gibbs sampler, and, eventually, the Metropolis within Gibbs (MWG) sampler, which is the sampler used in this thesis. The MH algorithm is introduced in order to eventually understand the MWG sampler, which is a Gibbs sampler that incorporates the MH sampler.

Unless other citations are mentioned, this appendix is based on [27, pp. 10-16 and pp. 20-21].

B.1 Metropolis-Hastings algorithm

The first algorithm introduced is the Metropolis-Hastings algorithm. In order to understand this algorithm and its components, Section A.3 in Appendix A is a prerequisite.

Algorithm 5 Metropolis-Hastings algorithm

Let the initial state $x^{(0)} \in \Omega \subseteq \mathbb{R}^d$ be such that $\pi(x^{(0)}) > 0$. For $n = 0, 1, \ldots$, given $x^{(n)}$, then

1. Generate a proposal $y^{(n+1)}$ from $q(x^{(n)}, y)$, and $u^{(n+1)} \sim \text{unif}[0, 1]$.
2. Set
$$x^{(n+1)} = \begin{cases} y^{(n+1)} & \text{if } u^{(n+1)} \leq H(x^{(n)}, y^{(n+1)}) \\ x^{(n)} & \text{otherwise.} \end{cases}$$

Notice that given $x^{(n)}$, $y^{(n+1)}$ is independent of everything else in the Metropolis-Hastings algorithm, and that the target density π only occurs within the Hastings ratio in the ratio $\frac{\pi(y^{(n+1)})}{\pi(x^{(n)})}$. Hence it is only necessary to know the target density up to proportionality, since the normalizing constants cancel out in this ratio. This means that when specifying the target density, it is sufficient to do so only up to proportionality. Finally, note that the Metropolis-Hastings algorithm is reversible with invariant density π, since, by construction, the resulting Markov chain fulfills the DBC, as shown in Appendix A. Moreover, it can be shown that if

$$q(x, y) > 0 \qquad \text{for all } x, y \in \Omega,$$

the Markov chain created by the Metropolis-Hastings sampler is π-irreducible and Harris recurrent. Finally, if this Markov chain is to be aperiodic, the event $X^{(n)} = X^{(n+1)}$ has to be possible, which in the Metropolis-Hastings sampler means that

$$\int_\Omega \int_\Omega \mathbb{1}[\pi(y)q(y, x) < \pi(x)q(x, y)]q(x, y)\pi(x)dydx > 0,$$

in which $\mathbb{1}[\cdot]$ is the indicator function. If the above conditions are met, the Metropolis-Hastings algorithm statisfies Theorem A.3.

B.2 Gibbs sampler

This section uses non-boldface, upper-case letter notation to denote a random vector, i.e. X is a random vector, and lower-case non-boldface letters to denote a realization of this random vector, i.e. x in this case. Moreover, boldface upper-case letters denote vectors of random vectors, e.g.

$$\boldsymbol{X} = \left[\left(X^{(0)}\right)^\top \left(X^{(1)}\right)^\top \ldots \left(X^{(k-1)}\right)^\top \right]^\top,$$

which is not to be confused with the notation used for matrices elsewhere in this thesis. Furthermore, boldface lower-case letters denote the vector of realizations of the random vectors, i.e.

$$\boldsymbol{x} = \left[\left(x^{(0)}\right)^\top \left(x^{(1)}\right)^\top \ldots \left(x^{(k-1)}\right)^\top \right]^\top.$$

The above notation holds true in the succeeding section, namely Section B.3, as well.

In the Gibbs sampler, the state space, $\Omega \subseteq \mathbb{R}^d$, is a product space, i.e.

$$\Omega = \Omega^{(0)} \times \Omega^{(1)} \times \ldots \times \Omega^{(k-1)}, \tag{B.1}$$

where $\Omega^{(0)} \subseteq \mathbb{R}^{d^{(0)}}, \Omega^{(1)} \subseteq \mathbb{R}^{d^{(1)}}, \ldots, \Omega^{(k-1)} \subseteq \mathbb{R}^{d^{(k-1)}}$, and $d^{(0)} + d^{(1)} + \ldots + d^{(k-1)} = d$. Let $\boldsymbol{X}$ be the random vector

$$\boldsymbol{X} = \left[\left(X^{(0)}\right)^\top \left(X^{(1)}\right)^\top \ldots \left(X^{(k-1)}\right)^\top \right]^\top \tag{B.2}$$

with state space Ω, following the density, π, where $X^{(i)}$ is the projection of $\boldsymbol{x}$ on $\Omega^{(i)}$, $i = 0, 1, \ldots, k-1$. Moreover, let $\boldsymbol{X}_{-i}$ denote the vector

$$\boldsymbol{X}_{-i} = \left[\left(X^{(0)}\right)^\top \left(X^{(1)}\right)^\top \ldots \left(X^{(i-1)}\right)^\top \left(X^{(i+1)}\right)^\top \ldots \left(X^{(k-1)}\right)^\top \right]^\top$$

that is, the vector of random vectors not containing the i'th random vector, with state space

$$\Omega_{-i} = \Omega^{(0)} \times \Omega^{(1)} \times \ldots \times \Omega^{(i-1)} \times \Omega^{(i+1)} \times \ldots \times \Omega^{(k-1)}.$$

The Gibbs sampler works by simulating a single random variable, $X^{(i)}$ given $\boldsymbol{X}_{-i}$. This can be achieved through various updating schemes. The updating scheme used in this thesis will be introduced later in this section.

The assumption that

$$\pi(\boldsymbol{x}) > 0 \qquad \text{for all } \boldsymbol{x} \in \Omega \tag{B.3}$$

is made.

Now, the density of $\boldsymbol{X}_{-i}$ is

$$\pi_{-i}(\boldsymbol{x}_{-i}) = \int_{\Omega_{-i}} \pi(x^{(0)}, \ldots, x^{(i-1)}, y^{(i)}, x^{(i+1)}, \ldots, x^{(k-1)}) dy^{(i)}, \qquad x_{-i} \in \Omega_{-i},$$

and the conditional density of $X^{(i)}$ given $\boldsymbol{x}_{-i}$ is

$$\pi^{(i)}(x^{(i)} \mid \boldsymbol{x}_{-i}) = \frac{\pi(x)}{\pi_{-i}(\boldsymbol{x}_{-i})}, \qquad x^{(i)} \in \Omega^{(i)}.$$

Let $K^{(i)}(\cdot \mid x_{-i})$ denote the conditional distribution of $X^{(i)}$ given $\boldsymbol{x}_{-i}$, i.e. for $A \subseteq \Omega^{(i)}$,

$$K^{(i)}(A \mid \boldsymbol{x}_{-i}) = P(X^{(i)} \in A \mid \boldsymbol{x}_{-i}) = \int_A \pi^{(i)}(x^{(i)} \mid \boldsymbol{x}_{-i}) dx^{(i)}. \tag{B.4}$$

In (B.4), the densities $\pi^{(i)}(x^{(i)} \mid \boldsymbol{x}_{-i})$ are referred to as the full conditionals. These are the only densities used for simulation when using the Gibbs sampler. Since a Bayesian network is specified in terms of a collection of conditional distributions, the Gibbs sampler is well suited for inference in Bayesian networks.

As mentioned ealier, the Gibbs sampler can be used with different updating schemes. In this thesis, a so-called cyclic updating scheme is used. Let

$$\boldsymbol{X}^{(n)} = \left[\left(X^{(0,n)}\right)^\top \left(X^{(1,n)}\right)^\top \ldots \left(X^{(k-1,n)}\right)^\top \right]^\top, \qquad n = 0, 1, \ldots, \tag{B.5}$$

be the n'th element of the Markov chain in Gibbs sampling. Given $\boldsymbol{X}^{(n)}$, a cyclic updating scheme in the Gibbs sampler generates the next element, $\boldsymbol{X}^{(n+1)}$ by updating the variables $X^{(0,n+1)}, X^{(1,n+1)}, \ldots, X^{(k-1,n+1)}$ according to

$$\begin{aligned}
X^{(0,n+1)} &\sim K^{(0)}\left(\cdot \mid X^{(1,n)}, \ldots, X^{(k-1,n)}\right) \\
X^{(1,n+1)} &\sim K^{(1)}\left(\cdot \mid X^{(0,n+1)}, X^{(2,n)}, \ldots, X^{(k-1,n)}\right) \\
&\vdots \\
X^{(k-1,n+1)} &\sim K^{(k-1)}\left(\cdot \mid X^{(0,n+1)}, X^{(1,n+1)}, \ldots, X^{(k-2,n+1)}\right).
\end{aligned}$$

The Markov chain

$$\left(X^{(0,0)}, X^{(1,0)}, \ldots, X^{(k-1,0)}, X^{(0,1)}, X^{(1,1)}, \ldots, X^{(k-1,1)}, \ldots\right),$$

which is created in the cyclic Gibbs sampler described above is of order $k-1$. Since

$$\begin{aligned} &X^{(i,n+1)} \mid \left(X^{(0,0)}, X^{(1,0)}, \ldots, X^{(i-1,n+1)}\right) \\ &\sim K^{(i)}\left(\cdot \mid X^{(0,n+1)}, \ldots X^{(i-1,n+1)}, X^{(i+1,n)}, \ldots, X^{(k-1,n)}\right), \end{aligned}$$

the order of the Markov chain follows since $X^{(i,n+1)}$ and $\left(X^{(0,0)}, X^{(1,0)}, \ldots, X^{(i-1,n)}\right)$ are independent given $\left(X^{(i+1,n)}, \ldots, X^{(k-1,n)}, X^{(0,n+1)}, \ldots, X^{(i-1,n+1)}\right)$. From this, it follows that

$$\left(\boldsymbol{X}^{(0)}, \boldsymbol{X}^{(1)}, \ldots\right)$$

is a Markov chain.

Using the cyclic updating scheme does not ensure reversibility of the resulting Markov chain. But each variable updating step in the cyclic Gibbs sampler fulfills the DBC. This is due to the fact that for any $x \in \Omega$ and $y^{(i)} \in \Omega^{(i)}$,

$$\pi(x)\pi^{(i)}(y^{(i)} \mid \boldsymbol{x}_{-i}) = \pi(x)\frac{\pi(y)}{\pi_{-i}(\boldsymbol{x}_{-i})} = \pi(y)\pi^{(i)}(x^{(i)} \mid \boldsymbol{x}_{-i}), \tag{B.6}$$

where $y = (x^{(0)}, \ldots, x^{(i-1)}, y^{(i)}, x^{(i+1)}, \ldots, x^{(k-1)})$. In (B.6), Definition A.14 has been utilized with $\pi^{(i)}(y^{(i)} \mid \boldsymbol{x}_{-i})$ as the transition kernel for the update of the i'th variable in the Gibbs sampler. Since each of these updating steps fulfills the DBC, it can be shown that the Markov chain in (B.5) has π as invariant density. Moreover, it can be shown that the assumption in (B.3) implies that the cyclic Gibbs sampler is π-irreducible, Harris recurrent, and aperiodic, and hence it fulfills theorem A.3.

B.3 Metropolis within Gibbs sampler

The last sampler in this chapter is the Metropolis within Gibbs sampler (MWG). The Gibbs sampler itself works when all of the full conditionals of the model are specified and easy to sample from. In some cases, one or more of the full conditionals may be hard to draw samples from. The MWG sampler overcomes this problem. This sampler works by updating the variables whose full conditional can be easily sampled using an ordinary Gibbs updating step, and updates the variables whose full conditional are hard to sample from by employing a Metropolis-Hastings update of these variables. Like in the Gibbs sampler, the MWG sampler works with the state space as a product space as in (B.1), with $\boldsymbol{X}$ a vector of random vectors as in (B.2), and $\boldsymbol{x}$ a realization of $\boldsymbol{X}$.

Consider $x^{(i)}$ the current value of the variable $X^{(i)}$, which has full conditional that is inconvenient to sample from. Instead, a Metropolis-Hastings update is employed. Let

$$q^{(i)}\left(y^{(i)} \mid \left(x^{(0)},\, \ldots,\, x^{(i-1)},\, x^{(i)},\, x^{(i+i)},\, \ldots,\, x^{(k-1)}\right)\right)$$

be a proposal density, where $y^{(i)}$ is a proposal for an update of $x^{(i)}$. Moreover, define the Hastings ratio as

$$H^{(i)}\left(x^{(i)}, y^{(i)} \mid \boldsymbol{x}_{-i}\right) = \frac{\pi^{(i)}\left(y^{(i)} \mid \boldsymbol{x}_{-i}\right) q^{(i)}\left(x^{(i)} \mid \left(x^{(1)}, \ldots, x^{(i-1)}, y^{(i)}, x^{(i+1)}, \ldots, x^{(k-1)}\right)\right)}{\pi^{(i)}\left(x^{(i)} \mid \boldsymbol{x}_{-i}\right) q^{(i)}\left(y^{(i)} \mid \left(x^{(1)}, \ldots, x^{(i-1)}, x^{(i)}, x^{(i+1)}, \ldots, x^{(k-1)}\right)\right)},$$

from which the acceptance probability is defined as

$$a^{(i)}(x, y^{(i)}) = \min\left\{1, H^{(i)}\left(x^{(i)}, y^{(i)} \mid \boldsymbol{x}_{-i}\right)\right\}.$$

If the proposal $y^{(i)}$ is rejected, $x^{(i)}$ is retained. Using the MWG sampler with a cyclic updating scheme as the one described in the Gibbs sampler in Section B.2 ensures that π is the invariant density of the resulting Markov chain. This follows from arguments similar to those made in (B.6). Unlike the Metropolis-Hastings and Gibbs samplers, the properties irreducibility and aperiodicity needed to fulfill Theorem A.3 need to be checked for a particular MWG sampler.

The MWG samplers used in this thesis are presented in the Chapters 9, 11, and 13. In Section 9.2 in Chapter 9, irreducibility and aperiodicity of the sampler for the single satellite case are established. Arguments similar to those presented in Section 9.2 can be made to establish irreducibility and aperiodicity for the remaining samplers used in this thesis.

C | Variable transformation method

This appendix is based on [15, pp. 86-87, 126-127]. When transforming the variables in a joint pdf, consisting of N variables, the variable transformation method is used. In this appendix, the case of continuous variables is considered. Notice that in this appendix, random variables are denoted by an upper-case letter, and a realization of such a variable is denoted by the corresponding lower-case letter.

Let $\left(X^{(0)}, X^{(1)}, \ldots, X^{(N-1)}\right)$ be a collection of random variables with a jointly continuous distribution and pdf $f_X\left(x^{(0)}, x^{(1)}, \ldots, x^{(N-1)}\right)$ with support $\mathcal{X} \subseteq \mathbb{R}^N$. Moreover, define the random variables $\left(Y^{(0)}, Y^{(1)}, \ldots, Y^{(N-1)}\right)$ as

$$Y^{(i)} = g^{(i)}\left(X^{(0)}, X^{(1)}, \ldots, X^{(N-1)}\right), \qquad i = 0, 1, \ldots, N-1,$$

where the functions

$$y^{(i)} = g^{(i)}\left(x^{(0)}, x^{(1)}, \ldots, x^{(N-1)}\right), \qquad i = 0, 1, \ldots, N-1, \tag{C.1}$$

define a one-to-one transformation from $\mathcal{X}$ to $\mathcal{Y}$, where $\mathcal{Y} \subseteq \mathbb{R}^N$ is the support of $\left(Y^{(0)}, Y^{(1)}, \ldots, Y^{(N-1)}\right)$. From here, let

$$\begin{aligned}
x &= \left(x^{(0)}, x^{(1)}, \ldots, x^{(N-1)}\right), \\
X &= \left(X^{(0)}, X^{(1)}, \ldots, X^{(N-1)}\right), \\
y &= \left(y^{(0)}, y^{(1)}, \ldots, y^{(N-1)}\right),
\end{aligned}$$

and

$$Y = \left(Y^{(0)}, Y^{(1)}, \ldots, Y^{(N-1)}\right).$$

Expressing $x^{(0)}, x^{(1)}, \ldots, x^{(N-1)}$ in terms of the transformed variables as

$$x^{(i)} = q^{(i)}\left(y\right), \qquad i = 0, 1, \ldots, N-1,$$

which are the inverse functions of those in (C.1). The inverse transformation yields the Jacobian determinant

$$\det(\boldsymbol{J}) = \det\left(\begin{bmatrix} \frac{\partial x^{(0)}}{\partial y^{(0)}} & \frac{\partial x^{(0)}}{\partial y^{(1)}} & \cdots & \frac{\partial x^{(0)}}{\partial y^{(N-1)}} \\ \frac{\partial x^{(1)}}{\partial y^{(0)}} & \frac{\partial x^{(1)}}{\partial y^{(1)}} & \cdots & \frac{\partial x^{(1)}}{\partial y^{(N-1)}} \\ \vdots & \vdots & \ddots & \vdots \\ \frac{\partial x^{(N-1)}}{\partial y^{(0)}} & \frac{\partial x^{(N-1)}}{\partial y^{(1)}} & \cdots & \frac{\partial x^{(N-1)}}{\partial y^{(N-1)}} \end{bmatrix}\right),$$

in which the assumption is that the partial derivatives are continuous and that the Jacobian determinant is not equal to zero within the set $\mathcal{Y}$.

Now, the aim is to find the pdf of the transformed variables, namely $f_Y(y)$. Let $A \subseteq \mathcal{X}$ and let $B \subseteq \mathcal{Y}$ denote the one-to-one transformation of the subset A. Then

$$\begin{aligned} p(Y \in B) &= p(X \in A) \\ &= \int \cdots \int_A f_X(x)\, dx^{(0)} dx^{(1)} \ldots dx^{(N-1)}. \end{aligned} \tag{C.2}$$

The first equality in (C.2) follows from the fact that the events are equally likely, since the transformation is one-to-one. Now, using a result from real analysis concerning the change of variables in integrals, (C.2) can be rewritten as

$$p(Y \in B) = \int \cdots \int_B f_X\left(q^{(0)}(y), q^{(1)}(y), \ldots, q^{(N-1)}(y)\right) \det(\boldsymbol{J}) dy^{(0)} dy^{(1)} \ldots dy^{(N-1)},$$

which implies that the pdf of the transformed variables is

$$f_Y(y) = f_X\left(q^{(0)}(y), q^{(1)}(y), \ldots, q^{(N-1)}(y)\right) \det(\boldsymbol{J})$$

when $y \in \mathcal{Y}$ and zero otherwise.

D Fisher and three-dimensional normal distribution

The Fisher distribution is related to the three-dimensional normal distribution. To see this, consider the random vector $\boldsymbol{x} \sim \mathcal{N}_3(\boldsymbol{\mu}, \kappa^{-1}\boldsymbol{I}_3)$ with mean value $\boldsymbol{\mu} \in \mathbb{S}^2$, $\kappa > 0$, and pdf

$$f_N(\boldsymbol{x} \mid \boldsymbol{\mu}, \kappa^{-1}\boldsymbol{I}_3) = \frac{1}{(2\pi)^{\frac{3}{2}}} \exp\left(-\frac{\kappa}{2}\left\|\boldsymbol{x} - \boldsymbol{\mu}\right\|^2\right). \tag{D.1}$$

The norm in (D.1) can be rewritten as

$$\begin{aligned} \left\|\boldsymbol{x} - \boldsymbol{\mu}\right\|^2 &= \left\|\boldsymbol{x}\right\|^2 + \left\|\boldsymbol{\mu}\right\|^2 - 2\boldsymbol{x}^\top\boldsymbol{\mu} \\ &= \left\|\boldsymbol{x}\right\|^2 + \left\|\boldsymbol{\mu}\right\|^2 - 2\left\|\boldsymbol{x}\right\|\boldsymbol{y}^\top\boldsymbol{\mu}, \end{aligned} \tag{D.2}$$

where $\boldsymbol{y} = \frac{\boldsymbol{x}}{\|\boldsymbol{x}\|}$. Rewriting (D.1) into spherical coordinates using the variable transformation method from Appendix C and the Jacobian determinant from (F.4), and inserting (D.2), yields

$$f_N((\theta, \phi), r \mid (\alpha, \beta), \kappa^{-1}\boldsymbol{I}_3) = \frac{r^2 \sin(\theta)}{(2\pi)^{\frac{3}{2}}} \exp\left(-\frac{\kappa}{2}(r^2 + \left\|\boldsymbol{\mu}(\alpha, \beta)\right\|^2 - 2r\boldsymbol{y}(\theta, \phi)^\top\boldsymbol{\mu}(\alpha, \beta))\right), \tag{D.3}$$

where $r = \|\boldsymbol{x}\|$,

$$\boldsymbol{y}(\theta, \phi) = \begin{bmatrix}\sin(\theta)\cos(\phi) & \sin(\theta)\sin(\phi) & \cos(\theta)\end{bmatrix}^\top,$$

and

$$\boldsymbol{\mu}(\alpha, \beta) = \begin{bmatrix}\sin(\alpha)\cos(\beta) & \sin(\alpha)\sin(\beta) & \cos(\alpha)\end{bmatrix}^\top,$$

where (α, β) are the spherical coordinates of the mean value. Conditioning (D.3) on the radius r results in

$$\begin{aligned} f_N((\theta, \phi) \mid (\alpha, \beta), \kappa^{-1}\boldsymbol{I}_3, r) &= \frac{f_N(r, (\theta, \phi) \mid (\alpha, \beta), \kappa^{-1}\boldsymbol{I}_3)}{h(r)} \\ &\propto f_N(r, (\theta, \phi) \mid (\alpha, \beta), \kappa^{-1}\boldsymbol{I}_3) \\ &\propto \sin(\theta)\exp(\kappa r\boldsymbol{y}(\theta, \phi)^\top\boldsymbol{\mu}(\alpha, \beta)), \end{aligned}$$

where $h(r)$ is the marginal density of r, which is constant when r is conditioned on. In conclusion, when conditioned on r, the density in (D.3) is proportional to a Fisher density.

E | Von Mises distribution

An often utilized probability distribution when making statistical inference on the circle is the von Mises distribution. The density for a von Mises distributed random variable $\theta \in [0, 2\pi)$ is given by

$$f_{VM}(\theta \mid \mu, \kappa) = \frac{1}{2\pi I_0(\kappa)} \cdot e^{\kappa \cos(\theta - \mu)}, \tag{E.1}$$

where

$$I_0(\kappa) = \frac{1}{2\pi} \int_0^{2\pi} e^{\kappa \cos(\theta)} d\theta$$

is the modified Bessel function of the first kind and order 0 [25, p. 36]. In (E.1), $\mu \in [0, 2\pi)$ is the mean, and $\kappa \geq 0$ is a concentration parameter. When a random variable is von Mises distributed, this is denoted $\theta \sim \mathrm{VM}(\mu, \kappa)$ in this thesis.

The von Mises distribution is unimodal and symmetric about its mean value. Notice that in the special case when $\kappa = 0$, the distribution reduces to the uniform distribution on the circle. For increasing κ-values, the probability mass of the distribution becomes more and more concentrated about its mode. An illustration of the von Mises distribution for a selection of different κ-values can be seen in Figure E.1.

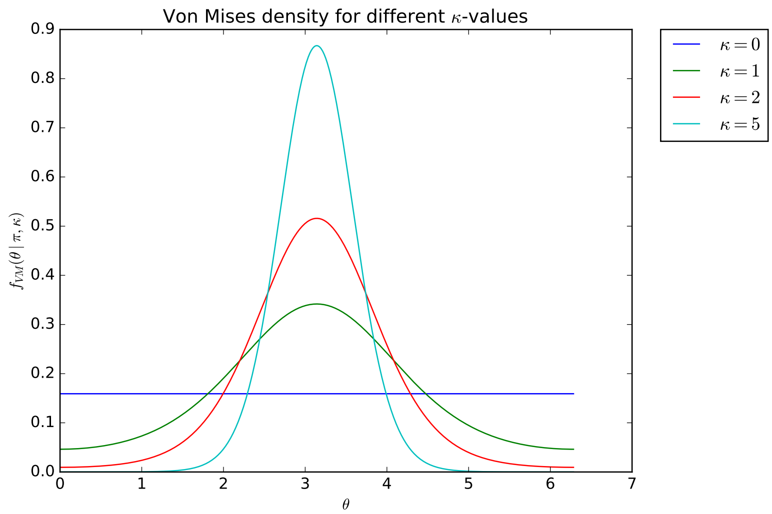

Figure E.1: The von Mises distribution for different κ-values and $\mu = \pi$.

F Spherical coordinates, rotation matrices, and Rodrigues' formula

F.1 Spherical coordinates

This section is based on [11, pp. 18-19]. Spherical coordinates are a representation of a point in three-dimensional space. Given a point $\boldsymbol{p}_s$ in three-dimensional space, it can be represented by the three quantities $r \in [0, \infty)$, $\theta \in [0, \pi]$, and $\phi \in [0, 2\pi)$. The radial distance, r, is the point's distance to the origin. The colatitude, θ, is the angle between the vector $\boldsymbol{p}_s$ and the z-axis. The longitude, ϕ, is the counter-clockwise measured angle spanned by the x-axis and the point $\boldsymbol{p}_*$, where $\boldsymbol{p}_*$ is the projection of $\boldsymbol{p}_s$ onto the (x, y)-plane. This is illustrated in Figure F.1.

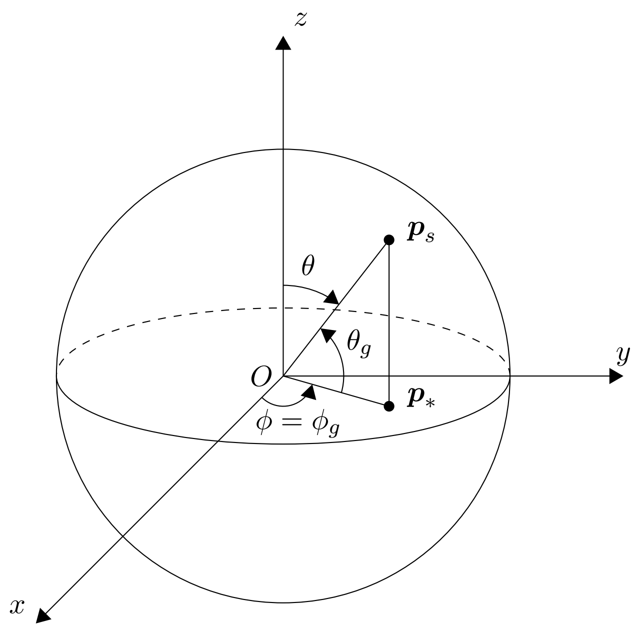

Figure F.1: Spherical coordinates, (r, θ, ϕ), and geographical coordinates, (r, θ_g, ϕ_g), of the point $\boldsymbol{p}_s$.

Represented in Cartesian coordinates, the point $\boldsymbol{p}_s$ is

$$p_s^{(0)} = r\sin(\theta)\cos(\phi), \quad p_s^{(1)} = r\sin(\theta)\sin(\phi), \quad p_s^{(2)} = r\cos(\theta).$$

The connection between the spherical coordinates and the geographical coordinates known simply as latitude and longitude is

$$\theta_g = \frac{\pi}{2} - \theta, \quad \phi_g = \phi, \tag{F.1}$$

where θ_g and ϕ_g are geographical latitude and longitude, respectively. To convert Cartesian coordinates into spherical coordinates, the formulas

$$r = \sqrt{\left(p_s^{(0)}\right)^2 + \left(p_s^{(1)}\right)^2 + \left(p_s^{(2)}\right)^2}, \quad \theta = \cos^{-1}\left(\frac{p_s^{(2)}}{r}\right), \quad \phi = \tan^{-1}\left(\frac{p_s^{(1)}}{p_s^{(0)}}\right) \tag{F.2}$$

are used. Given a vector $[x\,y\,z]^\top \in \mathbb{R}^3 \setminus \{0\}$, there exists a one-to-one correspondence between this vector and its spherical coordinate system representation, (r, θ, ϕ), i.e.

$$[x\,y\,z]^\top = r\begin{bmatrix}\sin(\theta)\cos(\phi) & \sin(\theta)\sin(\phi) & \cos(\theta)\end{bmatrix}^\top \leftrightarrow (r, \theta, \phi).$$

The Jacobian of the transformation from spherical to Cartesian coordinates is

$$\boldsymbol{J}(r,\theta,\phi) = \begin{bmatrix} \sin(\theta)\cos(\phi) & r\cos(\theta)\cos(\phi) & -r\sin(\theta)\sin(\phi) \\ \sin(\theta)\sin(\phi) & r\cos(\theta)\sin(\phi) & r\sin(\theta)\cos(\phi) \\ \cos(\theta) & -r\sin(\theta) & 0 \end{bmatrix}, \tag{F.3}$$

which has determinant

$$\det(\boldsymbol{J}(r,\theta,\phi)) = r^2\sin(\theta), \tag{F.4}$$

where $\det(\cdot)$ denotes the determinant of a matrix. The Jacobian and the Jacobian determinant are defined in Appendix C. Using (F.4), the surface measure of a sphere becomes

$$dS = r^2\sin(\theta)d\theta d\phi. \tag{F.5}$$

The sphere surface measure is illustrated in Figure F.2. Integrating over the ranges of θ and ϕ yields the total surface measure of the sphere

$$\int_0^{2\pi}\int_0^{\pi} r^2\sin(\theta)d\theta d\phi = 4\pi r^2.$$

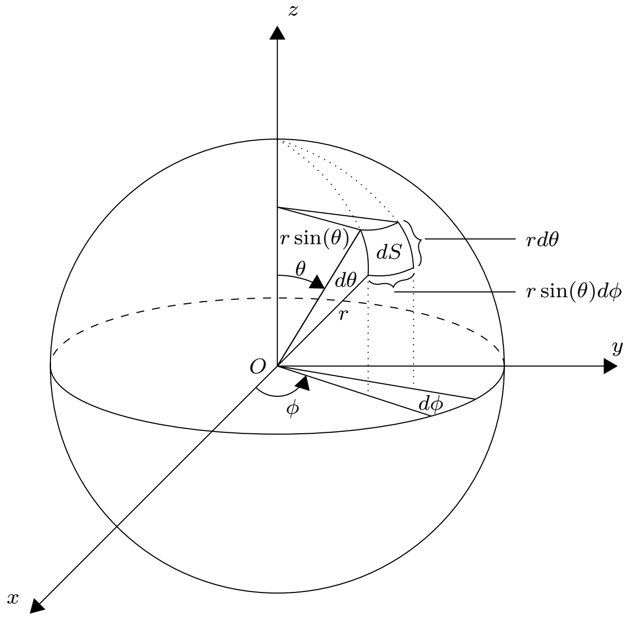

Figure F.2: Illustration of the surface measure dS.

F.2 Rotation matrices and Rodrigues' formula

This section is based on [34, pp. 22-23, 465-467], [3, pp. 9-12], and [20, p. 152]. In this thesis, rotations of $\mathbb{R}^3$ around an axis are needed. Specifically, rotations of $\mathbb{R}^3$ around an arbitrary axis and, as a special case of this, rotations around the z-axis are needed. In order to derive rotation of a point in $\mathbb{R}^3$ about the z-axis, the rotation matrix of a point in the (x, y)-plane

$$\begin{bmatrix} \cos(\beta) & -\sin(\beta) \\ \sin(\beta) & \cos(\beta) \end{bmatrix} \tag{F.6}$$

is used. Notice that the rotation is counter-clockwise if the rotation angle $\beta > 0$ and clockwise if $\beta < 0$. Now, for a given point $[x\, y\, z]^\top \in \mathbb{R}^3$ and a rotation angle β, let $[x_r\, y_r]^\top$ be the result of rotating $[x\, y]^\top$ using the rotation matrix in (F.6). Then the vector $[x_r\, y_r\, z]^\top$ is the rotation of $[x\, y\, z]^\top$ around the z-axis by an angle β. From this it follows that the rotation of $[x\, y\, z]^\top$ around the z-axis is given by

$$\begin{bmatrix} x_r \\ y_r \\ z \end{bmatrix} = \begin{bmatrix} \cos(\beta) & -\sin(\beta) & 0 \\ \sin(\beta) & \cos(\beta) & 0 \\ 0 & 0 & 1 \end{bmatrix} \begin{bmatrix} x \\ y \\ z \end{bmatrix},$$

from which the rotation matrix for rotating a point in $\mathbb{R}^3$ around the z-axis by an angle β is

$$\boldsymbol{R}_z(\beta) = \begin{bmatrix} \cos(\beta) & -\sin(\beta) & 0 \\ \sin(\beta) & \cos(\beta) & 0 \\ 0 & 0 & 1 \end{bmatrix}$$

In order to rotate a vector $\boldsymbol{v} \in \mathbb{R}^3$ around an arbitrary axis $\boldsymbol{k} \in \mathbb{S}^2$ by an angle ψ, Rodrigues' rotation formula is used. It is given by

$$\boldsymbol{v}_r = \boldsymbol{v}\cos(\psi) + (\boldsymbol{k}\times\boldsymbol{v})\sin(\psi) + \boldsymbol{k}(\boldsymbol{k}^\top\boldsymbol{v})(1-\cos(\psi)), \tag{F.7}$$

where $\boldsymbol{v}_r \in \mathbb{R}^3$ is the rotated vector. The expression in (F.7) is the vector form of Rodrigues' formula. For a geometric derivation of the vector form of Rodrigues' formula, see [3, pp. 9-12]. The matrix form of Rodrigues' formula is

$$\boldsymbol{v}_r = \boldsymbol{R}(\boldsymbol{k},\psi)\boldsymbol{v},$$

where

$$\boldsymbol{R}(\boldsymbol{k},\psi) = \cos(\psi)\boldsymbol{I} + \sin(\psi)\boldsymbol{K} + (1-\cos(\psi))\boldsymbol{k}\boldsymbol{k}^\top,$$

in which

$$\boldsymbol{K} = \begin{bmatrix} 0 & -k^{(2)} & k^{(1)} \\ k^{(2)} & 0 & -k^{(0)} \\ -k^{(1)} & k^{(0)} & 0 \end{bmatrix},$$

where $k^{(0)}$, $k^{(1)}$, and $k^{(2)}$ are the coordinates of the rotation axis, $\boldsymbol{k}$. For a derivation of the matrix form of Rodrigues' formula, see [20, pp. 151-152]. Notice that $\boldsymbol{R}_{rod}(\boldsymbol{z},\psi) = \boldsymbol{R}_z(\psi)$, and that Rodrigues formula is a counterclockwise rotation around the axis, $\boldsymbol{k}$, if $\psi > 0$, and clockwise if $\psi < 0$.

The surface measure in (F.5) is invariant under rotation. To see this, let $\boldsymbol{x},\boldsymbol{y} \in \mathbb{R}^N$ and let $\boldsymbol{A} \in \mathbb{R}^{N\times N}$ be a linear map such that $\boldsymbol{y} = \boldsymbol{A}\boldsymbol{x}$. With this set-up, the Jacobian matrix of this mapping is the $N \times N$ matrix $\boldsymbol{J}$ with entries [9, p. 96]

$$j^{(i,k)} = \frac{\partial y^{(i)}}{\partial x^{(k)}}, \qquad i,k = 0,1,\ldots,N-1.$$

Since

$$y^{(i)} = \sum_{m=0}^{N-1} a^{(i,m)}x^{(m)}, \qquad i = 0,1,\ldots,N-1,$$

and thus

$$\frac{\partial y^{(i)}}{\partial x^{(k)}} = a^{(i,k)} \qquad i,k = 0,1,\ldots,N-1,$$

it follows that for a linear map $\boldsymbol{A}$, $\boldsymbol{J} = \boldsymbol{A}$. A rotation is a linear map with determinant equal to one, and hence when rotating the sphere surface measure, and thus multiplying the measure with the Jacobian determinant of the mapping, the measure is not changed. In other words, if $\boldsymbol{A}$ is a rotation,

$$\det(\boldsymbol{J})dS = \det(\boldsymbol{A})dS = dS.$$

Written out the matrix form of Rodrigues' formula is, with a rotation axis $\boldsymbol{b} \in \mathbb{S}^2$, given by [8, p. 257]

$$\boldsymbol{R}(\boldsymbol{b},\psi) =$$

$$\begin{bmatrix} b_x^2 + (b_y^2 + b_z^2)\cos(\psi) & b_x b_y(1-\cos(\psi)) - b_z \sin(\psi) & b_x b_z(1-\cos(\psi)) + b_y \sin(\psi) \\ b_x b_y(1-\cos(\psi)) + b_z \sin(\psi) & b_y^2 + (b_x^2 + b_z^2)\cos(\psi) & b_y b_z(1-\cos(\psi)) - b_x \sin(\psi) \\ b_x b_z(1-\cos(\psi)) - b_y \sin(\psi) & b_y b_z(1-\cos(\psi)) + b_x \sin(\psi) & b_z^2 + (b_x^2 + b_y^2)\cos(\psi) \end{bmatrix},$$

where b_x, b_y, and b_z are the (x, y, z) coordinates of $\boldsymbol{b}$.

G | Carrier frequency offset estimator derivation

In this appendix, the derivations leading to the estimates of $\zeta_K^{(n)}$ and $\psi_K^{(n)}$ that minimize the non-linear least squares problem

$$f_\Delta^{(n)} = \sum_{p=0}^{P_s-1} \left| k^{(n,p)} - \left(E^{(n)}\right)^K e^{j\left(\zeta_K^{(n)} p + \psi_K^{(n)}\right)} \right|^2, \tag{G.1}$$

are found. Notice that (G.1) arises from setting $K = 4$, as evident from Section 4.3, but for ease of notation, K is retained in the succeeding derivations.

In (G.1), $k^{(n,p)}$ is the samples for a single AIS message raised to the K'th power as described in Section 4.3, and $\left(E^{(n)}\right)^K$ is the attenuation constant for the n'th AIS package raised to the K'th power.

Using the relation

$$|z_1 - z_2|^2 = |z_1|^2 + |z_2|^2 - 2\Re(z_1 \bar{z}_2),$$

in which $\Re(\cdot)$ denotes the real part of a complex number, and $\bar{z}$ denotes complex conjugation of the complex number z, (G.1) becomes

$$f_\Delta^{(n)} = \sum_{p=0}^{P_s-1} \left| k^{(n,p)} \right|^2 - 2\left(E^{(n)}\right)^K \Re\left(k^{(n,p)} e^{-j\left(\zeta_K^{(n)} p + \psi_K^{(n)}\right)} \right) + \left(E^{(n)}\right)^{2K}. \tag{G.2}$$

Minimizing (G.2) is done by maximizing the term

$$g\left(\zeta_K^{(n)}, \psi_K^{(n)}\right) = \sum_{p=0}^{P_s-1} \Re\left(k^{(n,p)} e^{-j\left(\zeta_K^{(n)} p + \psi_K^{(n)}\right)} \right). \tag{G.3}$$

Rewriting this term into polar form, $re^{j\phi}$, and using the relation

$$\Re(re^{j\phi}) = r\cos(\phi) = r\cos(\arg(re^{j\phi})),$$

(G.3) becomes

$$
\begin{aligned}
g\left(\zeta_K^{(n)}, \psi_K^{(n)}\right) &= \left|\sum_{p=0}^{P_s-1}\left(k^{(n,p)} e^{-j\left(\zeta_K^{(n)} p+\psi_K^{(n)}\right)}\right)\right| \cos\left(\arg\left(\sum_{p=0}^{P_s-1} k^{(n,p)} e^{-j\left(\zeta_K^{(n)} p+\psi_K^{(n)}\right)}\right)\right) \\
&= \left|\sum_{p=0}^{P_s-1}\left(k^{(n,p)} e^{-j\zeta_K^{(n)} p}\right)\right| \cos\left(\arg\left(\sum_{p=0}^{P_s-1} k^{(n,p)} e^{-j\zeta_K^{(n)} p}\right) - \psi_K^{(n)}\right),
\end{aligned}
\tag{G.4}
$$

because $|e^{-j\psi_K^{(n)}}| = 1$. From (G.4) it is seen that for fixed $\zeta_K^{(n)}$, $g\left(\zeta_K^{(n)}, \psi_K^{(n)}\right)$ is maximized when the estimate of $\psi_K^{(n)}$ is

$$
\hat{\psi}_K^{(n)}\left(\zeta_K^{(n)}\right) = \arg\left(\sum_{p=0}^{P_s-1} k^{(n,p)} e^{-j\zeta_K^{(n)}\cdot p}\right),
$$

which, when inserted into (G.4), yields

$$
g\left(\zeta_K^{(n)}, \hat{\psi}_K^{(n)}\left(\zeta_K^{(n)}\right)\right) = \left|\sum_{p=0}^{P_s-1}\left(k^{(n,p)} e^{-j\zeta_K^{(n)}\cdot p}\right)\right|.
$$

Hence the estimate of $\zeta_K^{(n)}$ is

$$
\hat{\zeta}_K^{(n)} = \underset{\zeta_K^{(n)}}{\operatorname{argmax}}\left|\sum_{p=0}^{P_s-1}\left(k^{(n,p)} e^{-j\zeta_K^{(n)}\cdot p}\right)\right|. \tag{G.5}
$$

In (G.5), it is seen that estimating $\hat{\zeta}_K^{(n)}$ is equivalent to estimating the highest value in the magnitude spectrum of $k^{(n,p)}$.

H | Frequency translation

This appendix describes signal frequency translation using a real and a complex mixer. It is based on [14, pp. 103-105].

An important operation in signal processing is being able to frequency translate the carrier frequency of a signal to a higher or lower frequency than the original signal. This is done using what is called a mixer. A mixer consists of a product modulator followed by a band-pass filter. There exist mixers for real numbers and mixers for complex numbers. These are explored in the next sections.

H.1 Real mixer

In the case where a real valued signal is considered, the mixer uses a cosine to translate the carrier frequency of the incoming signal. Consider the original signals

$$s_a(t) = A\cos(2\pi f_a t) \tag{H.1}$$

and

$$s_b(t) = B\cos(2\pi f_b t), \tag{H.2}$$

with carrier frequencies f_a and f_b, respectively. Multiplying the two signals above results in a signal with frequencies $f_a + f_b$ and $f_a - f_b$. To realize this, the following trigonometric identity

$$2\cos(2\pi f_a t)\cos(2\pi f_b t) = \cos(2\pi(f_a - f_b)t)\cos(2\pi(f_a + f_b)t)$$

is used. The product then becomes

$$s_m(t) = \frac{AB}{2}\left(\cos(2\pi(f_a - f_b)t) + \cos(2\pi(f_a + f_b)t)\right). \tag{H.3}$$

In (H.3), it is seen that the product of the two signals results in a signal with frequencies corresponding to the sum and difference of the two frequencies of the original signals. Depending on whether the goal is an up- or down-shift in frequency, called an up- and down-conversion, respectively, a band-pass filter is used to get rid of the unwanted frequency components.

H.2 Complex mixer

A complex mixer uses a complex exponential to translate the carrier frequency. The same principles used in the real mixer are used in the complex mixer. Consider the complex exponential

$$e^{j2\pi f_m t} = \cos(2\pi f_m t) + j\sin(2\pi f_m t), \tag{H.4}$$

with carrier frequency f_m. Multiplying (H.4) and (H.1) yields

$$s_c(t) = A(\cos(2\pi f_a t)\cos(2\pi f_m t) + j\cos(2\pi f_a t)\sin(2\pi f_m t)). \tag{H.5}$$

Applying trigonometric identities, (H.5) can be rewritten as

$$\begin{aligned} s_c(t) =& \frac{A}{2}(\cos(2\pi(f_a - f_m)t) + \cos(2\pi(f_a + f_m)t)) \\ &+ j\left(\sin(2\pi(f_a + f_m)t) - \sin(2\pi(f_a - f_m)t)\right). \end{aligned} \tag{H.6}$$

The real and imaginary parts of (H.6) are

$$\Re(s_c(t)) = \frac{A}{2}\left(\cos(2\pi(f_a - f_m)t) + \cos(2\pi(f_a + f_m)t)\right)$$

$$\Im(s_c(t)) = \frac{A}{2}\left(\sin(2\pi(f_a + f_m)t) - \sin(2\pi(f_a - f_m)t)\right),$$

where $\Re(\cdot)$ and $\Im(\cdot)$ represent the real and imaginary parts, respectively. It is seen that both the real and imaginary part consist of a difference of the frequencies and a summation of the frequencies. As with the real valued mixer, a filter can be applied to either keep the difference or the summation of the frequencies.

In the case where the summation of the frequencies is desired, a band-pass or a high-pass filter can be used to eliminate the lower (difference) frequencies. This results in the filtered signal,

$$s_f(t) = \frac{A}{2}\left(\cos(2\pi(f_a + f_m)t) + \sin(2\pi(f_a + f_m)t)\right).$$

I Digital modulation and complex baseband signal representation

In this appendix, an introduction is given to the principle of digital signal modulation, along with a description of the complex baseband representation of signals.

I.1 Digital modulation

Digital modulation is the process of modifying parameters of an analog carrier signal, $c(t)$, such that the carrier signal contains information about a digital information signal, $i(t)$. Usually, the carrier signal is a sinusoid with a relatively high frequency, f_c [38, p. 50], i.e.

$$c(t) = A\cos\left(2\pi f_c t\right),$$

where A is the carrier amplitude and f_c is the carrier frequency. The signal, $i(t)$, is usually relatively low frequency and is referred to as a baseband signal. Base- and passband signals are defined as

Definition I.1 (Base- and passband signals)
Let $z(t) \in \mathbb{R}$ be a signal and let $W \in \mathbb{R}_{>0}$. $z(t)$ is said to be baseband if

$$Z(\omega) \approx 0, \qquad |\omega| > W,$$

where $\omega = 2\pi f$ and $Z(\omega)$ is the Fourier transform of $z(t)$. Furthermore, let $f_c \in \mathbb{R}_{>0}$ such that $f_c > W$. $z(t)$ is said to be passband if

$$Z(\omega) \approx 0, \qquad |\omega \pm \omega_c| > W,$$

where $\omega_c = 2\pi f_c$ [23, pp. 16-17].

With Definition I.1 in place, the complex baseband representation of a passband signal is introduced.

I.2 Complex baseband representation

As mentioned earlier, when an information signal, $i(t)$, has been used to modulate a carrier signal, $c(t)$, the resulting signal is said to be passband. Carrying out digital signal processing (DSP) on passband signals is computationally expensive, due to the often high sample rates used to represent said signals [23, p. 18]. The passband signal has a complex-valued representation as a baseband signal. This representation is often called complex baseband, and contains all the information carried in the real valued passband signal. This complex baseband representation is often used in DSP, since it is computationally cheaper than carrying out DSP on a passband signal. Initially, define the pre-envelope of an absolutely integrable signal $z(t) \in \mathbb{R}$ as

$$z_+(t) = z(t) + j\hat{z}(t), \tag{I.1}$$

where $\hat{z}(t)$ is the Hilbert transformation of $z(t)$. The Fourier transform of (I.1) is

$$Z_+(\omega) = Z(\omega) + \operatorname{sgn}(\omega)Z(\omega), \tag{I.2}$$

where $\operatorname{sgn}(\cdot)$ is the sign function,

$$\operatorname{sgn}(x) = \begin{cases} -1 & \text{if } x < 0, \\ 0 & \text{if } x = 0, \\ 1 & \text{if } x > 0. \end{cases}$$

From (I.2) it is seen that the Fourier transform of $z_+(t)$ vanishes for negative frequencies, and is twice that of $Z(\omega)$ for positive frequencies, i.e.

$$Z_+(\omega) = \begin{cases} 2Z(\omega) & \text{if } \omega > 0, \\ Z(0) & \text{if } \omega = 0, \\ 0 & \text{if } \omega < 0. \end{cases}$$

Thus, the frequency content of the pre-envelope is contained only at the non-negative frequencies, i.e. $\omega \geq 0$. Even though $Z_+(\omega)$ does not contain the negative frequencies of $Z(\omega)$, no information from $Z(\omega)$ is lost. This is due to the fact that $z(t)$ is a real-valued signal, and thus its Fourier transform has the Hermitian symmetry property. Using the Fourier transform shift-theorem, the complex baseband representation of $z(t)$ can be defined in terms of the pre-envelope.

Definition I.2 (Complex baseband representation of a passband signal)
Let $z(t) \in \mathbb{R}$ be a passband signal with Hilbert transform $\hat{z}(t)$. Furthermore, let

$$z_+(t) = z(t) + j\hat{z}(t)$$

be the pre-envelope of $z(t)$. The complex baseband representation of $z(t)$ is defined as

$$z_{cb}(t) = z_+(t)e^{-j\omega_c t}$$

From Definition I.2, it is evident that the spectrum of $z_{cb}(t)$ is a version of that of $z_+(t)$, shifted to the origin. In other words, it is at baseband [14, p. 727]. Furthermore, since $z_{cb}(t)$ is defined in terms of $z_+(t)$, the passband signal can be recovered from $z_{cb}(t)$ as

$$z(t) = \mathrm{Re}[z_{cb}(t)e^{j\omega_c t}] \tag{I.3}$$

Moreover, since $z_{cb}(t)$ is a complex-valued signal, its general form is

$$z_{cb}(t) = z_I(t) + jz_Q(t), \tag{I.4}$$

where $z_I(t), z_Q(t) \in \mathbb{R}$ are baseband signals, referred to as the in- and quadrature-phase component of $z(t)$, respectively [14, p. 727]. Inserting (I.4) into (I.3), $z(t)$ can be expressed as

$$z(t) = z_I(t)\cos(\omega_c t) - z_Q(t)\sin(\omega_c t).$$

Lastly, the complex baseband representation in (I.4) is in Cartesian form. The corresponding polar form is

$$z_{cb}(t) = a(t)e^{j\phi(t)}, \tag{I.5}$$

where

$$a(t) = \sqrt{z_I(t)^2 + z_Q(t)^2}$$

and

$$\phi(t) = \tan^{-1}\left(\frac{z_Q(t)}{z_I(t)}\right).$$

Finally, from (I.5) and (I.3), it is seen that $z(t)$ can be expressed as

$$z(t) = \mathrm{Re}\left[a(t)e^{j\phi(t)}e^{j\omega_c t}\right] = a(t)\cos(\omega_c t + \phi(t)).$$

J Continuous phase modulation and Gaussian minimum shift keying

The information contained in an AIS message is contained in a length-256 bit-string, which is NRZI encoded. This NRZI encoded bit-string is then modulated onto a carrier wave. The modulation scheme used in AIS is Gaussian minimum shift keying (GMSK), which is part of a class of modulation schemes known as continuous phase modulation (CPM). CPM is a class of constant amplitude modulation techniques in which the phase of the carrier wave is continuously varied to convey information. These techniques are both power and spectrally efficient [42, p. 259]. They are power effective due to the fact that CPM waveforms have constant amplitude, and spectrally efficient since they have a narrow mainlobe with small sidelobes [36, p. 188]. In this appendix, intitially CPM is introduced, and, eventually, GMSK is introduced. GMSK is a modulating scheme in which a rectangular pulse is passed through a Gaussian filter in order to shape the pulse. These pulses are then modulated onto a carrier wave. Eventually, NRZI encoding is introduced.

J.1 Continuous phase modulation

CPM is a large selection of constant amplitude modulation techniques in which M-ary data symbols shape the phase of a carrier wave. The term M-ary data symbols refers to data symbols originating from an alphabet, $\mathcal{M} = \{\pm 1, \pm 3, \ldots \pm (M-1)\}$ consisting of M distinct symbols. In CPM, M is often a power of 2 [42, p. 260]. The CPM signal, i.e. the modulated carrier wave, is defined as [32, pp. 28-29]

$$s_c(t) = A\cos(\omega_c t + \phi(t, a_s)), \qquad nT_{sym} \leq t \leq (n+1)T_{sym} \tag{J.1}$$

where $a_s = \left(a^{(n)}\right)_{n=-\infty}^{\infty}$ is the sequence of data symbols with $a^{(n)} \in \mathcal{M}$, $\omega_c = 2\pi f_c$ is the angular carrier frequency, A is the signal amplitude, and $T_{sym} > 0$ is the symbol period, i.e. the time-duration of a data symbol. The phase of the CPM signal depends on the sequence of data symbols, showing that CPM varies the phase of the signal to convey information, instead of e.g. varying the amplitude as is done in other modulation schemes [42, p. 260]. The phase in (J.1) is defined as

$$\phi(t, a_s) = 2\pi h_m \sum_{i \leq n} a^{(i)} q(t - iT_{sym}), \tag{J.2}$$

where

$$q(t) = \int_{-\infty}^{t} g(\tau) d\tau. \tag{J.3}$$

In (J.2), $h_m > 0$ is known as the modulation index [14, p. 110]. Lastly, $g(t)$ is a non-negative function known as the frequency shaping function, and its integral, $q(t)$ is the phase shaping function. Along with h_m, $g(t)$ determines how the phase, $\phi(t, a_s)$, varies in response to the data symbols, a_s. Usually, $g(t)$ is zero outside the interval $0 \leq t \leq LT_{sym}$, where T_{sym} is the symbol period, and has a smooth pulse shape inside the interval [42, p. 260]. The number L determines the number of symbol periods in which $g(t) \neq 0$. If $L \leq 1$, the scheme is called full-response CPM, and the pulse is contained within a symbol period, T_{sym}. If $L > 1$, the scheme is called partial-response CPM [42, p. 260]. Several valid choices of $g(t)$ exists, and they should be normalized to integrate to $\frac{1}{2}$ [36, p. 189],

$$\int_{-\infty}^{\infty} g(t) dt = \frac{1}{2}. \tag{J.4}$$

An illustrative example is that of using a rectangular pulse as $g(t)$. This choice of $g(t)$ has support within the interval $0 \leq t \leq LT_{sym}$. In this case [42, p. 261],

$$g_{rec}(t) = \begin{cases} \frac{1}{2LT_{sym}} & 0 \leq t \leq LT_{sym}, \\ 0 & \text{otherwise.} \end{cases}$$

With $L = 1$, i.e. full-response CPM, the phase shaping function is [42, p. 261]

$$q_{rec}(t) = \int_{-\infty}^{t} \frac{1}{2T_{sym}} dt = \begin{cases} \frac{t}{2T} & 0 \leq t \leq T_{sym}, \\ \frac{1}{2} & t > T_{sym}. \end{cases}$$

J.2 Gaussian minimum shift keying

A special CPM case in which $g(t)$ is a pulse with the shape of a Gaussian density is considered. This Gaussian frequency shaping function is defined as [42, p. 263]

$$g(t) = \frac{1}{2T_{sym}} \left(Q\left(2\pi B_b \frac{t - \frac{T_{sym}}{2}}{\log(2)}\right) - Q\left(2\pi B_b \frac{t + \frac{T_{sym}}{2}}{\log(2)}\right)\right), \qquad 0 \leq B_b T_{sym} \leq 1 \tag{J.5}$$

where

$$Q(t) = \int_{t}^{\infty} \frac{1}{\sqrt{2\pi}} e^{-\frac{\tau^2}{2}} d\tau, \qquad -\infty \leq t \leq \infty,$$

and B_b is the -3 dB bandwidth of the lowpass Gaussian filter [32, p. 58] given by

$$h(t) = \frac{1}{\sqrt{2\pi\sigma^2}} e^{\left(-\frac{1}{2\sigma^2}\right)}, \tag{J.6}$$

where

$$\sigma^2 = \frac{\log(2)}{(2\pi B_b)^2}.$$

The frequency shaping function (J.5) is the result of passing a rectangular pulse through (J.6). The frequency-shaping function in (J.5) is the difference between two Gaussian Q-functions, separated by T_{sym} seconds. Using this frequency-shaping function ensures continuity of the phase in (J.2). This is evident from the fact that $g(t)$ is a smooth function, thus making its integral, the phase shaping function $q(t)$ in (J.3), smooth as well. Moreover, the phase in (J.2) is a weighted sum of time-shifted versions of the smooth function, $q(t)$. As time, t, progresses in (J.2), new weighted terms of $q(t-nT_{sym})$ are added. Since $q(t-nT_{sym})$ always starts from zero, and smoothly progresses to $\frac{1}{2}$, no sudden phase changes occur in (J.2), and the resulting phase is continuous [42, p. 265]. Using (J.5) results in the modulation technique known as Gaussian minimum shift-keying. GMSK is a partial-response CPM scheme with $h = \frac{1}{2}$. [32, p. 57]. In practice, it is necessary to time-truncate (J.5) due to its infinite support. The approximation

$$g(t) = \begin{cases} \frac{1}{2T_{sym}} \left[Q\left(\frac{2\pi B_b T_{sym}}{\sqrt{\log(2)}} \left(\frac{t}{T_{sym}} - 1 \right) \right) - Q\left(\frac{2\pi B_b T_{sym}}{\sqrt{\log(2)}} \frac{t}{T_{sym}} \right) \right] \\ 0 \end{cases} \tag{J.7}$$

is made, in which L is chosen in accordance with the value of the bandwidth-time product, $B_b T_{sym}$. The top entry in (J.7) is for

$$-(L-1)\frac{T_{sym}}{2} \leq t \leq (L+1)\frac{T_{sym}}{2} \tag{J.8}$$

and the bottom entry is for t values outside of this interval. Returning to the condition in (J.4), (J.7) should be normalized by a constant, C, in order to statisfy the condition. In practical scenarios, the constant is ignored, i.e. set equal to unity, for values $B_b T_{sym} \geq 0.25$ [32, p. 62]. In AIS, two such values are utilized, namely 0.3 and 0.4 [44, p. 1].

Inserting (J.3) in (J.2), interchanging the sum and the integral, and translating $g(\tau)$ results in

$$\phi(t, a_s) = 2\pi h \int_{-\infty}^{t} \sum_{i \leq n} a_n g(\tau - iT_{sym}) d\tau. \tag{J.9}$$

In (J.9) the term $\psi(a_s, t) = \sum_{i \leq n} a_n g(\tau - iT_{sym})$ is the sum of data symbols multiplied by the GMSK frequency shaping function. An example of this, with the data symbols being the NRZI string

$$a_s = (1, -1, 1, 1, -1, -1, 1, -1, -1, -1, 1, -1, 1, -1)$$

can be seen in Figure J.1, in which the blue line is the data symbol pulse train, and the green curve is the product between the data symbols and the GMSK frequency shaping function with $B_b T_{sym} = 0.4$. Moreover, zero-padding corresponding to one bit-length at both ends of the NRZI string has been made.

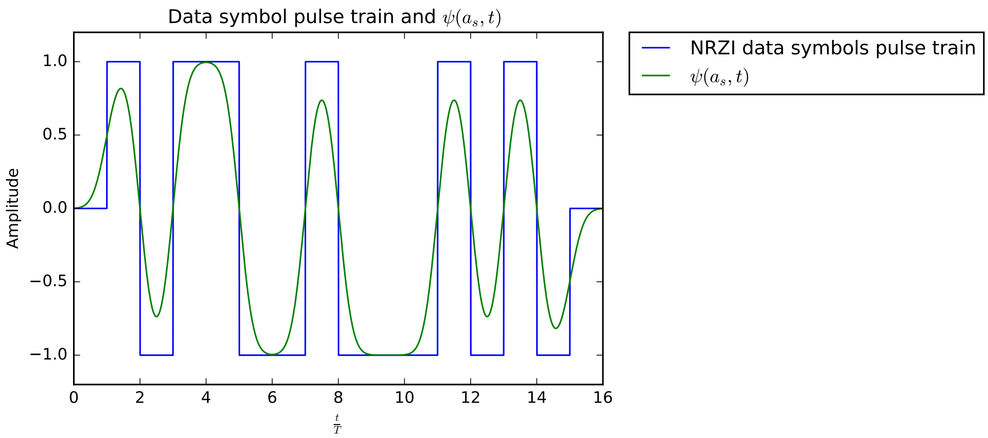

Figure J.1: NRZI data symbols pulse train (blue) and sum of produts between data symbols and time shifted frequency shaping functions (green).

J.3 GMSK bit error rate

In digital communication, the bit error rate (BER) is the probability that a transmitted bit will be incorrectly received, i.e. a 0 turns into a 1 and vice versa [28, p. 188]. When receiving and demodulating AIS signals on LEO satellites, GomSpace uses non-coherent GMSK modulation. Using this demodulation scheme, the BER can be seen as a function of Eb/N0 in Figure J.2. For a description of Eb/N0, see Section REF.

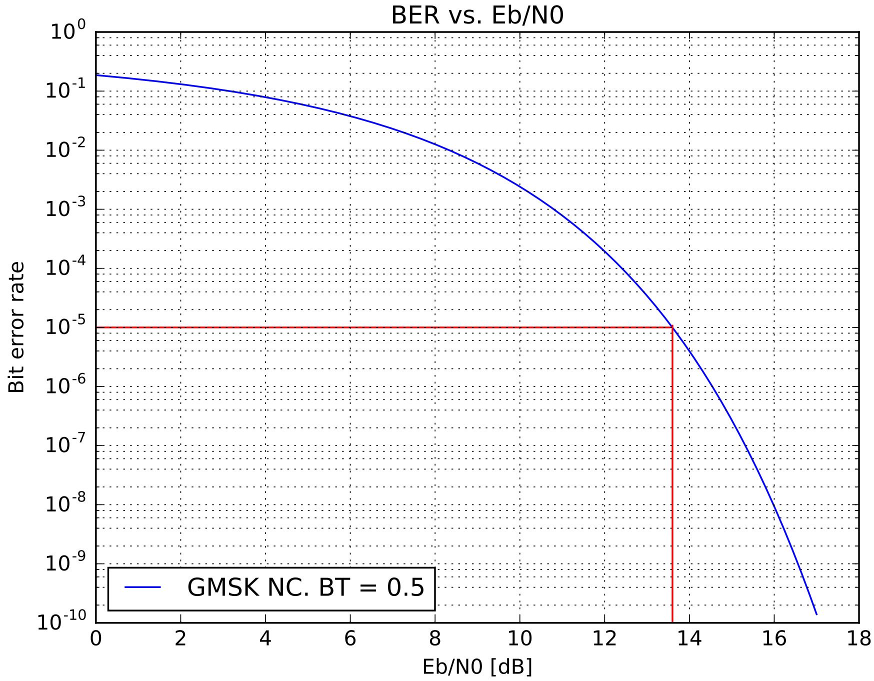

Figure J.2: Plot of BER vs. Eb/N0 for non-coherent GMSK demodulation with bandwidth-time product $B_bT_{sym} = 0.5$.

GMSK is based on a modulation scheme known as minimum shift keying (MSK). The BER for non-coherent demodulation of MSK signals is [18, p. 20]

$$P_M = \frac{1}{2}\text{erfc}\left(\sqrt{\frac{E_b}{2N_0}}\right), \tag{J.10}$$

in which

$$\text{erfc}(u) = \frac{2}{\sqrt{\pi}}\int_u^\infty \exp(-z^2)dz \tag{J.11}$$

is the complementary error function [14, p. 255]. Degradation of Eb/N0 is happening when transitting from MSK to GMSK. Using computer simulations, a plot of degradation, ϵ, in Eb/N0 vs. B_bT_{sym} product has been generated in [26, p. 1047]. This plot has been reprinted in this thesis, and can be seen in Figure J.3. As mentioned earlier, the B_bT_{sym} product used when transmitting AIS signals is 0.4, but when designing an AIS receiver, the recommendation is to design it with a B_bT_{sym} product of 0.5 [31, p. 12]. Hence, from Figure J.3, the degradation for $B_bT_{sym} = 0.5$ is approximately $\epsilon = 0.1$ dB.

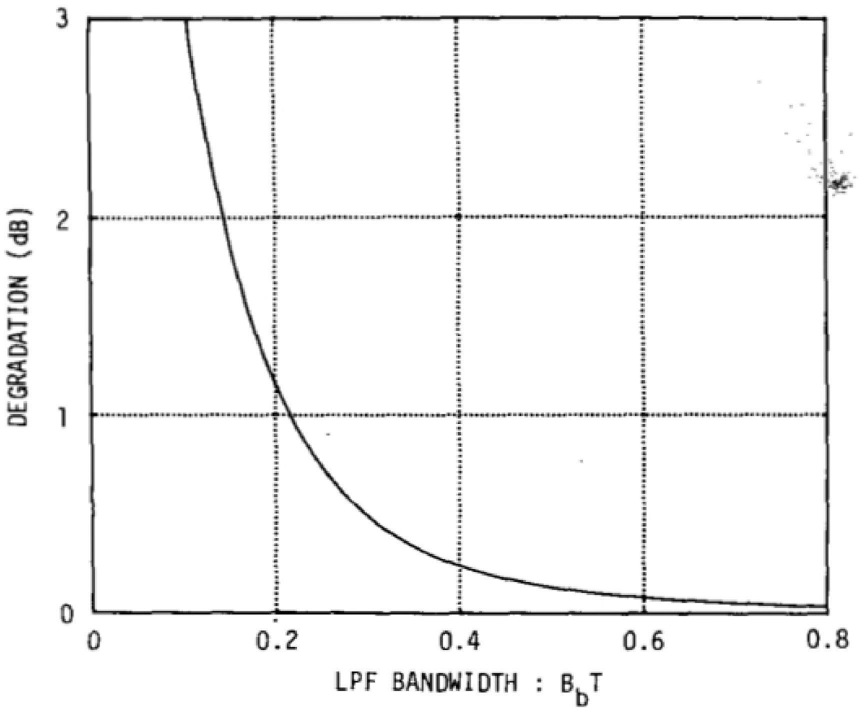

Figure J.3: Eb/N0 degradation in dB vs. B_bT_{sym} product. Figure reprinted from [26, p. 1047].

This degradation is to be subtracted from the MSK Eb/N0, and, in conjunction with (J.10), this yields the BER for non-coherent GMSK demodulation, namely

$$P_G = \frac{1}{2}\text{erfc}\left(\sqrt{\frac{1}{2}\left(\frac{E_b}{N_0} - \epsilon\right)}\right) \tag{J.12}$$

Figure J.2 is generated using (J.12) with $B_bT = 0.5$ and hence $\epsilon = 0.1$.

J.4 Non-return-to-zero bit encoding

The encoder used to encode the length-256 bit-string in AIS is a non-return-to-zero inverted (NRZI) encoder. The non-return-to-zero part refers to the fact that the voltage level in the physical signal does not rest at zero at any time.

Moreover, NRZI refers to two encoders, one being non-return-to-zero space (NRZS) and the other being non-return-to-zero mark (NRZM). In NRZS a 0 represents a change in voltage, usually represented by -1, whereas a 1 is represented by no change in voltage, and usually represented by a 1. NRZM is the opposite, in which a 1 represents a change in voltage. In AIS, however, NRZS is used [31, p. 15]. An example of data encoded using NRZS can be seen in Figure J.4.

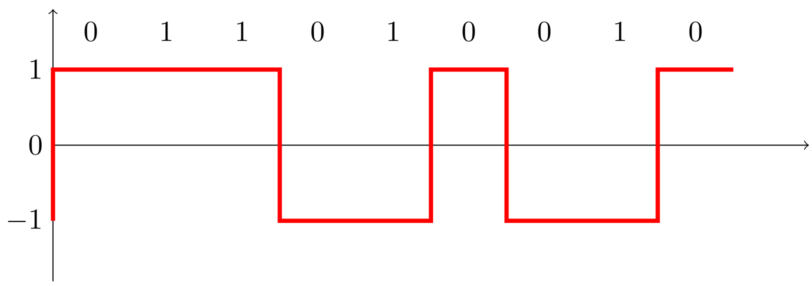

Figure J.4: Example of data encoded using NRZS.

K | Self-organized time-division multiple access (SOTDMA)

The self-organized time-division multiple access (SOTDMA) scheme determines when a vessel can transmit its AIS messages such that these messages do not overlap with those sent out by other nearby vessels. The SOTDMA scheme divides each minute into 2250 time slots, each of duration $26.\bar{6}$ ms. The time duration of an AIS message fits into one of these time slots. The main purpose of SOTDMA is to allow vessels to share the AIS radio channels witout interfering with each other. An illustration of the scheme is given in Figure K.1. A vessel reserves time slots for future transmissions with time intervals depending on its status, i.e. its speed and whether it is on a steady or changing course. These intervals can be found in Section 2.1, in which they are referred to as reporting intervals and denoted t_r. Vessels share a time reference, derived from GPS time, which allows each vessel to accurately determine the starting time of a given time slot in the SOTDMA scheme. Each transmission includes information about future reserved slots, lending knowledge to other vessels about which time slots are reserved and which ones are not [1]. Naturally, a vessel avoids using and reserving time slots currently in use or reserved by other vessels.

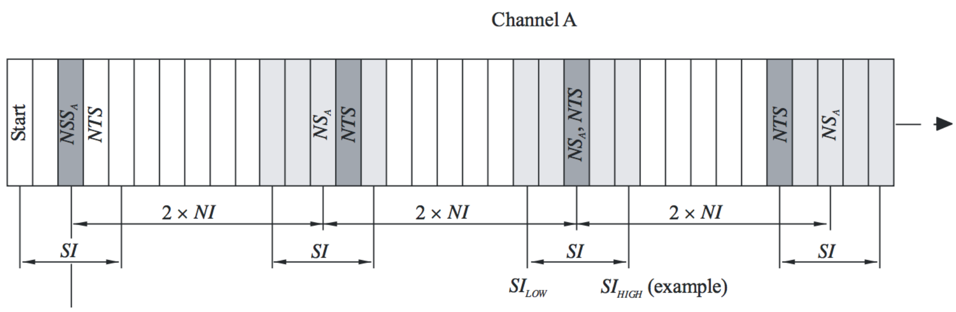

Figure K.1: The AIS channel 1 SOTDMA scheme. Figure reprinted from [31, pp. 33-38]. Notice that the source has named AIS channel 1 as Channel A.

The nominal start slot, NSS_A, in Figure K.1 is the first time slot in which a vessel is transmitting. When a vessel starts transmitting, NSS_A is chosen. This time slot will be used as a reference point when determining the nominal transmission slots, NTS, i.e. the future transmission slots. The nominal increment, i.e. the ideal time between transmission, is determined by

$$NI = \frac{2250}{R_r},$$

where $R_r = \frac{60}{t_r}$ is the number of reporting intervals per minute, referred to as the report rate.

Vessels using AIS alternate between transmitting over channel 1 and channel 2. Therefore, the ideal time between two transmissions over channel 1 is two times the nominal increment, NI. In order to find the next future transmission slot, i.e. NTS, the reference point, NSS_A, is translated forward by $2 \cdot NI$. Here, a selection interval, SI, centered around the nominal slot, NS_A is made. The nominal slot is the centre around which time slots are chosen for transmission. The time slot size of the selection interval, SI, is found by

$$SI = 0.2 \cdot NI,$$

where, as mentioned earlier the center of the interval is NS_A. Notice that for the first transmission from a vessel, NSS_A and NS_A coincide. Indside the selection interval, a transmission slot is chosen with all the possible time slots having equal probability of being chosen [31, pp. 33-38].

L White Gaussian noise: sampling and generation

In the first section of this appendix, continuous-time white Gaussian noise (WGN) is defined along with the definition of bandlimited WGN. Moreover, the effects that the sampling frequency and bandwidth have on the correlation between samples of bandlimited WGN when sampling it is described. The second section describes how discrete complex noise is generated and added to AIS signals in this thesis. Both sections are inspired by [19, pp. 583-586].

L.1 White Gaussian noise sampling

A continuous-time wide-sense stationary zero-mean Gaussian random process, $X(t)$, with power spectral density

$$P_X(f) = \frac{N_0}{2}, \qquad f \in \mathbb{R}$$

where $N_0 \in \mathbb{R}_+$ is a constant, and autocorrelation function

$$r_X(\tau) = \int_{-\infty}^{\infty} P_X(f) e^{j2\pi f\tau} df = \frac{N_0}{2}\delta(\tau), \tag{L.1}$$

where $\delta(\tau)$ is the unit impulse, is called continuous-time white Gaussian noise (WGN) [19, pp. 583-584]. An illustration of the power spectral density of this noise is seen as the horizontal solid line of value $\frac{N_0}{2}$ in Figure L.1.

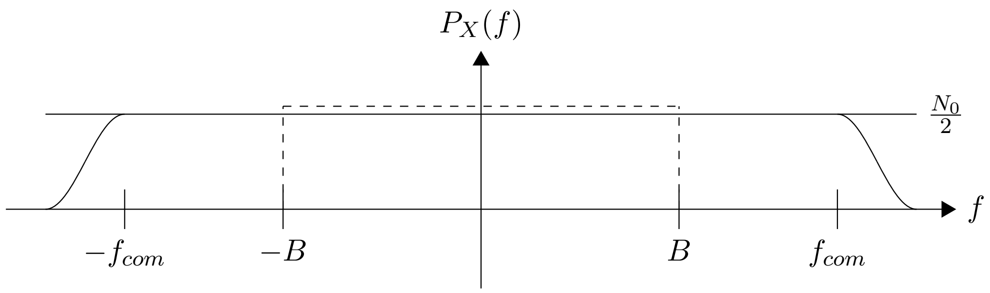

Figure L.1: Illustration of power spectral densities for WGN and thermal noise.

In many communication systems, WGN is used to model the noise in the system. The dominant noise source in communication systems is thermal noise. Experimentally, it has been shown that the power spectral density of thermal noise within a certain bandwidth B is well modelled using the power spectral density of WGN within the same bandwidth. The power spectral density is illustrated in Figure L.1 as constant for $-f_{com} < f < f_{com}$, and decreasing outside this frequency band.

WGN is not physically realizable, since the variance of WGN, $r_X(0) = \infty$, due to the nature of the unit impulse in (L.1). Passing WGN through an ideal low-pass filter with bandwidth B yields band-limited WGN, $X_l(t)$, with power spectral density

$$P_{X_l}(f) = \begin{cases} \frac{N_0}{2}, & |F| \leq B, \\ 0, & \text{otherwise}, \end{cases}$$

and autocorrelation function

$$\begin{aligned} r_{X_l}(\tau) &= \int_{-\infty}^{\infty} P_{X_l}(f) e^{j2\pi f\tau} df \\ &= \int_{-B}^{B} \frac{N_0}{2} e^{j2\pi f\tau} df \\ &= \frac{N_0}{2} \int_{-B}^{B} \cos(2\pi f\tau) df \qquad \text{(L.2)} \\ &= N_0 B \frac{\sin(2\pi B\tau)}{2\pi B\tau}, \qquad \text{(L.3)} \end{aligned}$$

where (L.2) follows from integrating an odd function over a symmetric interval. An illustration of the autocorrelation of the band-limited WGN is seen in Figure L.2.

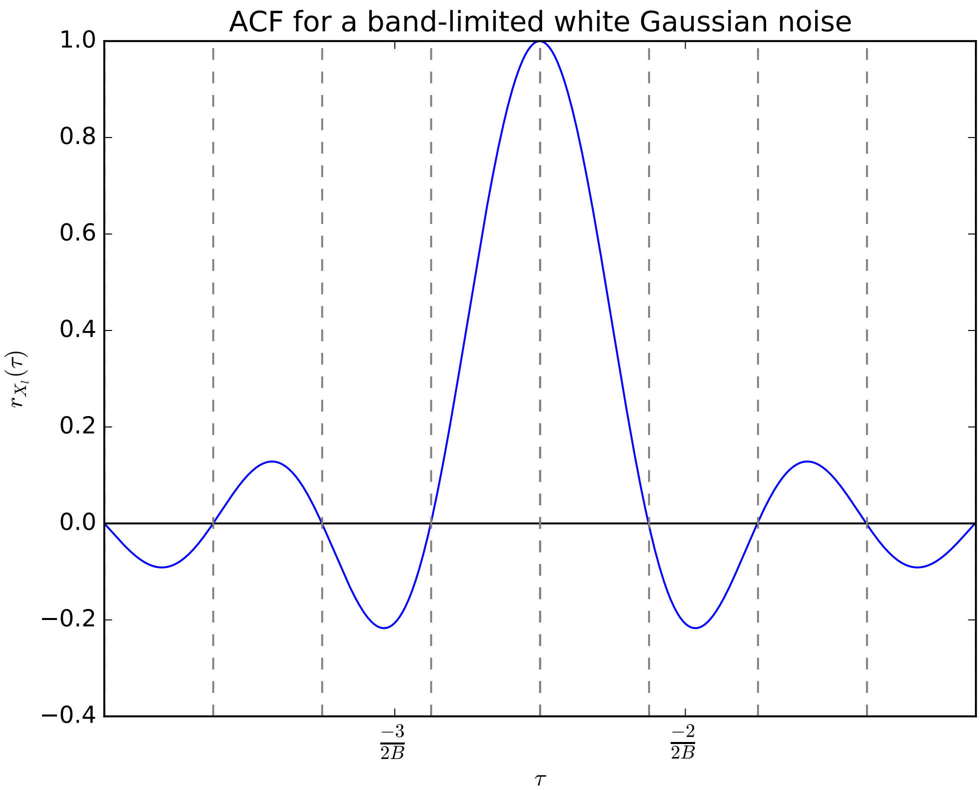

Figure L.2: Autocorrelation function for the filtered WGN, $X_l(t)$, with $N_0 = B = 1$.

The zero-crossings of this sinc function are separated by $\frac{1}{2B}$. These are illustrated by the vertical dashed lines in Figure L.2. In communication systems, the noise is sampled with sampling period T_s after the filtering. These samples can be represented as

$$X_l(nT_s) = X_l[n], \qquad n \in \mathbb{Z}.$$

If $X_l(t)$ is sampled at the Nyquist rate, $2B$, this corresponds to sampling the autocorrelation function in Figure L.2 at its zero-crossings. This is seen from the autocorralation function in (L.3), which, when sampled at the Nyquist rate is

$$r_{X_l}[k] = r_{X_l}(kT_s) = r_{X_l}\left(\frac{k}{f_s}\right) = r_{X_l}\left(\frac{k}{2B}\right),$$

which for $k = \pm 1, \pm 2, \ldots$ is zero, and for $r_{X_l}[0] = N_0 B$. Thus, the autocorrelation function for the filtered WGN, $X_l(t)$, sampled at the Nyquist rate is

$$r_{X_l}[k] = N_0 B \delta[k],$$

where $\delta[k]$ is the Kronecker delta function.

If $X_l(t)$ is sampled at a rate faster than the Nyquist frequency, i.e. $T_s < \frac{1}{2B}$, correlation is introduced in the noise samples. Effectively, sampling faster than the Nyquist frequency corresponds to sampling the autocorrelation function in (L.3) outside of its zero-crossings, and thus introducing correlation in the obtained noise samples.

L.2 White Gaussian noise generation

This section describes the complex noise generator in Figure L.3.

Recall the continuous-time AIS signal

$$y^{(n)}(t) = E^{(n)} x^{(n)}(t - \tau^{(n)}) e^{j2\pi\zeta^{(n)} t} + w^{(n)}(t) \qquad T_R^{(n)} \leq t \leq T_R^{(n)} + T_{AIS}, \tag{L.4}$$

for the n'th AIS message from (4.9), in which $w(t)$ is assumed band-limited circularly symmetric Gaussian noise with variance σ_w^2. This signal is the output of a low-pass filter, which in the following derivations is assumed to be ideal. GomSpace uses the bandwidth $B_{gs} = 7.5$ kHz in this filter, and a sampling frequency $f_{gs} = 38.4$ kHz. Considering the sampling of the AIS signal in (L.4), the sampling frequency used by GomSpace introduces correlation into the noise in the samples. This is due to the fact that $f_{gs} > 2B_{gs}$. From (4.11), P_s samples of the received AIS signal are given as

$$y^{(n)}(pT_s) = y^{(n,p)} = E^{(n)} e^{j\left(2\pi\zeta^{(n)} p + \phi^{(n,p)} + \psi^{(n)}\right)} + w^{(n,p)}, \qquad p = 0, 1, \ldots, P_s - 1. \tag{L.5}$$

The number of samples obtained by GomSpace in an AIS message is

$$P_{gs} = T_{AIS} \cdot f_{gs} = 1024.$$

GomSpace has provided software for generating and simulating the transmission and receival of AIS signals without noise. The continuous version of the n'th of these AIS signals is

$$z^{(n)}(t) = E^{(n)} x^{(n)}(t - \tau^{(n)}) e^{j2\pi\zeta^{(n)} t}, \qquad T_R^{(n)} \leq t \leq T_R^{(n)} + T_{AIS},$$

and its samples are

$$z^{(n,p)} = E^{(n)} e^{j\left(2\pi\zeta^{(n)} p + \phi^{(n,p)} + \psi^{(n)}\right)}, \qquad p = 0, 1, \ldots, P_{gs} - 1,$$

which are collected in the vector

$$\boldsymbol{z}^{(n)} = \begin{bmatrix} z^{(n,0)} & z^{(n,1)} & \ldots & z^{(n,P_{gs}-1)} \end{bmatrix}^\top.$$

In order to test GomSpace's carrier frequency offset etimator, which is described in Section 4.3, under different Eb/N0-values, an input-SNR (iSNR) is defined. Introducing T_{sym} as the symbol duration, the energy per symbol can be defined as

$$\tilde{E}_s = \int_{T_T^{(n)}}^{T_T^{(n)} + T_{sym}} |z^{(n)}(t)|^2 dt, \qquad T_T^{(n)} \leq t \leq T_T^{(n)} + T_{AIS},$$

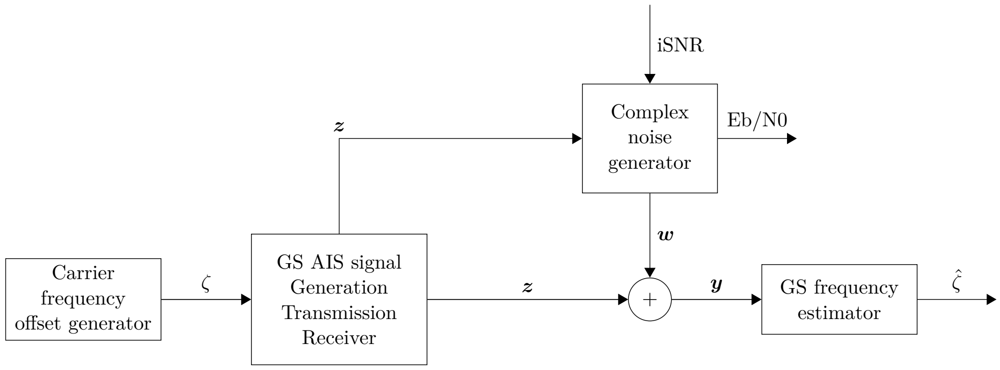

Figure L.3: Generation of carrier frequency offsets, AIS signals, noise, and carrier frequency offset estimate.

where $|\cdot|$ denotes the magnitude of a complex number. Moreover, the variance of $w(t)$ can be defined as

$$\tilde{\sigma}_w^2 = \int_{-B}^{B} S_w(f)df = B \cdot N_0,$$

where $S_w(f)$ is the power spectral density of $w(t)$ as shown in Figure L.4. For the remainder of this section, the superscript n is omitted, since this section is only concerned with the noise generation for a single AIS signal. With the above definitions, a continuous iSNR is defined as

$$iSNR_c = \frac{\tilde{E}_s}{\tilde{\sigma}_w^2}.$$

When the AIS signal is sampled, the discrete energy per symbol can be defined as

$$E_s = \sum_{m=0}^{M-1} |z^{(p)}|^2 \cdot T_s,$$

where M_s is the number of samples per symbol. An AIS message has 256 bits, and each bit corresponds to one symbol. Hence, in the case of GomSpace,

$$M_{gs} = \frac{P_{gs}}{256} = 4.$$

In this thesis, E_s is calculated as

$$E_s = \frac{1}{256} \sum_{p=0}^{P_{gs}-1} |z^{(p)}|^2 \cdot T_s. \tag{L.6}$$

Moreover, the discrete variance can be defined using the Figures L.5 and L.6. In Figure L.5, the frequency axis is a function of the sampling period, and in Figure L.6, the axis has been normalized by the sampling period. This yields

$$\sigma_w^2 = \int_{-\frac{1}{2}}^{\frac{1}{2}} \frac{N_0}{2} df = \int_{-B \cdot T_s}^{B \cdot T_s} \frac{N_0}{2} df = N_0 \cdot B \cdot T_s, \tag{L.7}$$

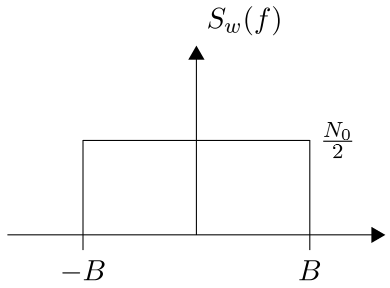

Figure L.4: PSD for $w(t)$.

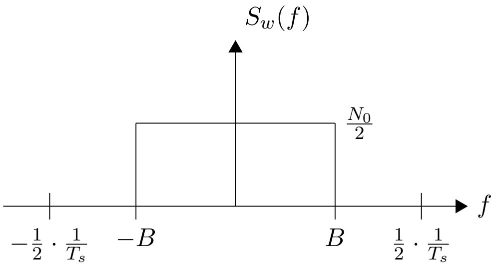

Figure L.5: PSD for $w(t)$.

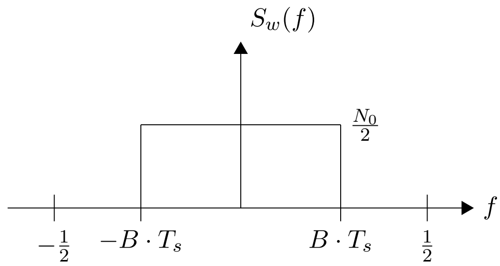

Figure L.6: PSD for $w(t)$.

and the discrete iSNR can be defined as

$$iSNR = \frac{E_s}{\sigma_w^2}. \tag{L.8}$$

In order to create a vector of zero-mean correlated noise samples, $\bar{\boldsymbol{w}} \in \mathbb{C}^{P_{gs}}$, the autocorrelation function is found from (L.3) as

$$r_{\bar{w}}[k] = r_{\bar{w}}\left(kT_s\right) = N_0 \frac{\sin\left(2\pi BkT_s\right)}{2\pi kT_s},$$

which gives the autocorrelation matrix as

$$\boldsymbol{R}_{\bar{w}} = \begin{bmatrix} r_{\bar{w}}[0] & r_w[1]^* & r_{\bar{w}}[2]^* & \dots & r_{\bar{w}}[P_{gs}-1]^* \\ r_{\bar{w}}[1] & r_{\bar{w}}[0] & r_{\bar{w}}[1]^* & \dots & r_{\bar{w}}[P_{gs}-2]^* \\ r_{\bar{w}}[2] & r_{\bar{w}}[1] & r_{\bar{w}}[0] & \dots & r_{\bar{w}}[P_{gs}-3]^* \\ \vdots & \vdots & \vdots & \ddots & \vdots \\ r_{\bar{w}}[P_{gs}-1] & r_{\bar{w}}[P_{gs}-2] & r_{\bar{w}}[P_{gs}-3] & \dots & r_{\bar{w}}[0] \end{bmatrix},$$

which, since the noise is zero-mean, is equal to the autocovariance matrix of $\bar{\boldsymbol{w}}$. In the autocorrelation matrix, the asterix denotes complex conjugation. Now, the noise is generated as

$$\bar{\boldsymbol{w}} = \boldsymbol{L}\boldsymbol{s}, \tag{L.9}$$

where $\boldsymbol{L}\boldsymbol{L}^H = \boldsymbol{R}_w$, in which $(\cdot)^H$ denotes the matrix conjugate transpose, and

$$\boldsymbol{s} = \boldsymbol{s}_r + j\boldsymbol{s}_i,$$

where

$$\boldsymbol{s}_r, \boldsymbol{s}_i \sim \mathcal{N}\left(\mathbf{0}, \frac{1}{2}\boldsymbol{I}\right).$$

Wanting to scale the noise generated in (L.9), the noise energy per symbol is defined as

$$E_n = \frac{1}{256}\sum_{p=0}^{P_{gs}-1} |\bar{w}^{(p)}|^2 \cdot T_s.$$

Moreover, defining a scaling constant

$$c = \frac{E_s}{E_n \cdot iSNR}, \tag{L.10}$$

the noise energy per symbol is scaled as

$$E_{n,scale}(c) = \frac{1}{256}\sum_{p=0}^{P_{gs}-1} |\sqrt{c} \cdot \bar{w}^{(p)}|^2 \cdot T_s. \tag{L.11}$$

From (L.8), (L.10), and (L.11) it is evident that $E_{n,scale}(c) = \sigma_w^2$, and hence, based on (L.7), the scaled version of N_0 is

$$N_{0,scale} = \frac{E_{n,scale}(c)}{B \cdot T_s}. \tag{L.12}$$

Lastly, the vector of correlated noise samples, $\boldsymbol{w} \in \mathbb{C}^{P_{gs}}$, with the desired Eb/N0 value relative to $\boldsymbol{z}$ is

$$\boldsymbol{w} = \sqrt{c} \cdot \bar{\boldsymbol{w}},$$

and the vector of AIS samples that is passed to GomSpace's carrier frequency offset estimator is

$$\boldsymbol{y} = \boldsymbol{z} + \boldsymbol{w}$$

Algorithm 6 Generating zero-mean correlated noise vector, $\boldsymbol{w} \in \mathbb{C}^P$

Input parameters: $\boldsymbol{z}$, $\boldsymbol{R}_{\bar{w}}$, B, $iSNR$, T_s.

Output: $\boldsymbol{w}$, $Eb/N0$.

1. Calculate E_s from (L.6).
2. Generate $\boldsymbol{s} = \boldsymbol{s}_r + j\boldsymbol{s}_i$ with $\boldsymbol{s}_r, \boldsymbol{s}_i \sim \mathcal{N}_P\left(\boldsymbol{0}, \frac{1}{2}\boldsymbol{I}\right)$.
3. Calculate $\boldsymbol{L}$ from $\boldsymbol{L}\boldsymbol{L}^H = \boldsymbol{R}_{\bar{w}}$.
4. Set $\bar{\boldsymbol{w}} = \boldsymbol{L}\boldsymbol{s}$.
5. Calculate E_n as $\frac{T_s}{256}\bar{\boldsymbol{w}}^H\bar{\boldsymbol{w}}$.
6. Calculate $c = \frac{E_s}{E_n \cdot iSNR}$.
7. Calculate $\boldsymbol{w} = \sqrt{c} \cdot \bar{\boldsymbol{w}}$.
8. Calculate $E_{n,scale}(c)$ according (L.11).
9. Calculate $N_{0,scale}$ according to (L.12).
10. set $N_0 = N_{0,scale}$.
11. Set $E_b = E_s$.

Notice that setting $E_b = E_s$ in the last step of the algorithm is valid when GMSK modulation is used. Using other modulation schemes, the relationship between E_b and E_s needs to be examined prior to carrying out the last step.

M | Azimuthal equidistant projection

Multiple projections for projecting points on a sphere onto a two dimensional plane exist. Each of these projections introduces some sort of distortion depending on which projection is used. Commonly used projections preserve properties such as area, distance, or shape [33, pp. 3-5] at the expense of distorting the others. This thesis utilizes the azimuthal equidistant projection (AEP), which, given a center point, preserve the distances between each projected point and the center point. Moreover, it ensures that all the projected points are at the correct azimuth relative to the reference point.

Given a reference point A, and two points B and C, the azimuth α from B to C is the angle between the great circle arcs AB and AC [33, p. 30], as illustrated in Figure M.1.

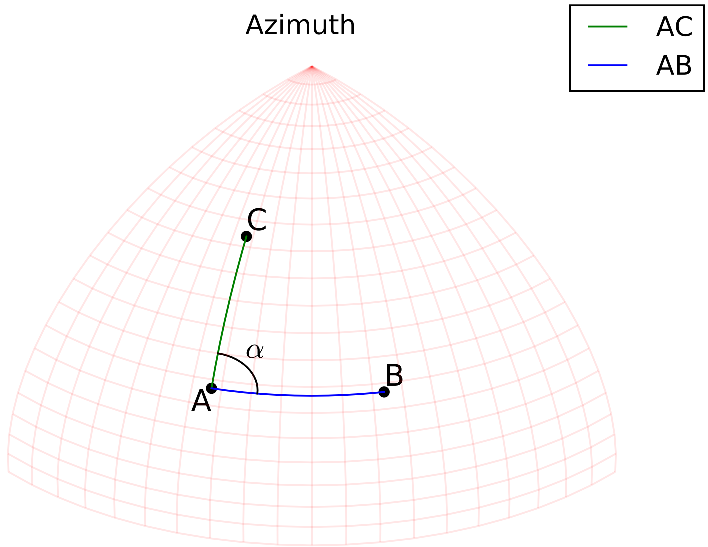

Figure M.1: Azimuth, α, between the great circle arcs spanned by the lines from A to C and A to B.

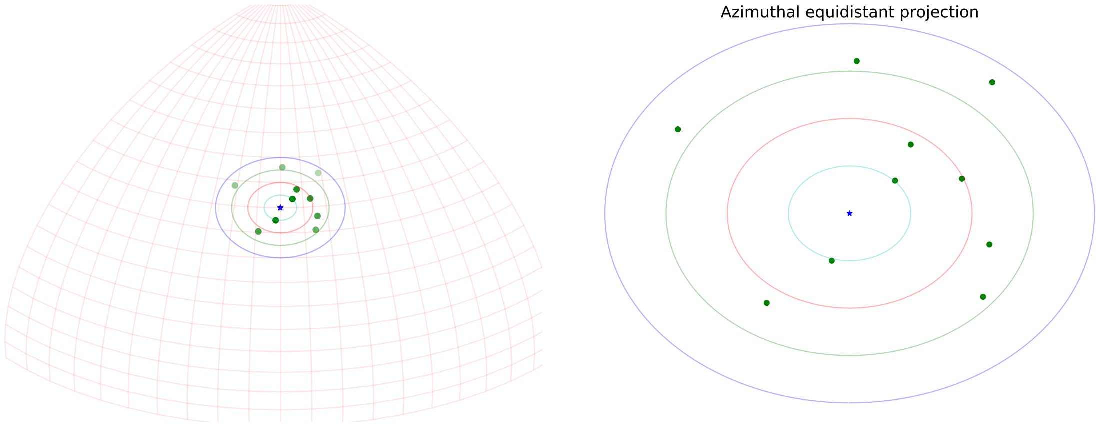

(a) **(b)**

Figure M.2: **(a)**: Points on the sphere and circles with different radii and center in the blue star. **(b)**: Azimuthal equidistant projection of the points and circles with blue star as center point.

Notice that distances and angles between two projected points, which are not the reference point, are distorted. An illustration of the projection can be seen in Figure M.2.

The procedure for using an AEP is to choose a point with geographical coordinates (θ_0, ϕ_0) on the sphere as the center point of the projection. Geographical coordinates are described in Section F.1. The (x, y)-coordinates of the projection of an arbitrary point given in geographical coordinates, (θ_g, ϕ_g), using the AEP, are given by [33, pp. 194-195]

$$x = r \cdot k \cdot \cos(\theta_g) \sin(\phi_g - \phi_0)$$
$$y = r \cdot k (\cos(\theta_0) \sin(\theta_g) - \sin(\theta_0) \cos(\theta_g) \cos(\phi_g - \phi_0)),$$

where r is the radius of the sphere,

$$k = \frac{c}{\sin(c)},$$

and

$$\cos(c) = \sin(\theta_0) \sin(\theta_g) + \cos(\theta_0) \cos(\theta_g) \cos(\phi_g - \phi_0).$$

N | Spoofing distance test for 6 and 2 s report interval results

This appendix shows the results from the spoofing distance tests carried out for when a vessel is moving at speeds corresponding to the report intervals of 6 and 2 s. The spoofing distance tests from which the results originate are described in Section 12.4.

N.1 Report interval 6 s

$t_r = 6$ s (Vessel position 1)										
d_s	Spoofing angles									
	0	1	2	3	4	5	6	7	8	9
0	0.2	0.0	0.0	0.0	0.0	0.0	0.0	0.0	0.0	0.0
0.5	0.1	0.1	0.1	0.0	0.0	0.0	0.0	0.2	0.0	0.1
5	0.1	0.0	0.8	0.0	1.8	0.9	0.0	0.0	1.3	2.0
10	57.9	0.1	9.2	81.9	19.8	99.8	1.0	32.4	44.3	100
15	100	100	94.6	100	100	100	47.8	59.8	100	100
20	100	100	100	100	100	100	98.5	100	100	100
25	100	100	100	100	100	100	100	100	100	100

Figure N.1: Table showing $\hat{S}$ for 10 different spoofing angles and different spoofing distances, d_s, for vessel position 1. Notice that d_s is given in km and the estimates $\hat{S}$ are given in percent. In all of the simulations, the number of received AIS messages was between 20 and 23.

$t_r = 6$ s (Vessel position 2)										
d_s	Spoofing angles									
	0	1	2	3	4	5	6	7	8	9
0	0.1	0.2	1.6	2.3	0.0	0.0	0.5	0.0	0.8	0.1
0.5	1.0	1.6	0.0	0.7	0.2	0.0	0.2	0.4	0.2	0.0
5	34.2	91.6	0.3	11.6	84.2	5.2	0.0	85.2	1.0	7.3
10	100	97.6	0.0	100	99.9	99.9	22.6	0.4	96.0	68.2
15	100	100	100	100	100	100	100	84.4	100	100
20	100	100	100	100	100	100	100	100	100	100
25	100	100	100	100	100	100	100	100	100	100

Figure N.2: Table showing $\hat{S}$ for 10 different spoofing angles and different spoofing distances, d_s, for vessel position 2. Notice that d_s is given in km and the estimates $\hat{S}$ are given in percent. In all of the simulations, the number of received AIS messages was between 44 and 46.

$t_r = 6$ s (Vessel position 3)										
d_s	Spoofing angles									
	0	1	2	3	4	5	6	7	8	9
0	0.2	0.7	0.3	0.0	0.0	0.0	0.0	0.1	0.0	0.0
0.5	0.0	0.1	0.2	0.3	0.0	0.2	0.0	0.3	0.0	0.1
5	0.0	0.1	13.1	0.0	0.0	25.8	69.7	97.0	13.3	0.3
10	67.4	100	100	0.0	0.4	1.0	100	96.1	86.5	0.1
15	99.3	100	99.7	18.0	0.3	96.7	100	100	100	35.5
20	100	100	100	100	0.0	100	100	100	99.5	21.3
25	100	100	100	100	0.0	100	100	100	100	63.8
30	100	100	100	100	0.0	100	100	100	98.7	0.6
35	100	100	100	100	2.25	100	100	100	100	98.1
40	100	100	100	100	12.6	100	100	100	100	99.7
45	100	100	100	100	100	100	100	100	100	96.2
50	100	100	100	100	92.3	100	100	100	100	100
55	100	100	100	100	75.3	100	100	100	100	100
60	100	100	100	100	100	100	100	100	100	100

Figure N.3: Table showing $\hat{S}$ for 10 different spoofing angles and different spoofing distances, d_s, for vessel position 3. Notice that d_s is given in km and the estimates $\hat{S}$ are given in percent. In all of the simulations, the number of received AIS messages was between 39 and 41.

$t_r = 6$ s (Vessel position 4)										
d_s	Spoofing angles									
	0	1	2	3	4	5	6	7	8	9
0	0.0	4.18	0.1	0.0	0.1	0.1	9.2	0.1	0.0	0.0
0.5	0.7	1.2	0.1	0.3	0.6	17.4	27.7	18.5	0.4	0.5
5	0.0	0.3	92.5	0.0	18.8	0.5	1.8	28.8	0.4	1.2
10	100	100	0.4	21.2	89	100	2.4	72.3	5.4	0.2
15	99.9	0.4	100	1.6	100	50.1	100	100	92.8	14.2
20	100	100	81.0	91.2	100	100	100	99.7	96.3	100
25	100	100	100	100	100	100	100	100	100	100

Figure N.4: Table showing $\hat{S}$ for 10 different spoofing angles and different spoofing distances, d_s, for vessel position 4. Notice that d_s is given in km and the estimates $\hat{S}$ are given in percent. In all of the simulations, the number of received AIS messages was between 45 and 47.

N.2 Report interval 2 s

$t_r = 2$ s (Vessel position 1)										
d_s	Spoofing angles									
	0	1	2	3	4	5	6	7	8	9
0	0.0	0.0	0.0	0.0	0.0	0.1	0.0	0.0	0.0	0.0
0.5	0.0	0.0	0.0	0.0	0.0	0.0	0.0	0.0	0.0	0.0
5	0.0	0.0	0.0	0.0	0.0	1.2	0.0	0.0	0.0	0.0
10	2.6	15.1	75.2	99.8	38.0	98.6	0.0	0.0	2.9	0.0
15	100	100	50.9	59.4	100	97.9	100	0.2	100	100
20	100	99.4	100	100	100	100	9.5	100	100	99.9
25	100	100	71.3	100	100	100	100	100	100	100
30	100	100	100	100	100	100	100	100	100	100
35	100	100	100	100	100	100	100	100	100	100

Figure N.5: Table showing $\hat{S}$ for 10 different spoofing angles and different spoofing distances, d_s, for vessel position 1. Notice that d_s is given in km and the estimates $\hat{S}$ are given in percent. In all of the simulations, the number of received AIS messages was between 64 and 73.

$t_r = 2$ s (Vessel position 2)										
d_s	Spoofing angles									
	0	1	2	3	4	5	6	7	8	9
0	0.0	0.0	0.0	0.0	0.0	0.0	0.0	0.0	0.0	0.0
0.5	0.0	0.0	0.0	1.6	0.3	0.0	0.0	0.2	0.0	0.0
5	0.0	0.1	0.0	0.2	0.0	85.5	0.0	1.2	0.0	0.0
10	100	0.0	0.0	72.4	0.7	14.4	0.0	89.5	1.4	48.7
15	94.5	99.0	93.4	94.4	75.8	55.8	100	99.3	100	100
20	100	100	100	100	100	100	100	100	100	100
25	100	100	100	100	100	100	100	100	100	100

Figure N.6: Table showing $\hat{S}$ for 10 different spoofing angles and different spoofing distances, d_s, for vessel position 2. Notice that d_s is given in km and the estimates $\hat{S}$ are given in percent. In all of the simulations, the number of received AIS messages was between 134 and 138.

$t_r = 2$ s (Vessel position 3)										
d_s	Spoofing angles									
	0	1	2	3	4	5	6	7	8	9
0	0.0	0.0	0.0	0.0	0.0	0.0	0.0	0.0	0.0	0.0
0.5	0.0	0.0	0.0	20.6	0.0	0.0	0.0	0.0	0.0	0.0
5	0.0	0.0	46.8	0.0	0.0	1.3	77.6	56.4	0.0	0.0
10	0.0	99.7	0.0	0.0	0.0	92.5	100	47.1	0.0	0.0
15	100	83.5	100	59.4	0.0	100	100	100	86.3	100
20	91.3	100	100	76.9	0.0	100	100	100	100	0.0
25	100	100	100	97.9	0.0	100	100	100	91.7	0.0
30	100	100	100	100	9.8	100	100	100	98.1	0.0
35	100	100	100	99.7	0.0	100	100	100	99.6	69.0
40	100	100	100	100	100	100	100	100	80.5	100
45	100	100	100	100	87.3	100	100	100	100	76.2
50	100	100	100	100	99.5	100	100	100	100	98.5
55	100	100	100	100	99.7	100	100	100	100	100

Figure N.7: Table showing $\hat{S}$ for 10 different spoofing angles and different spoofing distances, d_s, for vessel position 3. Notice that d_s is given in km and the estimates $\hat{S}$ are given in percent. In all of the simulations, the number of received AIS messages was between 120 and 125.

t_r = 2 s (Vessel position 4)										
d_s	Spoofing angles									
	0	1	2	3	4	5	6	7	8	9
0	0.0	0.0	0.0	0.0	0.0	0.0	0.0	0.0	0.0	0.0
0.5	0.0	0.0	0.0	0.0	0.0	0.1	0.1	0.0	0.1	0.0
5	0.5	0.0	0.4	0.2	0.0	1.0	0.0	0.0	13.3	0.5
10	0.7	36.7	0.0	6.8	16.2	1.5	0.0	45.2	0.0	97.5
15	0.0	0.1	100	96.3	94.2	0.0	0.0	0.0	99.4	100
20	99.3	78.2	2.2	95.3	100	100	100	1.1	99.9	100
25	100	100	0.9	100	100	100	100	81.7	100	100
30	100	100	100	100	100	100	100	100	100	100
35	100	100	100	100	100	100	100	100	100	100

Figure N.8: Table showing $\hat{S}$ for 10 different spoofing angles and different spoofing distances, d_s, for vessel position 4. Notice that d_s is given in km and the estimates $\hat{S}$ are given in percent. In all of the simulations, the number of received AIS messages was between 137 and 141.